Optimisation of a catalytic process for the CO2 purification derived from an oxyfuel combustion in the cement industry

Madan Behera

Thèse de Doctorat

Discipline : Chimie
Spécialité : Chimie théorique, physique, analytique

présentée à ***l'Ecole Doctorale en Sciences Technologie et Santé (ED 585)*** **de**
l'Université du Littoral Côte d'Opale
et
à l'Ecole doctorale en Sciences de l'Ingénieur et Technologie
de l'Université de Mons

par

Madan Mohan BEHERA

pour obtenir le grade de Docteur de l'Université du Littoral Côte d'Opale

Optimisation d'un procédé catalytique pour la purification du CO_2 issu de l'oxycombustion

Soutenue le 20 mars 2023, après avis des rapporteurs, devant le jury d'examen :

M^me^ Diane THOMAS, Professeur, Université de Mons	**Présidente**
M^me^ Valérie TSCHAMBER, Professeur, Université de Haute Alsace	**Rapportrice**
M^me^ Sabine VALANGE, Maître de Conférences HDR, Université de Poitiers	**Rapportrice**
M. André DECROLY, Professeur, Université de Mons	**Examinateur**
M. Thierry VISART DE BOCARME, Professeur, Université Libre de Bruxelles	**Examinateur**
M. Sébastien ROYER, Professeur, Université de Lille	**Examinateur**
M. Stéphane SIFFERT, Professeur, Université du Littoral Côte d'Opale	**Co-directeur**
M. Guy DE WEIRELD, Professeur, Université de Mons	**Co-directeur**
M. Christophe POUPIN, Maître de Conférences, Université du Littoral Côte d'Opale	**Membre Invité**

Acknowledgements

"*Life is a journey, not a destination.*"

—Ralph Waldo Emerson, *American essayist (1803-1882)*

As I worked toward my Ph.D., I was fortunate enough to cross paths with many wonderful people who have contributed to my development both at professional and personal level. I would like to begin by expressing my gratitude to my supervisors, Prof. Guy DE WEIRELD and Prof. Stéphane SIFFERT, for being such wonderful mentors and for providing me with ample amount of opportunities to learn and grow professionally. In addition, I'd like to express my gratitude to Dr. Christophe POUPIN for being an excellent advisor and for the many interesting brainstorming sessions on various scientific topics we had together that helped me achieve insightful results presented in my thesis. Lastly, I'd like to express my gratitude to the Région Hauts-de-France, Territoire d'Innovation de Grande Ambition (TIGA - Dunkerque l'énergie créative) and European Cement Research Academy GmbH, particularly Herr Martin Schneider and Herr Helmut Hoppe for their continuous technical and financial support.

Secondly, I'd like to express my gratitude to the President of the Jury, Prof. Diane THOMAS, for her guidance and input during the development of the kinetic model that forms an important part of this thesis, and for her insightful feedback during CSI/CAT meetings, which ultimately resulted in a stronger, more convincing thesis. In addition, I'd like to express my gratitude to Prof. Thierry VISART DE BOCARMÉ and Prof. André DECROLY, whose insightful questions and comments during our CSI/CAT meetings prompted me to consider certain aspect of the thesis from new perspectives. Moreover, I want to thank Prof. Sébastien ROYER for his contributions to this project in the form

of material synthesis and characterizations and for the productive interactions we had during our meetings. Last but not least, I'd like to express my gratitude to the *Rapportrices*, Prof. Valérie TSCHAMBER and Dr. Sabine VALANGE, for their time and effort in reviewing my thesis.

Thirdly, I am thankful to Prof. Marco DATURI at ENSICAEN (Caen, Normandy) for providing me with an opportunity to perform operando-infrared studies on my catalyst and Dr. Nuria Garca Moncada (then a Postdoctoral Researcher at ENSICAEN) for guiding me during the experiments. Moreover, I'd like to extend my gratitude to Dr. Carmen CIOTONEA (then Research Engineer at Université de Lille and now Assistant Professor at ULCO) for her help with the material synthesis and characterizations and for the discussions over our common love for different international cuisines.

Finally, I'd like to express my gratitude to *mes petites familles* who hosted me in Dunkerque and Mons and provided the warmth and support I needed during my stay. Thank you to everyone who has helped me out along the way: Muriel (for everything except the soup), Rebecca (for unwavering support through depressing quotes and funny instagram reels), Aida (for frequent invitations to coffee breaks), Thamy (for being a fantastic co-passenger in this bumpy ride), Mariebelle (for finger-licking food), Guillaume (for being the partner in craziness), Mahdi, Caroline, and Manon (for cheering me up at my lows by getting high together), Michel (for being a helpful friend), Sharad bhai (for being the elder brother I needed), Rita (for being a great friend) and Lilian (for the help in my thesis). Moreover, I would also like to thank Lucette for her continuous support in the lab and Prof. Renaud COUSIN and Prof. Cédric GENNEQUIN for the productive discussions we had in the lab. Further, I'd also like to express my gratitude to my colleagues: Dharmendra bhai, Atul Bhai, Julian, Miriam, Abir, Layla, Mireille, Shivani, Pedro, Nancy, Bastien, Margaux, Tarek, Somnath bhai, Lamia, and Marc for all the fun and house parties we had in Dunkerque. Furthermore, I am also thankful to my family in Mons: Eric, Rania, Adrien, Alexis, Simone, Valentin, Arnaud, Haidar, and Damien, for educating me about Belgian beers and culture and providing me with invaluable assistance during my thesis. In addition, I appreciate the encouragement and help I received from Rita, Dr. Nicolas HEYMANS, Dr. Marie-Eve DUPREZ, Dr. Lionel DUBOIS, Prof. March FRERE, Prof. Anne-Lise

HANTSON, Claudine, Oleksandr, Matthieu, and Christophe during my thesis. Finally, I'd like to express my gratitude to *mes frères*: Ozan, Martin, and Otmane, for all the valuable memories, fun and trips we had together.

Lastly, I'd like to express my gratitude to everyone who believed in me and supported me whenever I reached out for help: my mom and dad, my sister, my buddies back home (Akash, Sandy, and Lalit) and my small family in Germany (Sambit bhai, Anurag, Pranita, Asish, Binita, Saurav bhai, and Swikruti bhauja).

The only true wisdom is in knowing you know nothing. True wisdom comes to each of us when we realize how little we understand about life, ourselves, and the world around us.

Socrates

Abstract

Removal of NO_x from the industrial flue gas (*CO_2-purification* stage) prior to Carbon Capture Utilisation and Storage is important in order to avoid especially downstream corrosion and amine degradation. In this thesis, catalytic reduction of NO to non-toxic N_2 using CO, a co-existing gas component in the industrial flue gas stream, as a reductant has been proposed for NO_x removal step. The main objective of this study was to develop copper-cobalt-based materials as economically feasible and stable catalysts for the NO reduction by CO. This study outlines the development of catalytic material from Cu_6Al_2 mixed oxides derived from their Layered Double Hydroxides parent via thermal treatment under different gas atmospheres and then, studying the effect of Co content in the mixed oxides on the catalytic performance followed by the influence of treatment temperature on the catalytic performance. These investigations concluded that Co_4Cu_2Al mixed oxide material treated under the flow of CO_2 at a temperature of 400°C is the best catalyst for the NO reduction by CO reaction under the industrial flue gas condition. Moreover, the catalyst stability was confirmed by 6 cycles of light-off experiments. Furthermore, the catalytic performance of Co_4Cu_2Al sample was compared with commercial Pt supported on CeO_2 and Al_2O_3 and was found that the former shows superior catalytic activity than the latter. In addition, a kinetic model was developed for the reaction system using Langmuir Hinshelwood Hougen Watson kinetics and different global optimization solvers for parameter regression. Finally, the best catalyst has been synthesized and shaped as extrudes on a large scale to be used in a semi-pilot plant setup. Finally, this study also explored the activity of $La_yCo_{1-x}Cu_xO_3$ (y = 0.85 or 1; x = 0, 0.1, 0.2 and 0.25) perovskites for the NO reduction by CO reaction under industrial flue gas condition and were found

to be active but require further optimization in the material composition for superior catalytic activity and additional material characterization for in-depth understanding for the underlying reaction mechanism.

Keywords: CO_2 purification, heterogeneous catalysis, $DeNO_x$, reaction kinetics

Résumé

L'élimination des NO_x des gaz de combustion industrielle (étape de *purification du CO_2*), avant l'étape de capture, d'utilisation et de stockage du carbone, est importante en particulier pour éviter la corrosion et la dégradation des amines en aval. Dans cette thèse, la réduction catalytique de NO en N_2 non toxique, en utilisant le CO comme réducteur qui est un composant gazeux coexistant dans le flux de gaz de combustion industrielle, a été proposée pour l'étape d'élimination des NO_x. L'objectif principal de cette étude était de développer des matériaux à base de cuivre-cobalt comme catalyseur stable et économique pour la réduction du NO par le CO. Cette étude décrit le développement d'un matériau catalytique à partir d'oxydes mixtes Cu_6Al_2 dérivés de leurs hydroxydes doubles lamellaires par traitement thermique sous différentes atmosphères gazeuses, puis l'étude de l'effet de la teneur en Co dans les oxydes mixtes sur la performance catalytique, suivie de l'influence de la température de traitement sur la performance catalytique. Ces recherches ont conclu que le matériau d'oxyde mixte Co_4Cu_2Al traité sous le flux de CO_2 à une température de 400°C est le meilleur catalyseur pour la réduction de NO par la réaction de CO dans les conditions d'émissions industrielles. De plus, la stabilité du catalyseur a été confirmée par 6 cycles d'expériences. En outre, la performance catalytique de l'échantillon de Co_4Cu_2Al a été comparée à celle du Pt commercial supporté sur CeO_2 et Al_2O_3 et il a été constaté que le premier montre une activité catalytique supérieure à celle du second. En outre, un modèle cinétique a été développé pour le système réactionnel en utilisant la cinétique de Langmuir Hinshelwood Hougen Watson et différents solveurs d'optimisation globale pour la régression des paramètres. Enfin, le meilleur catalyseur a été synthétisé et mis en forme d'extrudés à grande échelle pour être utilisé dans une installation semi-pilote. Enfin, cette

Résumé

étude explore également l'activité des pérovskites $La_yCo_{1-x}Cu_xO_3$ (y = 0,85 ou 1 ; x = 0, 0,1, 0,2 et 0,25) pour la réduction du NO par la réaction du CO dans des conditions d'émissions industrielles. Ces pérovskites se sont avérées actives mais nécessitent une optimisation supplémentaire de la composition des matériaux pour une activité catalytique supérieure et des caractérisations supplémentaires pour une compréhension approfondie du mécanisme de réaction sous-jacent.

Mots-clés: Purification du CO_2, catalyse hétérogène, $DeNO_x$, cinétique de réaction

Contents

List of Tables

List of Figures

List of Abbreviations

$\boldsymbol{\theta_i}$	Fraction of available number of active sites covered by gas or intermediate species i, mol.kg_{cat}^{-1}
$\boldsymbol{\theta}$	Fraction of available number of active sites that are vacant, mol.kg_{cat}^{-1}
$\boldsymbol{\theta_t}$	Total number of active sites available in the catalyst, mol.kg_{cat}^{-1}
$\boldsymbol{\vartheta_i}$	Stoichiometric coefficient of the product i from the reactions
$\boldsymbol{\Delta}[\mathbf{S}]$	Adsorbed state of component Δ (Δ = reactant gas component, intermediate species or product gas component)
α_i	a group of reaction, adsorption, desorption and equilibrium constants as a function of temperature according to Arrhenius relation.
A	Frequency coefficient, $\mathrm{s}^{-1}.{\mathrm{g}_{\mathrm{cat}}}^{-1}.\mathrm{mol}^{-1}$
BET	Brunauer-Emmett-Teller
BJH	Barrett-Joyner-Halenda Analysis
CCUS	Carbon Capture Utilisation or Storage
CoCu-X	Cobalt Copper Aluminium Mixed Oxide derived from their hydrotalcite precursors after CO_2-treatment at X°C (X = 400 or 500)

CuAl-X	Copper Aluminum mixed oxide treated with X gas (X = CO/He, CO_2, He and air)
$Co_{6-x}Cu_xAl$	Copper Cobalt Aluminium Mixed Oxides derived from their hydrotalcite precursors after CO_2-treatment at 500°C (x = 0, 2, 4 or 6)
D_{BJH}	Average pore size measured by BJH method applied to the desorption branch
D_{CuO}	Average crystal domain size calculated using Debye-Scherrer equation based on (111) peak of 35° of the CuO pattern with Warren's correction
DRIFTS	Diffuse Reflectance Infrared Fourier Transmission Spectroscopy
Ea	Activation energy, $kJ.mol^{-1}$
ER	Eley-Rideal Kinetic Model
F_i	Molar flow rate of component i at the reactor outlet, $mol.s^{-1}$
F_o	Total molar feed flow rate, $mol.s^{-1}$
FTIR	Fourier Transform Infrared Spectroscopy
F_{obj}	Objective function
F_T	Total molar flow rate at the reactor outlet, $mol.s^{-1}$
GHSV	Gas Hourly Space Velocity, h^{-1}
H_2-TPR	H_2-Temperature Programmed Reduction
JCPDS	Joint Committee on Powder Diffraction Standards
k_i^f , k_i^b	Reaction Rate Constant for the rate-determining step i in either forward (f) or backward (b) direction
K_i^{ads} , K_i^{des}	Adsorption (ads) or Desorption (des) constant for the gas component i

$\mathbf{K_i^{eq}}$	Equilibrium (eq) constant for the reaction i (i = NO-O (NO oxidation to NO_2), CO-NO (NO reduction by CO) and CO-O (CO oxidation to CO_2)
$\mathbf{K_{p,\alpha}}$,$\mathbf{K_{p,\beta}}$, $\mathbf{K_{p,\gamma}}$	Equilibrium constants for NO reduction by CO, CO oxidation to CO_2 and NO oxidation to NO_2
LDH	Layered Double Hydroxides
LHHW	Langmuir-Hinshelwood-Hougen-Watson Kinetic Model
$\mathbf{N_{comp}}$	Number of gas components in the reaction system
$\mathbf{N_{exp}}$	Total number of rows in the experimental data matrix
$\mathbf{n^{inlet}}$ **(and** $\mathbf{n^{outlet}}$**)**	Number of moles of a gas component at the inlet (and outlet) of the reactor
$\mathbf{O_{ads}}$	Adsorbed state of oxygen atom on the catalytic surface
$\mathbf{P_o}$	Ambient pressure (1 bar)
$\mathbf{P/P_0}$	Ratio between the absolute to the saturation pressure
$\mathbf{P_i}$	Partial Pressure of gas component i, Pa
R	Universal gas Constant, $J.mol^{-1}.K^{-1}$
$\mathbf{R^2}$	Coefficient of Determination
RDS	Rate-Determining Step
$\mathbf{r_N}$, $\mathbf{r_{CO_2}}$, $\mathbf{r_{NO_2}}$	Reaction Rate, $mol^{-1}.s^{-1}.g_{cat}^{-1}$
$\mathbf{r_N^{net}}$, $\mathbf{r_{CO2}^{net}}$, $\mathbf{r_{NO2}^{net}}$	net reaction rate for NO reduction, CO oxidation and NO oxidation, $mol.g^{-1}.s^{-1}$
[S]	Vacant active site on the catalyst
$\mathbf{S_{BET}}$	Specific surface area determined by BET method, $m^2.g^{-1}$
$\mathbf{S_i}$	Selectivity towards component i

SSA	Specific Surface Area, $m^2.g^{-1}$
T_{50} (or T_{90})	Temperature for 50 % (or 90 %) conversion of CO to CO_2
TCD	Thermal Conductivity Detector
TGA	Thermo-Gravimetric Analysis
TPD	Temperature Programmed Desoprtion
V_μ	Micropore volume measured by t-plot method, $cm^3.g^{-1}$
V_p	Total pore volume measured at $P/P_0 = 0.98$, $cm^3.g^{-1}$
w_{cat}	Catalyst weight, g
$x_{i,j}^{exp}$, $x_{i,j}^{cal}$	Experimental or Calculated fractional conversion of component i corresponding to row number j of the experimental data matrix
X_i	Molar conversion of a component i
XANES	X-ray Adsorption Near-Edge Structure
XRD	X-Ray Diffraction
Y_i	Yield of component i

Chapter 1

Introduction and Thesis Outline

Global warming has become one of the most concerning problems across the globe. The uncapped release of greenhouse gases like the two major: carbon dioxide (CO_2) and methane (CH_4) (refer to Figure1.1) from anthropogenic sources has, both directly and indirectly, affected the living ecosystem on the earth. The uncapped emissions of these greenhouse gases have resulted in an alarming rise in the global temperature, which has resulted in intense droughts and heat waves, a more extended wildfire season, stronger storms, and a rise in the sea level due to the melting of the polar ice caps [1]. Therefore, it has become the top−most priority to take up drastic steps to mitigate the emissions of these greenhouse gases (GHGs) so as to restrict the global rise in temperature well within 1.5°C compared to pre-industrial levels as agreed upon in the Paris Agreement in the Conference Of the Parties (COP21) in November 2015 and reaffirmed in the COP26 summit held in Glasgow in 2021.

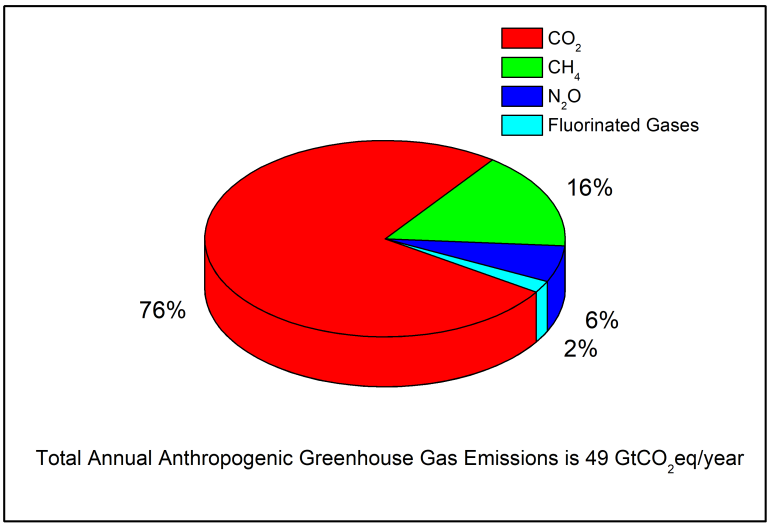

Figure 1.1 Total annual anthropogenic greenhouse gas emissions by groups of gases in 2010

1.1 Carbon Dioxide Emissions

CO_2 is one of the major greenhouse gases emitted from anthropogenic sources (see Figure1.1 – the data has been retrieved from the IPCC 5th Assessment Report published in 2014 [2]). The amount of anthropogenic CO_2 emissions into the atmosphere has risen from 27 Gt CO_2eq/year in 1970 to 49 Gt CO_2 eq/year in 2010 with an annual increase of 2.2% per year from 2000-2010 [2]. Moreover, a major part of these emissions is from power (40%), transportation (23%) and industrial (23%) sectors [3]. Therefore, in order to mitigate the greenhouse gas emissions into the atmosphere, it is important to mitigate the CO_2 emissions from the different economic sectors.

1.2 Cement Industries

According to International Energy Agency (IEA) [4], cement is the second largest direct CO_2-emitting industrial sector after iron and steel followed by other industries like textiles and beverages (26%), chemicals (15%), aluminium (3%) and Paper and Pulp industries (2%). Moreover, a part of these direct emissions is process emissions (65% for cement industries which amounts to 1.4 Gt/CO_2 eq/year in 2017 [4]) that result from the different physical and

chemical reactions during the industrial process. These emissions are hard to avoid and simply switching to renewable fuels will not help in mitigating these emissions. Therefore, Carbon Capture, Utilisation and Storage (CCUS) units need to be integrated with such processes to lower the carbon footprint of the final product.

In the case of the cement industries, the major CO_2 – producing step is the calcination of limestone ($CaCO_3$) at a temperature above 900°C (see Eq.1.1) [5]. The flue gas from the cement industries, therefore, consists of at least 18-20 vol% of CO_2, depending on the process of operation. which is higher than that in the flue gas from conventional power plants (8-11 vol%) [6]. To mitigate these CO_2 emissions, the Global Cement and Concrete Association (GCCA) ˘ an organisation representing 80% of the cement and concrete industries outside of China, has put forward a roadmap to develop net−zero cement and concrete products for the world until 2050 which can potentially reduce 36% of CO_2 emissions by integrating CCUS units with the cement industries [7].

$$CaCO_3 \xrightarrow{T>900^\circ C} CaO + CO_2 \tag{1.1}$$

1.3 Carbon Capture, Utilisation and Storage (CCUS)

CCUS technologies aim to capture the CO_2 from the targeted gas streams and transport it to either storage sites which are generally under geological formations or use it as a resource to create various valuable products such as syngas, formic acid, methanol etc.

Furthermore, three basic technologies are known to capture CO_2 [8]:

1. **Pre-combustion Capture**: This technology is applied before the fuel combustion step to produce fuels which are carbon-free. This technology is generally applied in the sectors like chemicals, fertilizers and synthetic fuels where hydrogen production and removal of CO_2 from the syngas is an important step.
2. **Oxyfuel Combustion**: In this technology, the fuel is combusted in an excess of oxygen instead of the ambient air. This means nitrogen is removed from the air in an additional separation plant before being used

in the combustion (or calcination in case of cement industries) process. This increases the CO_2 concentration in the flue gas significantly. Moreover, based on the composition of the CO_2 in the flue gas mixture (which is directly related to the O_2 concentration in the combustion chamber), this oxyfuel combustion technology can be categorised as partial oxyfuel combustion (20-60 vol% of CO_2) and oxycombustion (> 80 vol% of CO_2).

3. **Post-combustion capture**: In this technology, the carbon capture step is after the combustion or CO_2-producing process. The efficiency of the post-combustion capture process increases with an increase in the CO_2 concentration in the flue gas stream.

1.4 Importance of CO_2−Purification

Apart from CO_2, the flue gas from different industries consists of NO_x, O_2 and H_2O in different concentrations [6,9]. Out of these gas components, NO_x is identified as toxic both for human life and the carbon capture process and therefore, need to be removed from the flue gas before introducing it into the carbon capture step. In the post-combustion capture process, the presence of NO_x can react with the CO_2- absorbing amine solvents to form the nitrosamines and nitramines thereby affecting the efficiency of the carbon capture process [10]. In the case of oxycombustion process, the presence of NO_x can affect the CO_2-storage into geological structures due to the reaction with rocks thereby affecting the injectivity and storage integrity [11]. Also, in case of CO_2 leakage, toxic NO_x can be released into the environment [11]. Moreover, the presence of water in the flue gas can react with the NO_x to form an acidic mixture which can corrode the inner walls of the gas pipelines and also affects the CO_2 sequestration process [12,13]. Therefore, it is important to install a 'CO_2-purification' step before the carbon capture to remove this toxic NO_x component from the gas mixture that is further fed to the CCUS facility. This CO_2−purification can be achieved by different strategies namely: (1) Sour Compression: it uses a stripping medium (generally water) which absorbs NO_x from the flue gas at a pressure of 15-30 bars and forms acidic mixtures due to the formation of HNO_3 and HNO_2 thereby '*denitrifying*' the flue gas [13,14] and (2) Selective Catalytic Reduction (SCR) of NO by CO, a reductant that co-exists along with NO in the flue gas stream, into N_2 and

CO_2 [15] or by addition of NH^3 into the reaction system [16]. Moreover, this *denitrifying* step is generally accompanied by a dehydration unit which uses a solid adsorbent to remove water from the flue gas followed by a cryogenic unit which removes the residual inert gases from the flue gas mixture [13]. In this thesis, the focus will be on the catalytic reduction of NO by CO under industrial flue gas conditions.

As seen in the previous sections of this chapter, CCUS is important for cement industries in order to mitigate a majority of the associated CO_2 emissions. For this reason, European Cement Research Academy (ECRA) GmbH (Düsseldorf, Germany), an organisation of 40 leading cement producers of the world, has taken the initiative to develop state-of-the-art CO_2 capture, storage and utilisation strategies and technologies specifically for the cement industries. As a part of this initiative, an ECRA Chair has been constituted at Université de Mons (Mons, Belgium) to explore and develop different strategies and technologies in the field of carbon capture for different industrial sectors, especially cement. As a part of the research activities, this thesis explores the viability of the catalytic reduction technique for NO_x removal from the industrial flue gas as a step in CO_2-purification for carbon capture. Moreover, the different milestones of this thesis have been achieved by the close collaboration between Université du Littoral Côte d'Opale (Dunkerque, France) and Université de Mons (Mons, Belgium).

1.5 Thesis Objectives

The removal of the NO from the flue gas can be achieved by reducing NO to non-toxic N_2 with the help of a reductant like CO over a suitable catalyst. This reaction between NO and CO is henceforth indicated as the 'CO + NO' reaction. The main advantage of such a reaction is the simultaneous removal of CO and NO, both of which are toxic to the environment and human health. However, the presence of O_2, H_2O and CO_2 in the flue gas stream can affect the catalytic performance in reducing NO. Therefore, the main objective of this project is to develop an inexpensive catalyst (keeping in mind the industrial-scale application of this catalytic NO removal process) that showcases high NO reduction activity under oxidative and wet reaction conditions. In order to achieve this objective, the following milestones were realized:

1. Synthesis of probable catalysts suitable for NO removal at a lab−scale;
2. Material characterisation of the catalyst to investigate the corresponding catalytic activity;
3. Investigating the effect of the reactant gas composition on the activity of the best-performing catalyst and its stability with respect to catalytic test cycles;
4. Comparison of activities between the '*lab−synthesized*' and a commercial catalyst;
5. Development of a kinetic model for the reaction system and determination of model parameters through regression.

1.6 Thesis Outline

This thesis is divided into 5 chapters. The first chapter (Chapter 2) includes a bibliographic study of different catalytic materials, their preparation methodologies and pre−treatment protocols. Moreover, the chapter also discusses the NO reduction by CO reaction, the effect of other gas components like O_2, H_2O and CO_2 on the catalytic activity and outlines the different possible intermediate reaction steps and kinetic models for the NO reduction by CO reaction system and a brief overview of global optimization methods for determination of model parameters.

In Chapter 3, the synthesis protocols for layered−double hydroxides (LDH) and perovskites, conditions for different material characterization techniques and test parameters of catalytic activity experiments are presented.

In Chapter 4, the impact of the gas treatment of copper−aluminium−based LDH (CuAl−LDH) on the NO reduction by CO activity is discussed. The parent LDH was treated under different treatment gases like air, He, 1 vol% CO/He and CO_2 and was tested for its catalytic performance. The materials were further characterized for their composition, textural and reducibility properties. Upon comparison of catalytic activities, the CO_2 treatment was found to be effective for NO reduction by CO activity. The chapter further discusses the effect of the inclusion of second active metal i.e., Co, during the LDH synthesis on the NO reduction by CO activity. Furthermore, the

chapter also discusses the effect of different parameters like the content of Co in the mixed oxide and treatment temperatures on the catalytic activity. Various material characterization experiment results are also discussed in this chapter to comprehend the corresponding catalytic performances of the catalytic materials. Finally, the chapter also mentions the comparison between the best−performing Co_4Cu_2Al mixed oxide and commercially available supported precious metal (Pt) catalysts.

In Chapter 5, the effect of the reactant gas composition on the best performing catalytic material, Co_4Cu_2Al mixed oxide, is studied. In addition, the chapter mentions the development of different expressions of mathematical models based on the Langmuir Hinshelwood Hougen Watson (LHHW) kinetics and discusses about the strategy for effective parameter regression to investigate the fitness of the kinetic model to the available experimental data. The chapter also describes the parameters for large−scale synthesis of LDH form of Co_4Cu_2Al and the methodology for shaping of this material into extrudes.

Finally, in Chapter 6, the catalytic tests and material characterization of various potential perovskite materials are discussed. The chapter includes a non-exhaustive list of potential perovskite material compositions for NO reduction by CO activity and briefly discusses the effect of material composition and reactant gas composition on the NO reduction activity under industrial flue gas conditions.

References

[1] H.-O. Pörtner, D.C. Roberts, M. Tignor, E.S. Poloczanska, K. Mintenbeck, A. Alegría, M. Craig, S. Langsdorf, S. Löschke, V. Möller, A. Okem, B. Rama, IPCC, 2022: Climate Change 2022: Impacts, Adaptation and Vulnerability (Sixth Assessment Report), 2022. https://doi.org/10.1017/9781009325844.Front.

[2] O. Edenhofer, Y. Sokona, J.C. Minx, E. Farahani, S. Kadner, K. Seyboth, A. Adler, I. Baum, S. Brunner, B. Kriemann, J. Savolainen Web Manager Steffen Schlömer, C. von Stechow, T. Zwickel Senior Scientist, Climate Change 2014 Mitigation of Climate Change Working Group III Contribution to the Fifth Assessment Report of the Intergovernmental Panel on Climate Change, 2014.

[3] International energy Aganecy, Global energy-related CO_2 emissions by sector Analysis Data and statistics, Int. Energy Agency. (2022).

[4] International Energy Agency;, Transforming Industry through CCUS, 2019. https://doi.org/10.1787/09689323-en.

[5] E. Worrell, L. Price, N. Martin, C. Hendriks, L.O. Meida, Carbon Dioxide Emissions From the Global Cement Industry, 2001.

[6] A. Cores, L.F. Verdeja, S. Ferreira, Í. Ruiz-Bustinza, J. Mochón, J.I. Robla, C.G. Gasca, Iron ore sintering. Part 3: Automatic and control systems, DYNA. 82 (2015) pp. 227–236. https://doi.org/10.15446/dyna.v82n190.44054.

[7] GCCA, Concrete Future - The GCCA 2050 Cement and Concrete Industry Roadmap for Net Zero Concrete, Glob. Cem. Concr. Assoc. (2021) 48.

[8] A. Bannon, Colm, J. Damtoft, E. Geraghty, G. Kirchner, H. Kosmatka, Steven, R. Leese, H. Möller, M. Schneider, G. Spicher, R. van de Meer, P. Zelano, Carbon Capture Technology-Options and Potentials for the Cement Industry, Düsseldorf

(Germany), 2007. www.ecra-online.org.

[9] L. Dubois, S. Laribi, S. Mouhoubi, G. De Weireld, D. Thomas, Study of the Post-combustion CO_2 Capture Applied to Conventional and Partial Oxy-fuel Cement Plants, Energy Procedia, Elsevier Ltd, 2017: pp. 6181–6196. https://doi.org/10.1016/j.egypro.2017.03.1756.

[10] J. Wang, D. Ryan, E. J. Anthony, N. Wildgust, T. Aiken, Effects of Impurities on CO_2 Transport, Injection and Storage, Energy Procedia, 2011, pp.3071–3078.
https://doi.org/10.1016/j.egypro.2011.02.219

[11] A. Heydari-Gorji, Y. Belmabkhout, A. Sayari, Polyethylenimine-impregnated mesoporous silica: Effect of amine loading and surface alkyl chains on CO_2 adsorption, Langmuir. 27 (2011) 12411–12416. https://doi.org/10.1021/la202972t.

[12] B. Sass, B. Monzyk, S. Ricci, A. Gupta, B. Hindin, N. Gupta, Chapter 17 - Impact of SO_x and NO_x in Flue Gas on CO_2 Separation, Compression, and Pipeline Transmission A2 - Thomas, David C. BT - Carbon Dioxide Capture for Storage in Deep Geologic Formations, Carbon Dioxide Capture Storage Deep Geol. Form. 2 (2005) pp. 955–981.

[13] L.T. Murciano, V. White, F. Petrocelli, D. Chadwick, Sour compression process for the removal of SO_x and NO_x from oxyfuel-derived CO_2, Energy Procedia. 4 (2011) pp. 908–916. https://doi.org/10.1016/j.egypro.2011.01.136.

[14] N. Meunier, S. Laribi, L. Dubois, D. Thomas, G. De Weireld, CO_2 capture in cement production and re-use: First step for the optimization of the overall process, Energy Procedia. 63 (2014) pp. 6492–6503.
https://doi.org/10.1016/j.egypro.2014.11.685.

[15] M.M. Behera, C. Ciotonea, L. Olivet, L. Tidahy, S. Royer, D. Thomas, R. Cousin, G. De Weireld, C. Poupin, Impact of gas treatment of CuAl-LDH on

NO reduction by CO under oxidative conditions, Chem. Eng. J. 452 (2023). https://doi.org/10.1016/j.cej.2022.139543.

[16] L. Xu, C. Shi, B. Chen, Q. Zhao, Y. zhu, H. Gies, F.S. Xiao, D. D. Vos, T. Yokoi, X. Bao, U. Kolb, M. Feyen, S. Maurer, A. Moini, U. Müller, W. Zhang, Improvement of catalytic activity over Cu–Fe modified Al-rich Beta catalyst for the selective catalytic reduction of NO_x with NH_3, Microporous and Mesoporous Materials 236 (2016) pp. 211-217. https://doi.org/10.1016/j.micromeso.2016.08.042

Chapter 2

Literature Studies

The focus of this thesis is to remove NO from industrial flue gas as a step in CO_2-purification. One of the promising way to accomplish this treatment is by converting NO into non-toxic N_2 using CO as the reductant over an appropriate catalyst. The equation for the reaction between NO and CO is Eq.2.1.

$$CO + NO \rightarrow \frac{1}{2}N_2 + CO_2 \tag{2.1}$$

Since the turn of the last century, this CO+NO reaction has been put to use, most notably in catalytic converters for the treatment of automobile exhaust gases [1-5]. In such catalytic converters, platinum group metals (PGM) catalysts (such as Pt, Pd, and Rh) supported on materials such as alumina are used. These catalysts, collectively known as *three-way catalysts'*, are effective at removing NO by converting it to non-toxic N_2 (also oxidizes CO and hydrocarbons), but they are also expensive, making their use in industrial-scale applications economically challenging. In addition, the presence of a large amount of O_2 in the industrial flue gas stream may reduce the NO reduction activity of these catalysts because, under lean-burn conditions, the three-way catalysts act as an oxidation catalyst, oxidizing NO_x to NO_2 rather than reducing it [6]. Because of this, it is crucial to discover a less expensive and efficient substitute for PGMs in facilitating the CO + NO reaction under lean-burn conditions.

According to reports, transition metal oxides (Cu, Co, Mn, etc.) exhibit equivalent NO reduction activity and are less expensive than their precious-metal counterpart. Numerous research on NO reduction activity over transition metal-based catalysts under various reaction conditions have been published in the scientific literature. In the sections that follow, different factors that affect the NO-Selective Catalytic Reduction (*SCR*) activity of the transition-metal based catalysts are discussed.

2.1 Catalysts for NO-SCR by CO

In this section, two different types of studies related to reactant gas mixtures are considered: (1) CO, NO and an inert gas such as He or Ar (see Table 2.1) and (2) CO, NO and other gas components like O_2, H_2O, CO_2 along with an inert gas vector (see Table 2.2). Factors such as active metal loading, the composition of active metals in the catalyst, reaction temperature, catalyst preparation method, and composition of reactant feed gas mixture influence NO-SCR by CO activity over heterogeneous catalysts, especially transition-metal-based catalysts. Finding the *sweet spot* between catalyst composition and synthesis parameters is essential for maximizing catalytic activity. The effect of these variables on NO-SCR activity has been the subject of numerous studies. This section provides a brief overview of these studies and their corresponding conclusions.

2.1.1 Effect of Active metal Loading

The concentration of metal(s) active for SCR activity in the material greatly affects its catalytic performance. Simply increasing the metal loadings may or may not improve the catalytic activity [7-12]. The studies in the literature have reported that there is an optimum active metal loading for maximum NO-SCR activity and increasing the metal loading further will deteriorate the NO-SCR activity. The increase in NO-SCR activity is due to the increase in the number of active sites in the catalyst (given by the increase in metal loading), however high metal loadings lead to the agglomeration of the active metal particles and leading to an increase in particle size and lowering of SCR activity.

Hu et al. [7] studied NO-SCR activity over (1.5-27 wt%) CuO supported on Al_2O_3 (and CeO_2) catalytic samples and reported that catalytic activity

increased with the increase in the metal loading up until 11 wt% for CuO supported on Al_2O_3 (and 4.85 wt% for CuO supported on CeO_2) sample and then decreased due to the formation of large crystalline CuO species. Patel et al. [17] synthesized 4-10 wt% CuO on Santa Barbara Amorphous (SBA)-15 supports and compared their NO-SCR activities. 8.65 wt% CuO loading demonstrated maximum SCR activity, and activity was reduced with increasing CuO loading. Patel et al. [9] concur with Hu et al. [7] that aggregation of active metal species at high metal loadings decreases catalytic activity. Gu et al. [10] examined NO-SCR activity over different CuO loadings (0.5-2 mmol Cu^{2+}/100 m^2) deposited on CeO_2 supports. XRD and H_2-TPR material characterization techniques showed a decrease in active metal dispersion and reducibility with an increase in loading. Zhang et al. [11] examined the effect of Fe loading (2-8 wt%) on NO-SCR activity. The authors identified 4 wt% to be the optimal Fe loading for CO+NO reaction due to the presence of more catalytically active Fe_2O_3 species. Similar observations were also reported by Yamamoto et al. [12] over Cu/Al_2O_3 catalytic materials.

In addition to single active metal loading studies, binary metal loading also affects NO-SCR activity. Chen et al. [13] increased the loading of Cu and Co in $CuCo/TiO_2$ catalyst without altering the molar ratio between copper and cobalt (Cu:Co = 1:2). Observations regarding the optimum loading amount were found to be similar to that in Hu et al. [7] and Patel et al. [9] studies. Additionally, the authors studied the effect of Cu:Co ratio in the 30% active metal-loaded sample on NO-SCR activity and concluded that the interaction between Cu and Co species plays an important role in the NO-SCR activity. Similar observations and conclusions have been reported by Stegenga et al. [14] regarding copper-chromium/carbon catalysts.

Table 2.1 Literature studies on CO + NO reaction

Catalyst	Reaction Conditions					CO conversion		NO Conversion[1] (%)	N_2 Selectivity (%)	Ref
	Reaction temperature (°C)	Hourly Space velocity	NO content	CO content	Inert Gas Content	T_{50}[2] (°C)	T_{90}[2] (°C)			
(1.5-27.2 wt%) Cu/Al_2O_3	100 and 200	2500 h^{-1} and 5000 h^{-1}	5 vol%	10 vol%	He	––	––	50% at 10 wt% CuO loading, 2500 h^{-1} and 200°C	100	[7]
(0.4-9.3 wt%) Cu/CeO_2	100 and 200	2500 h^{-1} and 5000 h_{-1}	5 vol%	10 vol%	He	––	––	100% at 6.5 wt% CuO loading, 2500 h^{-1} and 200°C	100	[7]
CuAlO (mixed oxide)	50-500	35000 h^{-1}	1 vol%	1 vol%	He	300	350	Cu:Al = 4.9 and 350°C	90	[8]

[1]The conversion values indicate the molar conversion of NO into NO_2, N_2O and N_2

[2]T_{50} and T_{90} indicates the reaction temperatures corresponding to 50% and 90% conversion of CO to CO_2

(4-10) wt% Cu/SBA-15	350-550	48000 $ml.g^{-1}.h^{-1}$	500 ppm	500 ppm	He	––	––	8.5 wt% copper loading sample	100	[9]
(1-4 wt%) X-MCM-41 (X= Cu, Ni, Fe, Co, Ru)	150-450	48000 $ml.g^{-1}.h^{-1}$	250 ppm	750 ppm	He	––	––	100% at 250°C for 1 wt% Ni-MCM-41	100	[15]
4 wt% Cu/carbon modified Al_2O_3	25-250	26000 h^{-1}	1200 ppm	1200 ppm	Ar	––	––	100% at 250°C	––	[16]
(5-6 wt%) CuO/(ZrO_2-Al_2O_3)	100-450	12000 $ml.g^{-1}.h^{-1}$	5 vol%	10 vol%	He	––	––	100% at 450°C	100% at 450°C	[17]
Cu/TiO_2-ZrO_2	100-600	5000 h^{-1}	6 vol%	6 vol%	He	250	300	100% at 400°C for 6 wt% Cu loading and 10 wt% ZrO_2 loading	100% 350°C (formation of N_2O at T < 300°C reported)	[18]
7 wt% NiO/CeO_2 or TiO_2 or ZrO_2	100-600	120000 h_{-1}	0.25 vol%	0.25 vol%	He	150	200	100% at 200°C for NiO/CeO_2	100%	[19]

(0.5-2 mmol CuO/100 m^2 CeO_2) CuO/CeO_2	100-200	12000 h^{-1}	5 vol%	10 vol%	He	––	––	90% at 200°C for 2 mmol CuO/100 m^2 CeO_2	70%	[10]
(2-10 wt%) Fe-Ba/ZSM-5	200-400	5000 h^{-1}	0.1 vol%	0.2 vol%	N_2	––	––	100% at T > 325°C	100%	[11]
NiO/CeO_2	100-300	9000 $ml.g^{-1}.h^{-1}$	2.5 vol%	5 vol%	He	––	––	100% at T > 200°C	95% at 300°C (N_2O formation reported for T < 200°C)	[20]
Fe_xNi_{1-x}-MOFs (x = 0 – 1)	100-450	30000 h^{-1}	0.05 vol%	0.1 vol%	He	––	––	100% at T > 300°C for x = 0.33 sample	100% at T = 250°	[21]
$Co_xCu_1Al_1$ mixed oxide (x = 1 to 7)	25-250	27000 $ml.g^{-1}.h^{-1}$	0.8 vol%	0.85 vol%	He	––	––	100% at T > 100°C for x = 7	100% at T = 250°C	[22]
$LaB_{0.5}B'_{0.5}O_3$ (B = Fe and Mn; B' = Cu, Co, Fe, Mn)	100-450	12000 h^{-1}	0.3 vol%	0.3 vol%	Ar	352	425	100% at 450°C for $LaMn_{0.5}Cu_{0.5}O_3$	90% at T = 450°C for $LaMn_{0.5}Cu_{0.5}O_3$	[23]

M/TiO_2 (M = Cr, Mn, Fe, Ni, Cu)[3]	200	50000 h^{-1}	400 ppm	400 ppm	He	−−	−−	90% for 10 wt% MnO_x $/TiO_2$	100%	[24]
4 wt% CuO-CeO_2	100-350	24000 ml g^{-1} h^{-1}	5 vol%	10 vol%	He	−−	−−	90% at 350°C for CuO-CeO_2 prepared by wet-impregnation method (CuCe-IM)	100% at 350°C for CuCe-IM	[25]
CuO-CoO/γ-Al_2O_3	100-325	12000 h^{-1}	2.5 vol%	5 vol%	He	−−	−−	100% NO conversion at 325°C for sample with Cu:Co molar ratio of 5:3	100% at 325°C for sample with Cu:Co molar ratio of 5:3	[26]

[3]It should be noted that the authors used 2 vol% of O_2 in the reaction feed mixture. However, the authors have not commented on the effect of oxygen content in the reaction feed stream on the CO + NO activity. The focus of this paper is on the effect of different transition metals supported on TiO_2 on the CO + NO activity under similar reaction conditions and therefore, has been included in this table.

2.1.2 Effect of Support

The type of catalytic supports also affects the catalytic activity (here, NO-SCR activity) [7,16–19]. Hu et al. [7] and Wang et al. [19] reported superior NO-SCR activity over CeO_2-supported catalyst sample. Good dispersion of active metal due to strong interaction between the metal-support resulting in better reducibility of these samples was reported to be the reason for higher NO conversion activity than other samples.

Modifications of the support also affected the NO-SCR activity. Yu et al. [17] reported the effect of Zr amount in the support material of Al_2O_3-ZrO_2 on the overall catalytic activity and found that increasing the Zr content in the support material formed Cu-O-Zr that was considered to be the active site for NO activation for reduction reaction. Similar to Yu, Jiang et al. [18] also studied the effect of Zr content in the support material on the CO + NO activity but for 6 wt% CuO-ZrO_2/TiO_2. The authors found that increasing the amount of Zr in the catalyst enhanced the SCR activity. Good copper dispersion and stabilization of copper particles by Zr, thanks to the strong interaction between the both were the reasons for enhancement in the catalytic activity. In another study, Nickolov et al. [16] altered the alumina support by adding different amounts of carbon and reported the difference in the NO conversion performance. Addition of carbon was found to improve the dispersion of copper which was considered to be the reason for enhancement in the NO conversion activity.

Certain transition metals and their composition in binary and ternary metal catalysts play an important role in the NO-SCR by CO activity. Different studies report different transition metals as superior to others which can be accounted for the different catalytic test conditions and support materials used. Patel et al. [15] performed the CO+NO activity experiments over metal oxides (metals: Ru, Co, Ni, Fe and Cu) doped Mobil Composition of Matter No. 41 (MCM-41) and identified Ru-MCM-41 as the best performing sample based of NO conversion activity (100% NO conversion achieved at 250°C) while Fe-MCM-41 was reported as the worst performing catalyst sample (less than 20% of NO conversion at 450°C). Moreover, the authors observed good NO conversion performance for Cu-MCM-41 which achieved 80% of conversion at

450°C. The authors reported that the bond strength between the metal cation and oxygen is decisive in NO bonding on the catalyst surface which in turn governs the NO reduction activity on that catalyst sample. In another study, Sreekanth and Smirniotis [24] performed the CO + NO activity (in presence of 2 vol% O_2) over Cr, Mn, Fe, Ni, and Cu oxide supported on TiO_2 samples. The authors reported that the Mn/TiO_2 sample showed the highest NO conversion of 95% among all the samples and was stable for 6 hours. The presence of different oxidation states and high oxygen storage capacity were the reasons for the superior catalytic activity.

Apart from monometallic catalysts, the composition of active metals in binary and ternary metal-based materials also affects the SCR activity. Different studies like that by Oliveira Corrêa et al. [8], Liu et al. [22] and Tarjomannejad et al. [23] have been reported in the literature and unanimously concluded that the interaction between the active metals in the material can be correlated with the corresponding SCR activity. Oliveira Corrêa et al. [8] performed CO + NO reaction over Cu-Al mixed oxide catalytic samples with different Cu:Al ratios and reported that the sample with Al/(Al+Cu) ratio of 0.5 showed the best catalytic activity which was because of small CuO particles and strong Cu-Al interaction. In another study, Liu et al. [22] reported the effect of Co content in CoCu-Al mixed oxides on NO-SCR activity and found Co:Cu:Al molar ratio of 7:1:1 to be the best-performing catalyst. The superior catalytic activity was related to the facile activation of lattice oxygen to form oxygen vacancy sites, the active site considered for NO dissociation, upon introduction of Cu into the Co-Al mixed oxides. Like Corrêa and Liu, Tarjomannejad et al. [23] also studied the SCR activity over mixed oxides of perovskite-type: $LaB_{0.5}B'_{0.5}O_3$ where B = Fe or Mn and B' = Fe, Mn, Co or Cu. The authors observed that $LaMn_{0.5}Cu_{0.5}O_3$ was the best-performing sample which was again related to the 'synergistic' interaction between Mn and Cu resulting in better reducibility of the material and more structural defects than the other samples. Similar studies have also been reported by Huang et al. [21] but over Fe_xNi_{1-x}-MOFs for Fe/ (Fe + Ni) molar ratios of 0 to 1. The best-performing catalyst was found to be $Fe_{0.33}Ni_{0.67}$-MOF with the expected '*synergistic*' interaction between the active metals leading to enhanced reducibility of the sample materials.

2.1.3 Effect of Preparation Method

The method of preparation of the catalyst can affect the active metal dispersion, particle size, metal-support interaction, concentration of different metal oxidation states and catalytic surface [25,27,28]. The change in these material properties affects the corresponding NO-SCR activities.

Yao [25] and Sun [28] reported the effect of the copper-ceria catalyst preparation method on the SCR activity. Yao et al. [25] prepared CuO-CeO_2 mixed oxide samples by mechanical mixing (MMM), impregnation (IM), grinding (GM), hydrothermal (HTM) and co-precipitation (CPM) methods while Sun et al. [28] prepared two different CuO-CeO_2/γ-Al_2O_3 samples: (1) co-impregnation (CI) and (2) stepwise impregnation (SI). In both studies, the authors concluded that the amount of active Cu(I) species and the reducibility of the sample were key factors affecting the catalytic activities. For Yao et al., the wet-impregnated sample showed the best SCR activity followed by a co-precipitated sample while for Sun et al., the step-wise impregnated sample was superior in SCR activity to the co-impregnated sample. In another study, Li et al. [29] reported the effect of the ion-exchange method on the NO-SCR activity for Fe/ZSM-5 catalysts. The authors compared the aqueous ion exchange, hydrothermal ion exchange, and solid-state ion-exchange methods of catalyst preparation. The authors concluded that the type of ion exchange affects the Fe content in the catalyst which resulted in different catalytic activities. In their case, the sample prepared by the solid-state ion exchange method showed the best catalytic performance. Unlike the previous studies on the impact of the preparation methods, Yu et al. [17] studied the influence of the promoter (here, Zr) addition method into the catalytic sample CuO/Al_2O_3 on the NO-SCR activity. The two different addition methods were the two-step wet impregnation and coprecipitation-impregnation method. The authors observed that the co-precipitate-wet-impregnated sample was better in catalytic performance than the just wet-impregnated sample attributed to the high specific surface area, good active metal dispersion and strong interaction between Cu and Zr.

In addition to the catalyst synthesis methodology, the synthesis parameters like the calcination temperature can also affect the NO-SCR activity [30–32]. Panahi et al. [30] compared the catalytic activities of Fe-Cu/ZSM-5 prepared

at different calcination and impregnation temperatures. The authors reported that the optimum preparation condition was 577°C and 43.5°C of calcination and impregnation temperature respectively. Finally, the authors reported that the active metal dispersion, considered an important factor for SCR activity, was a function of calcination and impregnation temperature but was more sensitive to the calcination temperature. Lopes et al. [31] also studied the effect of the calcination temperature of the Cu-Ni mixed oxides on the SCR activity and found that increasing the calcination temperature decreased the surface area, increased the crystallinity, and decreased the reducibility of active species thereby deteriorating the catalytic activity. Different from the previous two reported studies, Zhang et al. [32] calcined the catalytic support of CeO_2 at different temperatures before depositing CoO_x particles on it. The authors found that increasing the calcination temperature of the support increased the crystalline size of the catalyst materials, and decreased the number of defect sites in the catalyst but did not affect the overall catalytic activity of the samples.

In summary, transition metal oxide catalysts have been found to be active for the CO + NO reaction and are affected by the type of supports, active metal type and composition, preparation method and active metal loading in the sample. However, in a real case scenario, the reactant gas mixture will also consist of gases like O_2, H_2 and CO_2 apart from CO and NO which can be promoters or inhibitors for the CO + NO reaction. Therefore, it is important to assess the catalytic performance of the materials under real gas conditions.

2.1.4 Effect of Reactant Gas Composition

As mentioned in the previous section of this chapter, the presence of impurities like O_2, H_2 and CO_2 can be either inhibitors or promoters for the CO + NO reactions. Various literature studies have reported the effect of these impurities on the NO reduction performance of the catalysts. Some of these studies are discussed further in this section and are summarized in Table 2.2 and in Figure 2.1.

Table 2.2 Summary of literature studies on the influence of reactant gas composition on the CO + NO activity

Catalyst	Reaction Conditions							CO conversion		NO conversion (%)	N_2 Selectivity (%)	Ref
	Hourly Space velocity	NO	CO	O_2	H_2O	CO_2	Other Gases	T_{50} (°C)	T_{90} (°C)			
Fe-Co/ASC[4]	20000 h^{-1}	1000 ppm	1000 ppm	0-1 vol%	––	––	N_2	150 (0.1-1 vol% O_2) and 250 (0 vol% O_2)	180 (0.1-1 vol% O_2) and 330 (1 vol% O_2)	100% (0 vol% O_2) 40% (1 vol% O_2) at 350°C	11% at 200-250°C and 100% for T > 300°C	[33]
Cu-Ce/CNT[5]	12600 h^{-1}	250 ppm	5000 ppm	0-0.5 vol%	––	––	He	––	220 (similar for 0-0.5 vol%)	96% (0 vol% O_2) and < 10% (0.5 vol% O_2) at 220°C	100	[27]
Cu or Ce or CuCe-MgAlO	––	600 ppm	1.4 vol%	0.5 vol%	1 vol%	––	500 ppm SO_2 and He	––	250 for CuCe-catalyst [6]	100% at 300°C for CuCe-catalyst [6]	100% (for all catalysts) [6] [7]	[34]

[4]ASC: Activated SemiCoke
[5]CNT: Carbon NanoTube
[6]The measurement of CO and NO conversions are made without including SO_2 in the feed stream
[7]The CuCe-catalyst is inert to the presence of SO_2 and showcased 100% NO conversion and N_2 selectivity at 720°C

Fe-Mo/Al_2O_3	8000 h^{-1}	1000 ppm	0-4 vol%	0-1 vol%	−−	−−	He	−−	−−	100% (0 vol% O_2) and 0% (O_2/CO ratio > 0.6) at 700°C	100	[35]

Cu or Fe/TiO_2	75000 h^{-1}	5000 ppm	5000 ppm	0.12 vol%	3 vol%	––	34 ppm of SO_2 and He	450 (for Cu/TiO_2) and 500 (for Fe/TiO_2)	–– [8]	**(i)** For Cu/TiO_2: 60% under CO + NO and CO + NO + O_2, 40% under CO + NO + H_2O and 0% under CO + NO + SO_2 **(ii)** For Fe/TiO_2 – 60% under CO + NO, 40% under CO + NO + O_2 and CO + NO + SO_2, 60% under CO + NO + H_2O	100	[36]

[8]The catalysts showed the maximum CO conversion of less than 60% at maximum reaction temperature of 500°C in the presence of NO, CO and He in the reaction feed

0.5 wt% Cu/Al_2O_3	––	1 vol%	1 vol%	0.5 vol%	––	––	Ar	150	200	32% (0 vol% O_2) and 20% (5 vol% O_2) at 500°C	100 (0 vol% O_2) and 0 (5 vol% O_2) at 500°C [9]	[12]
$CuCo/TiO_2$	20000 h^{-1}	0.1 vol%	1 vol%	2-10 vol%	4 vol%	––	0.025 vol% SO_2 and N_2	––	––	100% under CO + NO, 56% under CO + NO+ (6-10 vol%) O_2, 92% under CO + NO + H_2O, 100% under CO + NO + SO_2 and 40% under CO + NO + H_2O + SO_2	100	[13]

[9] All the NO is converted to NO_2 at 500°C over 0.5 wt% Cu/Al_2O_3

10 wt% fe or Cr/Al_2O_3	15000 h^{-1}	1.25 vol%	2.5 vol%	−−	0.7 vol%	−−	Ar	−−	−−	100% at 400°C under CO + NO and 600°C under CO + NO + 1.5 vol% H_2O	100	[37]
Cu+CuO [10]	1360000 h^{-1}	11.6 vol%	10.7 vol%	0-5 vol%	3 vol%	−−	He	−−	−−	99% under CO + NO + H_2O at 300°C 89% under CO + NO at 200°C, 0% under CO + NO + 5 vol% O_2	42% under CO + NO + H_2O	[38]

[10]The authors also studied the CO + NO reaction over Cu/SiO_2 and $Cu/CuAl_2O_4$ catalysts but did not investigate the effect of H_2O and O_2

(2-25 wt%) Cu-Cr/C	45000 h^{-1}	1330 ppm	1330 ppm	––	3 vol%	2.7-10 vol%	He	––	––	100% at 327°C under CO + NO, 100% at 377°C under CO + NO + H_2O, and CO + NO + CO_2 [11]	100	[14]
CoAl mixed oxides	22400 h^{-1}	0.02 vol%	0.5 vol%	10 vol%	8.2 vol%	20 vol%	He	193	220	40% at 240°C (without H_2O) and at 300°C (with H_2O)	57	[40]

[11]The activity of NO conversion was measured for both the CO_2 concentrations i.e., 2.7 and 10 vol%

10 wt% Cu (or Mn)-Ce-Fe-Co/TiO_2	10000 h^{-1}	200 ppm	200 ppm	1-6 vol%	5-15 vol%	––	50 ppm SO_2 and N_2	––[12]	200 under CO + NO + 6 vol% O_2	95% under CO + NO and 60% under CO + NO + 10 vol% H_2O + 50 ppm SO_2 and 6 vol% O_2	100	[39]
CaO	––	650 ppm	0-4 vol%	0-4 vol%	––	2-16 vol%	N_2	––[13]	––	81% under 0 vol% CO_2 and 23% under 16 vol% CO_2 at 850°C	100	[41]

[12]The authors investigated the effect of O_2, H_2O and SO_2 on the NO and CO conversion at 200°C and lowest CO conversion of 60% was reported at this temperature

[13]The authors have observed 100% CO conversion to CO_2 at 850°C and have not reported T_{50} and T_{90} temperatures for CO conversion

Fe-Co/ASC	12000 h^{-1}	800 ppm	1600 ppm	––	5-10 vol%	15 vol%	100 ppm SO_2 and N_2	––	––	55% under CO + NO, 25% under CO + NO + 10 vol% H_2O + CO_2 and 35% under CO + NO + SO_2 at 200°C	100	[42]

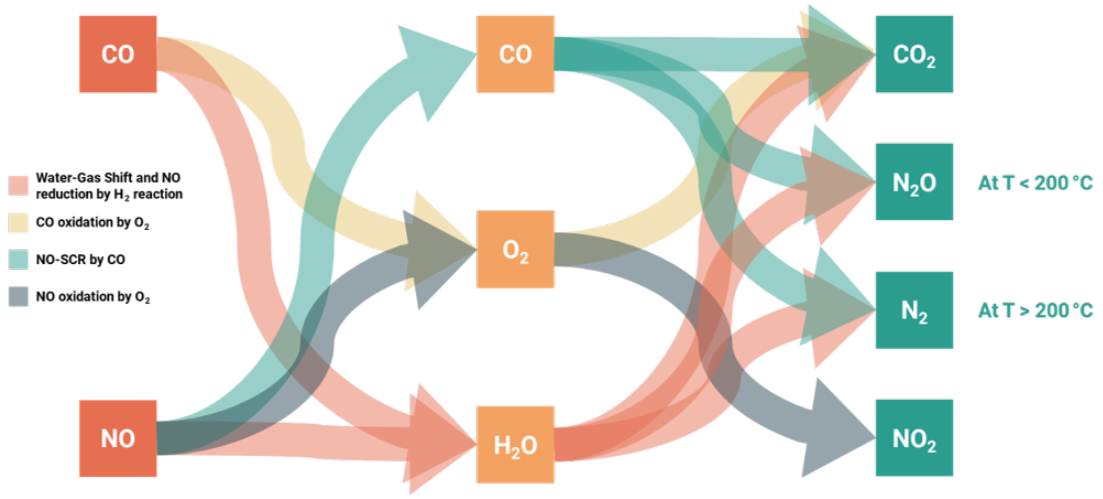

Figure 2.1 Possible side reactions based on the reactant gas composition

2.1.4.1 Effect of O_2

The presence of O_2 in the feed stream along with CO and NO can favourably react with CO and NO to form CO_2 and NO_2 respectively. These reactions are represented in Eq. (2.2) and Eq. (2.3). These side reactions affect the reaction between NO and CO and therefore, affect the NO conversion and N_2 selectivity.

$$CO + \frac{1}{2}O_2 \rightarrow CO_2 \tag{2.2}$$

$$NO + \frac{1}{2}O_2 \rightarrow NO_2 \tag{2.3}$$

Cheng et al. [33], Gholami et al. [27], Wen et al. [34], Li et al. [35] and Sierra-Pereira et al. [36] have reported a decrease in NO conversion caused by the presence of O_2 in the reaction feed. The decrease in NO conversion was more pronounced as the O_2 concentration in the reactant feed increased. Due to the preferential oxidation of CO by O_2 in the reactant stream, insufficient CO, a necessary reductant for NO reduction, was available. In consequence, the NO conversion yield diminished in the presence of O_2. Contrary to these previous results, Wen et al. [34] observed an increase in NO conversion activity as the O_2 concentration in the reaction feed gas mixture increased over a CuCeMgAlO mixed oxide catalyst. This increase in NO conversion activity was attributed to

the transformation of Cu(I) species into Cu(II) species, which is the active site for NO adsorption.

In addition to the formation of CO_2, the presence of excess O_2 in the reaction feed can react with NO to produce NO_2, as shown in Eq (2.3). The above-mentioned studies did not report the formation of NO_2 under oxidative reaction conditions, with the exception of Gholami et al. [27], who observed a maximum of 2 ppm of NO_2 in the outlet stream. Yamamoto et al. [12] and Chen et al. [13] reported a significant decrease in NO reduction activity in the presence of O_2 as NO_2 concentration in the outlet stream increased. Yamamoto et al. [12] observed no NO reduction activity and an 18% NO oxidation yield over 0.5 wt% Cu/Al_2O_3 in the presence of 10 vol% O_2, whereas Chen et al. [13] reported a 56% NO conversion yield over Cu-Co/TiO_2 catalysts for 4-10 vol% O_2 content.

In summary, it can be concluded from the different studies that the O_2 in the reaction feed reacts with the CO and NO to form CO_2 and NO_2 thereby hindering the CO + NO reaction thereby decreasing the catalytic reduction of NO.

2.1.4.2 Effect of H_2O

The presence of water in the reaction feed can either inhibit or promote NO reduction activity. Different studies addressing either or both effects are discussed further in this section.

- ***Inhibition Effect***
  The presence of water in the reaction stream can compete with the reactant molecules (here, CO and NO) for the active sites in the catalyst thereby delaying the catalytic activity. This delay in the catalytic activity under wet reaction conditions has been reported in several studies [14,36–38]. Moreover, the catalytic activity was restored after the removal of water from the reactant stream. This provides additional evidence for the occurrence of competitive adsorption between the reactant molecules and water molecules for the same active sites on the catalyst. Additionally, certain active metals like Fe are reportedly inert to the presence of water in the reactant stream. Sierra-Pereira et al. [36] prepared 10 wt% Fe/TiO_2 catalyst and observed no effect on NO conversion activity in the

presence of 3 vol% of H_2O while Pan et al. [39] observed no effect on NO conversion activity over CuCeFeCo/TiO_2 and MnCeFeCo/TiO_2 catalysts upon addition of 10 vol% H_2O into the reaction stream.

- ***Promotional Effect***
  Apart from the inhibition effect, the presence of water in the reactant stream can be beneficial for the NO reduction activity due to the occurrence of water gas shift reaction (*WGS*) (see Eq. (2.4)) because of not only the coexistence of CO and H_2O in the reactant stream but also the presence of certain metals like Cu and Co in the catalyst materials that are reportedly active for WGS [34,40]. The H_2 produced from the WGS reaction is a stronger reductant for NO than CO and therefore, contributes to the NO reduction activity thereby improving N_2 selectivity [34] even under oxidative conditions [40].

$$CO + H_2O \rightleftharpoons CO_2 + H_2 \tag{2.4}$$

2.1.4.3 Effect of CO_2

Industrial flue gases contain a significant amount of CO_2 (the proportion of the component varies based on the industrial process and operating conditions) which may affect the NO-SCR activity [43]. However, only a few studies in the literature have reported the effect of CO_2 concentration on the CO + NO activity over a transition metal-based catalyst. The presence of CO_2 in the reactant feed stream competes with NO for the common active sites (typically, the oxidized state of the active sites [14]) resulting in a decrease in the NO conversion activity [14,41,42]. According to the reports in the literature, CO_2 reacts with the oxidised active sites to form carbonates and inhibits the adsorption of NO [14]. Additionally, the coexistence of CO_2 and H_2O in the reactant feed stream further degrades the NO reduction activity but the activity can be restored by removing these components from the reactant feed stream which implies that the decrease in the NO reduction activity was due to the competitive adsorption among CO_2, NO and H_2O for the common active sites [42].

2.1.5 Effect of Pre-treatment Conditions

In addition to the type of active metal, the amount of active metal, and the type of supports, the type of pre-treatment procedure performed on the catalytic material prior to the activity test can influence the overall CO + NO activity. To improve the catalytic properties by inducing different active species, modifying the redox behaviour of the active metal in the catalyst, and modifying the interaction of the active metal with the supports, samples are pre-treated under various oxidizing, inert, and/or reducing gas atmospheres. In this section, the effect of different pre-treatment gases on CO+NO catalytic activity is briefly discussed.

2.1.5.1 Treatment under reducing gas atmosphere

The reductive pre-treatment of the catalyst materials is generally carried out under the flow of H_2 [8] or CO [10,44] at an elevated temperature. This reductive treatment forms metal species with oxidation states lower than that in the catalyst prior to the pre-treatment [8,10,44] and oxygen vacant sites [10,44]. The formation of both sites is the reason for enhancement in NO reduction activity. However, the reductive treatment facilitate the sintering of the active metal, which can have a negative effect on catalytic activity [44].

2.1.5.2 Treatment under oxidising gas atmosphere

The pre-treatment of catalysts in the air or O_2 results in the formation of active metal species with different oxidation states, thereby ensuring the presence of different active sites for CO and NO, which is necessary for NO-SCR by CO [8,45–47]. This pre-treatment under oxidising gas atmosphere can ensure higher oxygen defect sites, oxidation states of active metal suitable for the NO reduction by CO reaction and small crystalline size. All these factors can facilitate superior catalytic activity [46,47]. However, in some studies treatment of a catalyst under a reducing gas atmosphere showed superior catalytic activity than the one treated under an oxidising condition [8,44]. In summary, the formation of the active metal species on the catalyst surface and their stability during the reaction is crucial for the catalytic performance.

2.1.5.3 Treatment under inert gas atmosphere

Pre-treatment of the catalytic samples under an inert atmosphere partially reduces active metal species at elevated temperatures and therefore, forms a

material with active metal in different oxidation states [48]. This auto-reduction phenomenon under an inert gas atmosphere has been reported by Teixeria et al. [48], Liu and Robota [49], Lopes et al. [31] and Larsen et al. [50] over CuAl mixed oxide, Cu-Ni mixed oxides and Cu-ZSM5 catalysts respectively. In these studies, the authors have treated the sample at a temperature in the range of 300-550°C and have reported a reduction of Cu(II) species to Cu(I) and Cu(0) species.

2.1.5.4 Redox treatment

In redox pre-treatment, the catalyst sample is subjected to thermal treatment under a reducing gas atmosphere (CO [51] or H_2 [45]) followed by treatment under an oxidising atmosphere (O_2 [45,51]) at an elevated temperature. Such a treatment is advantageous over a single-step reductive or oxidative treatment because the former ensures the co-existence of different oxidation states of active metals in the catalyst which is reportedly desirable for higher CO + NO activity [45,51]. This redox treatment also enhanced the dispersion of the active metal particles in the catalyst [45] and enhanced the metal-support interaction, thereby creating lattice oxygen sites that are potential sites for oxygen-deficient sites [51]. These are the two most important factors for NO-SCR by CO activity; consequently, redox pre-treatment improves the sample's overall catalytic performance [45,51].

2.1.5.5 Effect of pre-treatment temperature

In addition to the nature of the gas environment utilized for the pre-treatment of the catalytic samples, the temperature at which the samples were pre-treated has a significant effect in determining the material properties of the final sample, which in turn affects its catalytic activity. The temperature rise in the treatment decreases the surface area of the catalyst and increases the crystalline size of the metal particles due to the possible agglomeration of active metal particles [46,52–55]. Some studies such as Shu et al. [52] reported a decrease in the NO conversion activity with the increase in the treatment temperature from 300-600°C while other studies like Du et al. [53] reported low treatment temperatures on mixed oxides to degrade the catalytic activity due to incomplete decomposition of the parent structure. In addition, increasing the treatment temperature facilitates strong metal-support interactions, resulting in the formation of metal species [54,55] with low reducibility, which further

decreases the NO-SCR activity since the redox behaviour of the catalyst material plays a significant role in its catalytic performance.

2.2 Reaction Kinetics for CO + NO Reaction

Based on the catalytic activities under different reaction conditions and over different catalytic samples, some authors have outlined the possible reaction mechanism for the NO reduction by CO reaction both for PGMs and transition metal oxide-based catalysts. Since the focus of this thesis is on transition metal oxide-based catalysts, the studies reported on such catalytic materials are only discussed in this section. Nevertheless, the kinetics observed on noble-metal catalysts (not discussed here) have been reported to be similar to that observed on transition metal oxide-based catalysts. Further, different kinetic models, various possible elementary kinetic steps governing the reaction mechanism and different global optimisation algorithms for parameter regression are also discussed in this section.

2.2.1 Reaction Mechanism for NO reduction by CO (*CO + NO*)

The mechanism for CO + NO reaction over transition metal oxides-based catalysts that have been widely reported in the literature [18] are shown in Eq. (2.5) - Eq. (2.13). The [S] in these equations stands for vacant active site on the catalyst surface and X[S] represents the adsorbed state of component X.

$$CO + [S] \rightarrow CO[S] \tag{2.5}$$

$$NO + [S] \rightarrow NO[S] \tag{2.6}$$

$$NO[S] + [S] \rightarrow N[S] + O[S] \tag{2.7}$$

$$CO[S] + O[S] \rightarrow CO_2 + 2[S] \tag{2.8}$$

$$NO[S] + N[S] \rightarrow N_2O[S] + [S] \tag{2.9}$$

$$NO[S] + N[S] \rightarrow N_2 + O[S] + [S] \tag{2.10}$$

$$N_2O[S] \rightarrow N_2O + [S] \tag{2.11}$$

$$N_2O[S] \rightarrow N_2 + O[S] \tag{2.12}$$

$$N[S] + N[S] \rightarrow N_2 + 2[S] \tag{2.13}$$

At low reaction temperatures ($T < 200°C$) [13,18,56], the dissociation of adsorbed NO species (NO[S]) into adsorbed N (N[S]) and O (O[S]) species is very limited and Eq. (2.13) occurs very slowly. Therefore, the adsorbed NO species react with N[S] to form N_2O[S] (Eq. (2.11)). At higher reaction temperatures, dissociation of NO[S] (Eq. (2.7)) is much faster than in the lower temperatures and therefore, promotes the formation of N_2 according to Eq. (2.13). Moreover, the N_2O[S] dissociation is facilitated at high reaction temperature leading to the formation of N_2 according to Eq. (2.12).

Additionally, certain studies like that by Cheng et al. [57] report the formation of NCO species as the reaction intermediate during CO + NO reaction. The adsorbed CO (CO[S]) reacts with surface N species (N[S]) formed through Eq. (2.7) to form NCO[S] species according to Eq. (2.14). These NCO species can either decompose at $T > 200°C$ forming CO_2 according to Eq. (2.15) or can possibly react with NO from the reaction gas mixture to form CO_2 and N_2 according to Eq. (2.16).

$$N[S] + CO[S] \rightarrow NCO[S] + [S] \tag{2.14}$$

$$NCO[S] + [S] \rightarrow CO[S] + N[S] \tag{2.15}$$

$$NCO[S] + NO \rightarrow CO_2 + N_2 + [S] \tag{2.16}$$

2.2.2 Reaction Mechanism Based on Reactant Gas Mixture

As seen in the first part of this chapter, the industrial flue gas can contain gas components other than CO and NO. These gas components can influence the catalytic performance. The elementary steps considered for the presence of different gas components in the reaction system are discussed further in this section.

2.2.2.1 Presence of O_2

O_2 is considered to undergo dissociative adsorption on the catalyst surface on the catalytic surface [35] as shown in Eq. (2.17). Li et al. [35] described the possible reaction kinetics steps for CO + NO in the presence of O_2. The O species formed from the dissociative adsorption of O_2 can further react with the adsorbed CO species to form CO_2 as already shown in Eq. (2.8). Moreover, adsorbed NO species can react with these O species to form NO_2 according to Eq. (2.18) and Eq. (2.19)[58].

$$O_2 + 2[S] \rightarrow 2O[S] \tag{2.17}$$

$$NO[S] + O[S] \rightarrow NO_2[S] + [S] \tag{2.18}$$

$$NO_2[S] \rightarrow NO_2 + [S] \tag{2.19}$$

2.2.2.2 Presence of H_2O

As seen previously, presence of H_2O in the reaction gas feed can reportedly show a promotional effect in NO reduction due to the occurrence of water-gas shift reaction [34,40]. The reaction kinetics for water-gas shift reaction is a well-studied topic. The widely accepted reaction mechanism [59,60] is the

surface adsorption of CO and H_2O according to Eq. (2.5) and Eq. (2.20), dissociation of H_2O[S] into H[S] and OH[S] according to Eq. (2.21) followed by further dissociation of OH[S]species into O[S] and H[S] (following Eq. (2.22)) and finally, reaction between CO[S] and O[S] to form CO_2 (as shown in Eq. (2.8)) and reaction between two H[S] species to form H_2 as shown in Eq. (2.23).

$$H_2O + [S] \rightarrow H_2O[S] \tag{2.20}$$

$$H_2O[S] + [S] \rightarrow H[S] + OH[S] \tag{2.21}$$

$$OH[S] + [S] \rightarrow H[S] + O[S] \tag{2.22}$$

$$2H[S] \rightarrow H_2 + 2[S] \tag{2.23}$$

However, some authors have reported a different mechanism for the water gas shift reactions, popularly termed as the '*carboxyl mechanism*' [60,61]. In this alternative mechanism, CO[S] and OH[S] react with each other to form COOH[S] species (See Eq. (2.24)) which further disintegrates into CO_2[S] and H[S] according to Eq. (2.25). Moreover, the COOH[S] can react with OH[S] species to form CO_2[S] and H_2O[S] species according to Eq. (2.26). Finally, the desorption of CO_2[S] and association of two H[S] species occurs according to Eq. (2.27) and Eq. (2.23) respectively.

$$CO[S] + OH[S] \rightarrow COOH[S] + [S] \tag{2.24}$$

$$COOH[S] + [S] \rightarrow CO_2[S] + H[S] \tag{2.25}$$

$$COOH[S] + OH[S] \rightarrow CO_2[S] + H_2O[S] \tag{2.26}$$

$$CO_2[S] \rightarrow CO_2 + [S] \tag{2.27}$$

Furthermore, since it is reported that the occurrence of a water-gas shift reaction enhances NO reduction, it is important to understand the reaction mechanism for NO + H_2 reaction. According to the literature, NO can react with H_2 more readily than CO and therefore, easily reduce NO to produce N_2. The possible reaction mechanisms have been discussed by Yang et al. [62] for NO + H_2 reaction over CoO supported on Nickel Phosphate Versailles Santa Barbara (VSB)-5 catalyst. The H_2 undergoes dissociative adsorption on the surface of the catalyst as shown in Eq. (2.28) followed by reaction with the already adsorbed NO species (as shown in Eq. (2.6)) to form adsorbed NOH species (NOH[S]). Further, this NOH[S] species dissociates into N[S] and OH[S] species according to Eq. (2.30) and this N[S] species reacts with another N[S] species to form N_2 according to Eq. (2.13). The authors also mentioned the reaction steps for the reduction of N_2O by H_2 at low reaction temperatures where the H[S] species reacts with the adsorbed N_2O species (N_2O[S]) to form N_2 and H_2O according to Eq. (2.31).

$$H_2 + 2[S] \rightarrow 2H[S] \tag{2.28}$$

$$NO[S] + H[S] \rightarrow NOH[S] + [S] \tag{2.29}$$

$$NOH[S] + [S] \rightarrow N[S] + OH[S] \tag{2.30}$$

$$N_2O[S] + 2H[S] \rightarrow N_2 + H_2O + 3[S] \tag{2.31}$$

To summarize, gas components other than CO and NO can influence CO + NO activity by following different reaction pathways over different catalytic materials. The various possible side products depending on the reactant gas composition, which have already been discussed in this section, has already been pictorially represented in Figure 2.1.

2.2.3 Kinetic Models

The other aspect of reaction mechanisms is developing a numerically fitting kinetic model. For the modelling of kinetics involved in the CO + NO reaction system, two different kinetic models are mainly proposed in the literature: (i) Langmuir-Hinshelwood-Hougen-Watson (LHHW) and (ii) Eley-Rideal (ER). These kinetic models are discussed briefly further in this section.

2.2.3.1 LHHW Model

LHHW model was first developed by Hougen and Watson in 1947 [63] where the authors used the mono-layer Langmuir adsorption model and either a surface reaction between the adsorbed species or reaction of the adsorbed species with a component from the fluid surrounding the catalyst. A general LHHW model includes the following steps (these steps are illustrated in Figure 2.2):

1. adsorption of the reactant molecules on the active sites of the catalytic surface
2. reaction of the adsorbed species
   a) with the adjacent adsorbed species ('*dual-site mechanism*')
   b) with free adsorbed species ('*single site mechanism*')
   c) self-dissociation ('*dissociative adsorption*')
3. desorption of product species from the catalytic surface

One of these reaction steps is considerably slow as compared with other reactions and is termed as the *rate-determining step* (RDS) while the rest of the reaction steps are considered to be at equilibrium. For a general reaction between A and B forming a product C (see Eq. (2.32)), the different elementary steps are shown in Table 2.3.

$$A + B \rightarrow C \tag{2.32}$$

It can be observed from this table (referring Table 2.3) that the surface reaction step (step no. 3) is assumed to be the *rate-determining step* (RDS) while all other elementary steps are in equilibrium. However, it should be

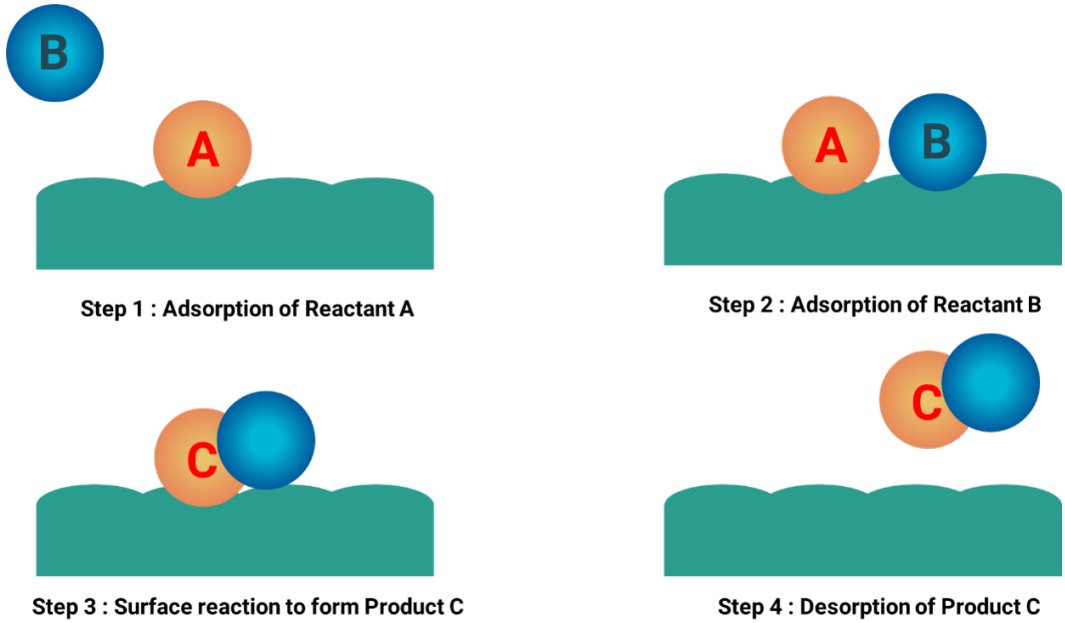

Figure 2.2 Elementary steps considered in LHHW kinetics

noted that each of these elementary steps can be a rate-determining step (while the rest other steps are assumed to be in equilibrium) depending on the reaction conditions and material properties. For example, specifically for CO + NO reaction, Angelidis and Papapetrou [64] considered reaction between adsorbed NO and CO species on NiO/Al_2O_3 to form atomic N species as the rate determining step and achieved a correlation factor between calculated and experimental reaction rate values of 0.995 while Tarjomannejad et al [23] considered the dissociation of adsorbed NO species into atomic N and O species as the rate-determining step over $LaB_{0.5}B_{0.5}O_3$ (B = Fe, Mn; B´ = Fe, Mn, Co,

Table 2.3 Elementary steps based on LHHW kinetics for a general reaction A + B → C

Elementary Step	Description	Step No.
$A + [S] \rightleftharpoons A[S]$	Adsorption of reactant A on the active site of the catalyst	1
$B + [S] \rightleftharpoons B[S]$	Adsorption of reactant B on the active site of the catalyst	2
$A[S] + B[S] \rightleftharpoons C[S] + [S]$	Surface reaction between adsorbed reactant species	3
$C[S] \rightleftharpoons C + [S]$	Desorption of product C	4

Table 2.4 Elementary steps based on ER kinetics for a general reaction A + B → C

Elementary Step	Description	Step No.
$A + [S] \rightleftharpoons A[S]$	Adsorption of reactant A on the active site of the catalyst	1
$A[S] + B \rightleftharpoons C[S]$	Surface reaction between adsorbed reactant species	2
$C[S] \rightleftharpoons C + [S]$	Desorption of product C	3

Cu) perovskites and achieved a correlation factor of 0.99 between experimental and calculated CO and NO conversion values.

2.2.3.2 ER Model

ER kinetic model is very similar to LHHW kinetic model. The main difference between these two models is that in ER model, only one of the reactant species is adsorbed onto the active site of the catalyst while the other reactant species react with this adsorbed species directly from the bulk fluid medium. In other words, for a general reaction as shown in Eq. (2.32), either the adsorption of reactant species B on the catalyst surface is omitted and this B species reacts directly with adsorbed A species to form the product C species followed by the desorption of product C species from the catalyst surface, similar to that in

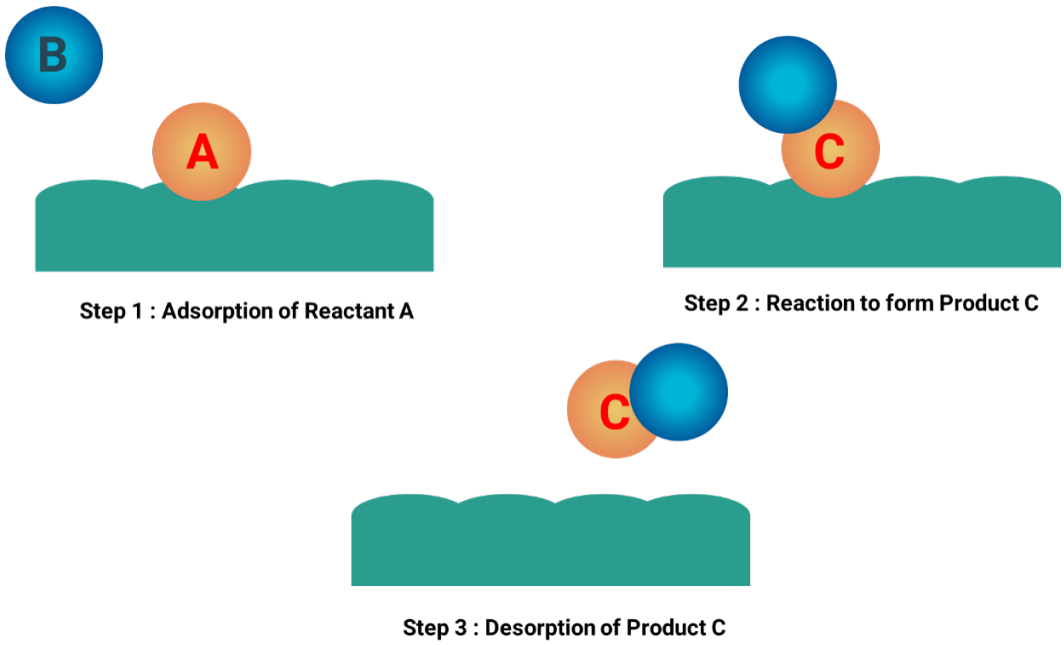

Figure 2.3 Elementary steps considered in ER kinetics

LHHW kinetics. Therefore, the elementary steps for ER kinetics are enlisted in Table 2.4 and illustrated in Figure 2.3.

However, to the best of my knowledge, ER kinetics for CO + NO reaction over transition metal oxide-based catalysts have not been reported in the literature. There are certain studies like that of Dai et al [65] and Bai et al [66] who have proposed ER kinetics based on their respective experimental data but have not derived the reaction rate equations and have not assessed its fitness to their corresponding experimental data.

2.2.4 Determination of Kinetic Model Parameters

As previously discussed in this chapter, the industrial flue gas contains different gas components and can interact with each other in different possible reaction pathways. Including these multiple side reactions in the reaction model yields to an expression with many model parameters that need to be determined. This makes the objective function highly non-linear and contain multiple local minima (known as '*non-convex problem*'). Because of this, conventional Newtonian gradient-based solvers might not yield satisfactory results. Hence, global optimisation routines like simulated annealing and genetic algorithms have been developed to address such non-convex problems. In this thesis, 'Global Optimisation Toolbox' available in MATLAB 2020a will be used to perform parameter regression and therefore, the different global optimisation solvers available in this toolbox are discussed briefly further in this section.

Simulated Annealing (SA) : This is an optimisation technique that mimics the annealing technique used in metallurgy where a metal is heated and then cooled down slowly to avoid any defects [67]. In this technique, the algorithm firstly chooses an initial set of possible parameter values known as 'trial point' and evaluates the objective function known as the 'Internal Energy of the System' or 'E'. Then the algorithm generates a new set of parameter values by random perturbations in the previous parameter values and then evaluates E for this new set of parameter values. If the new E value is lower than the older one, then this new set of parameters is chosen as the starting point for the next iteration. If not, then a probability for the acceptance of this new point is calculated using 'temperature' and the change in E value. The value of temperature of 'T'

is decreased subsequently towards zero. The algorithm stops computing when the change in the E value is below the function tolerance limits.

General Pattern Search (GPS) : In this algorithm, the solver searches a set of unknown parameter values known as mesh around the current point which the one determined in the previous iteration. The solver determines the new set of parameter values by adding the current parameter values with a scalar quantity multiplied by a set of vectors determined by the Mesh Adaptive Search Algorithm (MADS). If the solver finds the new set of parameter values to improve the objective function value, then this new set becomes the current set for the next iteration [68].

Particle Swarm Optimisation (PSO) : In this technique, the solver generates a set of initial values of unknown parameters and evaluates the objective function values. After each iteration, the solver decides the velocities of each individual solution into the known space of search and reevaluates the objective function. The individuals move in the direction of minimizing objective function value and eventually reach the optimal solution.

Genetic Algorithm (GA) : GA is a stochastic, population-based algorithm that searches the solution by mutation and crossover among population members [69,70]. In GA, the algorithm begins with a random initial population which is nothing but the set of initial solution to the objective function. An initial population is a matrix of multiple rows implying multiple initial solutions (which are the values of parameters to be regressed) and the number of columns is equal to the number of parameters to be regressed. The set of solutions in the initial population which have the best fitness values (which means minimum possible objective function values) are chosen as the parents for producing children for the next generation. The new population thus formed is used to check if the criteria is reached or not i.e., whether the change in the objective function value is within the tolerance limit or not. Once this criterion is met, the algorithm returns the best solution i.e., the best regressed value of the unknown parameters. In MATLAB, the GA can be used for single objective function (‘*ga*’) or

multiple objective function (‘*gamultiobj*’).

Surrogate Optimization : In this technique, the solver evaluates the objective function for a thousand of different sets of possible solutions and then chooses the set of solutions with minimum objective function value. The solver balances between the exploration to find global minimum and speed to achieve the minimal point in less possible function evaluations. More information about the algorithm of the solver has been provided by Gutmann [71].

The choice of the solver for the parameter regression depends on mainly on the characteristics of the objective function. The strategy for choosing a global optimisation solver has been documented by MATLAB 2020a. For searching a global solution to the non-smooth problem, MATLAB recommends firstly to use GPS followed by Surrogate Optimisation, PSO, GA and finally SA. The order of usage of these solvers is based on the efficiency in finding the global solution for the problem. However, gradient-based non-linear solvers can be used along with these global optimisation solvers to further improve the objective function value. For example, Eftaxias et al [67] compared the efficiency of conventional Levenberg-Marquardt (L-M) algorithm with Simulated Annealing (SA) method for various complexity of objective functions. The authors concluded that as the increase in the number of variables to be determined increased, L-M method failed to give lower objective function values than the SA solver. However, SA solver involved a greater number of function evaluations implying more computation time. Moreover, the authors used the solution provided by the SA solver as the initial guess for the L-M solver and this further improved the objective function value. This lowered the objective function value from 1880 in case of just SA solver to 1777 with SA and L-M solver. Therefore, using *hybrid functions* like SA with L-M can improve the solution.

2.3 Conclusion

In conclusion, the performance of NO reduction by CO reaction depends on various factors like material properties of catalyst or type and temperature of treatment and process parameters like reactant gas mixture. Evidently,

not many studies presenting the CO + NO reaction in an industrial flue gas condition has been reported in the literature. Therefore, in this thesis, this gap in the study of the influence of industrial flue gas components like CO_2, O_2 and H_2O on the catalytic activity of the CO + NO reaction has been addressed. Moreover, there are not many studies reporting the kinetic models and reaction rate equations for NO reduction by CO under industrial flue gas condition. This gap in the literature has also been addressed in this thesis. And finally, for the determination of the different model parameters in the reaction rate expression derived from the LHHW or ER kinetics, different global optimisation solvers have been used and compared with the experimental data.

References

[1] K. Jellinek, Über Zersetzungsgeschwindigkeit von Stickoxyd und Abhängigkeit derselben von der Temperatur, Zeitschrift Für Anorg. Chemie. 49 (1906) 229–276.
doi.org/10.1002/zaac.19060490121.

[2] Q. Sun, Z. Wang, D. Wang, Z. Hong, M. Zhou, X. Li, A review on the catalytic decomposition of NO to N_2 and O_2 catalysts and processes, Catal. Sci. Technol. 8 (2018) 4563–4575. doi.org/10.1039/c8cy01114a.

[3] M. Iwamotol, H. Hamada, Elsevier Science Publiihers B.V., Amsterdam Removal of Nitrogen Monoxide from Exhaust Gases through Novel Catalytic Processes, 1991.

[4] M. Haneda, Y. Kintaichi, I. Nakamura, T. Fujitani, H. Hamada, Comprehensive study combining surface science and real catalyst for NO direct decomposition, Chem. Commun. 2 (2002) 2816–2817. doi.org/10.1039/b207619e.

[5] J.Z. Luo, L.Z. Gao, Y.L. Leung, C.T. Au, The decomposition of NO on CNTs and 1 wt% Rh/CNTs, Catal. Letters. 66 (2000) 91–97.
doi.org/10.1023/a:1019035220233.

[6] T. Morita, N. Suzuki, N. Satoh, K. Wada, H. Ohno, Study on low NO_x emission control using newly developed lean NO_x catalyst for diesel engines, SAE Tech. Pap. (2007). doi.org/10.4271/2007-01-0239.

[7] Y. Hu, L. Dong, M. Shen, D. Liu, J. Wang, W. Ding, Y. Chen, Influence of supports on the activities of copper oxide species in the low-temperature NO + CO reaction, 2001.

[8] C.L. Oliveira Corrêa, Y.E. Licea, L. Amparo Palacio, F.M. Zanon Zotin, Ef-

fect of composition and thermal treatment in catalysts derived from Cu-Al hydrotalcites-like compounds in the NO reduction by CO, Catal. Today. 289 (2017) 133–142.
doi: 10.1016/j.cattod.2016.08.023.

[9] A. Patel, T.E. Rufford, V. Rudolph, Z. Zhu, Selective catalytic reduction of NO by CO over CuO supported on SBA-15: Effect of CuO loading on the activity of catalysts, Catal. Today. 166 (2011) 188–193. doi: 10.1016/j.cattod.2010.05.040.

[10] X. Gu, H. Li, L. Liu, C. Tang, F. Gao, L. Dong, Promotional effect of CO pretreatment on CuO/CeO_2 catalyst for catalytic reduction of NO by CO, J. Rare Earths. 32 (2014) 139–145. doi: 10.1016/S1002-0721(14)60043-0.

[11] X. Zhang, C. Ma, X. Cheng, Performance of Fe-Ba/ZSM-5 catalysts in NO + O_2 adsorption and NO + CO reduction, Int. J. Hydrogen Energy. 42 (2017) 7077–7088. doi: 10.1016/j.ijhydene.2017.01.067.

[12] T. Yamamoto, T. Tanaka, R. Kuma, S. Suzuki, F. Amano, Y. Shimooka, Y. Kohno, T. Funabiki, S. Yoshida, NO reduction with CO in the presence of O_2 over Al_2O_3-supported and Cu-based catalysts, Phys. Chem. Chem. Phys. 4 (2002) 2449–2458.
doi: 10.1039/b201120b.

[13] X. Chen, J. Zhang, Y. Huang, Z. Tong, M. Huang, Catalytic reduction of nitric oxide with carbon monoxide on copper-cobalt oxides supported on nano-titanium dioxide, J. Environ. Sci. 21 (2009) 1296–1301. doi: 10.1016/S1001-0742(08)62418-3.

[14] S. Stegenga, R. van Soest, F. Kapteijn, J.A. Moulijn, Nitric oxide reduction and carbon monoxide oxidation over carbon-supported copper-chromium catalysts, Appl. Catal. B, Environ. 2 (1993) 257–275. doi: 10.1016/0926-

3373(93)80001-T.

[15] A. Patel, P. Shukla, T.E. Rufford, V. Rudolph, Z. Zhu, Selective catalytic reduction of NO with CO using different metal-oxides incorporated in MCM-41, Chem. Eng. J. 255 (2014) 437–444. doi: 10.1016/j.cej.2014.06.032.

[16] R. Nickolov, N. Stankova, M. Khristova, D. Mehandjiev, Copper oxide supported on carbon modified alumina as catalyst for reduction of NO with CO, J. Colloid Interface Sci. 265 (2003) 121–128. doi: 10.1016/S0021-9797(03)00278-9.

[17] Q. Yu, X. Yao, H. Zhang, F. Gao, L. Dong, General Effect of ZrO_2 addition method on the activity of Al_2O_3-supported CuO for NO reduction with CO: Impregnation vs coprecipitation, "Applied Catal. A, Gen. 423–424 (2012) 42–51. doi: 10.1016/j.apcata.2012.02.017.

[18] X. Jiang, G. Ding, L. Lou, Y. Chen, X. Zheng, Effect of ZrO_2 addition on CuO/TiO_2 activity in the NO + CO reaction, Catal. Today. 93–95 (2004) 811–818.
doi: 10.1016/j.cattod.2004.06.074.

[19] Y. Wang, A. Zhu, Y. Zhang, C.T. Au, X. Yang, C. Shi, Catalytic reduction of NO by CO over NiO/CeO_2 catalyst in stoichiometric NO/CO and $NO/CO/O_2$ reaction, Appl. Catal. B Environ. 81 (2008) 141–149. doi: 10.1016/j.apcatb.2007.12.005.

[20] C. Tang, B. Sun, J. Sun, X. Hong, Y. Deng, F. Gao, L. Dong, Solid state preparation of $NiO\text{-}CeO_2$ catalyst for NO reduction, Catal. Today. 281 (2017) 575–582. doi: 10.1016/j.cattod.2016.05.026.

[21] L. Huang, Y. Shi, W. Xiong, Y. Ding, Y. qi Zhang, Facile design of highly effective Fe-modified bimetallic Fe_x–Ni_{1-x}-MOFs catalysts with rodlike structures

for low-temperature NO reduction by CO, J. Mater. Sci. 56 (2021) 9914–9928. doi: 10.1007/s10853-021-05875-5.

[22] Y.W. Yu Liu, Xuezhong Wang, Xiangguang Yang, Co-Cu-Al mixed oxides derived from hydrotalcite-like compound for NO reduction by CO, (1999).

[23] A. Tarjomannejad, A. Farzi, A. Niaei, D. Salari, NO reduction by CO over $LaB_{0.5}B_{0.5}O_3$ (B = Fe, Mn, B=Fe, Mn, Co, Cu) perovskite catalysts, an experimental and kinetic study, J. Taiwan Inst. Chem. Eng. 78 (2017) 200–211. doi: 10.1016/j.jtice.2017.05.034.

[24] P.M. Sreekanth, P.G. Smirniotis, Selective reduction of NO with CO over titania supported transition metal oxide catalysts, Catal. Letters. 122 (2008) 37–42.
doi: 10.1007/s10562-007-9365-5.

[25] X. Yao, F. Gao, Q. Yu, L. Qi, C. Tang, L. Dong, Y. Chen, NO reduction by CO over CuO-CeO_2 catalysis: effect of preparation methods, Catal. Sci. Technol. (2013). doi: 10.1039/c3cy20805b.

[26] Y. Lv, H. Zhang, Y. Cao, L. Dong, L. Zhang, K. Yao, F. Gao, L. Dong, Y. Chen, Investigation of the physicochemical properties of CuO-CoO binary metal oxides supported on γ-Al_2O_3 and their activity for NO removal by CO, J. Colloid Interface Sci. 372 (2012) 63–72. doi: 10.1016/j.jcis.2012.01.014.

[27] Z. Gholami, G. Luo, Low-temperature selective catalytic reduction of NO by CO in the presence of O_2 over Cu:Ce catalysts supported by multi-walled carbon nanotubes, Ind. Eng. Chem. Res. (2018). doi: 10.1021/acs.iecr.8b01343.

[28] J. Sun, C. Ge, X. Yao, W. Zou, X. Hong, C. Tang, L. Dong, Influence of different impregnation modes on the properties of CuO-CeO_2 /Al_2O_3 catalysts for NO reduction by CO, Appl. Surf. Sci. 426 (2017) 279–286. doi: 10.1016/j.apsusc.2017.07.069.

[29] J. Li, M. Zhao, M. Zhang, X. Cheng, J. Chang, Z. Wang, J. Fu, Y. Sun, X. Liu, NO_x reduction by CO over Fe/ZSM-5: A comparative study of different preparation techniques, Int. J. Chem. React. Eng. 18 (2020) 1–16. doi: 10.1515/ijcre-2019-0063.

[30] P.N. Panahi, D. Salari, A. Niaei, S.M. Mousavi, NO reduction over nanostructure M-Cu/ZSM-5 (M: Cr, Mn, Co and Fe) bimetallic catalysts and optimization of catalyst preparation by RSM, J. Ind. Eng. Chem. 19 (2013) 1793–1799. doi: 10.1016/j.jiec.2013.02.022.

[31] D. Lopes, F. Zotin, L.A. Palacio, Copper-nickel catalysts from hydrotalcite precursors: The performance in NO reduction by CO, Appl. Catal. B Environ. 237 (2018) 327–338. doi: 10.1016/j.apcatb.2018.06.007.

[32] S. Zhang, J. Lee, D.H. Kim, T. Kim, NO reduction by CO over CoO_x/CeO_2 catalysts: Effect of support calcination temperature on activity, Mol. Catal. 482 (2020).
doi: 10.1016/j.mcat.2019.110703.

[33] X. Cheng, L. Wang, Z. Wang, M. Zhang, C. Ma, Catalytic Performance of NO Reduction by CO over Activated Semicoke Supported Fe / Co Catalysts, Ind. Eng. Chem. Res. (2016). doi: 10.1021/acs.iecr.6b00804.

[34] B. Wen, M. He, E. Schrum, C. Li, NO reduction and CO oxidation over Cu/Ce/Mg/Al mixed oxide catalyst in FCC operation, J. Mol. Catal. A Chem. 180 (2002) 187–192. doi: 10.1016/S1381-1169(01)00427-7.

[35] J. Li, S. Wang, L. Zhou, G. Luo, F. Wei, NO reduction by CO over a Fe-based catalyst in FCC regenerator conditions, Chem. Eng. J. 255 (2014) 126–133. doi: 10.1016/j.cej.2014.06.015.

[36] C.A. Sierra-Pereira, E.A. Urquieta-González, Reduction of NO with CO on CuO or Fe_2O_3 catalysts supported on TiO_2 in the presence of O_2, SO_2 and water steam, Fuel. 118 (2014) 137–147. doi: 10.1016/j.fuel.2013.10.054.

[37] T.P. Kobylinski, B.W. Taylor, The catalytic chemistry of nitric oxide. I. The effect of water on the reduction of nitric oxide over supported chromium and iron oxides, J. Catal. 31 (1973) 450–458. doi: 10.1016/0021-9517(73)90317-5.

[38] R.T. Rewick, H. Wise, Reduction of nitric oxide by carbon monoxide on copper catalysts, J. Catal. 40 (1975) 301–311. doi: 10.1016/0021-9517(75)90260-2.

[39] K.L. Pan, C.W. Young, G.T. Pan, M.B. Chang, Catalytic reduction of NO by CO with Cu-based and Mn-based catalysts, Catal. Today. 348 (2020) 15–25. doi: 10.1016/j.cattod.2019.08.038.

[40] J. Akil, C. Ciotonea, S. Siffert, S. Royer, L. Pirault-Roy, R. Cousin, C. Poupin, NO reduction by CO under oxidative conditions over CoCuAl mixed oxides derived from hydrotalcite-like compounds: Effect of water, Catal. Today. (2021). doi: 10.1016/j.cattod.2021.05.014.

[41] K. Dam-Johansen, P.F.B. Hansen, S. Rasmussen, Catalytic reduction of nitric oxide by carbon monoxide over calcined limestone: reversible deactivation in the presence of carbon dioxide, Appl. Catal. B, Environ. 5 (1995) 283–304. doi: 10.1016/0926-3373(94)00049-2.

[42] P. Sun, X. Cheng, Y. Lai, Z. Wang, C. Ma, J. Chang, NO_x reduction by CO

over ASC catalysts in a simulated rotary reactor: effect of CO_2, H_2O and SO_2, RSC Adv. 8 (2018) 36604–36615. doi: 10.1039/c8ra07658h.

[43] M.M. Behera, C. Ciotonea, L. Olivet, L. Tidahy, S. Royer, D. Thomas, R. Cousin, G. De Weireld, C. Poupin, Impact of gas treatment of CuAl-LDH on NO reduction by CO under oxidative conditions, Chem. Eng. J. 452 (2023). doi: 10.1016/j.cej.2022.139543.

[44] C. Ge, L. Liu, X. Yao, C. Tang, F. Gao, L. Dong, Treatment induced remarkable enhancement of low-temperature activity and selectivity of copper-based catalysts for NO reduction, Catal. Sci. Technol. 3 (2013) 1547–1557. doi: 10.1039/c3cy20698j.

[45] L.F. Liotta, G. Pantaleo, G. Di Carlo, G. Marcì, G. Deganello, Structural and morphological investigation of a cobalt catalyst supported on alumina-baria: Effects of redox treatments on the activity in the NO reduction by CO, Appl. Catal. B Environ. 52 (2004) 1–10. doi: 10.1016/j.apcatb.2004.03.003.

[46] T.J. Huang, T.C. Yu, Calcination conditions on copper/alumina catalysts for carbon monoxide oxidation and nitric oxide reduction, Appl. Catal. 71 (1991) 275–282.
doi: 10.1016/0166-9834(91)85085-A.

[47] K.M. Lee, G. Kwon, S. Hwang, J. Boscoboinik, T.J. Kim, Investigation of NO reduction by CO reaction over oxidized and reduced NiOx/CeO_2 catalysts, Catal. Sci. Technol. 11 (2021).

[48] C.D.O.P. Teixeira, S.D.S. Montani, L.A. Palacio, F.M.Z. Zotin, The effect of preparation methods on the thermal and chemical reducibility of Cu in Cu-Al oxides, Dalt. Trans. 47 (2018) 10989–11001. doi: 10.1039/c8dt01150h.

[49] D.J. Liu, H.J. Robota, In situ XANES characterization of the Cu oxidation

state in Cu-ZSM-5 during NO decomposition catalysis, Catal. Letters. 21 (1993) 291–301. doi: 10.1007/BF00769481.

[50] S.C. Larsen, A. Aylor, A.T. Bell, J.A. Reimer, Electron Paramagnetic Resonance Studies of Copper Ion-Exchanged ZSM-5, (1994) 11533–11540.

[51] J. Chen, J. Zhu, Y. Zhan, X. Lin, G. Cai, K. Wei, Q. Zheng, Characterization and catalytic performance of Cu/CeO_2 and $Cu/MgO\text{-}CeO_2$ catalysts for NO reduction by CO, Appl. Catal. A Gen. 363 (2009) 208–215. doi: 10.1016/j.apcata.2009.05.017.

[52] J.S. Shu, W.S. Xia, Y.J. Zhang, T. Cheng, M.R. Gao, Low-temperature catalytic reduction of nitrogen monoxide with carbon monoxide on copper iron and copper cobalt composite oxides, Chinese J. Chem. Phys. 21 (2008). doi: 10.1088/1674-0068/21/04/393-400.

[53] X. Du, T.L. Yao, Q. Wei, H. Zhang, Y. Huang, Investigation of FeNi Mixed-Oxide Catalysts for the Reduction of NO by CO: Physicochemical Properties and Catalytic Performance, Chem. - An Asian J. 14 (2019) 2966–2978. doi: 10.1002/asia.201900782.

[54] J. Yan, M.C. Kung, W.M.H. Sachtler, H.H. Kung, Co/Al_2O_3 Lean NO_x Reduction Catalyst, J. Catal. 172 (1997) 178–186.

[55] A. Alejandre, F. Medina, P. Salagre, X. Correig, J.E. Sueiras, Preparation and study of Cu-Al mixed oxides via hydrotalcite-like precursors, Chem. Mater. 11 (1999) 939–948. doi: 10.1021/cm980500f.

[56] G.Z. Gassan–zedeh, S.F. Seyidbayova, The heterogeneous catalytic reduction of NO and N_2O mixture by carbon monoxide, Appl. Catal. B Environ. 42 (2003) 359–367. doi: 10.1016/j.apsusc.2010.01.075.

[57] X. Cheng, A. Zhu, Y. Zhang, Y. Wang, C.T. Au, C. Shi, A combined DRIFTS and MS study on reaction mechanism of NO reduction by CO over NiO/CeO_2 catalyst, Appl. Catal. B Environ. 90 (2009) 395–404. doi: 10.1016/j.apcatb.2009.03.033.

[58] R. Aslam, M.R. Usman, M.F. Irfan, A comparative study of LHHW and ER kinetic models for NO oxidation over Co_3O_4 catalyst, J. Environ. Chem. Eng. 4 (2016) 2871–2877. doi: 10.1016/j.jece.2016.05.035.

[59] C. V. Ovesen, P. Stoltze, J.K. Nørskov, C.T. Campbell, A kinetic model of the water gas shift reaction, J. Catal. 134 (1992) 445–468. doi: 10.1016/0021-9517(92)90334-E.

[60] A.A. Gokhale, J.A. Dumesic, M. Mavrikakis, On the mechanism of low-temperature water gas shift reaction on copper, J. Am. Chem. Soc. 130 (2008) 1402–1414. doi: 10.1021/ja0768237.

[61] C.H. Lin, C.L. Chen, J.H. Wang, Mechanistic studies of water-gas-shift reaction on transition metals, J. Phys. Chem. C. 115 (2011) 18582–18588. doi: 10.1021/jp2034467.

[62] Q. Yang, Z. Chen, D. Zhou, W. Shen, S. Naito, Effect of cobalt substitution on nanoporous nickel phosphate VSB-5 catalyst for the catalytic reduction of NO by H_2, Catal. Today. 297 (2017) 64–69. doi: 10.1016/j.cattod.2017.03.010.

[63] A. Hougen, O., M. Watson, K., Chemical Process Principles (Part Three): Kinetics and Catalysis, John Wiley and Sons Inc., New York (USA), 1947.

[64] T.N. Angelidis, M. Papapetrou, A kinetic study of NO reduction by CO over a NiO/Al_2O_3 catalyst, Stud. Surf. Sci. Catal. 133 (2001) 131–138. doi: 10.1016/s0167-2991(01)81955-8.

[65] X. Dai, W. Jiang, W. Wang, X. Weng, Y. Shang, Y. Xue, Z. Wu, Supercritical water syntheses of transition metal-doped CeO_2 nano-catalysts for selective catalytic reduction of NO by CO: An in situ diffuse reflectance Fourier transform infrared spectroscopy study, Cuihua Xuebao/Chinese J. Catal. 39 (2018) 728–735. doi: 10.1016/S1872-2067(17)63008-0.

[66] Y. Bai, X. Bian, W. Wu, Catalytic properties of CuO/CeO_2 -Al_2O_3 catalysts for low concentration NO reduction with CO, Appl. Surf. Sci. 463 (2019) 435–444.
doi: 10.1016/j.apsusc.2018.08.229.

[67] S. Fatemi, M. Masoori, R. Bozorgmehry Boozarjomehry, Application of genetic algorithm in kinetic modeling and reaction mechanism studies, Iran. J. Chem. Chem. Eng. 24 (2005) 37–46.

[68] S.K. Rao, R. Imam, K. Ramanathan, S. Pushpavanam, Sensitivity analysis and kinetic parameter estimation in a three way catalytic converter, Ind. Eng. Chem. Res. 48 (2009) 3779–3790. doi: 10.1021/ie801244w.

[69] R.E. Hayes, F.H. Bertrand, C. Audet, S.T. Kolaczkowski, Catalytic Combustion Kinetics: Using a Direct Search Algorithm to Evaluate Kinetic Parameters from Light-Off Curves, 81 (2003) 1192–1199.

[70] A. Pandya, J. Mmbaga, R.E. Hayes, W. Hauptmann, M. Votsmeier, Global Kinetic Model and Parameter Optimization for a Diesel Oxidation Catalyst, Top. Catal. 52 (2009) 1929–1933. doi: 10.1007/s11244-009-9361-7.

[71] A. Eftaxias, J. Font, A. Fortuny, A. Fabregat, F. Stu, Nonlinear kinetic parameter estimation using simulated annealing, 26 (2002) 1725–1733.

[72] A. Pedlow, G. McCullough, A. Goguet, K. Hansen, Optimization of Kinetic Parameters for an Aftertreatment Catalyst, SAE Tech. Pap. 2014-Octob (2014).

doi: 10.4271/2014-01-2814.

[73] M.J. Azarhoosh, R. Halladj, S. Askari, Presenting a new kinetic model for methanol to light olefins reactions over a hierarchical SAPO-34 catalyst using the Langmuir-Hinshelwood-Hougen-Watson mechanism, J. Phys. Condens. Matter. 29 (2017). doi: 10.1088/1361-648X/aa85f0.

Chapter 3

Experimental Protocols and Techniques

This chapter outline the two different synthesis protocols for the development of the catalytic materials namely Layered Double Hydroxide (LDH) and Conventional Citrate Method (CCM) routes. The primary focus of this thesis is on mixed metal oxide-based catalysts synthesized via LDH route. Moreover, it has been demonstrated in the final chapter of this thesis that perovskites, synthesized by CCM route, are also active for NO reduction by CO reaction under industrial flue gas conditions and therefore, can be considered as a potential material which need to be developed further for maximum catalytic activity. Furthermore, this chapter also outlines the protocols used for various material characterization techniques and lab-scale catalytic test experiments.

3.1 Catalytic Material Synthesis

This section discusses about the LDH and CCM synthesis protocols used for the development of two different catalytic materials, namely mixed metal oxides and perovskites respectively. This section reinforces that the primary focus of this thesis is on the mixed metal oxides synthesized via the LDH route, while studies on perovskites are mentioned only to demonstrate it as a potential catalytic material.

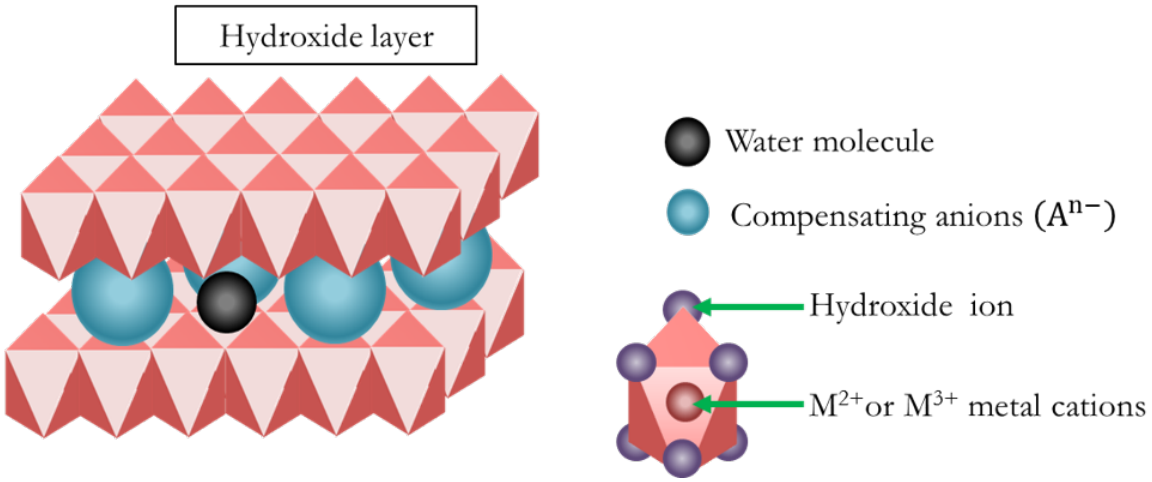

Figure 3.1 Schematic representation of a LDH structure

3.1.1 LDH Route

A general LDH structure is generally made up of sheets of metal hydroxides stacked over one another and separated by charge compensating anions and water molecules as shown in Figure 3.1. The general formula for LDH is: $[M^{2+}_{1-x}M^{3+}_{x}(OH)_2]^{x+}(A^{n-})_{x/n}.mH_2O$; where M^{2+}, M^{3+} and A represent the divalent metal cations, trivalent metal cations and charge compensating anions respectively [1]. Due to the availability of numerous divalent and trivalent metal cation pairs, various LDH materials can be synthesized [1–3]. There are different methods of synthesis of a hydrotalcite-like compound namely: co-precipitation, sol-gel and urea method [1]. Conventionally, the co-precipitation method is used for the synthesis of LDH materials [1] and therefore, this methodology is also used for this synthesis of the catalytic materials in this study.

For the LDH synthesis by co-precipitation, nitrate salts of the metals were used as the precursors. Firstly, aqueous solution of required amount of metal salts (calculated in terms of molar ratios of the active metals in the final LDH) was added dropwise into an aqueous solution of 1 M Na_2CO_3 (procured from ACROS, 99.5 wt.% purity) under a continuous stirring. The pH of the overall solution was maintained at a pre-determined value (depends on the metals used in the LDH preparation because using below a threshold value will result in the formation of other structures like malachite along with LDH structure) by adding 2 M NaOH to the solution. Secondly, the overall

solution was aged at room temperature for 18 h. Thirdly, the precipitate was recovered by filtration and washed with hot deionised water (60°C) until the pH stabilized at 7. Finally, the precipitate was dried at 60°C for 48 h. This dried precipitate was the required LDH that was further used for the preparation of mixed oxides. Mixed oxides were prepared by thermal treatment where the LDH sample was heated from room temperature to an elevated temperature ($T \geq 350°C$) at a heating rate of $1°C.min^{-1}$ under a treatment gas (He, CO_2, 1 vol% CO/He or air) flowing at a rate of 60 $ml.min^{-1}$.

After a plateau of 4 h at this elevated temperature, the sample was cooled down to room temperature under the same treatment gas. During the thermal treatment, the loosely bonded water molecules, surface hydroxides and interlayer water and anions (carbonate ions in this study) are removed leading to the rupture of lamellar structure and formation of mixed oxides [4–6]. The schematic representation of the overall material synthesis by LDH route is shown in Figure 3.2.

3.1.2 CCM Route

The perovskites were prepared by the CCM route. Firstly, the nitrate salts of the corresponding A-site and B-site metals and citric acid (hereafter, represented as 'CA') in an equimolar ratio ($(n_{A\text{-nitrates}} + n_{B\text{-nitrates}})/n_{CA} = 1$) were mixed with a small amount of deionised water under continuous agitation and then the final solution was left under agitation for 2 hours. Thirdly, the solution was transferred to a flask and evaporated at 40°C at a pressure of 70 mbar (the pressure was decreased progressively towards 70 mbar) until formation

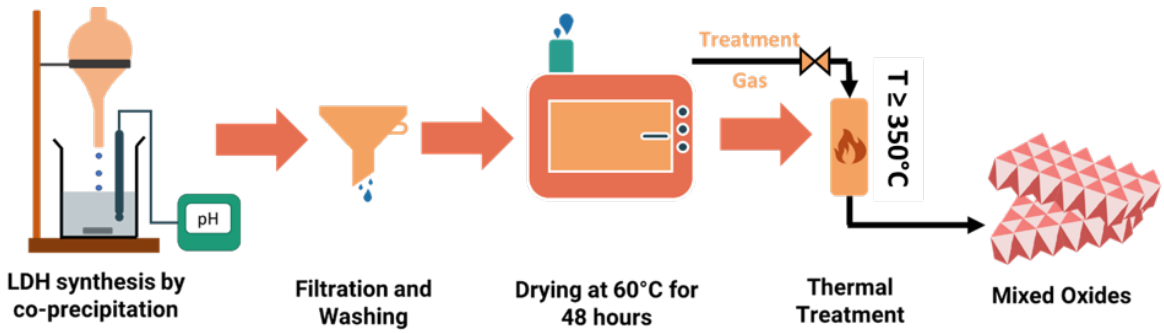

Figure 3.2 Schematic representation of mixed oxides synthesis via LDH route

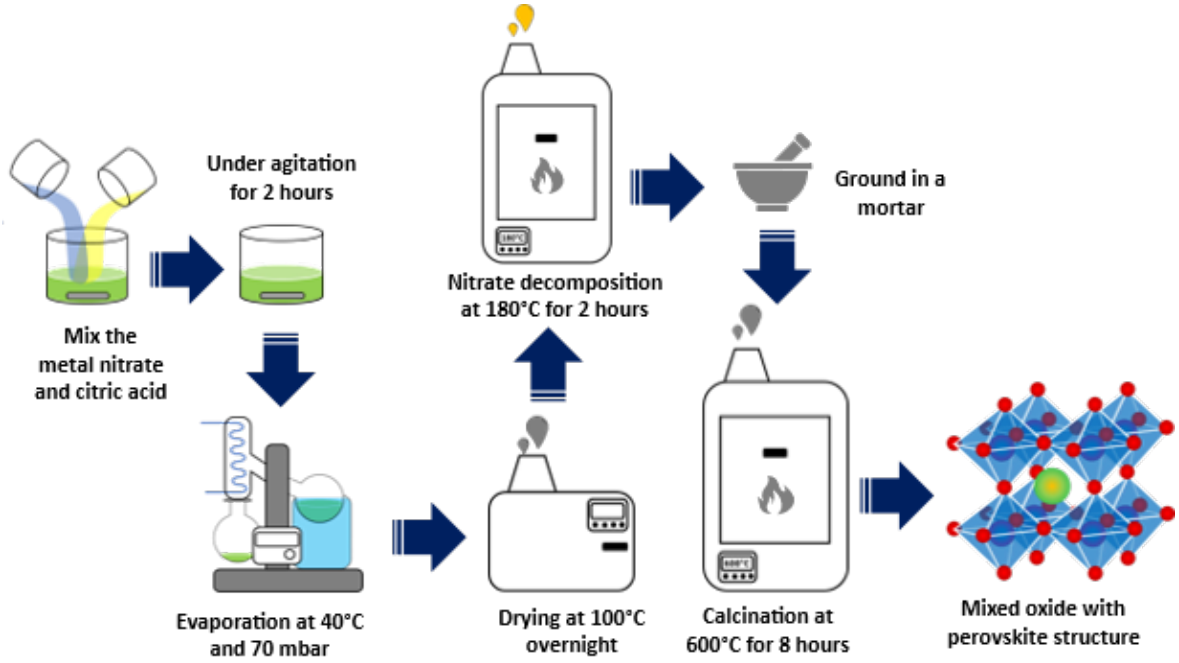

Figure 3.3 Schematic representation of protocol of synthesis of perovskite materials

of a viscous liquid. Fourthly, this liquid was dried in air at 100°C overnight. Finally, the nitrates in the solid obtained after the drying step were removed by decomposition inside a muffle furnace and at a temperature of 180°C for 2 hours (heating rate from room temperature to 180°C was 2°C.min^{-1}). After this step, the sample was ground in a mortar before calcining it at a temperature of 600°C (or more) for 8 hours and at a heating rate of 2°C.min^{-1}. The material thus obtained was the mixed oxide with perovskite structure. A summary of the synthesis protocol is represented schematically in Figure 3.3.

3.2 Material Characterization

Physicochemical properties of the mixed oxides derived from the LDH and CCM routes were studied through different material characterization techniques. The methodology followed for each of these characterization techniques are mentioned further in this section.

3.2.1 N_2-Physisorption

The experiments were performed at 77 K on a 3Flex (version 5.03) system from Micromeritics. The samples were first heated under vacuum at 90°C for 1 h and at 350°C for 4 h, using a VacPrep 061 system from Micromeritics. Specific

surface areas were computed using Brunauer-Emmett-Teller (B.E.T.) theory applied on the linear part of B.E.T. plot. Micropore volume was evaluated by t-plot method [7]. Average pore size and pore size distribution was obtained applying Barret-Joyner-Halenda (B.J.H.) method [8] on the desorption branch of the isotherm. Finally, pore volume was measured at $P/P_0 = 0.98$ on the adsorption branch.

3.2.2 X-Ray Diffraction (XRD)

The analyzes were performed at room temperature using a Bruker D8 Advance diffractometer, equipped with a copper anticathode ($\lambda_{K\alpha 1} = 0.15406$ nm), a monochromator and a LynxEye detector. The data was recorded by applying a 0.02 ° step ranging from 5 ° to 80 °. Integration time was fixed at 2 s per step. The identification of the crystalline phases was performed by comparison with the JCPDS (Joint Committee on Powder Diffraction Standards) database established by the ICDD (International Center for Diffraction Data) institution. Moreover, the average crystallite sizes were calculated using the Debye Scherrer equation (refer Eq. (3.1)) with Warren's correction (refer Eq. (3.2)).

$$D = \frac{K\lambda}{\beta cos\theta} \tag{3.1}$$

where,

D = average crystalline size

K = dimensionless shape factor which varies with the actual shape of crystallite (here, 0.9).

λ = X-ray wavelength (here, 0.15406 nm)

β = line broadening at half the maximum intensity (FWHM) with Warren's correction (refer Eq. 3.2)

θ = Bragg angle

$$\beta = \sqrt{{\beta_{sample}}^2 - {\beta_{quartz}}^2} \tag{3.2}$$

where,

β_{quartz} = instrumental broadening determined by the FWHM of X-ray reflection of quartz having particles larger than 150 nm.

β = FWHM of the sample

3.2.3 H_2-Temperature Programmed Reduction (TPR)

The experiments were conducted on an Autochem II 2920 apparatus equipped with a Thermal Conductivity Detector (TCD) (Micromeritics instrument). The samples (20 mg) were loaded in a U-shaped quartz reactor and reduced under a flow composed of 5 vol% H_2/Ar (total flow rate of 30 mL.min^{-1}). The analyses were performed from 50°C to 900°C, applying a temperature ramp of 5°C.min^{-1}.

In the case of CuAl- mixed oxide samples (discussed in Chapter 4), the reduction degree of copper (Red (%)) was calculated according to Eq. (3.3).

$$Red(\%) = \frac{H_2 - Exp}{H_2 - Th} \times 100 \tag{3.3}$$

where,

$Red(\%]$ = Reduction degree of Copper

$H_2 - Exp$ = experimental H_2 consumption

$H_2 - Th$ = the theoretical amount of H_2 that should be consumed assuming all the copper are initially present in Cu^{2+} state and reduced to their metallic state (Cu^0).

3.2.4 Thermogravimetric Analysis (TGA)

The experiments were performed using SDT Q600 (TA Instruments). A known mass of the samples (approx. 10 mg) was heated under controlled atmosphere from 20°C to 1000°C, applying a heating ramp of 5°C.min^{-1}. The analyses were conducted under air and under CO_2 with a total flow rate of 100 mL.min^{-1}.

3.2.5 Fourier Transform Infra-red Spectroscopy (FTIR)

The measurements were performed using Nicolet iS50 manufactured by Thermo Scientific between 400-4000 cm^{-1}, 50 acquisitions per spectrum and a resolution of 4 cm^{-1}. The analyses were made using Attenuated Total Reflectance (ATR) module on powdered form of the sample at ambient pressure and temperature.

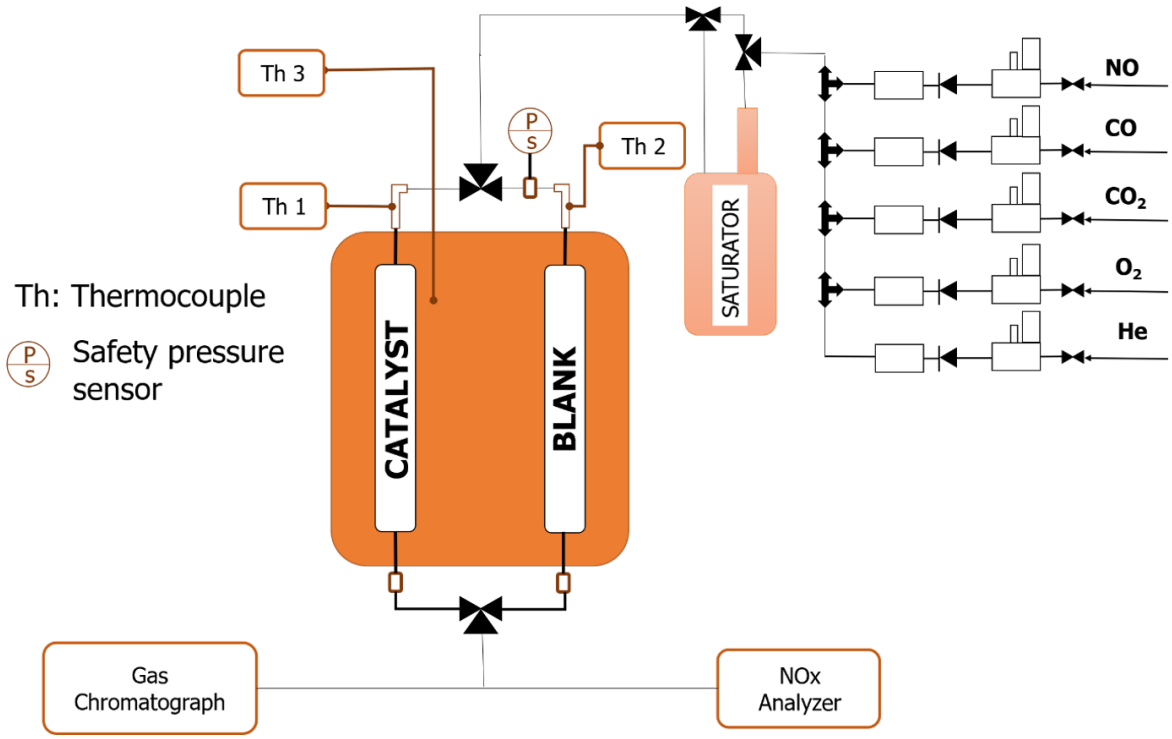

Figure 3.4 Schematic representation of lab-scale catalytic activity test setup

3.3 Lab-Scale Catalytic Activity Tests

Prior to the catalytic test, 150 mg of catalyst was pelletized, crushed, and sieved at the 350-500 μm size interval. Then, the catalyst was diluted with SiC to maintain the same Gas Hourly Space Velocity (GHSV) for all the catalytic tests. For certain catalytic activity tests, non-diluted samples were used to mimic real-world application. The catalyst sample was then positioned in a tubular continuous-flow reactor (internal diameter of 6 mm; length of 9.8 cm). The schematic representation of the catalytic activity setup is shown in Figure 3.4.

Additionally, before the catalytic test, the sample was pre-treated under He (or N_2) flow at 200°C for 90 min (heating ramp = 1.5°C.min^{-1}; total flow rate = 60 (or 200) mL.min^{-1}). After the reactor was cooled down to the desired temperature, the reaction feed composed of 20.4 vol% CO_2- 0.13 vol% CO - 0.05 vol% NO - 8.8 vol% O_2 - 8.2 vol% H_2O – balanced He (or N_2) was stabilized on the system using the blank reactor column (shown in Figure 3.4). The total gas flow rate was 200 mL.min^{-1}, given a GHSV of 22400 h^{-1}. The catalytic experiments were conducted in the temperature interval 50 - 500°C at atmospheric pressure. The conversion and yields were measured

under stabilized regime, after 8-10 min at the selected temperature. The gas composition was analysed by a NO_x analyser (SERVOMEX Model Xentra 4900) and a Gas Chromatograph (Global Analyzer Solutions - GAS model 1300). The conversion (X), selectivity (S) and yields (Y) were calculated according to Eq. (3.4), Eq. (3.5) and Eq. (3.5) respectively.

$$X(\%) = \frac{n^{inlet} - n^{outlet}}{n^{inlet}} \times 100 \tag{3.4}$$

$$S(\%) = \frac{\vartheta_i n_i^{outlet}}{\sum_{i=1}^{N_{comp}} \vartheta_i n_i^{outlet}} \times 100 \tag{3.5}$$

$$Y_i(\%) = X \times S_i \times 100 \tag{3.6}$$

where, n^{inlet} and n^{outlet} are the number of moles of CO or NO at the inlet and outlet of the reactor; ϑ_i is the stoichiometric coefficient of the product i from the reactions, and n_i^{outlet} is the number of moles of the component i at the reactor outlet.

For the catalytic tests over perovskite-based mixed oxide samples, N_2 instead of He was used for the sample pre-treatment prior to the activity test and as a gas vector during the activity test. Moreover, the concentration of the gas components at the outlet of the reactor were determined using MATRIX MG-2 Mid-infra-red Gas Phase Spectroscopy instrument provided by Bruker. The IR measurements are performed for a spectral range of 650-5000 cm^{-1}. The rest of the parameters for the catalytic activity test and the calculation of conversion, selectivity and yield are the ones used in case of the mixed oxide samples synthesized by LDH-route.

References

[1] D.P. Debecker, E.M. Gaigneaux, G. Busca, Exploring, tuning, and exploiting the basicity of hydrotalcites for applications in heterogeneous catalysis, Chem. - A Eur. J. 15 (2009) 3920–3935. doi: 10.1002/chem.200900060.

[2] M. Fernandez-Garcia, M. Alvarez, I. Rodriguez-Ramos, A. Guerrero-Ruiz, G.L. Haller, New insights on the mechanism of the NO reduction with CO over alumina-supported copper catalysts, J. Phys. Chem. 99 (1995) 16380–16382. doi: 10.1021/j100044a027.

[3] D. Lopes, F. Zotin, L.A. Palacio, Copper-nickel catalysts from hydrotalcite precursors: The performance in NO reduction by CO, Appl. Catal. B Environ. 237 (2018) 327–338. doi: 10.1016/j.apcatb.2018.06.007.

[4] C.L. Oliveira Corrêa, Y.E. Licea, L. Amparo Palacio, F.M. Zanon Zotin, Effect of composition and thermal treatment in catalysts derived from Cu-Al hydrotalcites-like compounds in the NO reduction by CO, Catal. Today. 289 (2017) 133–142. doi: 10.1016/j.cattod.2016.08.023.

[5] V. Muñoz, F.M.Z. Zotin, L.A. Palacio, Copper-aluminum hydrotalcite type precursors for NOx abatement, Catal. Today. 250 (2015) 173–179. doi: 10.1016/j.cattod.2014.06.004.

[6] A. Alejandre, F. Medina, P. Salagre, X. Correig, J.E. Sueiras, Preparation and study of Cu-Al mixed oxides via hydrotalcite-like precursors, Chem. Mater. 11 (1999) 939–948. doi: 10.1021/cm980500f.

[7] A. Galarneau, F. Villemot, J. Rodriguez, F. Fajula, B. Coasne, Validity of the t-plot method to assess microporosity in hierarchical micro/mesoporous materials, Langmuir. 30 (2014) 13266–13274. doi: 10.1021/la5026679.

[8] E.P. Barrett, L.G. Joyner, P.P. Halenda, The Determination of Pore Volume and Area Distributions in Porous Substances. I. Computations from Nitrogen Isotherms, J. Am. Chem. Soc. 73 (1951) 373–380. doi: 10.1021/ja01145a126.

Chapter 4

Copper and Cobalt -Mixed Oxide Catalysts

Copper-aluminum based LDH is employed as the starting material in order to develop a catalytic material with an optimised active metal composition and synthesis technique for the highest NO-SCR by CO performance. The synthesis parameters that are studied in this work are the type of pre-treatment gas atmosphere, the composition of active metals in the material, and the material pre-treatment temperature. Copper is reportedly an active material for NO reduction by CO activity, and its LDH preparation via co-precipitation is rather straightforward. Moreover, previous literature studies (refer to Chapter 2) have demonstrated the effect of material pretreatment: the nature of pretreatment gas and pretreatment temperature have significant impact on the NO reduction by CO activity. Therefore, CuAl LDH was initially synthesised to investigate the influence of material pre-treatment under different gas atmospheres on NO-SCR performance[1]. Second, cobalt, an additional active metal for NO-SCR activity, was added to this Cu-Al LDH by co-precipitation at various Cu:Co molar ratios to determine the optimal Co content for NO-SCR performance. Finally, the influence of the pre-treatment temperature on this optimal Cu:Co molar ratio catalytic material is investigated. This optimised approach for preparing

[1]The study related to the impact of gas pretreatment of CuAl-LDH on the NO reduction by CO activity has been published. The reference to this article is as follows: [70]

mixed oxides will be applied to large-scale catalyst synthesis for semi-pilot experiments. Lastly, the thermal stability of the final catalytic material and its catalytic performance in comparison to Pt-containing catalysts were evaluated.

4.1 Effect of Pre-treatment Gas Atmosphere

By treating the LDH with various gases at an elevated temperature of 500°C, different CuAl mixed oxide samples were derived from the common parent LDH. The following gases were used to prepare these mixed oxides: air, He, 1 vol% CO in He, and CO_2. These thermally activated samples are referred to as CuAl-X, where X represents the gas treatment used. As a result, the gas-treated samples discussed in this study are CuAl-air, CuAl-He (treatment with 100% He), CuAl-CO/He (1 vol% CO in He), and CuAl-CO_2 (treatment with 100% CO_2).

4.1.1 Material Characterization Results

Various material characterization experiments like N_2-physisorption, H_2-TPR, XRD, TGA and FTIR were performed on the CuAl mixed oxide samples to determine the corresponding physico-chemical properties. The results of each of these material characterization experiments are discussed in this section.

4.1.1.1 N_2-physisorption

Adsorption and desorption isotherms recorded from the N_2-physisorption analysis are shown in Figure 4.1. The shape of the isotherm obtained is a mix of Type II and Type IV(a) [1]. At high P/P_0 (> 0.70), a step of adsorption is observed which corresponds to the capillary condensation of N_2 in large mesopore or small macropores. Therefore, it can be concluded that a large distribution of the pores, is observed in the mixed oxide samples. These results are in agreement with the results reported in the literature [2] according to which the thermal decomposition of LDH-type materials leads to the formation of an oxide that can be described as crystalline particles aggregated together, the porosity being associated with the intra-aggregate (small porosity) and inter-aggregate (large porosity) voids [1]. The shape of the hysteresis loops for all the CuAl-X samples belongs to the H3-type hysteresis loop, which is generally attributed to non-rigid aggregates of plate-like particles that confirm the above described morphology [1]. Similar results for CuAl mixed oxides derived from LDH pre-

cursors have also been reported by Hadi et al. and González-Olevra et al. [2,3]. Further, specific surface area (SSA), pore volume and average pore diameter

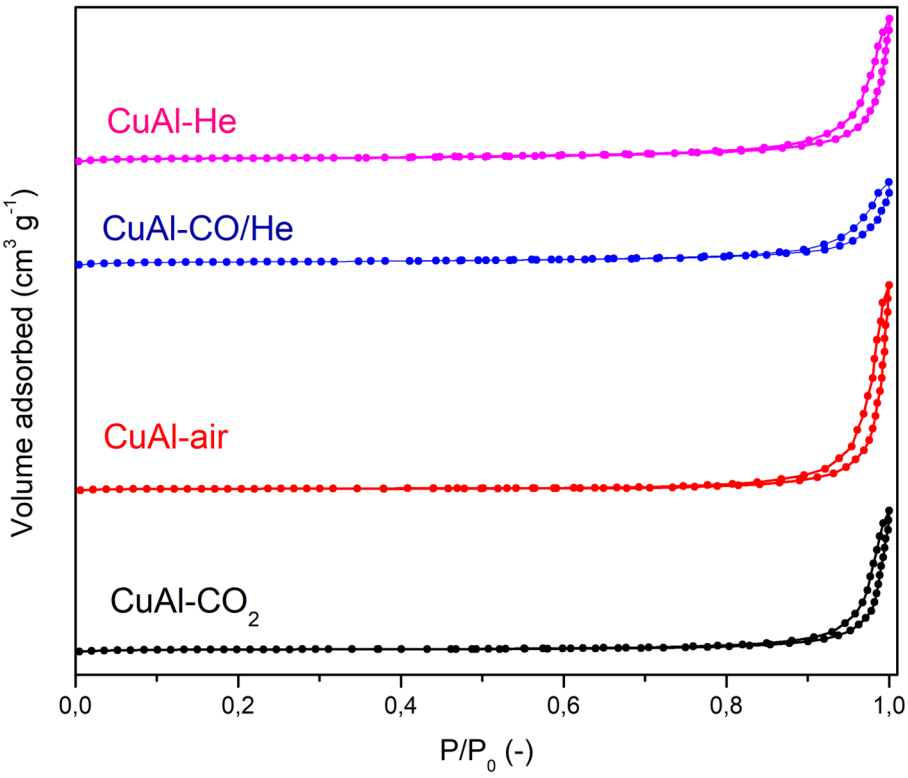

Figure 4.1 N_2-adsorption and desorption isotherm obtained for CuAl-X samples

calculated for the CuAl-X materials are listed in Table 4.1. It can be observed that SSA for CuAl-air and CuAl-CO_2 materials are comparable i.e., 39 $m^2.g^{-1}$ while CuAl-He exhibited a slightly lower SSA, i.e., 34 $m^2.g^{-1}$ and the lowest SSA was measured for CuAl-CO/He, i.e., 25 $m^2.g^{-1}$. In summary, irrespective of the thermal treatment applied to the LDH, specific surface area of the resulting mixed oxide material remained modest, below 50 $m^2.g^{-1}$. Moreover, the slightly lower SSA for the mixed oxide obtained after reductive treatment (CuAl-CO/He) of the parent LDH can be ascribed to the sintering of particles upon treatment, leading to low metal dispersion [4–6].

Upon comparing the total specific pore volume (V_p) of the CuAl-X materials, it was observed that the highest pore volume of 0.18 $cm^3.g^{-1}$ was recorded for CuAl-CO_2 while the lowest specific pore volume was recorded for CuAl-CO/He (0.12 $cm^3.g^{-1}$). This pore volume is mostly generated in

Table 4.1 Textural properties of CuAl-X samples

Sample	S_{BET} ($m^2.g^{-1}$)[a]	V_μ ($cm^3.g^{-1}$)[b]	V_p ($cm^3.g^{-1}$)[c]	D_{BJH} (nm)[d]	D_{CuO} (nm)[e]
CuAl-He	34	0.002	0.14	18.7	19
CuAl-CO/He	25	0.002	0.12	22.6	31[f]
CuAl-air	39	0.003	0.12	15.5	16
CuAl-CO_2	39	0.002	0.18	19.8	21

[a] S_{BET} = specific surface area measured by the B.E.T method
[b] V_μ = micropore volume measured by t-plot treatment
[c] V_p = total pore volume measured at $P/P_0 = 0.98$
[d] D_{BJH} = average pore size measured by B.J.H method applied to the desorption branch
[e] D_{CuO} = average crystal domain size calculated using the Debye–Scherrer equation based on (111) peak of 35° of the CuO pattern with Warren's correction
[f] The crystalline diameter is for Cu(0) species in CuAl-CO/He

mesopores since all the CuAl-X samples present minor micropore volume (V_μ, i.e. always less than 0.003 $cm^3.g^{-1}$ as calculated from t-plot data treatment). However, the absence of microporosity formation is not surprising since the transformation of LDH into oxide particle aggregates will mostly lead to large porosity (meso-macropores). Similar observations were also reported by Hadi et al [2] where the authors prepared the CuAl mixed oxides from air-calcination of parent LDH, which was prepared via the same methodology as described in our studies. The authors additionally performed SEM-EDX studies and observed a good dispersion of metal particles (however, the SEM-EDX studies were performed only on the CuCeAl mixed oxide sample but the reason for the good dispersion was attributed to the synthesis of mixed oxides from the thermal decomposition of parent LDH). Moreover, the average pore diameters (D_{BJH}), calculated considering BJH method applied to the desorption branch (see Appendix A), are found to vary from 15.5 nm (CuAl-air) and 22.6 nm (CuAl-CO/He). Despite the significant difference in the average pore volume values, all catalysts present broad pore size distributions, ranging from 2 nm to a maximum at $\sim$ 50 nm, typically in the mesoporous range. Therefore, it can be stated that the gas treatment condition has a limited effect on pore size distribution. However, the occurrence of more pronounced sintering of active metal particles during the reductive gas treatment (here, CO/He) on its LDH precursor could explain the slightly higher average pore volume [7] measured over the CuAl-

CO/He catalyst. To conclude, the nature of the gas used for the treatment has a minor effect on the porosity of catalysts, a porosity that is produced by the oxide particle arrangement in the form of large aggregates.

4.1.1.2 XRD

XRD analysis were performed for the parent CuAl HT precursor and CuAl-X samples issued from thermal activation under different atmospheres, and results are shown in Figure 4.2. The diffractogram obtained for CuAl HT sample shows reflections characteristic of copper-aluminum LDH phase, $Cu_6Al_2(OH)_{16}CO_3.4H_2O$ - JCPDS No. 037-0630, in addition to reflections ascribed to oxide phase (CuO, JCPDS No. 48-1548). This result differs from that reported by Mu$\tilde{n}$oz and Alejandre [8,9], who showed formation of malachite which generally appears due to the low pH of the final solution during the synthesis of the LDH [10]. Mu$\tilde{n}$oz et al. used a pH of 9 while Alejandre et al. used a pH of 8 for their corresponding LDH synthesis which are lower than in this study, i.e. 10.5. Additionally, CuO phases at 32°, 39° and 53° and $CuAlO_2$ phase at 37° were also observed in the diffractogram of CuAl HT sample material.

Thermal treatment of LDH phase leads to the removal of interlayer water molecules, dehydroxylation, and removal of carbonate species as CO_2 that is taking place, damaging the LDH- specific lamellar structure [8,9,11], and leading to the formation of induced mixed oxide phases. As can be expected, the decomposition occurs whatever the gas treatment applied, LDH diffraction peaks are absent on activated solids, while CuO diffraction peaks are observed (JCPDS: 48-1548) for thermal gas treatment under He, air, and CO_2 (named CuAl-He, CuAl-air and CuAl-CO_2 samples respectively). Thermal treatment did not have a strong influence on CuO crystallites size ($\sim$ 20 nm) (see Table 4.1). Comparable crystal domain sizes are reported by Hadi et al. (i.e., 17 nm) [2] after the thermal decomposition of Cu-Al LDH. For comparison, Alejandre et.al [9] obtained a slightly lower crystal domain size, 12 nm, however authors started with a material containing malachite phase. In the case of the activation under CO/He atmosphere, diffraction peaks attributed to the CuO was not observed. Only metallic Cu phase was visible on the diffractogram. The calculated average crystalline size of the metallic copper, 31 nm, reflects a poor dispersion of the metallic copper phase in this solid after activation step. Under this last activation conditions, CO acts as a reducer of Cu(+II) species

from the hydrotalcite phase, leading to metallic particles formation. Worth to mention that we do not observe, by XRD, $CuAl_2O_4$ spinel type phase formation, whatever gas composition used for the treatment, which is in accordance of results presented in the literature where spinel formation is observed only at temperatures above 650°C [9].

4.1.1.3 H_2-TPR

Further, the CuAl mixed oxides reducibility evolution was investigated by H_2-TPR, and the corresponding reduction profiles are shown in Figure 4.3. Reduction profiles of CuAl-CO_2, CuAl-He and CuAl-air exhibited four reduction peaks while that of CuAl-CO/He showed only three. For the three first samples, the first reduction peak (denoted as α) was observed between 204-234°C and can be attributed to easily reducible and accessible copper nanoparticles (NPs) as well-dispersed Cu(II) species. This reduction peak can also be attributed to the reduction of copper dimers $[Cu^{2+}\text{-}O^{2-}\text{-}Cu^{2+}]^{2+}$ or copper monomers which

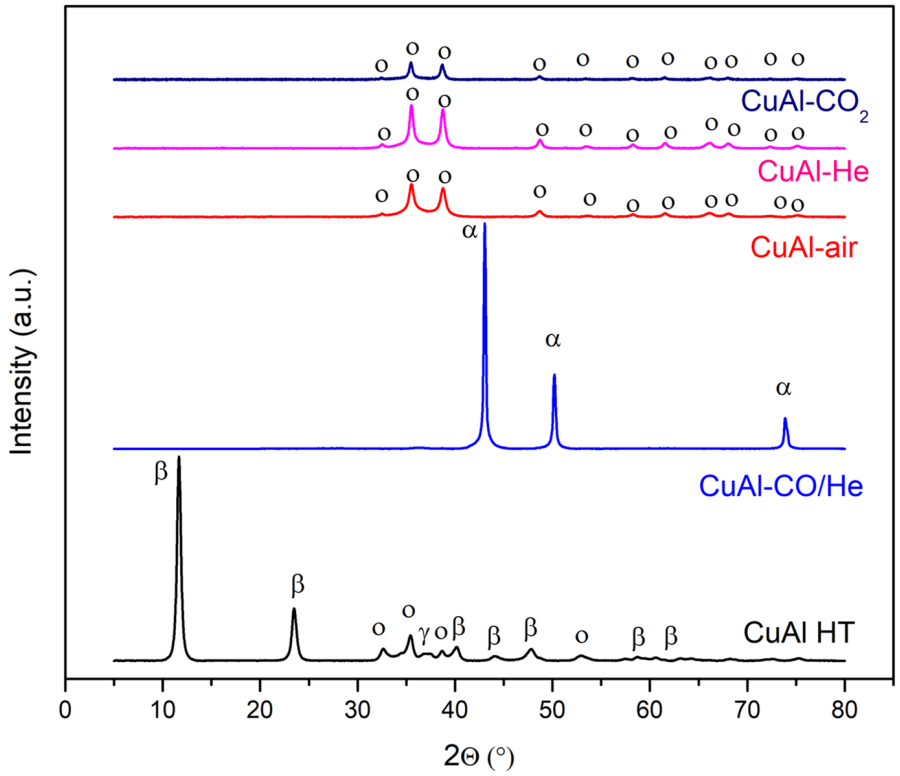

Figure 4.2 XRD of untreated CuAl HT precursor and CuAl-X mixed oxide samples. α = metallic Cu - JCPDS: 04-0836; o = CuO - JCPDS: 48-1548, β = Hydrotalcite phase - JCPDS: 037-0630, γ = $CuAlO_2$-JCPDS: 40-1037

are reduced to Cu^{+} as previously observed by Texeira et al. [12]. The second reduction peak (denoted as β) was observed between 246-260°C and can be attributed to the reduction of larger CuO cluster species which are affected by the copper-aluminum interaction since its reduction temperature is lower than that of the pure (bulky) CuO [12]. There are conflicting statements regarding the third and fourth reduction peaks reported in the literature. The third reduction peak (denoted as γ) was observed between 276-286°C and can be attributed to the reduction of large bulk-like CuO species which were formed due to thermal treatment [13–15]. The fourth reduction peak (denoted as λ) was observed between 313-318°C and can be attributed to reduction of Cu_2O to metallic Cu [8,15] thereby anticipating that CuO species were reduced by a two-step reduction process: CuO$\rightarrow$ Cu_2O $\rightarrow$ Cu. However, this peak can be also attributed to the reduction of large bulk-like/crystalline CuO species, even larger than the ones reduced under γ peak [2,16]. The presence of the bulk-like/crystalline CuO in the samples were also detected during the XRD analysis. Moreover, the reduction peaks observed in the TPR profile of CuAl-CO/He have shifted to temperatures lower than that of CuAl-He, CuAl-CO_2 and CuAl-air samples implying that the copper species in former are more reducible than the latter samples. These reducible CuO species could come from the oxidised copper due to the exposure of sample material to the ambient air. A similar explanation was also reported by Gonçalves et al. [17] where XANES characterization experiment detected the presence of 4% of Cu(II) species while the rest were metallic copper species in the sample that was obtained after H_2-treatment at 200°C.

Further, the H_2-consumption of each reduction peak was derived from the deconvolution and is also summarised in Table 4.2. In this table, the reduction percentage (red%) was calculated by considering the theoretical Cu content in the sample i.e., 45.85 wt%. Upon comparing CuAl-X samples on the basis of total H_2-consumption, similar to XRD analysis results (refer Figure 4.2), the presence of majority of Cu^0 and probably very few reducible copper species in the CuAl-CO/He sample resulted in a limited consumption of H_2 (see Table 4.2). Interestingly, the specific H_2-consumption for CuAl-CO_2 sample is higher than that of CuAl-air and CuAl-He even if these three samples showcase similar textural properties from N_2-physisorption (refer Table 4.1 and Figure 4.1) and

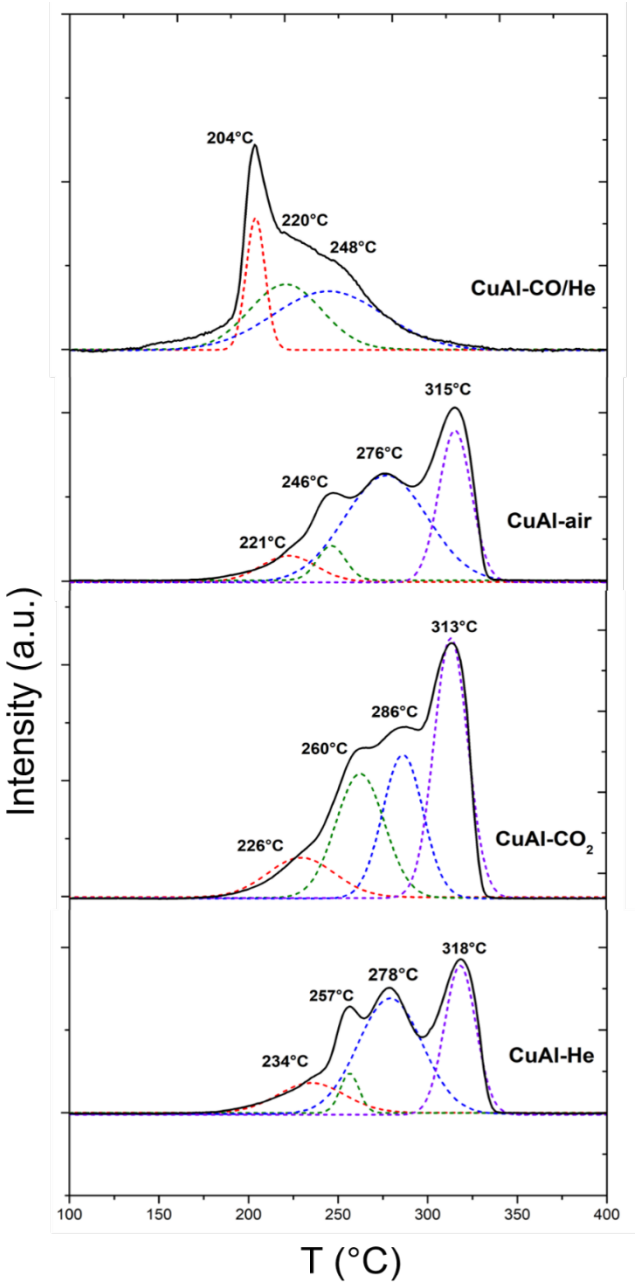

Figure 4.3 H_2-TPR reduction profile of CuAl-X mixed oxide samples. Reduction peaks indicated in dotted lines: α = red, β = green, γ = blue and λ = violet; Experimental curve thick solid line = black

XRD (refer Figure 4.2) and TPR profiles.

4.1.1.4 TGA

Thermogravimetric Analysis (TGA) was carried out to study the decomposition of CuAl HT under the flow of air and CO_2 since CuAl-CO_2 shows higher specific H_2-consumption than CuAl-air or CuAl-He (the latter two samples show

Table 4.2 Reduction characteristics for different CuAl-X samples

Sample	H_2 consumption ($mmol.g^{-1}$)					Red(%)[a]
	Tot. H_2 cons.[b] ($mmol.g^{-1}$)	T_1/α[c]	T_2/β[c]	T_3/γ[c]	T_4/λ[c]	
CuAl-air	9.941	221 / 0.900	246 / 0.598	276 / 5.503	315 / 3.068	66.76
CuAl-He	9.917	234 / 1.320	257 / 0.497	278 / 4.971	318 / 3.117	66.60
CuAl-CO/He	1.045	204 / 0.336	220 / 0.179	248 / 0.467	−−	0.07
CuAl-CO_2	10.630	226 / 1.232	260 / 2.790	286 / 2.691	313 / 4.055	71.39

[a] Reduction degree of copper
[b] Experimental H_2-consumption from TPR analysis
[c] $T_{1\text{-}4}$ = Peak reduction temperature (°C) / H_2-consumed by each curve calculated after deconvolution of experimental H_2 consumption curve

similar textural and redox properties and therefore, air was chosen for the TGA analysis). The weight loss curves of CuAl HT under air and CO_2 were compared (see Figure 4.4). The weight loss curve for CuAl HT under air can be divided into three zones, while that of CuAl HT heated under CO_2 can be divided into four zones (see Table 4.3). Firstly, the weight loss recorded at temperatures below 200°C is due to the loss of weakly bonded interlayer water molecules [9]. However, below 200°C, emission of small amount of CO_2, NO and NO_2 have also been reported in the literature and these emissions have been attributed to the decomposition of loosely bonded carbonate and nitrate anions which could be present at the edges of the interlayers of these hydrotalcite-like materials [9,18]. In this study, for temperatures below 200°C, the thermal decomposition of CuAl HT under CO_2 showed a weight loss of 8% while under air, the weight loss was recorded to be 14.1%. Secondly, the weight loss in CuAl HT samples for the temperature range 200-650°C can be attributed to the weight loss due to dehydroxylation and decarbonation resulting in the emission of CO_2 and water [9]. In certain studies reported in the literature, the second weight loss zone has been attributed to the dehydration and dehydroxylation while the third weight loss zone has been attributed to the removal of interlayer carbonate anions or decarbonation [19–21]. Therefore, for CuAl

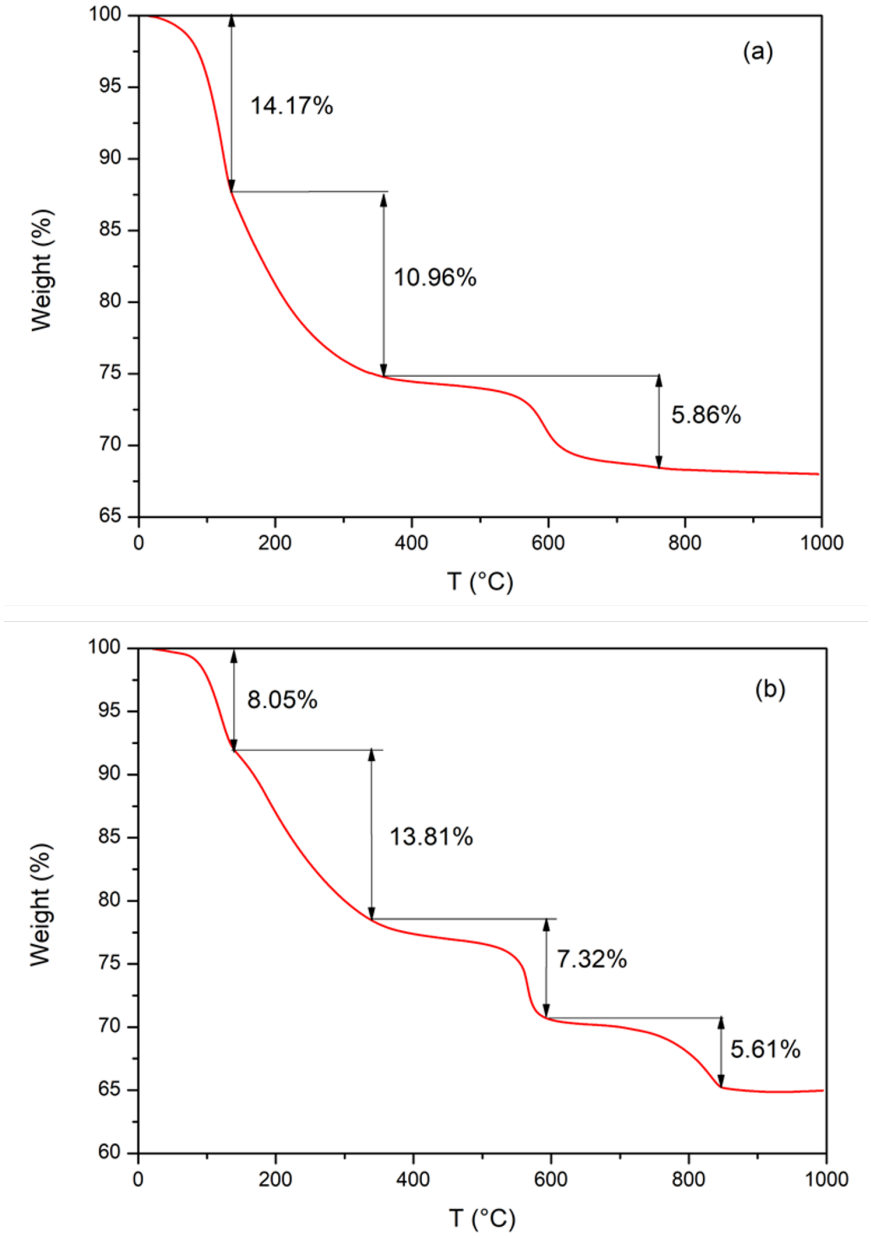

Figure 4.4 TGA curves for CuAl HT samples heated under (a) air and (b) CO_2

HT under air and CO_2, it can be anticipated that the weight loss commences with dehydroxylation at T > 200°C followed by decarbonation at T > 400°C [21]. However, there is also a probability of dehydroxylation and decarbonation taking place simultaneously [22]. Further, the total weight loss recorded until 650°C for thermal decomposition of CuAl HT under air was 16.8%, while that under CO_2 was 21.1%. This increase in weight loss can be probably attributed to the loss of excess carbonate species formed by the interaction of CO_2 with the sample at low temperatures in the latter case [23]. Finally, a weight

Table 4.3 TGA results obtained for CuAl HT and CuAl-CO_2 samples

Sample	Tot. wt. loss (wt%)[a]	T_1 (°C), W_1 (%)[b]	T_2 (°C), W_2 (%)[b]	T_3 (°C), W_3 (%)[b]	T_4 (°C), W_4 (%)[b]
CuAl-air	32.0	30-160, 14.1	160-360, 10.9	360-640, 5.9	––
CuAl-CO_2	35.0	30-160, 8.0	160-360, 13.8	360-600, 7.3	600-840, 5.6

[a] Total weight loss recorded for the sample (%)
[b] T (°C) = Temperature range of weight loss; W (%) = weight loss at the corresponding temperature range

loss of 5.6% was reported for the decomposition of CuAl HT under CO_2 while no observable weight loss was recorded for decomposition under air for the temperature range of 650-1000°C. This loss in weight for temperatures above 650°C can be attributed to the decomposition of strongly bonded interlayer carbonate anions present in the form of oxycarbonates [18]. However, Alejandre et al. have reported similar results at temperatures greater than 530°C and have attributed such behaviour to bidentate carbonate ligands decomposition (refer Figure 4.5)[9]. This explanation was in line with their Fourier-Transform Infrared results. Therefore, they concluded that in general, brucite-like structures have two different types of carbonates: monodentate and bidentate in the interlayer region where the former decomposes at a temperature lower than that of the latter. Formation of monodentate and bidentate carbonates by CO_2 adsorption onto basic sites of different LDHs have also been reported by Prinetto and Coenen [23,24]. Therefore, it can be concluded that CuAl-CO_2 sample also contains mono-and bidentate carbonates formed by adsorption of CO_2 onto the surface of the sample.

4.1.1.5 FTIR

In order to further investigate the change in the material during the treatment of the parent CuAl HT under air and CO_2, Infra-Red (IR) measurements were performed on CuAl-CO_2 and CuAl-air samples treated under the flow of their respective activation gas atmospheres at temperatures of 100°C, 300°C and 500°C. The samples are represented as CuAl-X-Y where X denotes the type of gas treatment (= CO_2 or air) and Y denotes the temperature of treatment (100, 300

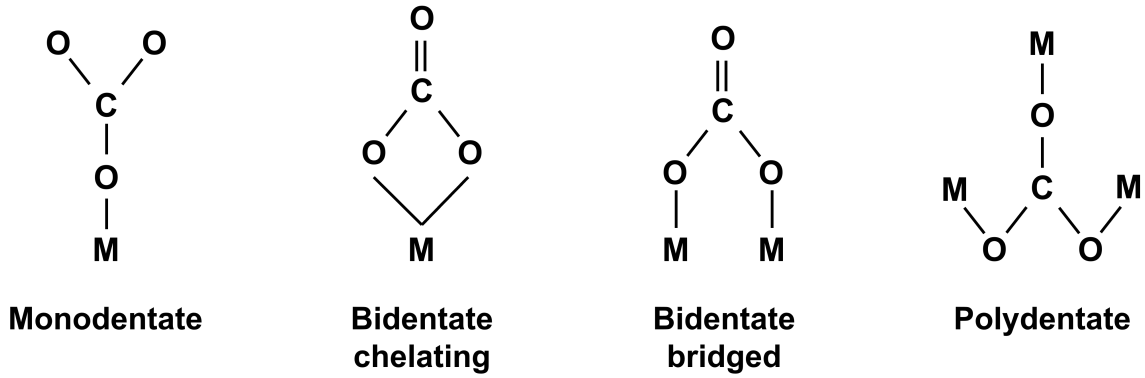

Figure 4.5 Different carbonate species formed in the CuAl-CO_2 sample (illustration recreated from Coenen et al.[23])

or 500°C). The IR spectra thus obtained for different CuAl-air and CuAl-CO_2 samples were compared with parent LDH spectra separately. The IR spectra of the different CuAl-air treated at different temperatures are shown in Figure 4.6. In Figure 4.6(a), CuAl HT sample exhibited a strong intense peak at 1350 cm^{-1} which is typical of LDH and is attributed to the vibrations of interlayer carbonate anions [25]. Also, the bands in the IR spectra of CuAl HT observed between 590 cm^{-1} and 860 cm^{-1} can be attributed to the lattice stretching vibrations of metal-oxygen and bending vibrations of metal-hydroxide bonds [25,26]. Moreover, the broad signal for CuAl HT between 2515 cm^{-1} and 3750 cm^{-1} (see Figure 4.6(b)) and single band at 1630 cm^{-1} is generally attributed to OH-stretching vibrations from brucite-like layers and interlayer water molecules [9,25].

Upon heating LDH sample under air at 100°C, the intense carbonate band at 1350 cm^{-1} reduces to two partially overlapping bands at 1350 cm^{-1} and 1500 cm^{-1} which are attributed to vibrations of strongly bonded polydentate carbonate anions [27]. Also, bands at 1218 cm^{-1} and 1067 cm^{-1} are attributed to monodentate or bidentate carbonate species and symmetric vibration mode of carbonate anions respectively [25,27] while bands below 854 cm^{-1} are attributed to the metal-oxygen and metal-hydroxide vibrations [25,26]. Moreover, band at 1630 cm^{-1}, observed in CuAl HT and attributed to the stretching vibrations of the interlayer OH-species, is completely vanished because of the sample dehydroxylation which is in accordance with the corresponding TGA for 50-150°C temperature range (refer Figure 4.4(a)). Further, presence of broad

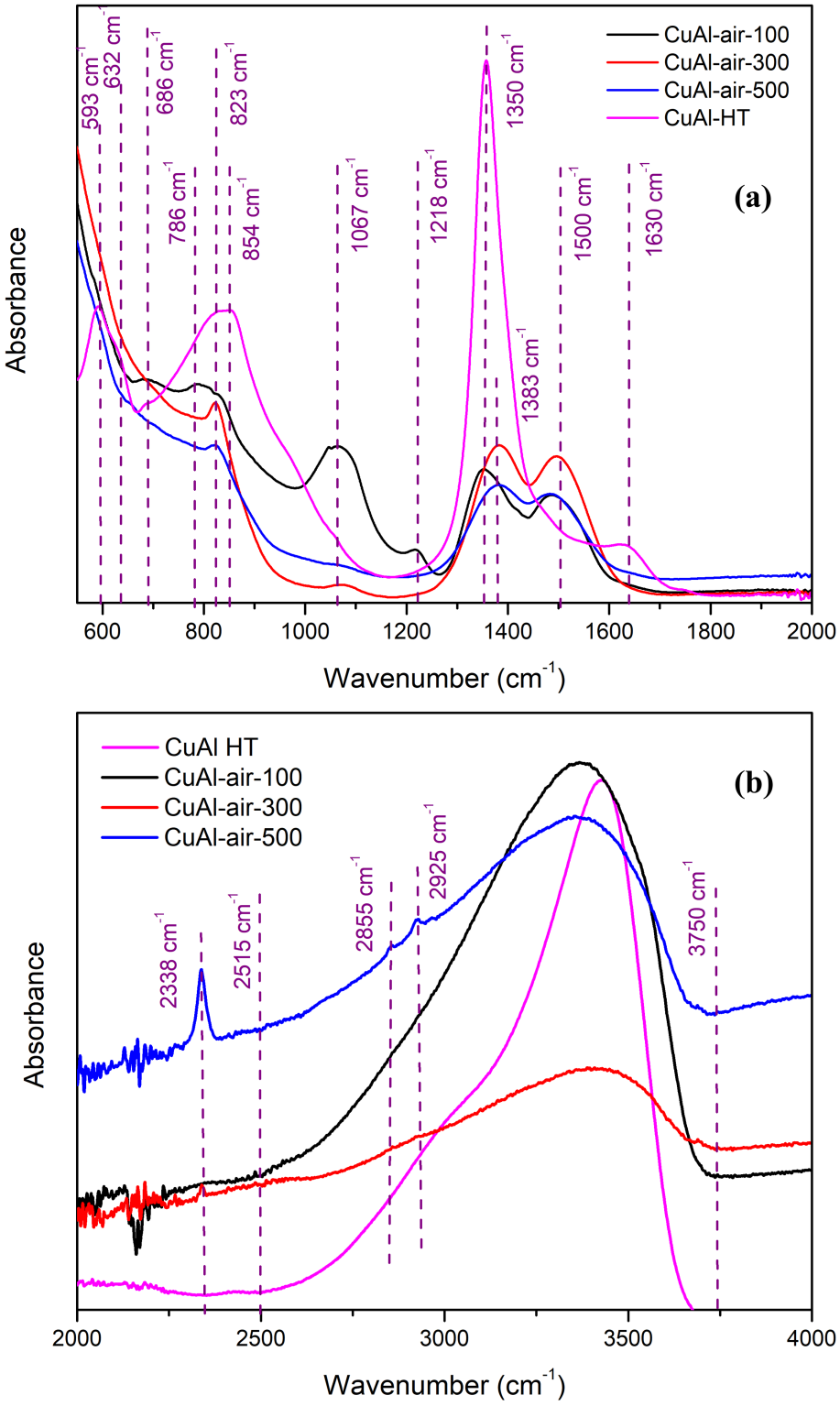

Figure 4.6 Comparison of IR spectra for CuAl-air samples treated at different temperatures. The IR spectra are divided into two regions based on the wavenumber ranges: (a) 500-2000 cm^{-1} & (b) 2000-4000 cm^{-1}

band between 2515 cm^{-1} and 3750 cm^{-1} indicates that CuAl-air-100 sample consists of water molecules. This is possible because the sample after the gas treatment was exposed to the ambient air and therefore can have absorbed moisture. Upon further increasing treatment temperature to 300°C (see the IR spectra for CuAl-air-300 in Figure 4.6), intensity of bands at 1067 cm^{-1} and 1218 cm^{-1} attributed to carbonate species is greatly reduced due to the sample decarbonation. Similar result was observed in the TGA of CuAl HT under air flow where a weight loss attributed to the carbonate molecules removal was recorded between 200°C and 400°C (refer Figure 4.4(a)). The bands attributed to the more stable polydentate carbonate species still exists but with an increase in the wavenumber from 1350 cm^{-1} to 1383 cm^{-1} for one of the partially overlapping carbonate signals similar to that observed for CuAl-air-100 sample. Moreover, like CuAl-air-100 sample, CuAl-air-300 sample also exhibited a broad band between 2515 cm^{-1} and 3750 cm^{-1} due to the absorption of moisture by the sample upon exposure to the ambient atmosphere. Additionally, a low-intensity signal at 2338 cm^{-1} was observed which is attributed to adsorbed CO_2 asymmetric vibration mode [28]. Again, presence of these signals in the sample is due to the sample exposure to ambient atmosphere resulting in the adsorption of these impurities onto the sample surface. This adsorption of CO_2 can occur during the sample exposure to ambient atmosphere. Finally, IR spectra for the CuAl-air-500 sample was observed to be similar to that of CuAl-air-300 sample. The band at 2338 cm^{-1} attributed to the adsorption of CO_2 due to the sample exposure to ambient atmosphere was also observed for CuAl-air-500. However, the occurence of IR bands at 2855 cm^{-1} and 2925 cm^{-1} were unexpected since they are attributed to the C-H stretching vibrations [29] but such C-H interaction is not possible in this case. Therefore, the reason for occurrence of these IR peaks is still unknown. Hence, upon comparison of the IR spectra of CuAl-air-Y samples, it can be concluded that the process of dehydroxylation and decarbonation takes place during the CuAl HT treatment under air flow which is in accordance to TGA of CuAl HT under the flow of air.

Same as CuAl-air-Y samples, IR spectra for CuAl-CO_2 sample treated at different temperatures were compared and is shown in Figure 4.7. In this figure, the IR spectra for CuAl HT is the same as that shown in Figure 4.6 since same parent LDH was used for the gas pretreatment. In Figure 4.7(a), it can be

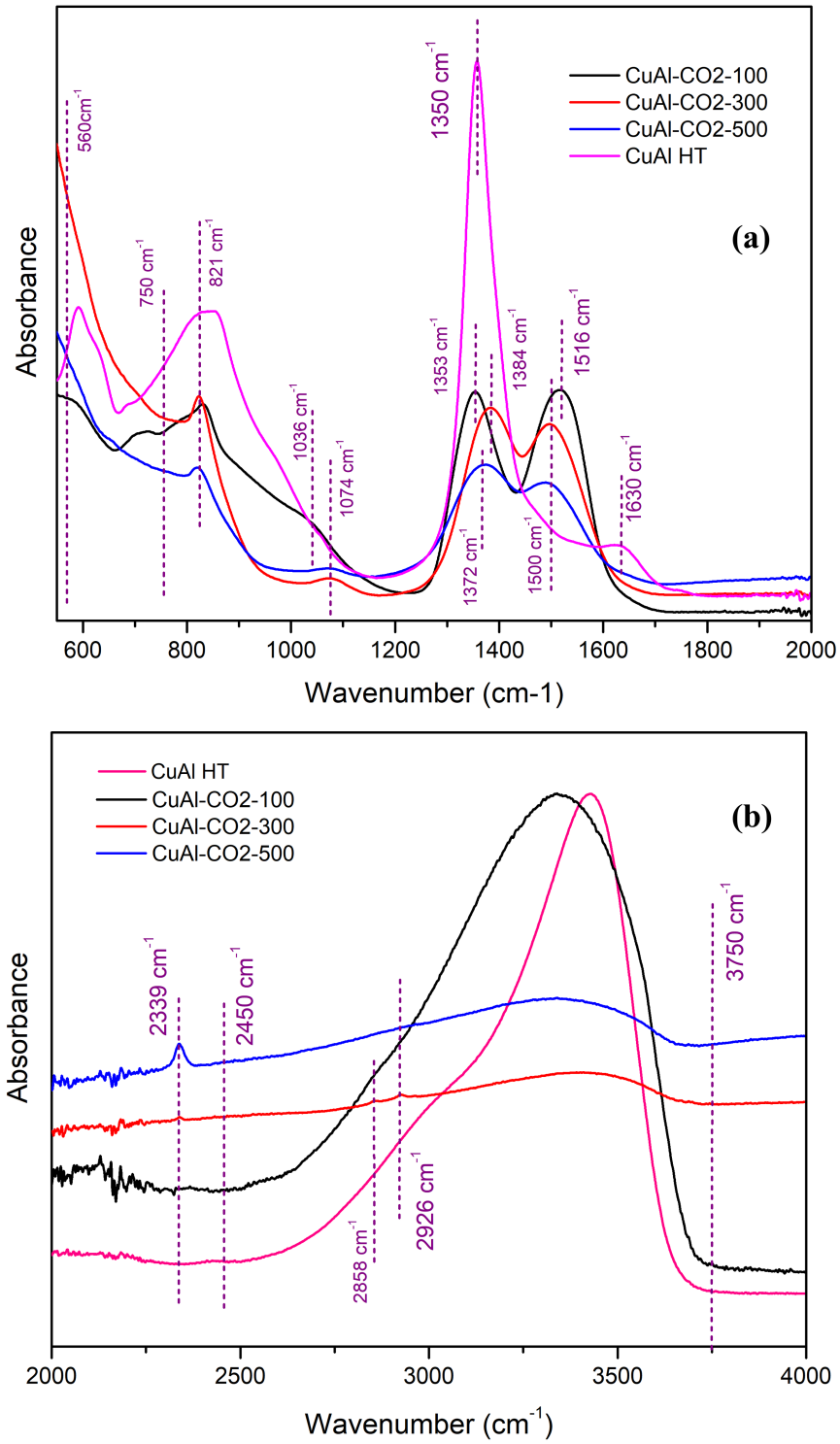

Figure 4.7 Comparison of IR spectra for CuAl-CO_2 samples treated at different temperatures. The IR spectra are divided into two regions based on the wavenumber ranges: (a) 500-2000 cm^{-1} & (b) 2000-4000 cm^{-1}

observed that the high-intense band at 1350 cm^{-1} attributed to the carbonate species in LDH structure is reduced to lower-intensity bands at 1353 cm^{-1} and 1516 cm^{-1} which are attributed to stable polydentate carbonate species [27] obtained upon treatment of CuAl HT under the CO_2-flow at 100°C. Moreover, the OH-stretching vibration band at 1630 cm^{-1} observed in the IR spectrum for CuAl HT sample is lost for CuAl-CO_2-100 sample indicating the removal of OH species from sample due to the increase of treatment temperature to 100°C. These losses of carbonates and OH species from the sample during the gas treatment are in accordance with the TGA results of CuAl HT under CO_2 flow where the loss of carbonates (decarbonation) and OH species (dehydroxylation) were observed by sample weight loss between the temperatures of 50-150°C (refer Figure 4.4(b)). Additionally, the peaks between 593-1036 cm^{-1} can be attributed to metal-oxygen and metal-hydroxide interactions vibrations [30]. Further, for CuAl-CO_2-300 sample, signals in wavenumber range of 500-2000 cm^{-1} in the corresponding IR spectrum (see Figure 4.7(b)) are similar to that observed for CuAl-CO_2-100 sample except for an additional band at 1076 cm^{-1} which is attributed to bidentate carbonate species [25]. Presence of such a signal in case of CuAl-CO_2-300 is expected because of the CO_2 reaction with the sample forming different types of carbonate species. Also, band at 1036 cm^{-1} is absent for CuAl-CO_2-300 sample indicating the removal of OH species (dehydroxylation) upon increase of treatment temperature to 300°C. Furthermore, upon comparing IR spectrum between wavenumbers of 500 cm^{-1} and 2000 cm^{-1} of CuAl-CO_2-300 with that of CuAl-CO_2-500, it is observed that the band at 1076 cm^{-1} still exists when the treatment temperature was increased from 300 to 500°C further supporting the presence of remaining bidentate carbonates which are considered to be more stable than their monodentate counterpart. These carbonate species are removed when the sample is treated beyond 600°C as observed in the TG analysis for CuAl-CO_2 (refer Figure 4.4(b)). Also, the polydentate carbonate species still exists for all CuAl-CO_2-Y samples.Finally, upon comparing the IR spectra of all the CuAl-CO_2 samples with that of CuAl HT for a wavenumber region of 2000-4000 cm^{-1} (see Figure 4.6(b)), a broad signal between 2450 cm^{-1} and 3750 cm^{-1} is observed for all the samples which are attributed to OH-stretching vibrations [9,25]. The presence of this broad signal for CuAl-CO_2 samples indicate that the samples had absorbed moisture

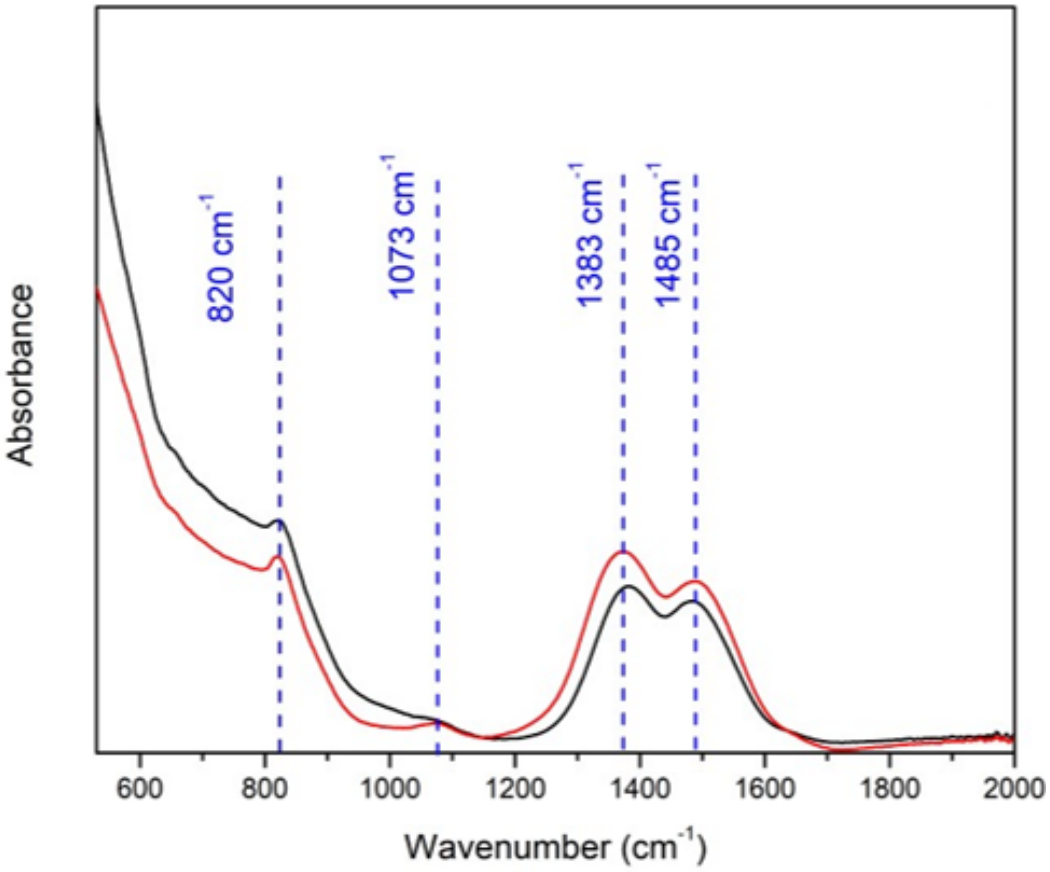

Figure 4.8 IR spectra for CuAl-air-500 (black line) and CuAl-CO_2-500 (red line) samples for a wavenumber range of 500-2000 cm^{-1}

because of their exposure to ambient atmosphere, as in case of CuAl-air-Y samples. Moreover, the presence of bands at 2338 cm^{-1} attributed to the CO_2 adsorbed [28] which can originated from impurities upon exposure of samples to ambient atmosphere. However, similar to FTIR results for CuAl-air samples, IR peaks at 2885 cm^{-1} and 2925 cm^{-1} attributed to C-H stretching vibrations [29] had been observed and reason for their occurrence is still unknown. Hence, it is concluded that CuAl HT treatment under CO_2 flow at 500°C led to not only removal of water molecules and less stable carbonate species but also formation of new and more stable carbonate species (bidentate and polydentate species) due to reaction between CO_2 and the sample surface and/or bulk.

In order to better visualise the presence of different species in CuAl-air and CuAl-CO_2 samples, the IR spectra for CuAl-air-500 and CuAl-CO_2-500 samples and for the wavenumber range of 500-2000 cm^{-1} were further

compared as shown in Figure 4.8. In this figure, it can be observed that CuAl-CO_2-500 sample exhibit 4 peaks comparing with only 3 peaks exhibited by CuAl-air-500 sample in their corresponding IR spectra. The peaks at 1383 cm^{-1} and 1485 cm^{-1} are attributed to the presence of monodentate, bidentate and/or polydentate carbonate species (due to the reaction between CO_2 with the bulk [31], possible only for CuAl-CO_2-500 sample) in the samples [23,31]. This indicates that both samples contain different carbonate species up until 500°C. This is in accordance with their corresponding TGA measurements (see Figure 4.4) where the recorded weight loss between 500-650°C has been attributed to the removal of the less stable (generally monodentate) carbonate species. Also, the peak recorded at 820 cm^{-1} is attributed to the stretching vibrations of metal-oxygen bonds [30]. Finally, the low intensity peak at 1073 cm^{-1} can also be observed only for CuAl-CO_2-500 sample and can be attributed to bidentate carbonates which are generally considered to be more stable than the monodentate carbonates [23]. Therefore, presence of this peak further supports the explanation for the weight loss of CuAl-CO_2 (see TGA plot in Figure 4.4) beyond 650°C which has been attributed to the removal of bidentate carbonates.

The presence of these additional bidentate carbonates on CuAl-CO_2 can also probably explain the highest H_2-consumption (per gram of catalyst) by this sample among all CuAl-X samples (refer Table 4.2). Reaction between surface carbonate species and H_2 reportedly forms intermediate formiate species [32–35]. Lin and co-authors [34] studied the dynamic behaviour of bidentate carbonate and formiate species during the reverse water gas-shift reaction over Cu/CeO_2 at 250°C and 1 atm pressure. The authors noticed that upon switching off the flow of CO_2 in the reactant gas stream mixture of CO_2/H_2/He, surface carbonate species concentration diminished while concentration increased again upon switching on CO_2 flow. Therefore, authors concluded that bidentate carbonate species reacted with H_2 to form CO and H_2O. Therefore, in the present work, a similar reaction between the bidentate (and probably with monodentate) carbonates and H_2 during the TPR experiment can occur, which resulted in the surplus consumption of H_2 and exhibited the highest specific H_2-consumption among the CuAl-X samples. In other words, the H_2 consumed during the TPR analysis was both by the bidentate carbonates and reducible copper species on CuAl-CO_2. Nevertheless, the TPR analysis can be

used to support the presence of additional reducible species (here, bidentate carbonates) on the CuAl-CO_2 species, as also observed from the TGA (refer Figure 4.4) and FTIR analyses (refer Figure 4.8).

4.1.2 Catalytic Activity Results

For performing catalytic activity tests over the CuAl-X samples, 150 mg of each of these samples was diluted with SiC. Conversion curves of CO as a function of the reaction temperature and NO reduction/oxidation yields at temperatures corresponding to peak NO reduction yield (or NO oxidation yield when no NO reduction activity is observed), obtained for different CuAl-X mixed oxides, are shown in Figure 4.9. Additionally, the light off curves for NO reduction and oxidation yield with the increase in reaction temperature is shown in Appendix A. Tests were conducted in presence (8.2 vol%, indicated as 'CuAl-X + H2O') and in absence of water in the reactant gas stream. The conversion curves obtained shown no direct correlation between the catalytic performance of CuAl-X samples and the specific surface area. Indeed, under dry conditions, all catalysts present similar temperatures of CO conversion, while surface area varies slightly (from 25 $m^2.g^{-1}$ to 39 $m^2.g^{-1}$). Three of the catalysts are presenting oxidised Cu species (treated under air, He and CO_2) and comparable surface area. On the contrary, the catalyst heated under CO/He is presenting Cu mostly in the metallic form, and a lower surface area (refer Table 4.1).

Further, expectedly, presence of water in the gas stream greatly affected the overall catalytic conversions. In Figure 4.9(a), it can be observed that the presence of water reduced the CO oxidation thereby shifting the CO conversion curve to temperatures higher than that under dry reaction conditions, by roughly 60°C at 50% CO conversion for three of the four catalysts. Only CuAl-CO/He exhibited a more important temperature shift, by 100°C at 50% conversion. Similar effect of water in the reaction feed on CO oxidation was reported by Shiau and Avgouropoulosa [36,37]. The authors have explained that decrease in CO oxidation activity originates from the competitive adsorption of H_2O and CO on the same active sites. However, the authors did not specify the active Cu sites for CO_2 and H_2O adsorption. Additionally, a possible water-induced sintering of the active metal (here, Cu) in the catalyst can further

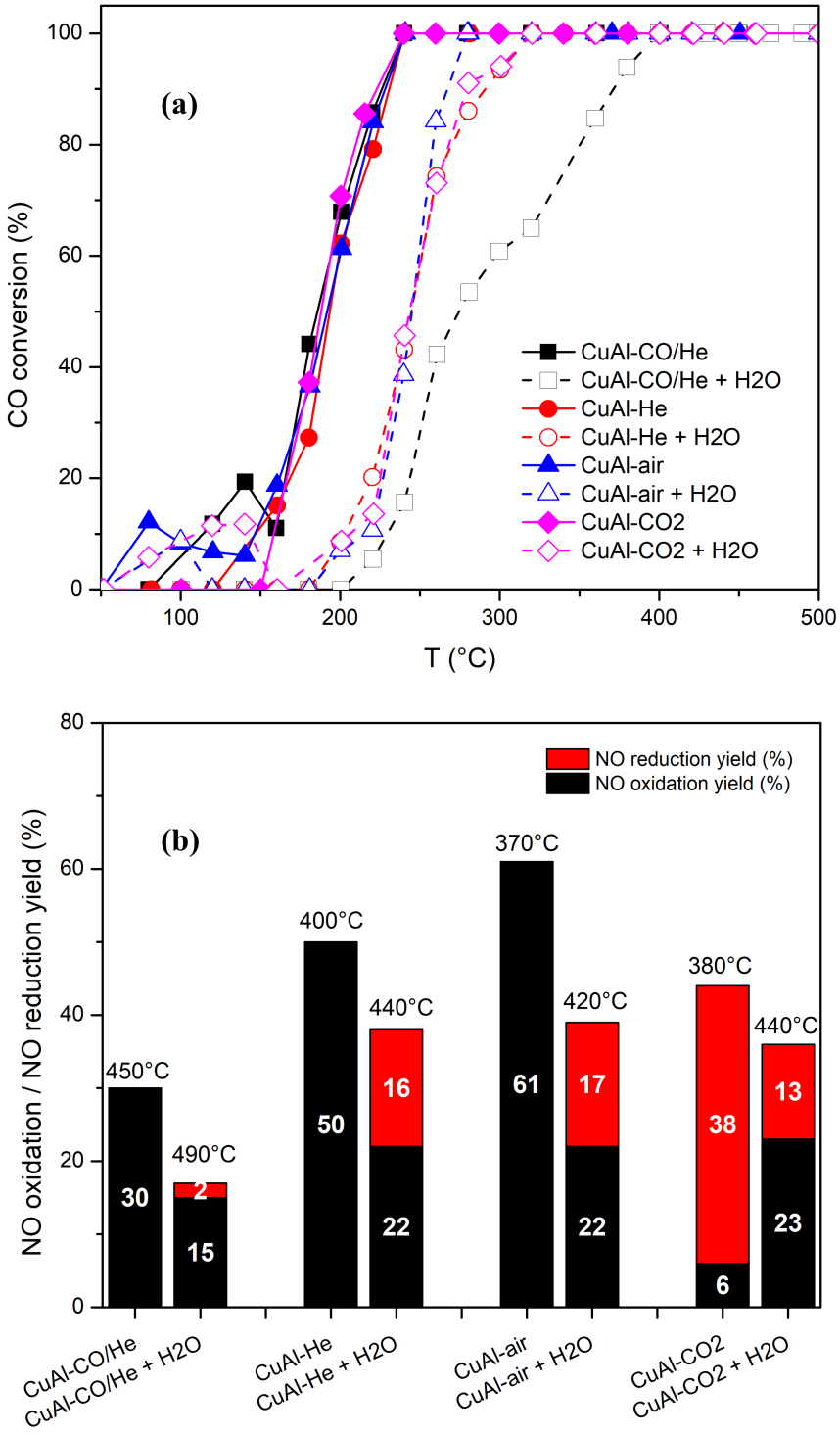

Figure 4.9 a) CO conversion as a function of reaction temperature, for CuAl-X materials, in the presence and absence of water (b) NO oxidation and reduction yield at temperature corresponding to the peak NO reduction (or oxidation when no NO reduction activity is observed) for CuAl-X materials

degrade the catalytic performance of the sample [38].

However, on the NO conversion yield, no reduction occurs without water and only NO oxidation is observed, except when the catalyst is activated under CO_2 atmosphere (refer Table 4.4 for the selectivity towards NO reduction and Figure 4.9(b) for the NO reduction and oxidation yields with the peak reduction/oxidation yields). Activity between samples for NO conversion greatly differs, CuAl-air being the more active with 61% yield at 370°C (Cu(II) species) while CuAl-CO/He presents a half yield at 450°C (Cu(0) species). CuAl-CO_2 catalyst is presenting 44% total conversion, with 38% being on NO reduction. Whatever the activation procedure, the presence of water in gas stream lowers down the NO conversion by 18% (CuAl-CO_2) to 43% (CuAl-CO/He). A competitive adsorption between NO and H_2O also exists resulting in the lowering of NO conversion yield in presence of water when compared with that in absence of water [39]. More importantly, presence of water promotes the NO reduction reaction for all CuAl-X samples, except in the case of CuAl-CO_2. This improvement in NO reduction activity for most of the catalysts in presence of water can be explained by the occurrence of water gas shift reaction at low temperature over Cu-catalyst, that results in the production of H_2 a more effective reductant than CO for NO [40]. Similar observations have also been reported in our previous studies on CuAl and CoAl mixed oxide samples for similar reaction conditions [41]. The XPS studies of the fresh and spent catalysts were performed to investigate the change in the material properties of the samples during the reaction. The results showed an increase in the concentration of the adsorbed O species on the catalytic surface after the reaction which supposedly promoted NO oxidation. Moreover, it was concluded that the surface O species facilitates water-gas shift reaction under wet reaction conditions (in reference to the observations reported in [42]) thereby promoting NO reduction activity.

While the catalysts treated under air, He or CO/He atmosphere are totally ineffective for the NO reduction reaction when the reaction is performed under dry conditions, only the CuAl-CO_2 sample present a substantial reduction yield. It seems that the monodentate/bidentate carbonates, observed to be stable at high temperature (Figure 4.4) can affect the NO conversion route, which also implies that there are two different active sites for NO and CO

Table 4.4 Selectivity of NO conversion towards NO reduction for different CuAl-X samples under dry and wet reaction conditions

Sample	Reaction Conditions	Selectivity towards NO reduction (%)	Peak NO reduction temperature (°C)
CuAl-air	with water	43	420
	without water	0	370
CuAl-He	with water	42	440
	without water	0	400
CuAl-CO/He	with water	10	490
	without water	0	450
CuAl-CO_2	with water	40	440
	without water	83	380

reaction, which is in accordance to the CO + NO reaction mechanism that have been reported by various authors in the literature [43–45]. The carbonates formed by the adsorption of CO_2 during the gas-treatment are expected to be at strong basic sites [23,24] and NO being an acidic gas, has the affinity towards these basic sites in the catalyst. The preferential formation of carbonates leads to a decrease in site availability for NO adsorption, which could explain a total activity in NO conversion lower for CuAl-CO_2 than for CuAl-air and CuAl-He samples. Moreover, the observed NO reduction activity over CuAl-CO_2 sample in the absence of water can be ascribed to the reaction between NO and carbonate species at the catalytic surface. Indeed, Li et al. [46] performed in situ NO-CO reaction followed by DRIFTS on 12 wt% CuO/$Ce_{0.9}Zr_{0.1}O_2$ mixed oxide. They observed that upon introducing NO_2 onto the CO-saturated catalyst, the carbonate species that were previously formed under CO/N_2 gas flow significantly reduced. In addition, bidentate nitrate and nitrite species formed on the catalyst surface by reaction between adsorbed NO and surface carbonate species. Further steps resulted in the formation of N_2 and CO_2 gas products. Therefore, over CuAl-CO_2 catalyst containing stable surface monodentate/bidentate carbonate, NO can adsorb on free Cu(II) surface sites to form nitrate intermediates. These nitrate intermediates react with mono- and bidentate carbonate species already present on the catalyst, allowing N_2 and CO_2 production that desorb from catalyst surface.

Finally, when reaction is performed under wet conditions, CuAl-CO_2 showed NO conversion and CO conversion activities similar to that of CuAl-air

and CuAl-He samples. Reportedly, adsorption of water on the mixed oxides surface partially decomposes the monodentate and bidentate carbonates present on the surface of CuAl-CO_2 [23,24]. Coenen et al. [23] studied the adsorption of CO_2 and H_2O on hydrotalcites via in-situ FTIR studies. When the authors introduced a gas mixture of 12 vol% H_2O balanced by N_2 on to the LDH sample containing pre-adsorbed CO_2 in different forms of carbonates, the IR peaks attributed to the bidentate carbonates reduced in intensity implying their decomposition by H_2O. Consequently, the authors proposed the formation of bicarbonates because of the reaction between the bidentate carbonates and H_2O. This can explain the decrease in the NO reduction yield for CuAl-CO_2 sample under the current wet reaction condition. Furthermore, under such wet reaction conditions, CuAl-CO_2 sample presents a surface state that becomes close to that of air, and He activated samples, with liberated basic sites. NO can then adsorb on these basic sites, being further converted to NO_2 obviously aided by the presence of excess of O_2 in the reactant gas stream, thereby increasing the overall NO oxidation yield compared to that in absence of water. Additionally, the observed NO reduction activity in case of CuAl-CO_2 even after partial decomposition of active carbonate species can be due to reaction with CO and/or by H_2 (produced from the water-gas shift reaction). However, it is difficult to quantify what fraction of NO reduction was due to the CO and rest by H_2.

Summarising this work, CuAl HT was synthesised and treated under the flow of air, He, CO/He and CO_2 at 500°C to form CuAl-X mixed oxides. The CuAl-X samples were characterised using techniques like N_2-physisorption, XRD, TGA and H_2-TPR. XRD results showed that crystalline CuO species were formed upon gas treatment for CuAl-He, CuAl-air and CuAl-CO_2 while metallic Cu was predominantly formed for CuAl-CO/He which was responsible for its poor catalytic performance. The CO_2-treatment on CuAl HT formed crystallites size similar to CuAl-He and CuAl-air and generated small nanoparticles of CuO as indicated from reducibility measurements (and the presence of an α reduction peak at 226°C). Moreover, TGA and FTIR results indicated the presence of monodentate, and bidentate carbonates formed due to adsorption of CO_2 on CuAl HT during the treatment process. Presence of these carbonate species facilitates NO reduction in the absence of water. This catalytic behaviour of

CuAl-CO_2 further indicated the presence of separate active sites for NO and CO adsorption and that the NO adsorption sites were partially occupied by these carbonate species which lowered its total NO conversion when compared with CuAl-air and CuAl-He but increased the selectivity towards NO reduction. Nevertheless, all the CuAl-X samples showed a delayed CO conversion and lowered total NO conversion yield but greater selectivity towards NO reduction in the presence of water when compared with reaction in absence of water (except for CuAl-CO_2). Thus, the results are highlighting the benefit of the CO_2-treatment on CuAl-LDH implying it to be a promising method for preparing mixed oxide catalyst from CuAl-LDH precursor improving the NO reduction ability during the CO + NO reaction.

4.2 Effect of Cobalt Content

As observed in the preceding section of this chapter, CO_2 pre-treatment of the parent LDH produces stable bidentate carbonate species that are active for NO reduction by CO reaction. In addition, earlier research has indicated that bimetallic catalysts can have greater NO-SCR activity than their monometallic

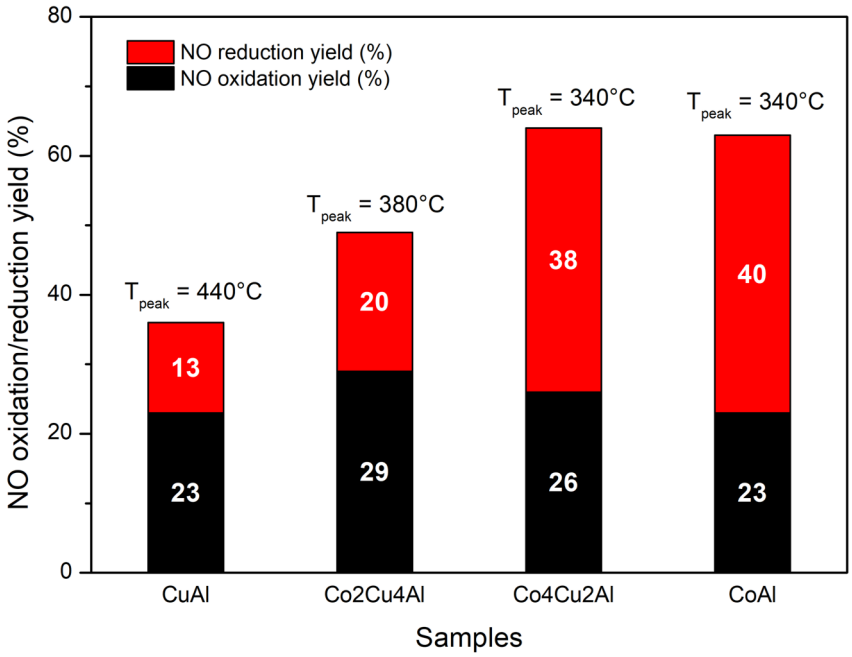

Figure 4.10 NO oxidation and NO reduction yield for different CO_2-treated CoCu samples under wet reaction conditions (T_{peak} = reaction temperature at the peak of NO oxidation/reduction yield

Table 4.5 T_{50} and T_{90} temperatures of CO conversion for different CoCuAl samples treated under CO_2

Sample	T_{50} (°C)[a]	T_{90} (°C)[a]
CuAl	240	270
Co_2Cu_4Al	220	260
Co_4Cu_2Al	200	240
CoAl	200	240

[a] T_{50} and T_{90} are the temperatures at which 50% and 90% of the conversion of the component (here, CO to CO_2) is reached respectively.

counterparts [11,48,49]. Cobalt is one of the potential active metals for SCR activity [41,50]. In this section, the effect of the Co content in the copper-containing mixed oxides produced from their respective parent LDH on the material properties of the mixed oxides and, ultimately, its effect on the NO-SCR by CO performance is investigated.

In the present study, the molar ratio of Co:Cu in the mixed oxide was varied from 0 to 2 (namely CuAl, Co_2Cu_4Al and Co_4Cu_2Al) and additionally Co_6Al (henceforth indicated as *CoAl*) mixed oxide sample were used for this study. Each of the mixed oxides was derived from their corresponding parent LDH via CO_2-treatment at 500°C for 4 hours and at a heating rate of 1°C/min. Their corresponding catalytic activity under wet reaction conditions are shown in Table 4.5 (CO conversion activity) and Figure 4.10 (NO reduction/oxidation yield).

It was observed from Table 4.5, the CO conversion of the mixed oxides were improved with the introduction of Co into the sample which is indicated by the shift of the T_{50} and T_{90} to lower temperatures. In comparison with the Co_4Cu_2Al mixed oxide, the CoAl mixed oxide showed similar T_{50} and T_{90} temperatures for CO conversion. Moreover, in Figure 4.10, a significant enhancement in the NO reduction performance under wet reaction conditions with the introduction of Co in the mixed oxide can be seen. Additionally, there is a slight increase in the total NO conversion yield and selectivity towards NO reduction activity for CoAl mixed oxide sample. This superior catalytic activity demonstrated by cobalt containing samples over CuAl mixed oxide is related to the reducibility of the active metal species in the mixed oxide

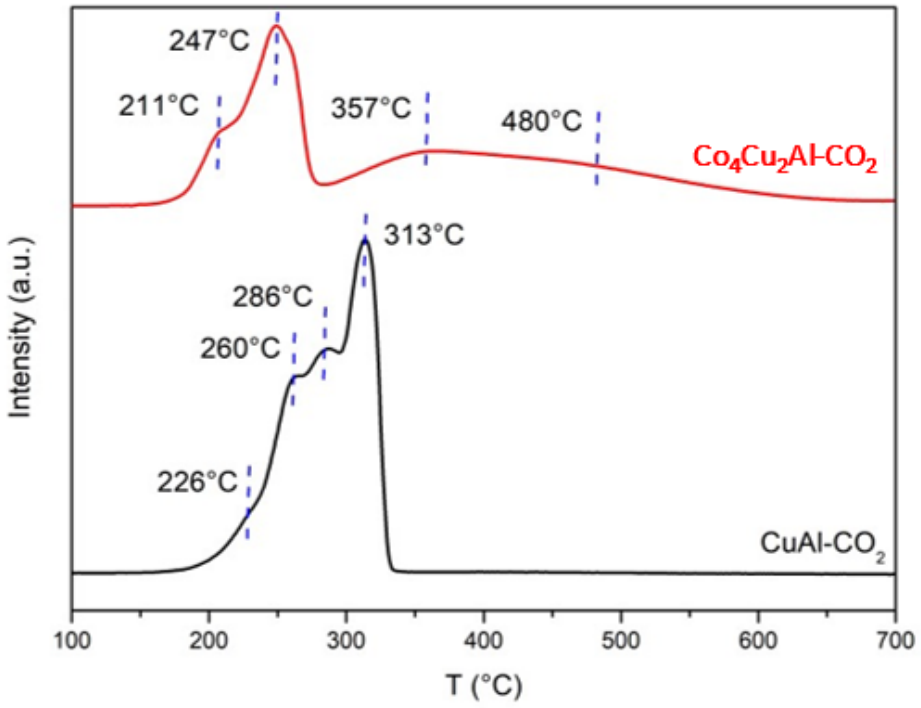

Figure 4.11 H_2-TPR analyses of CuAl-CO_2 and Co_4Cu_2 mixed oxide samples

samples [41,51]. Previous studies have shown that the reduction of species in CoAl mixed oxide commences at a temperature lower than the CuAl mixed oxide [41]. Further, introduction of Co in the CuAl mixed oxide sample also improves the reducibility of the material and the redox characteristics improve with the increase in Co content [51]. For comparison, the H_2-TPR analyses for CuAl and Co_4Cu_2Al mixed oxide samples synthesised in this study are shown in Figure 4.11. In this figure, it can be observed that the reduction peak attributed to well dispersed Cu(II) species in the sample shifted from 226°C in CuAl-CO_2 sample to 211°C in Co_4Cu_2Al sample. Moreover, peaks attributed to the reduction of CoCu spinels, Co_3O_4 and CoO species were also observed for the Co_4Cu_2Al sample at 247°C, 357°C and 480°C respectively [50–57] which is expected in a binary mixed oxide sample. Furthermore, upon comparing the specific H_2-consumptions for these sample, it was observed that Co_4Cu_2Al sample consumed more H_2 per sample weight (i.e., 12.369 mmol.g^{-1}) than CuAl-CO_2 mixed oxide sample (i.e., 10.630 mmol.g^{-1} ; refer Table 4.2) implying that there are more reducible species in the former sample than in the latter.

Although CoAl mixed oxide showed better catalytic activity especially in terms of NO reduction yield, Co_4Cu_2Al was chosen as the catalytic material for further tests because (i) the catalytic performance between CoAl and Co_4Cu_2Al are similar (ii) Co is a costlier metal than Cu and therefore, lowering down its content in the mixed oxide will lower the overall cost of the catalyst and (iii) presence of Cu along with Co forms spinel structures which stabilises the Co species and avoid sintering of the particles during the reaction. Hence, Co_4Cu_2Al mixed oxide was utilised further to investigate the effect of the CO_2-treatment temperature on the corresponding catalytic performance.

4.3 Effect of Treatment Temperature

According to the previous reports in the literature (refer Chapter 2), the temperature of treatment for the catalyst materials influences the physicochemical properties thereby affecting the overall catalytic performance. To further optimise the catalytic activity of the catalyst, Co_4Cu_2Al mixed oxides were prepared from their common parent LDH by thermal treatment under the flow of CO_2 at 350°C, 400°C, 450°C and 500°C at a heating rate of 1°C/min. The mixed oxides thus derived are hereafter named as CoCu-T where T = 350, 400, 450 or 500 – the treatment temperatures. Different material characterizations and comparison of their corresponding catalytic activities are discussed further in this section.

4.3.1 Material Characterization Results

Material characterization experiments like N_2-physisorption, XRD and TGA were performed to assess the influence of pre-treatment temperature on the physicochemical properties of the mixed oxides.

4.3.1.1 N_2-physisorption

The N_2-isotherms of the CoCu-T mixed oxides and their pore size distributions are shown in Figure 4.12 and their different textural properties are enlisted in Table 4.6. An increase in the total pore volume of the CoCu-T mixed oxides with the increase in the treatment temperature can be observed. However, no direct correlation can be established between the specific surface area and treatment temperature and average pore diameter and treatment temperature. These results are contrary to the trends popularly reported in the literature [55,58,59].

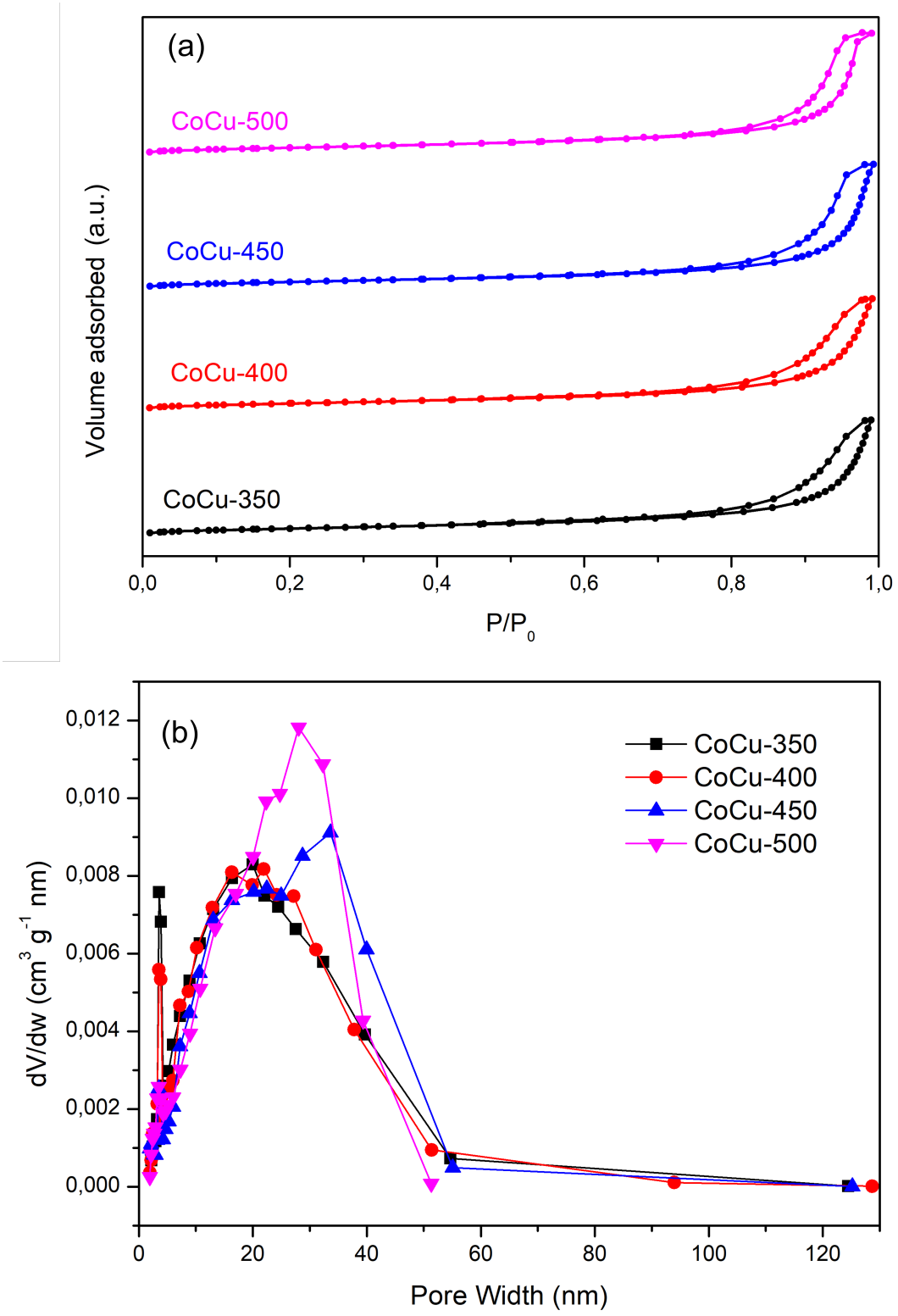

Figure 4.12 Textural properties of CoCu-T samples (a) N_2 adsorption and desorption isotherm (b) Pore size distribution by BJH method applied on the desorption branch

Table 4.6 Textural properties of CoCu-400 and CoCu-500 samples (g_{cat} = weight of catalyst in grams)

Sample	$S_{BET}(m^2.g^{-1})^a$	$V_\mu(cm^3.g^{-1})^b$	$V_p(cm^3.g^{-1})^c$	$D_{BJH}(nm)^d$
CoCu-350	66	0.0028	0.23	17.9
CoCu-400	63	0.0025	0.24	18.0
CoCu-450	64	0.0026	0.26	20.5
CoCu-500	61	0.0009	0.28	19.6

[a] S_{BET} = specific surface area measured by the B.E.T method
[b] V_μ = micropore volume measured by t-plot treatment
[c] V_p = total pore volume measured at $P/P_0 = 0.95$
[d] D_{BJH} = average pore size measured by B.J.H method applied to the desorption branch

Generally, with the increase in the treatment temperature the specific surface area should decrease owing to the sintering of the particles [55,58,59], but these comments should be treated with caution as the difference between the samples are very small and insignificant. Moreover, increase in the treatment temperature should also widen the pore diameter and increase the total pore volume [55,59]. Out of these three common trends, the influence of the treatment temperature on the pore volume of the mixed oxides considered in this study is more pronounced. Further, in Figure 4.12(a), the N_2 adsorption and desorption isotherm on different CoCu-T samples have the shape representing a mix of Type II-Type IV(a) similar to the CuAl-X samples (refer Figure 4.1) [1]. The adsorption step at $P/P_0 > 0.70$ represents the capillary condensation of N_2 most importantly in large mesopores or small macropores. Also, the shape of the hysteresis loops for all the CoCu-T samples, like the CuAl-X samples, belongs to H3-type hysteresis loop, which is generally attributed to non-rigid aggregates of plate-like particles that confirms the above described morphology [1]. Furthermore, in Figure 4.12(b), the pore size varies between 5-50 nm which can be attributed to mesopores, similar to CuAl-X samples. Finally, it could be concluded that the treatment temperature has minimal effect on the physicochemical properties of the Co_4Cu_2Al mixed oxides.

4.3.1.2 XRD

The XRD analysis of CoCu-T samples are shown in Figure 4.13. The diffractogram of CuAl-CO_2 has also been shown in this figure for comparison. It can be seen that the treatment temperature affects the crystallinity of the mixed ox-

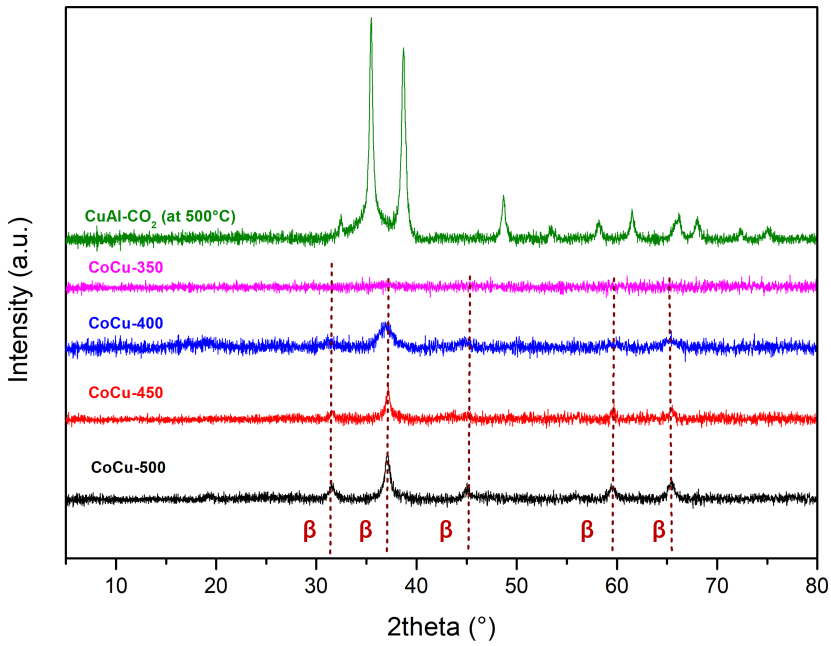

Figure 4.13 XRD analysis of CoCu-T samples: β = Co_3O_4 (JCPDS-42-1467), $CuAl_2O_4$ (JCPDS-78-0556), $CuCo_2O_4$ (JCPDS-01-1155) and/or $CoAl_2O_4$ (JCPDS-44-0160)

ides. The diffractogram corresponding to CoCu-350 shows no diffraction signals while the diffraction signals become more prominent upon increasing the treatment temperature implying enhancement in the crystallinity of the mixed oxide sample, as also reported in the literature [55,58,60]. These low intensity broad peaks in CoCu-T (especially for T = 400,450 and 500°C) can be attributed to the presence of Co_3O_4 (JCPDS-42-1467), $CuAl_2O_4$ (JCPDS-78-0556), $CuCo_2O_4$ (JCPDS-01-1155) and/or $CoAl_2O_4$ (JCPDS-44-0160). Since the diffraction peaks for Co_3O_4, CuAl and CoAl spinels overlap with each other, it is difficult to identify these species. Moreover, an evident difference between the diffractograms between CuAl-CO_2 and CoCu-T samples is the absence of CuO peaks in the latter which can be due to either incorporation of Cu species into Co-Cu spinel structure or CuO is very well dispersed in the CoCu-T samples therefore, left undetected.

4.3.1.3 TGA

Thermo-Gravimetric Analysis of the Co_4Cu_2Al-LDH under the flow of CO_2 is shown in Figure 4.14. From this figure, it can be observed that the LDH lost

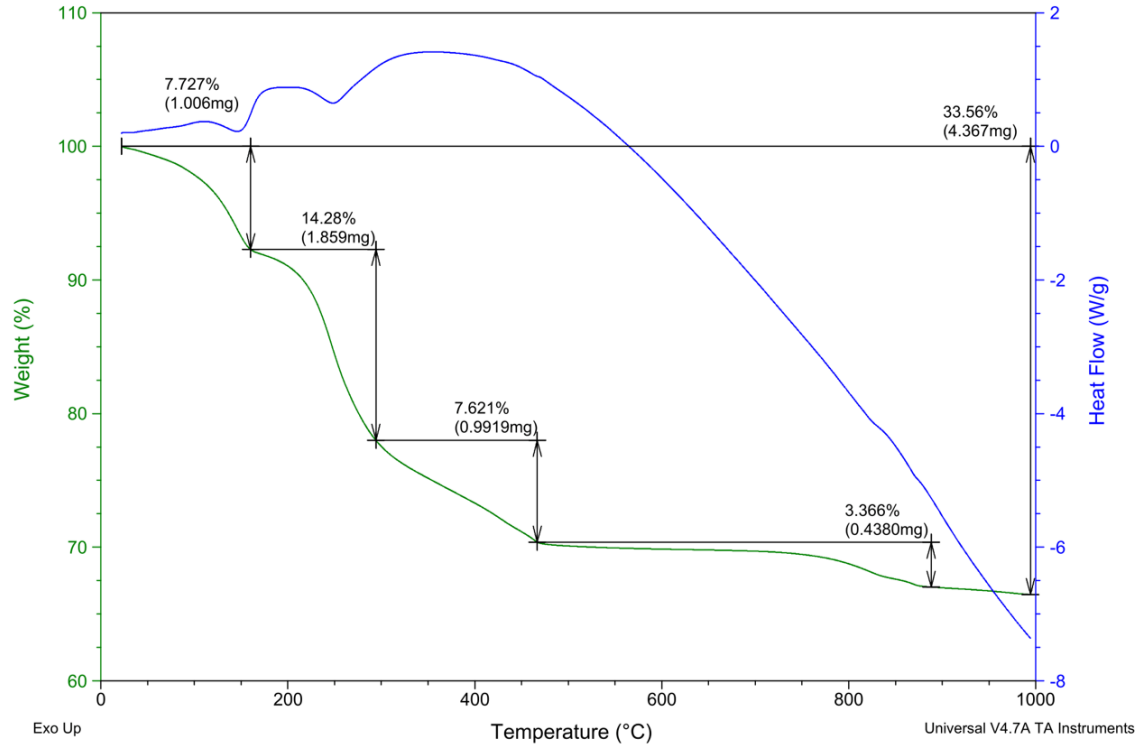

Figure 4.14 Thermo-Gravimetric Analysis (TGA) of Co_4Cu_2Al-LDH sample

its weight in 4 stages like that observed for CuAl-LDH sample (see in Figure 4.4(b)). The weight loss recorded until 200°C was due to the loss of interlayer water along with the loss of loosely bonded carbonate anions as CO_2. The second and third weight loss zone between 200-450°C can be attributed to loss of interlayer water molecules and CO_2 from the carbonate anions due to the destruction of the layered structure respectively. The fourth weight loss observed in the range of 450-900°C can be attributed to the removal of more stable bidentate and/or polydentate carbonate species. Velu et al. [51] reported such a weight loss peak at 580°C and it was more visible for high cobalt concentration in the mixed oxide sample. They attributed this weight loss to the removal of oxycarbonate (chemically represented as $M^{II}M_x^{II}O_y\,(CO_3)_2$) formed due to the reaction between brucite-like sheet and carbonate anions. Similar observations were also made in this study for the TGA under CO_2 for the CuAl-LDH. This analysis also implies that the amount of carbonates in the CoCu-T samples decreases with increase in the treatment temperature i.e., CoCu-350 > CoCu-400 > CoCu-450 > CoCu-500.

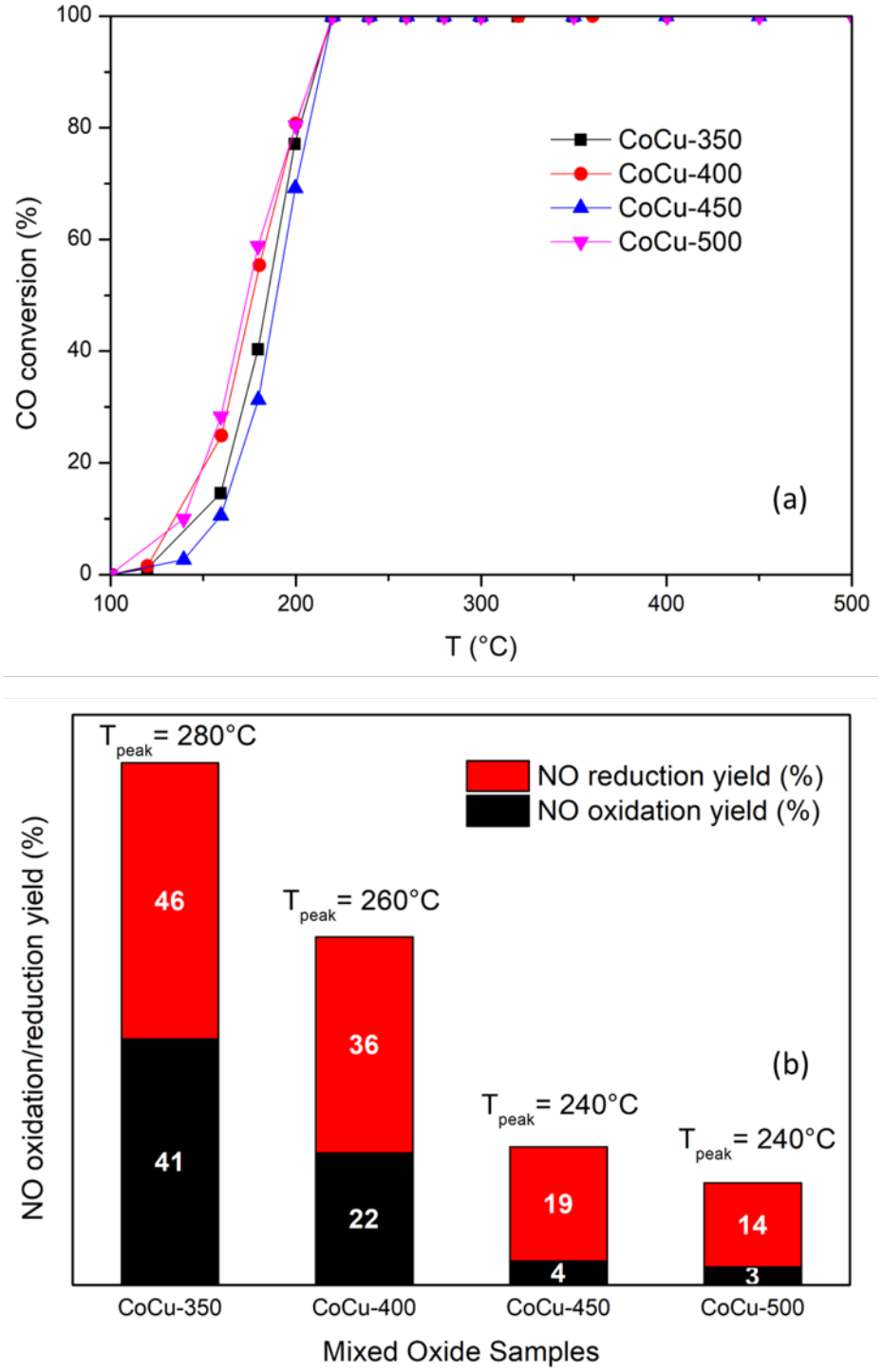

Figure 4.15 Catalytic activity of CoCu-T samples under wet reaction conditions (a) CO conversion activity and (b) NO oxidation/reduction yield

4.3.2 Catalytic Activity Results

For the comparison of the catalytic performance of CoCu-T samples, the catalyst was not diluted with SiC, unlike the catalytic activity studies reported previously

in this chapter and N_2 was used instead of He as the gas vector so as to simulate the real-world operational conditions. The corresponding catalytic activities of CoCu-T samples under wet reaction conditions (in presence of 8.2 vol% of H_2O) are shown in Figure 4.15. It can be seen that the catalytic activity of the samples does not correlate with the corresponding textural properties enlisted in Table 4.6. In Figure 4.15(a), it can be seen that the treatment temperature has very minimal effect on the CO conversion activity of the CoCu-T samples. The T_{50} temperatures for the CoCu-T samples varies between 160-185°C while the corresponding T_{90} temperatures are nearly the same i.e., 220°C.

In addition, in Figure 4.15(b), the treatment temperature has a clear effect on the NO conversion performance of the CoCu-T samples. The NO conversion yield decreases as the treatment temperature rises, and the temperature corresponding to the peak NO reduction yield (T_{peak}) shifts to lower temperatures. A correlation exists between the concentration of carbonate species available in the corresponding CoCu-T sample and an increase in the NO conversion yield as the treatment temperature decreases. As seen in the TGA under the flow of CO_2 for the parent LDH of the CoCu-T samples, (refer Figure 4.14), the concentration of carbonate species decreases with increasing temperature from 350 to 500°C. Since carbonate species are believed to facilitate NO reduction reaction by interacting with intermediate nitrate and nitrite species [46,47], CoCu-350 which has the highest concentration of carbonate species among all the CoCu-T samples showcased the highest NO reduction yield followed by CoCu-400, CoCu-450 and CoCu-500 samples. This variation in the NO conversion activity and no appreciable change in the CO conversion activity with the different treatment temperatures indicate that the CoCu-T mixed oxide samples have different active sites for NO and CO adsorption and followed by their corresponding surface reactions i.e., dissociation of N-O into N and O species and combination of N species to form N_2 and reaction between surface CO and O species to form CO_2 respectively.

Furthermore, the corresponding N_2 selectivity of CoCu-T samples (refer Table 4.7) increases with the increase in the treatment temperature. Although CoCu-350 showcased the highest NO reduction yield with relatively low N_2 selectivity, but the highest N_2 selectivity was recorded for CoCu-450 and CoCu-500 samples. This behaviour can be because of various of reasons like (i)

Table 4.7 NO conversion yield and N_2 selectivity for CoCu-T samples under wet reaction conditions

Sample	T_{peak} (°C)	NO conversion yield (%)	N_2 Selectivity (%)
CoCu-350	280	87	53
CoCu-400	260	58	62
CoCu-450	240	23	83
CoCu-500	240	17	82

formation of Cu-Co and Co_3O_4 at higher treatment tempertures (refer XRD analyses in Figure 4.13) which are active sites for NO reduction by CO therefore, promoting N_2 selectivity [71,72] (ii) the sintering of the active metals in the mixed oxides with the increase in the treatment temperature (indicated by the increase in the crystallinity of the CoCu-T samples with the treatment temperature as observed under XRD, refer Figure 4.13) which could explain the decrease in the NO conversion yield [9,61–63] and (ii) certain carbonate species found at the lower treatment temperatures can react with the NO to form bridging and/or monodentate nitrate species which can further react with NO to form NO_2 (however, for such a reaction to occur, good reducibility of the active species in the catalytic material is required) [64]. Since there is a direct correlation of N_2 selectivity and NO conversion yield with the treatment temperature, one can expect that both concentration of carbonate species and formation of active spinel structures are important factors for optimal NO conversion and N_2 selectivity performance. Therefore, CoCu-400 sample was the catalyst of choice as it showed good NO reduction yield and N_2 selectivity.

4.4 Thermal Stability

Based on the superior N_2 selectivity and appreciable NO conversion yield, CoCu-400 sample was chosen as the final catalytic material for large-scale synthesis, semi-pilot tests and additional activity tests for development of kinetic model. However, before moving forward with the large-scale synthesis and kinetic studies, it is important to assess the thermal stability of this material under the reaction conditions. To assess the thermal stability, CoCu-400 sample was subjected to a prompt thermal ageing via 6 light-off curves under the wet reactant gas flow using He as the gas vector and the catalyst sample was diluted

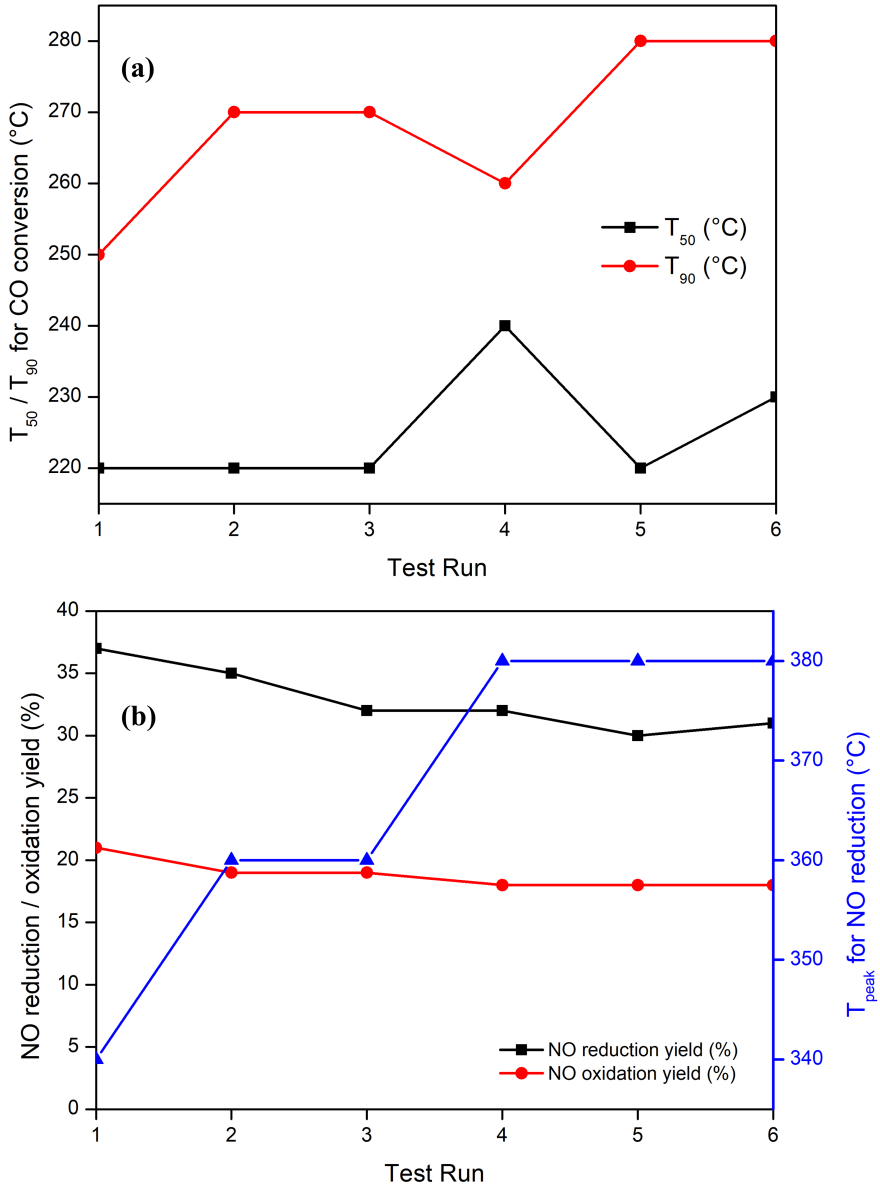

Figure 4.16 Variation of (a) T_{50} and T_{90} temperatures for CO conversion and (b) NO conversion yield with catalytic activity test runs

with SiC to reduce thermal effect in the catalytic reactor. The change in the catalytic activity observed from the corresponding light-off curve during each test run was recorded. The results are shown in Figure 4.16. Upon comparing the T_{50} and T_{90} temperatures of CO conversion during each test run (refer Figure 4.16(a)), it can be observed that the T_{90} temperatures increase with the number of test runs while comparatively, not much appreciable change was observed in the T_{50} temperature of the CO conversion. In addition, upon

comparing the NO reduction yield during test runs (refer Figure 4.16(b)), it can be concluded that the NO reduction yield decreased from the 1st run (yield = 38%) to 3rd run (yield = 32%) and remained almost stable up until 6th run (30% < yield < 32%). Interestingly, not much change in the NO oxidation yield over the test runs was recorded (18% < yield < 21%)). Furthermore, upon comparing the T_{peak} temperatures for the corresponding peak NO reduction yield (refer Figure 4.16(b)), it can be concluded that the T_{peak} increased from 340°C in the 1st run to 380°C in the 4th run and was stable until the 6th run. These results suggest that the CoCu-400 material possess a good thermal stability.

4.5 Activity Comparison with Commercial Catalysts

For the industrial application, it is important that the catalytic material is economically feasible and demonstrate appreciable catalytic performance under the industrial operating condition. Platinum Group Metals (PGMs) have been in use for the catalytic removal of NO_x from the automotive exhaust gas for decades now and are known to possess impressive catalytic activity, especially NO_x reduction by CO [65]. Use of the PGMs as catalyst material for the NO reduction by CO reaction under industrial flue gas conditions have been reported in the literature [66,67]. Therefore, the catalytic activity of the lab synthesised CoCu-400 sample is compared with that of commercial 1 wt% Pt/Al_2O_3 [2] and lab-synthesised 1 wt% Pt/CeO_2 [2] samples . For this comparison, each of the samples was diluted with SiC and introduced with a reactant gas mixture containing N_2 as the gas vector. Moreover, the Pt-containing samples were reduced under H_2 flow (10 vol% H_2/N_2 at a flow rate of 60 ml.min^{-1}) at a heating rate of 5°C.min^{-1} and maintained at 500°C for 4 hours in order to ensure the presence of active Pt^0 species in the samples [66,67]. The catalytic activity results are shown in Figure 4.17. In Figure 4.17(a), the CO conversion activity of the samples are compared. It can be observed that the Pt-containing

[2]The catalytic activity of 1 wt% Pt/Al_2O_3 (here, a lab-synthesised and not a commercial one as mentioned in this thesis) and 1 wt% Pt/CeO_2 under oxidative and wet reaction conditions (similar but not the same to the reactant gas composition considered in this thesis) have been previously reported by Akil et al [66,67] and was found to show appreciable NO reduction activity

samples showed CO oxidation at temperatures lower than that of CoCu-400. At 80°C, more than 50% of CO was converted to CO_2 over Pt-containing samples

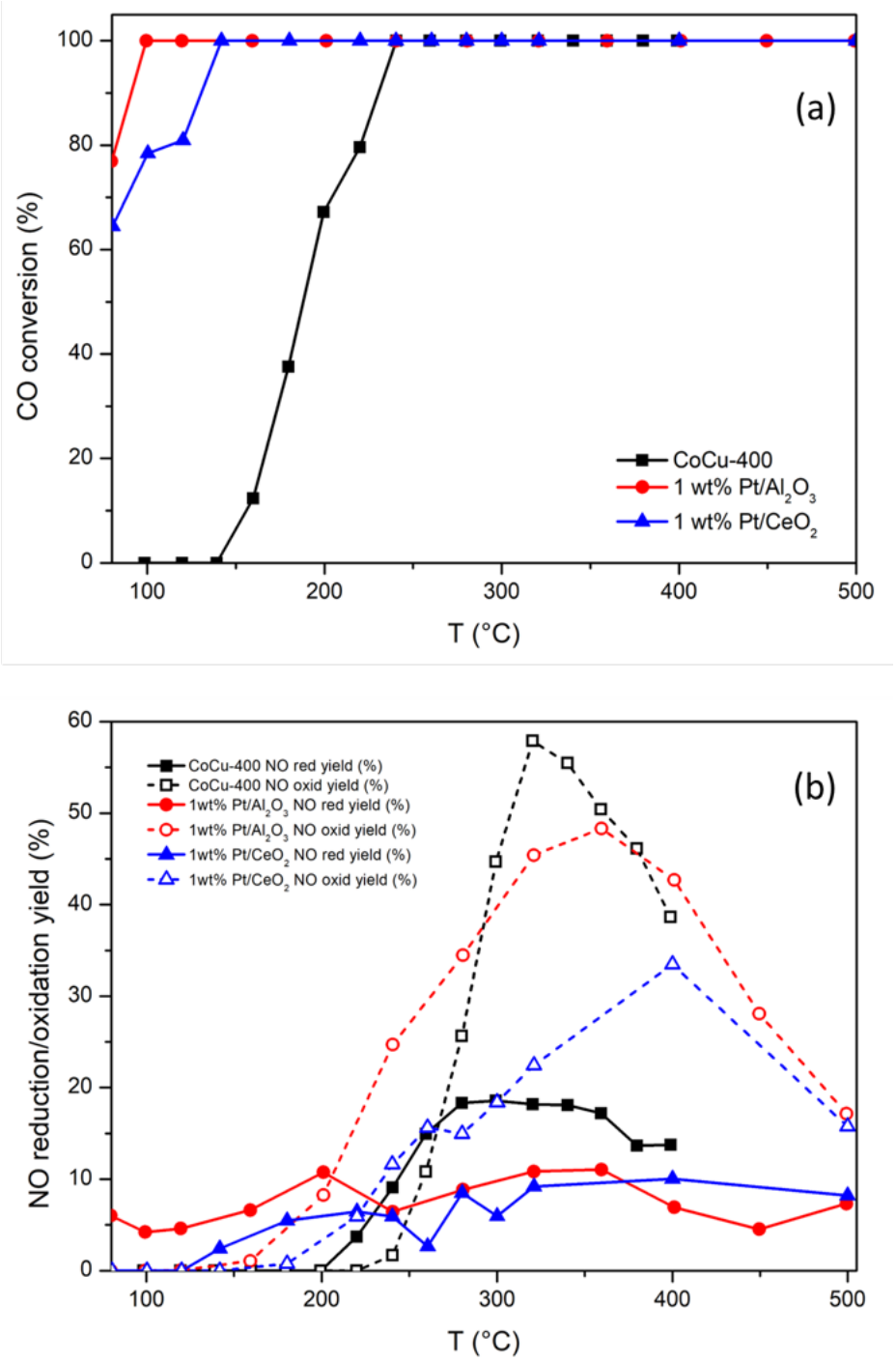

Figure 4.17 Comparison of (a) CO conversion and (b) NO oxidation / reduction yield over CoCu-400 with 1wt% Pt/Al_2O_3 and 1 wt% Pt/CeO_2 under wet reaction condition with N_2 as the gas vector

whereas, over CoCu-400 sample, the CO conversion commenced only after 150°C with T_{90} temperature of 240°C against 150°C in case of 1 wt% Pt/CeO_2 and 100°C in case of 1 wt% Pt/Al_2O_3. In addition, in Figure 4.17(b), it can be observed that the maximum NO reduction yield for CoCu-400 sample (i.e., 20% for a temperature range of 250-350°C) is higher than that of Pt-containing samples (maximum NO reduction yield reached was 10% for the temperature range of 200-500°C). Regarding the NO oxidation yield, CoCu-400 sample shows maximum yield of 60% at 320°C followed by 1 wt% Pt/Al_2O_3 which shows a maximum yield of 45% at 350°C and lastly, 1 wt% Pt/CeO_2 which shows a maximum yield of 30% at 400°C. Even though (PGM) are known to possess high catalytic activity for NO_x reduction, their activity is majorly diminished in the presence of excess amount of O_2 and H_2O due to the blocking of active sites by O_2 [68], consumption of reactant molecules by the excess O_2 to form NO_2 and CO_2 [69] and sintering of the active metal particles under wet conditions thereby lowering the metal accessibility and decreasing the NO reduction activity [66]. Hence, it is concluded that the lab-synthesised CoCu-400 sample overpowers the Pt-containing commercial (1 wt% Pt/Al_2O_3) and lab-synthesised (1 wt% Pt/CeO_2) samples in NO reduction activity in an oxidative and wet reaction condition.

4.6 Conclusion

In the first part of this section, the effect of gas treatment type on the catalytic activity of CuAl mixed oxide samples was investigated. The CO_2 treatment of the CuAl-LDH sample produces surface bidentate and/or polydentate carbonate species, which facilitate the formation of nitrate and/or nitrite species, which are active intermediates for the formation of N_2. Following this observation, this gas was used to treat Co-Cu LDHs with different Co:Cu ratios, and the catalytic activity of the resulting mixed oxides was compared. It was found that increasing the Co content of the mixed oxide enhanced NO reduction activity. The effect of treatment temperature on the corresponding catalytic activity was finally investigated using Co_4Cu_2Al mixed oxide. The temperature of the treatment had no discernible effect on the textural properties of the mixed oxides. XRD analyses demonstrated that as the treatment temperature increased, the crystallinity of the mixed oxides increased. Regarding the effect

of the treatment temperature on the catalytic performance, the treatment temperature variation had no effect on the CO conversion activity but had a significant effect on the NO conversion activity. On the basis of the NO conversion yield and N_2 selectivity exhibited by the various CoCu-T samples, the CoCu-400 sample was selected as the final catalytic material for further research. In addition, the thermal stability of CoCu-400 by 6 test runs of light-off curves and comparison of its activity with Pt-containing commercial catalysts were evaluated. The conclusion was that the material shows superior NO reduction activity over the Pt-containing catalysts and possesses significant thermal stability under oxidative and wet reaction conditions. As a result, the CoCu-400 sample was selected as the material of interest for kinetic model development.

References

[1] M. Thommes, K. Kaneko, A. V Neimark, J.P. Olivier, F. Rodriguez-reinoso, J. Rouquerol, K.S.W. Sing, Physisorption of gases , with special reference to the evaluation of surface area and pore size distribution (IUPAC Technical Report), Pure Appl. Chem. 87 (2015) 1051–1069. doi: 10.1515/pac-2014-1117.

[2] H. Dib, R. El Khawaja, G. Rochard, C. Poupin, S. Siffert, R. Cousin, CuAlCe Oxides Issued from Layered Double Hydroxide Precursors for Ethanol and Toluene Total Oxidation, Catalysts. 10 (2020) 870–884. doi:10.3390/catal10080870.

[3] R. González-Olvera, C.I. Urquiza-Castro, G.E. Negrón-Silva, D. Ángeles-Beltrán, L. Lomas-Romero, A. Gutiérrez-Carrillo, V.H. Lara, R. Santillan, J.A. Morales-Serna, Cu–Al mixed oxide catalysts for azide–alkyne 1,3- cycloaddition in ethanol–water, RSV Adv. 6 (2016) 63660–63666. doi: 10.1039/C6RA10097J.

[4] J. Laine, F. Severino, A. López-Agudo, J.L.G. Fierro, Structural changes in a Cu/Al_2O_3 catalyst when used for oxidation of carbon monoxide, J. Catal. 129 (1991) 297–299. doi: 10.1016/0021-9517(91)90033-Z.

[5] T.J. Huang, T.C. Yu, Calcination conditions on copper/alumina catalysts for carbon monoxide oxidation and nitric oxide reduction, Appl. Catal. 71 (1991) 275–282.
doi: 10.1016/0166-9834(91)85085-A.

[6] J.T. Sun, I.S. Metcalfe, M. Sahibzada, Deactivation of $Cu/ZnO/Al_2O_3$ methanol synthesis catalyst by sintering, Ind. Eng. Chem. Res. 38 (1999) 3868–3872.
doi: 10.1021/ie990078s.

[7] J.T. Richardson, J.L. Propp, Pore Size Effects on Sintering of Ni/Al_2O_3 Catalysts, J. Catal. 98 (1986) 457–467.

[8] V. Muñoz, F.M.Z. Zotin, L.A. Palacio, Copper-aluminum hydrotalcite type precursors for NO_x abatement, Catal. Today. 250 (2015) 173–179.
doi: 10.1016/j.cattod.2014.06.004.

[9] A. Alejandre, F. Medina, P. Salagre, X. Correig, J.E. Sueiras, Preparation and study of Cu-Al mixed oxides via hydrotalcite-like precursors, Chem. Mater. 11 (1999) 939–948. doi: 10.1021/cm980500f.

[10] S. Xiao, Y. Zhang, P. Gao, L. Zhong, X. Li, Z. Zhang, H. Wang, W. Wei, Y. Sun, Highly efficient Cu-based catalysts via hydrotalcite-like precursors for CO_2 hydrogenation to methanol, Catal. Today. 281 (2017) 327–336. doi: 10.1016/j.cattod.2016.02.004.

[11] C.L. Oliveira Corrêa, Y.E. Licea, L. Amparo Palacio, F.M. Zanon Zotin, Effect of composition and thermal treatment in catalysts derived from Cu-Al hydrotalcites-like compounds in the NO reduction by CO, Catal. Today. 289 (2017) 133–142.
doi: 10.1016/j.cattod.2016.08.023.

[12] C.D.O.P. Teixeira, S.D.S. Montani, L.A. Palacio, F.M.Z. Zotin, The effect of preparation methods on the thermal and chemical reducibility of Cu in Cu-Al oxides, Dalt. Trans. 47 (2018) 10989–11001. doi: 10.1039/c8dt01150h.

[13] N. Blanch-Raga, A. Eduardo Palomares, J. Martínez-Triguero, G. Fetter, P. Bosch, Cu Mixed Oxides Based on Hydrotalcite-Like Compounds for the Oxidation of Trichloroethylene, 18 (2021) 23. doi: 10.1021/ie4024935.

[14] P.B. Himelfarb, F.E. Wawner, A. Bieser, S.N. Vines, Oxidation states of copper during reduction of cupric oxide in methanol catalysts, J. Catal. 83 (1983) 469–471.
doi: 10.1016/0021-9517(83)90072-6.

[15] J.M. Dumas, C. Geron, A. Kribii, J. Barbier, Preparation of supported copper catalysts. II. Reduction of copper/alumina catalysts, Appl. Catal. 47 (1989). doi: 10.1016/S0166-9834(00)83256-X.

[16] B. Bridier, N. Lopez, J. Pérez-Ramírez, Partial hydrogenation of propyne over copper-based catalysts and comparison with nickel-based analogues, J. Catal. 269 (2010) 80–92. doi: 10.1016/j.jcat.2009.10.019.

[17] R. V. Gonçalves, R. Wojcieszak, H. Wender, C. Sato B. Dias, L.L.R. Vono, D. Eberhardt, S.R. Teixeira, L.M. Rossi, Easy access to metallic copper nanoparticles with high activity and stability for CO oxidation, ACS Appl. Mater. Interfaces. 7 (2015) 7987–7994. doi: 10.1021/acsami.5b00129.

[18] S. Velu, C.. Swamy, Synthesis and physicochemical properties of a new copper-manganese- aluminium ternary hydrotalcite-like compound, J. Mater. Sci. Lett. 15 (1996) 1674–1677.

[19] F.J.W.J. Labuschagne, D.M. Molefe, W.W. Focke, I. Van Der Westhuizen, H.C. Wright, M.D. Royeppen, Heat stabilising flexible PVC with layered double hydroxide derivatives, Polym. Degrad. Stab. 113 (2015) 46–54.
doi: 10.1016/j.polymdegradstab.2015.01.016.

[20] W.T. Reichle, Catalytic reactions by thermally activated, synthetic, anionic clay minerals, J. Catal. 94 (1985) 547–557. doi: 10.1016/0021-9517(85)90219-2.

[21] L. Moyo, W.W. Focke, D. Heidenreich, F.J.W.J. Labuschagne, H.J. Radusch, Properties of layered double hydroxide micro- and nanocomposites, Mater. Res. Bull. 48 (2013) 1218–1227. doi: 10.1016/j.materresbull.2012.11.040.

[22] R. Espinal, E. Taboada, E. Molins, R.J. Chimentao, F. Medina, J. Llorca, Cobalt hydrotalcite for the steam reforming of ethanol with scarce carbon production, RSC Adv. 2 (2012) 2946–2956. doi: 10.1039/c2ra00936f.

[23] K. Coenen, F. Gallucci, B. Mezari, E. Hensen, M. van Sint Annaland, An in-situ IR study on the adsorption of CO_2 and H_2O on hydrotalcites, J. CO_2 Util. 24 (2018) 228–239. doi: 10.1016/j.jcou.2018.01.008.

[24] F. Prinetto, G. Ghiotti, R. Durand, D. Tichit, Investigation of acid-base properties of catalysts obtained from layered double hydroxides, J. Phys. Chem. B. 104 (2000) 11117–11126. doi: 10.1021/jp002715u.

[25] J. Li, S. Zhang, Y. Chen, T. Liu, C. Liu, X. Zhang, M. Yi, Z. Chu, X. Han, A novel three-dimensional hierarchical CuAl layered double hydroxide with excellent catalytic activity for degradation of methyl orange, RSC Adv. 7 (2017) 29051–29057.
doi: 10.1039/c7ra03848h.

[26] F. Qiao, W. Shi, J. Dong, W. Lv, S. Ai, Functional hybrids of layered double hydroxides with hemin: Synergistic effect for peroxynitrite-scavenging activity, RSC Adv. 4 (2014) 44614–44620. doi: 10.1039/c4ra08200a.

[27] C. Drouet, P. Alphonse, A. Rousset, IR spectroscopic study of NO and CO adsorptions on nonstoichiometric nickel-copper manganites, Phys. Chem. Chem. Phys. 3 (2001) 3826–3830. doi: 10.1039/b101523k.

[28] K.L. Kauffman, J.T. Culp, A. Goodman, C. Matranga, FT-IR study of CO_2 adsorption in a dynamic copper(II) benzoate-pyrazine host with CO_2-CO_2 interactions in the adsorbed state, J. Phys. Chem. C. 115 (2011) 1857–1866. doi: 10.1021/jp102273w.

[29] M. Hajibeygi, M. Shabanian, M. Omidi-Ghallemohamadi, Development of

new acid-imide modified Mg-Al/LDH reinforced semi-crystalline poly(amide-imide) containing naphthalene ring; study on thermal stability and optical properties, Appl. Clay Sci. 139 (2017) 9–19. doi: 10.1016/j.clay.2017.01.011.

[30] M. Shabanian, M. Hajibeygi, A. Raeisi, FTIR characterization of layered double hydroxides and modified layered double hydroxides, Elsevier Ltd, 2020. doi: 10.1016/b978-0-08-101903-0.00002-7.

[31] J.C. Lavalley, Infrared spectrometric studies of the surface basicity of metal oxides and zeolites using adsorbed probe molecules, Catal. Today. 27 (1996) 377–401.

[32] Y. Wang, W. Gao, K. Li, Y. Zheng, Z. Xie, W. Na, J.G. Chen, H. Wang, Strong Evidence of the Role of H_2O in Affecting Methanol Selectivity from CO_2 Hydrogenation over Cu-ZnO-ZrO_2, Chem. 6 (2020) 419–430. doi: 10.1016/j.chempr.2019.10.023.

[33] R. Sahki, O. Benlounes, O. Chérifi, R. Thouvenot, M.M. Bettahar, S. Hocine, Effect of pressure on the mechanisms of the CO_2/H_2 reaction on a CO-precipitated CuO/ZnO/Al_2O_3 catalyst, React. Kinet. Mech. Catal. 103 (2011) 391–403. doi: 10.1007/s11144-011-0311-6.

[34] L. Lin, S. Yao, Z. Liu, F. Zhang, N. Li, D. Vovchok, A. Martínez-Arias, R. Castaneda, J. Lin, S.D. Senanayake, D. Su, D. Ma, J.A. Rodriguez, In Situ Characterization of Cu/CeO_2 Nanocatalysts for CO_2 Hydrogenation: Morphological Effects of Nanostructured Ceria on the Catalytic Activity, J. Phys. Chem. C. 122 (2018) 12934–12943. doi: 10.1021/acs.jpcc.8b03596.

[35] A.M. Bahmanpour, F. Héroguel, M. Kllç, C.J. Baranowski, L. Artiglia, U. Röthlisberger, J.S. Luterbacher, O. Kröcher, Cu-Al Spinel as a Highly Active and Stable Catalyst for the Reverse Water Gas Shift Reaction, ACS Catal. 9 (2019) 6243–6251.

doi: 10.1021/acscatal.9b01822.

[36] C.Y. Shiau, M.W. Ma, C.S. Chuang, CO oxidation over CeO_2-promoted Cu/γ-Al_2O_3 catalyst: Effect of preparation method, Appl. Catal. A Gen. 301 (2006) 89–95. doi: 10.1016/j.apcata.2005.11.018.

[37] G. Avgouropoulos, T. Ioannides, H. Matralis, Influence of the preparation method on the performance of CuO-CeO_2 catalysts for the selective oxidation of CO, Appl. Catal. B Environ. 56 (2005) 87–93. doi: 10.1016/j.apcatb.2004.07.017.

[38] A. Prašnikar, A. Pavlišič, F. Ruiz-Zepeda, J. Kovač, B. Likozar, Mechanisms of Copper-Based Catalyst Deactivation during CO_2 Reduction to Methanol, Ind. Eng. Chem. Res. 58 (2019) 13021–13029. doi: 10.1021/acs.iecr.9b01898.

[39] C.A. Sierra-Pereira, E.A. Urquieta-González, Reduction of NO with CO on CuO or Fe_2O_3 catalysts supported on TiO_2 in the presence of O_2, SO_2 and water steam, Fuel. 118 (2014) 137–147. doi: 10.1016/j.fuel.2013.10.054.

[40] D.B. Pal, R. Chand, S.N. Upadhyay, P.K. Mishra, Performance of water gas shift reaction catalysts: A review, Renew. Sustain. Energy Rev. 93 (2018) 549–565.
doi: 10.1016/j.rser.2018.05.003.

[41] J. Akil, C. Ciotonea, S. Siffert, S. Royer, L. Pirault-Roy, R. Cousin, C. Poupin, NO reduction by CO under oxidative conditions over CoCuAl mixed oxides derived from hydrotalcite-like compounds: Effect of water, Catal. Today. (2021). doi: 10.1016/j.cattod.2021.05.014.

[42] G.C. Chinchen, M.S. Spencer, K.C. Waugh, D.A. Whan, Promotion of methanol synthesis and the water-gas shift reactions by adsorbed oxygen on supported copper catalysts, J. Chem. Soc. Faraday Trans. 1 Phys. Chem. Condens. Phases. 83 (1987) 2193–2212. doi: 10.1039/F19878302193.

[43] Y. Fu, Y. Tian, P. Lin, A low-temperature IR spectroscopic study of selective adsorption of NO and CO on CuO/γ-Al_2O_3, J. Catal. 132 (1991) 85–91. doi: 10.1016/0021-9517(91)90249-4.

[44] Y.H. Qin, L. Huang, J.X. Zheng, Q. Ren, Low-temperature selective catalytic reduction of NO with CO over A-Cu-BTC and AO_x/CuO_y/C catalyst, Inorg. Chem. Commun. 72 (2016) 78–82. doi: 10.1016/j.inoche.2016.08.018.

[45] X. Zhang, X. Cheng, C. Ma, Z. Wang, Effects of the Fe/Ce ratio on the activity of CuO/CeO_2-Fe_2O_3 catalysts for NO reduction by CO, Catal. Sci. Technol. 8 (2018) 3336–3345. doi: 10.1039/c8cy00709h.

[46] P. Li, L. Feng, F. Yuan, D. Wang, Y. Dong, X. Niu, Y. Zhu, Effect of surface Copper species on NO + CO reaction over xCuO-$Ce_{0.9}Zr_{0.1}O_2$ catalysts: In situ DRIFTS studies, Catalysts. 6 (2016) 15–24. doi: 10.3390/catal6080124.

[47] X. Cheng, X. Zhang, D. Su, Z. Wang, J. Chang, C. Ma, NO reduction by CO over copper catalyst supported on mixed CeO_2 and Fe_2O_3: Catalyst design and activity test, Appl. Catal. B Environ. 239 (2018) 485–501. doi: 10.1016/j.apcatb.2018.08.054.

[48] Y.W. Yu Liu, Xuezhong Wang, Xiangguang Yang, Co-Cu-Al mixed oxides derived from hydrotalcite-like compound for NO reduction by CO, React. Jinet. Catal. Lett Vol.68, NO.2, 399-405 (1999).

[49] A. Tarjomannejad, A. Farzi, A. Niaei, D. Salari, NO reduction by CO over $LaB_{0.5}B'_{0.5}O_3$ (B = Fe, Mn, B'=Fe, Mn, Co, Cu) perovskite catalysts, an experimental and kinetic study, J. Taiwan Inst. Chem. Eng. 78 (2017) 200–211. doi: 10.1016/j.jtice.2017.05.034.

[50] X. Chen, J. Zhang, Y. Huang, Z. Tong, M. Huang, Catalytic reduction of nitric oxide with carbon monoxide on copper-cobalt oxides supported on nano-titanium dioxide, J. Environ. Sci. 21 (2009) 1296–1301. doi: 10.1016/S1001-0742(08)62418-3.

[51] S. Velu, K. Suzuki, S. Hashimoto, N. Satoh, F. Ohashi, S. Tomura, The effect of cobalt on the structural properties and reducibility of CuCoZnAl layered double hydroxides and their thermally derived mixed oxides, J. Mater. Chem. 11 (2001) 2049–2060. doi: 10.1039/b101599k.

[52] G. Fierro, M. Lo Jacono, M. Inversi, R. Dragone, P. Porta, TPR and XPS study of cobalt-copper mixed oxide catalysts: Evidence of a strong Co-Cu interaction, Top. Catal. 10 (2000) 39–48. doi: 10.1023/a:1019151731177.

[53] L. Zhang, X. Yao, Y. Lu, C. Sun, C. Tang, F. Gao, L. Dong, Effect of precursors on the structure and activity of CuO-CoO_x/γ-Al_2O_3 catalysts for NO reduction by CO, J. Colloid Interface Sci. 509 (2018) 334–345. doi: 10.1016/j.jcis.2017.09.031.

[54] A.M. Carrillo, J.G. Carriazo, Cu and Co oxides supported on halloysite for the total oxidation of toluene, Appl. Catal. B Environ. 164 (2015) 443–452. doi: 10.1016/j.apcatb.2014.09.027.

[55] A. Biabani-Ravandi, M. Rezaei, Z. Fattah, Low-temperature CO oxidation over nanosized Fe-Co mixed oxide catalysts: Effect of calcination temperature and operational conditions, Chem. Eng. Sci. 94 (2013) 237–244. doi: 10.1016/j.ces.2013.02.002.

[56] A. Bialas, P. Niebrzydowska, B. Dudek, Z. Piwowarska, L. Chmielarz, M. Michalik, M. Kozak, P. Kuśtrowski, Coprecipitated Co-Al and Cu-Al oxide catalysts for toluene total oxidation, Catal. Today. 176 (2011) 413–416. doi: 10.1016/j.cattod.2010.11.021.

[57] D. Li, Y. Fan, Y. Ding, X. Wei, Y. Xiao, Preparation of cobalt-copper-aluminum spinel mixed oxides from layered double hydroxides for total oxidation of benzene, Catal. Commun. 88 (2017) 60–63.
doi: 10.1016/j.catcom.2016.09.035.

[58] M. Kang, E.D. Park, J.M. Kim, J.E. Yie, Cu-Mn mixed oxides for low temperature NO reduction with NH_3, Catal. Today. 111 (2006) 236–241.
doi: 10.1016/j.cattod.2005.10.032.

[59] X. Yao, Y. Xiong, W. Zou, L. Zhang, S. Wu, X. Dong, F. Gao, Y. Deng, C. Tang, Z. Chen, L. Dong, Y. Chen, Correlation between the physicochemical properties and catalytic performances of $Ce_xSn_{1-x}O_2$ mixed oxides for NO reduction by CO, Appl. Catal. B Environ. 144 (2014) 152–165. doi: 10.1016/j.apcatb.2013.06.020.

[60] L. Chmielarz, M. Rutkowska, P. Kuśtrowski, M. Drozdek, Z. Piwowarska, B. Dudek, R. Dziembaj, M. Michalik, An influence of thermal treatment conditions of hydrotalcite-like materials on their catalytic activity in the process of N_2O decomposition, J. Therm. Anal. Calorim. 105 (2011) 161–170. doi: 10.1007/s10973-011-1284-4.

[61] J.S. Shu, W.S. Xia, Y.J. Zhang, T. Cheng, M.R. Gao, Low-temperature catalytic reduction of nitrogen monoxide with carbon monoxide on copper iron and copper cobalt composite oxides, Chinese J. Chem. Phys. 21 (2008). doi: 10.1088/1674-0068/21/04/393-400.

[62] X. Du, T.L. Yao, Q. Wei, H. Zhang, Y. Huang, Investigation of Fe - Ni Mixed-Oxide Catalysts for the Reduction of NO by CO: Physicochemical Properties and Catalytic Performance, Chem. - An Asian J. 14 (2019) 2966–2978. doi: 10.1002/asia.201900782.

[63] J. Yan, M.C. Kung, W.M.H. Sachtler, H.H. Kung, Co/Al_2O_3 Lean NO_x Reduction Catalyst, J. Catal. 172 (1997) 178–186.

[64] K. Liu, F. Liu, L. Xie, W. Shan, H. He, DRIFTS study of a Ce-W mixed oxide catalyst for the selective catalytic reduction of NOx with NH_3, Catal. Sci. Technol. 5 (2015) 2290–2299. doi: 10.1039/c4cy01550a.

[65] Z. Xu, Y. Li, Y. Lin, T. Zhu, A review of the catalysts used in the reduction of NO by CO for gas purification, Environ. Sci. Pollut. Res. 27 (2020) 6723–6748. doi: 10.1007/s11356-019-07469-w.

[66] J. Akil, S. Siffert, L. Pirault-Roy, S. Royer, F. Shen, W. Chen, R. Cousin, C. Poupin, Investigation of catalysts M/CeO_2 (M = Pt, Rh, or Pd) for purification of CO_2 derived from oxycombustion in the absence or presence of water, Environ. Sci. Pollut. Res. 28 (2021) 12521–12532. doi: 10.1007/s11356-020-11252-7.

[67] J. Akil, S. Siffert, L. Pirault-Roy, D.P. Debecker, F. Devred, R. Cousin, C. Poupin, Effect of precious metals on NO reduction by CO in oxidative conditions, Appl. Sci. 10 (2020). doi: 10.3390/app10093042.

[68] D. Mantri, P. Aghalayam, Detailed surface reaction mechanism for reduction of NO by CO, Catal. Today. 119 (2007) 88–93.
doi: 10.1016/j.cattod.2006.08.002.

[69] T. Kolli, K. Rahkamaa-Tolonen, U. Lassi, A. Savimäki, R.L. Keiski, Comparison of catalytic activity and selectivity of $Pd/(OSC + Al_2O_3)$ and $(Pd + OSC)/Al_2O_3$ catalysts, Catal. Today. 100 (2005) 297–302.
doi: 10.1016/j.cattod.2004.09.064.

[70] M.M. Behera, C. Ciotonea, L. Olivet, L. Tidahy, S. Royer, D. Thomas, R. Cousin, G. De Weireld, C. Poupin, Impact of gas treatment of CuAl-LDH on NO reduction by CO under oxidative conditions, Chem. Eng. J. 452 (2023). doi:

10.1016/j.cej.2022.139543.

[71] D. Stoyanova, M. Christova, P. Dimitrova, J. Marinova, N. Kasabova, D. Panayotov, Copper-cobalt oxide spinel supported on high-temperature aluminosilicate carders as catalyst for CO-O_2 and CO-NO reactions, Appl. Catal. B Environ. 17 (1998) 233–244.
https://doi.org/10.1016/S0926-3373(98)00011-3.

[72] D. Mehandjiev, D. Panayotov, M. Khristova, Catalytic Reduction of NO with CO over $Cu_xCo_{3-x}O_4$ Spinels, React. Kinet. Catal. Lett. 33 (1987) 273–277.

Chapter 5

Large-Scale Material Synthesis and Kinetic Modelling

After the study conducted in Chapter 4, it was observed that Co_4Cu_2Al-400-CO_2 treated mixed oxide is an efficient catalyst for the NO reduction by CO under the industrial flue gas condition i.e., under O_2 excess, CO_2-rich and humid reaction condition. Therefore, the LDH form of this catalyst was synthesized on a large-scale and shaped in the form of extrudes in order to be used in the future on a semi-pilot scale setup. Furthermore, possible models governing the reaction kinetics of the system is developed using LHHW kinetics and the model parameters are determined by a global optimization method using 70 set of experimental data obtained from changing the reactant gas composition at the reactor inlet and recording the corresponding change in the catalytic activity. Finally, the fitness of each of these models were assessed and the best fitting model was chosen.

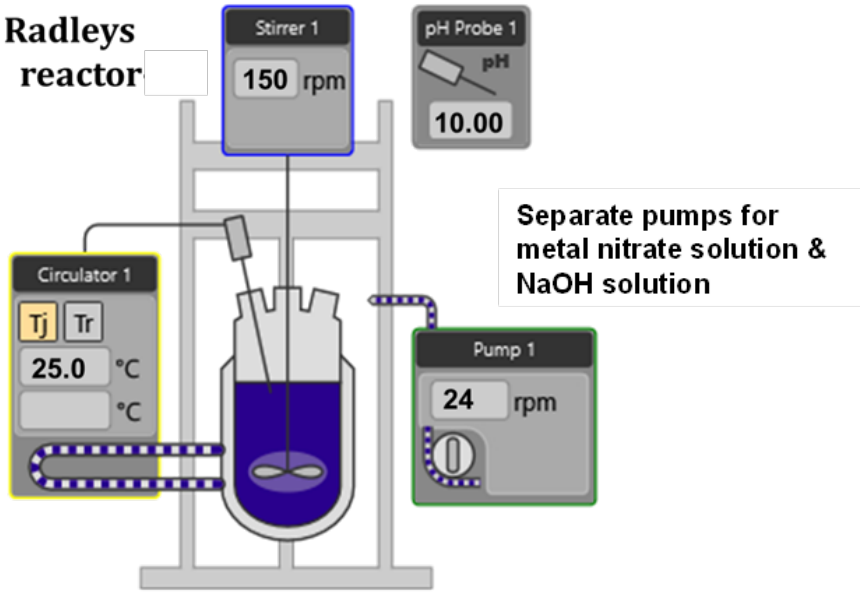

Figure 5.1 Schematic representation of the large-scale synthesis setup

5.1 Large-Scale Material Synthesis

Co_4Cu_2Al-LDH was synthesized at a large scale to be used in the semi-pilot scale catalytic reactor setup (size of the reactor: 0.6 L) at Université de Mons (UMONS). The parent LDH precursor was synthesized in a 10 L batch reactor facility at Unité de Catalyse et Chimie du Solide (UCCS) Lab in Université de Lille following the co-precipitation method. The schematic representation of the large-scale synthesis apparatus is shown in Figure 5.1. A comparison between the lab-scale and large-scale synthesis is shown in Table 5.1. It should be noted that the LDH synthesis at the lab-scale was scaled up from 10 g to 50 g of the final product with no change in the concentration of NaOH and Na_2CO_3 concentration in their respective aqueous solutions. From Table 5.1, it can be seen that a higher concentration of metal nitrate precursor, Na_2CO_3 and NaOH aqueous solutions were used for the large-scale synthesis as compared to the lab-scale synthesis because of the objective to complete the synthesis in two batches (so as to reduce the probability of any difference in the material properties for the whole batch) and the reactor volume was not enough to use the same concentration of the solutions as used in the lab-scale synthesis. Moreover, XRD analyses were conducted on both the batches to ensure consistency in the LDH structural properties (refer Figure 5.2). Further, the prepared LDH batch was

crushed and extruded by making a paste of LDH (60% water and rest LDH) and pushing it through a 3 mm diameter nozzle (see Figure 5.3). The extrudes thus prepared were further dried in an oven for several days at a temperature of 35-40°C so as to develop adequate mechanical strength. In future, these extrudes will be treated under the flow of CO_2 in a semi-pilot scale reactor to achieve the mixed metal oxide form prior to performing the catalytic test at the same semi-pilot setup.

Table 5.1 Comparison of lab-scale and large-scale Co_4Cu_2Al-LDH synthesis

Sample weight of LDH (g)	$Co(NO_3)_2$ $.6H_2O$ (g)	$Cu(NO_3)_2$ $.3H_2O$ (g)	$Al(NO_3)_3$ $.9H_2O$ (g)	x (M) /NaOH (L)[a]	x (M) $/Na_2CO_3$ (ml)[b]	x (L) of H_2O[c]	
						In Precursor	In Reactor
50	73.1	30.02	46.4	1 / 0.5	1 / 150	1	0.5
600	850.8	353.1	548.4	8 / 1.8	2 / 900	2.5	2

[a]Concentration (in M) and volume (in L) of NaOH solution
[b]Concentration (in M) and volume (in L) of Na_2CO_3 solution
[c]Volume of water (L) used for the nitrate precursor solution and in the reactor (in order to achieve a height of the Na_2CO_3 solution in the reactor such that the bulb of the pH probe is perfectly inside the solution.

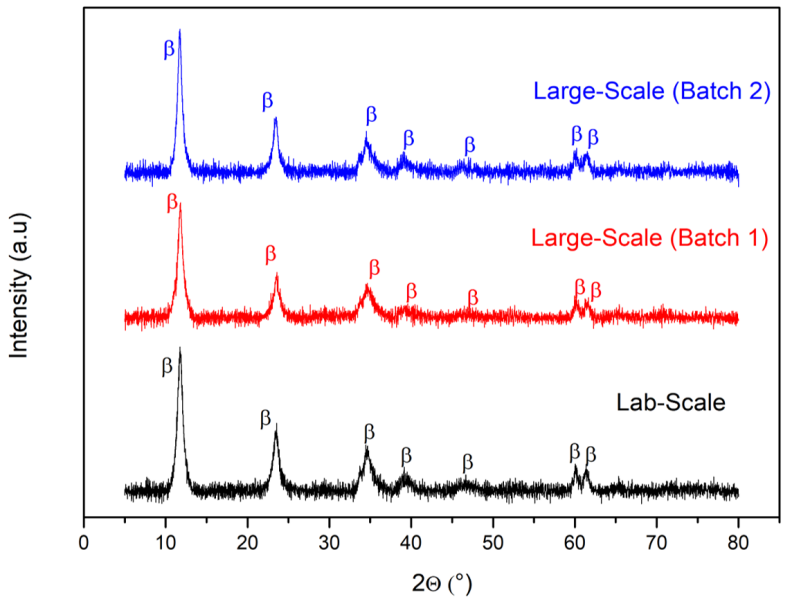

Figure 5.2 Comparison of XRD plots for lab-scale and large-scale synthesized Co_4Cu_2Al-LDH sample

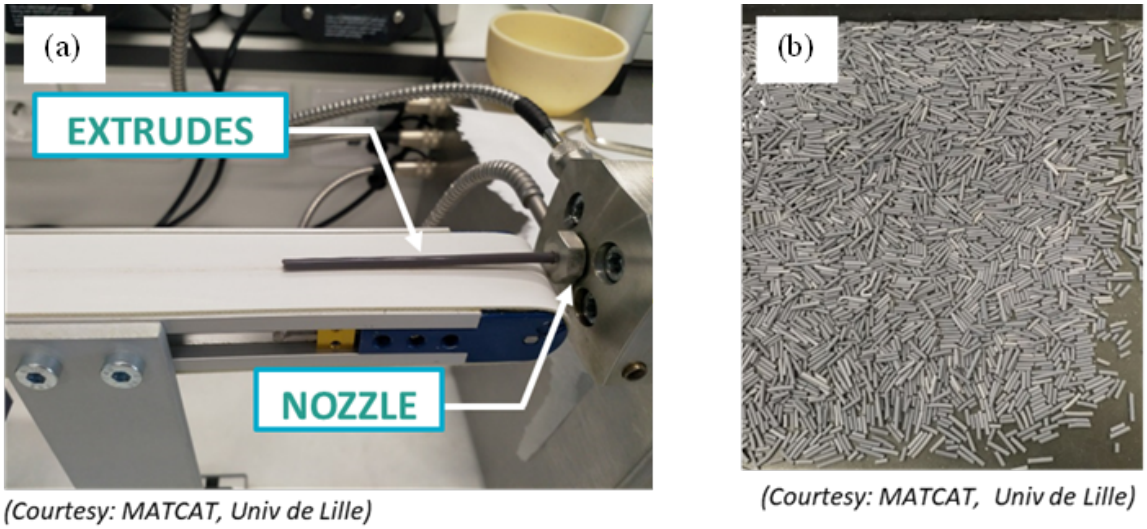

Figure 5.3 Shaping of Co_4Cu_2Al-LDH sample synthesized at the large scale: (a) formation of extrudes from the paste of LDH and water (b) Extrudes dried for several days

5.2 Influence of Feed Gas Composition and Catalyst Weight

In this section, the effect of the reactant gas composition on the catalytic performance of Co_4Cu_2Al-400-CO_2 sample is assessed. The content of each gas component in the reactant gas mixture (20.4 vol% CO_2, 8.6 vol% O_2, 0.13 vol% CO, 475 ppm NO, 8.2 vol% H_2O and rest balanced by He) was altered and its corresponding effect on the catalytic activity was recorded. The possible explanations for each of the behaviors is further discussed in this section.

5.2.1 Effect of CO Content

As mentioned earlier, the function of CO in the reactant gas mixture is that of a reducing agent for NO reduction, preferably to non-toxic N_2. Therefore, amount of CO in the reactant gas mixture was increased from 0.13 vol% to 0.5 vol% keeping the composition of the other gas components constant (the amount of He was adjusted according to the change in CO content to keep the proportion of the other gas components constant). The effect of this change on the catalytic performance is shown in Figure 5.4. It can be observed from the figure that with the increase in the CO content from 0.13 vol% to 0.5 vol%, there was a shift of CO conversion curve to higher temperatures. Moreover, a small decline in the

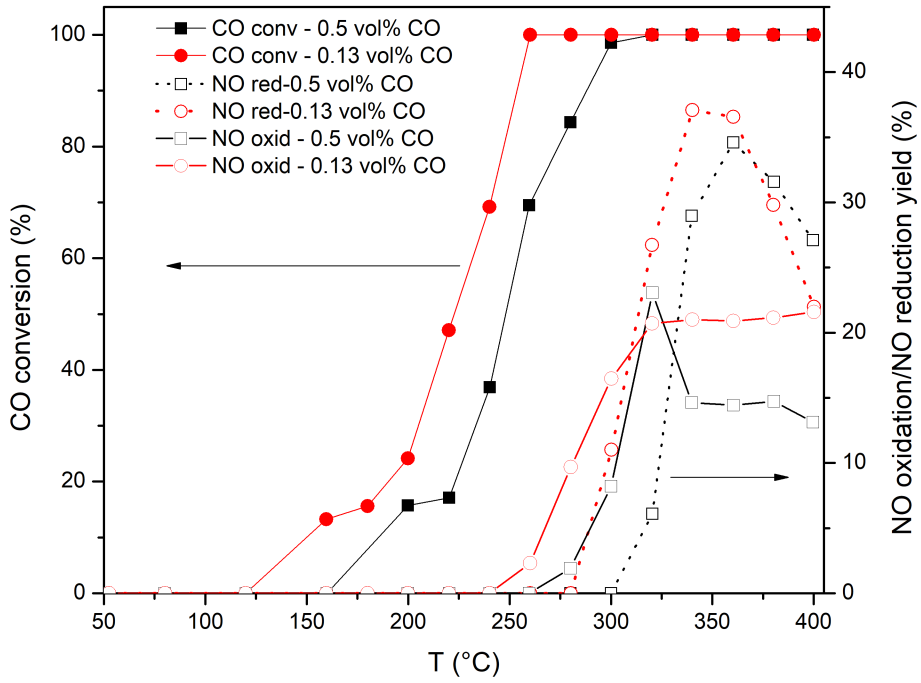

Figure 5.4 Effect of CO content on the catalytic performance of CoCu-400 catalytic sample

NO reduction yield from 38% at 340°C to 35% at 360°C was observed and there was a distinctive decline in the NO oxidation yield from 23% at 300-400°C to 13-15% from 320-400°C. In summary, NO conversion yield decreased, and CO conversion was delayed with the increase in CO content in the reaction feed gas mixture. One possible reason for such a catalytic behaviour can be CO poisoning. CO is known to be adsorbed strongly on reduced surfaces thereby blocking NO adsorption and affecting the CO + NO reaction [1–3].

5.2.2 Effect of NO Content

To assess the effect of NO content in the reactant gas mixture on the overall catalytic performance, two cases have been considered: (i) 300 ppm and (ii) 475 ppm. The resulting catalytic performances for each of these cases are shown in Figure 5.5. It can be observed from the figure that increasing the content of NO in the reactant gas stream did not significantly affect the overall catalytic activity. The NO content in the reactant gas stream was altered by only 175 ppm, therefore, the effect of NO on the catalytic performance was

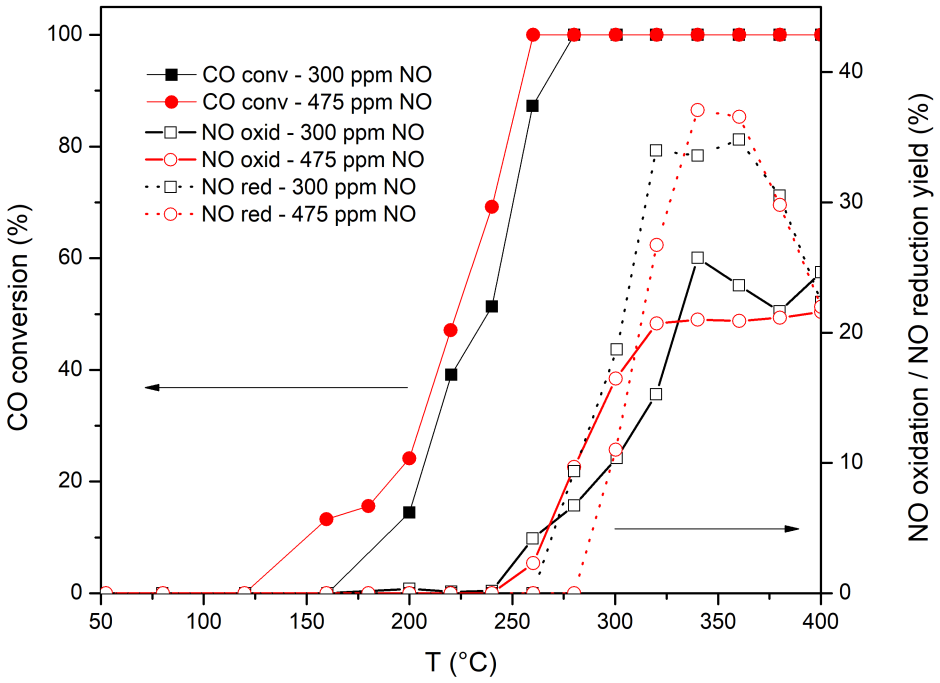

Figure 5.5 Effect of NO content in the reaction gas mixture on catalytic performance of CoCu-400 sample

not that pronounced. However, any further alteration in the NO content is restricted by the operational constraints of the catalytic test setup therefore, the investigations on the influence of NO content could not be further performed. It is also interesting to keep in mind the NO concentration in industrial flue gasses will be limited due to a DeNOX treatment in kiln

5.2.3 Effect of CO_2 Content

In order to investigate the effect of CO_2 content on the overall catalytic performance, the composition of the gas component in the reactant gas stream was increased from 20 vol% to 60 vol% without changing the content of rest of the gas components. The catalytic activity resulting from these two conditions are compared and shown in Figure 5.6. A shift to the higher temperature for the CO conversion and NO reduction yield peak was observed upon increasing the CO_2 content in the system. However, a considerable decrease in the NO oxidation yield was also recorded with this increase in the CO_2 content. This effect on CO and NO conversion activity can be attributed to the weak-acidic

nature of CO_2 and its strong adsorption on metal oxides like CuO forming stable carbonates which are decomposed only at T > 300°C [4]. On the other hand, NO adsorbs on the oxide surfaces and form nitrate and nitrite species which are the important intermediate steps for NO reduction and oxidation activity [5–7]. It can be speculated that a competitive adsorption exists between these two gas components for the same active sites on the catalyst. This possibly explains the decrease in the NO conversion yield with the increase of CO_2 content in the reaction feed gas. The existence of this competitive adsorption of CO_2 and NO was also reported by Yang et al over Fe/ZSM-5 catalyst for NO_x [8]. To investigate the effect of CO_2 on NO_x adsorption, the authors introduced 10 vol% CO_2 and observed a maximum of 27% decrease in NO adsorption amount at 1 $g.cm^{-3}$ of NO concentration which was attributed to the competitive adsorption between CO_2 and NO for the same type of active sites on the surface of the catalyst. Similar observations were also reported by Wang et al [9] during introduction of 5 vol% CO_2 into the reactant gas mixture of 1000 ppm NO and 3 vol% O_2 at 200°C for reduction of NO_x with NH_3 over

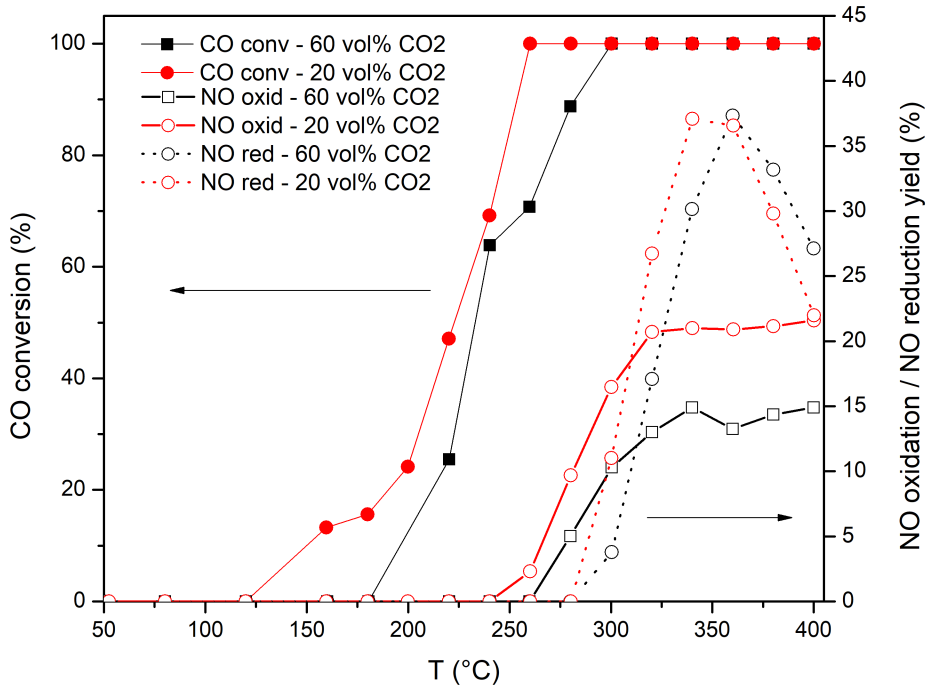

Figure 5.6 Effect of CO_2 content on the catalytic performance of CoCu-400 sample

$Fe_{0.4}Ce_{0.6}O_{2-\delta}$ catalyst. The DRIFTS and NO-TPD results under presence and absence CO_2 conditions showed that the formation of nitrate species on the catalyst surface was inhibited in the presence of CO_2 in the reactant mixture because CO_2 adsorbed dominantly on Fe-O-Ce species, the only active sites for NO adsorption, in the catalyst.

5.2.4 Effect of H_2O Content

To investigate the effect of water content in the reactant gas stream on the catalytic performance of CoCu-400 sample, three experimental cases were considered: (i) 8.2 vol% (or wet reaction consition) (ii) 4.2 vol% and (iii) 0 vol% (or dry reaction condition). The catalytic performances under each of these cases were compared and are shown in Figure 5.7. It can be observed that a decrease in the water content from 8.2 vol% to 4.2 vol% accelerated CO conversion but declined NO reduction yield with an increase in the NO oxidation yield. Moreover, upon reducing the water content to zero, it was observed that CO conversion activity was accelerated, NO reduction yield was

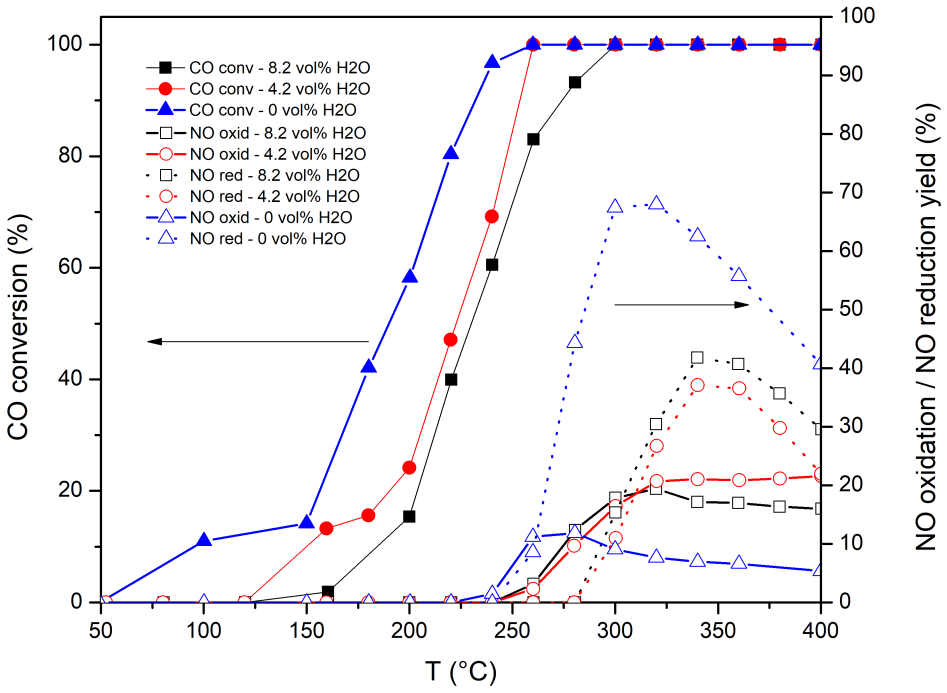

Figure 5.7 Effect of H_2O content in the reactant gas stream on the catalytic performance of CoCu-400 sample

enhanced with its peak shifting to comparatively lower temperatures and NO oxidation yield was declined. Presence of water in the reactant gas stream competitively adsorbs on the active sites in the catalyst and therefore lowers the availability of free active sites for CO and NO [10]. However, moisture driven sintering of the active metal particles can also degrade the catalytic performance which can be confirmed from material characterization experiments on the sample procured after the activity test [11].

5.2.5 Effect of O_2 Content

The O_2 content in the feed gas composition was decreased from 8.6 vol% to 4 vol% without any change to the proportion of other gas components in the mixture. The influence of this lowering of O_2 content on the catalytic activity can be seen in Figure 5.8. It can be seen from this figure that no appreciable change in the CO conversion and NO reduction activity is observed. However, the NO oxidation yield decreased from 20% to 15 vol% with a decrease in the O_2 content from 8.6 vol% to 4 vol%. This also indicates that the total

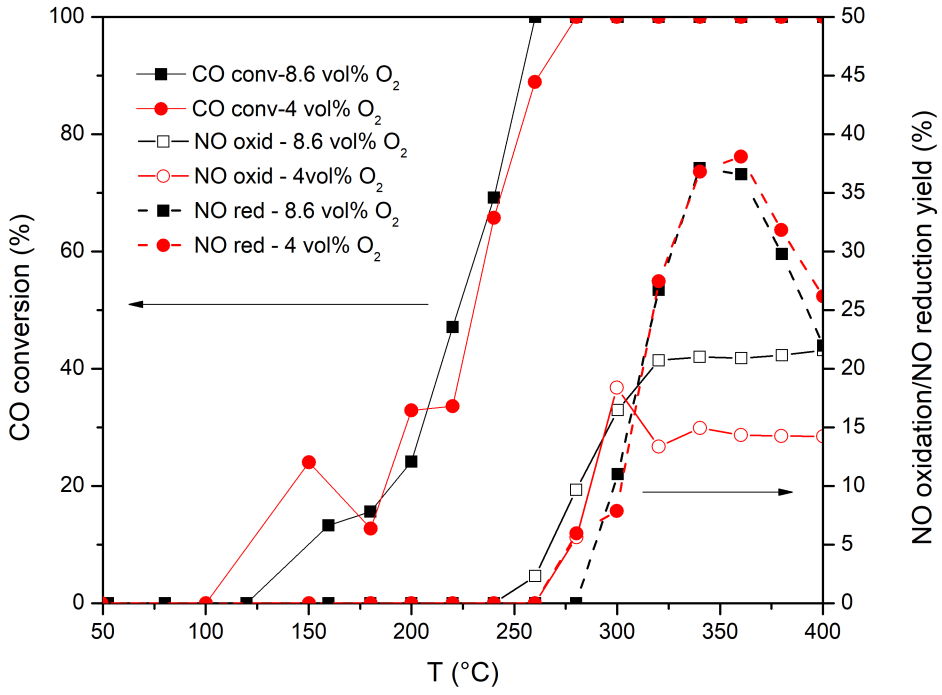

Figure 5.8 Effect of O_2 content on the catalytic performance of CoCu-400 sample

NO conversion activity decreased with a decrease in the O_2 content. These results are contrary to the observations reported by Cheng et al. [12] and Gholami et al. [13] where the authors observed a decrease in NO conversion activity with an increase in the O_2 concentration in the feed stream. However, Wen et al. [14] observed a similar phenomenon to that observed in this study, but over CuCeMgAl-O mixed oxide catalyst. The authors reported that the presence of O_2 in the reactant feed stream oxidizes the catalyst surface and forms oxidized species of active metals that are conducive to NO adsorption and therefore enhance the NO conversion activity but at the expense of a decreased in CO adsorption on the catalyst surface. Furthermore, the presence of water triggers a water-gas shift-like reaction that facilitates CO oxidation and NO reduction activities (because of the reaction between NO and H_2 produced by the water-gas shift reaction).

5.2.6 Effect of Catalyst Weight

The weight of the catalyst in the reactor was varied keeping the Gas Hourly Space Velocity constant (i.e., 22400 h^{-1}) by compensating the remaining bed volume with SiC. The three experimental cases considered for this analysis were: (i) 762 mg (ii) 381 mg and (iii) 150 mg. The corresponding catalytic performances are plotted and compared in Figure 5.9. Expectedly, increasing the catalytic weight in the reactor accelerated the CO conversion activity, enhanced the NO reduction yield with its peak shifting to lower temperature and a slight decline in the NO oxidation yield. Such a difference in the catalytic behaviour is due to the presence of a large number of active sites for the surface reactions.

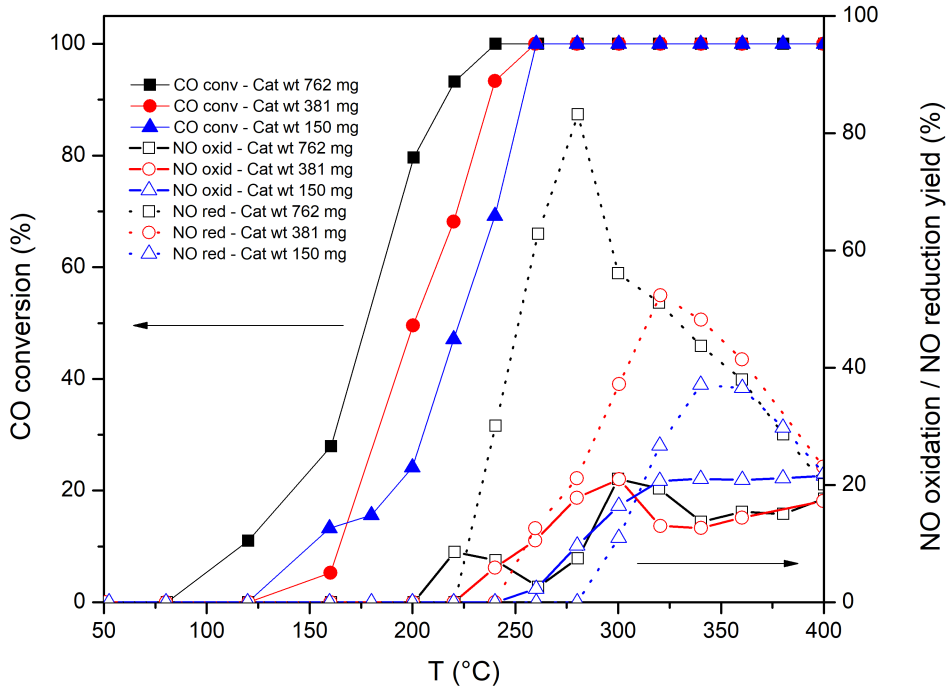

Figure 5.9 Effect of catalyst weight on the catalytic performance of CoCu-400 sample

5.3 Kinetic Modelling

To simulate the catalytic behavior under operating conditions, a mathematical model governing the reaction kinetics of the reaction system over CoCu-400 is developed. Literature studies popularly report the kinetic model for CO + NO reaction, specifically under automotive exhaust gas mixture which is close to that in industrial flue gas, based on Langmuir-Hinshelwood-Hougen-Watson kinetics (see Chapter 2). Therefore, in this study, the kinetic model is developed based on the LHHW kinetics. The derivation of the reaction rate expressions, development of the system of ordinary differential equations for the reaction system and regression of model parameters are discussed further in this section.

5.3.1 Development of the Kinetic Model

For the development of the reaction rate equations, certain assumptions were considered:

- Langmuir-Hinshelwood-Hougen-Watson (LHHW) kinetic model based on

one-site mechanism was considered for the simplicity of the model

- CO_2 and H_2O do not participate in the reaction but compete with other reactants for the common active sites in the catalyst. Therefore, these two components are included in the adsorption term in the denominator of the reaction rate expression.

The different main reactions ($K_{p,\alpha}$, $K_{p,\beta}$ and $K_{p,\gamma}$ represent the reaction equilibrium constants) and their corresponding elementary steps are shown in Eq. (5.1)-(5.2) and Table 5.2 respectively.

$$\mathrm{CO} + \mathrm{NO} \overset{K_{p,\alpha}}{\rightleftharpoons} \mathrm{CO_2} + \frac{1}{2}\mathrm{N_2} \tag{5.1}$$

$$\mathrm{CO} + \frac{1}{2}\mathrm{O_2} \overset{K_{p,\beta}}{\rightleftharpoons} \mathrm{CO_2} \tag{5.2}$$

$$\mathrm{NO} + \frac{1}{2}\mathrm{O_2} \overset{K_{p,\gamma}}{\rightleftharpoons} \mathrm{NO_2} \tag{5.3}$$

5.3.2 Reaction Rate Expressions

As previously discussed in the literature studies in Chapter 2, the rate-limiting step for NO reduction by CO reaction is usually considered to be the dissociation of adsorbed NO species into adsorbed N and O species on the catalyst (see step no. 3 in Table 5.2). However, for NO oxidation to NO_2 and CO oxidation to CO_2, there are different possible rate determining steps (RDS) (see Table 5.3). Since all these individual reactions take place simultaneously in the reaction system, it is important to derive the reaction rates considering these possible RDS and reaction equilibrium steps. Based on the different possible rate-determining steps for each individual main reaction, there are in total 15 possible combinations of rate-determining steps. These combinations are enlisted in Table 5.4.

Further in this report, based on each of these combinations of rate determining steps, the reaction rate equations namely (i) rate of NO reduction to N_2 (r_N) (ii) rate of NO oxidation to NO_2 (r_{NO_2}) and (iii) rate of CO oxidation to CO_2 (r_{CO_2}) are derived from replacing the site coverage terms for different reactant, product and intermediate components by the relations derived from the assumption of equilibrium state for all the elementary steps except for

Table 5.2 Elementary steps for each of the individual main reaction

Main Reaction	Elementary Step	Step No.
NO reduction by CO	$CO + [S] \rightleftharpoons CO[S]$	1
	$NO + [S] \rightleftharpoons NO[S]$	2
	$NO[S] + [S] \rightleftharpoons N[S] + O[S]$	3
	$CO[S] + O[S] \rightleftharpoons CO_2[S] + [S]$	4
	$N[S] + N[S] \rightleftharpoons N_2 + 2[S]$	5
	$N_2[S] \rightleftharpoons N_2 + [S]$	6
	$CO_2[S] \rightleftharpoons CO_2 + [S]$	7
CO Oxidation to CO_2	$CO + [S] \rightleftharpoons CO[S]$	8
	$O_2 + 2[S] \rightleftharpoons 2O[S]$	9
	$CO[S] + O[S] \rightleftharpoons CO_2[S] + [S]$	10
	$CO_2[S] \rightleftharpoons CO_2 + [S]$	11
NO Oxidation to NO_2	$NO + [S] \rightleftharpoons NO[S]$	12
	$O_2 + 2[S] \rightleftharpoons 2O[S]$	13
	$NO[S] + O[S] \rightleftharpoons NO_2[S] + [S]$	14
	$NO_2[S] \rightleftharpoons NO_2 + [S]$	15

Here, [S] represents the vacant active sites in the catalyst and X[S] represents the adsorbed state of component X

the rate-determining steps. Each of these possible sets of rate-determining or rate-limiting steps can be used to derive different reaction rate expressions. In order to demonstrate the reaction rate derivation, 'Form-10' (refer Table 5.4) has been used as an example and the corresponding reaction rate expressions are discussed in the next section.

5.3.3 Derivation of Reaction Rate Expressions

To demonstrate the derivation of reaction rate expressions for a kinetic model in this section, Form-10 is chosen. It can be seen from Table 5.4 that, for 'Form 10', the rate-determining steps are surface reaction between adsorbed CO and O species, surface reaction between adsorbed NO and O species and surface dissociation of NO into N and O species. Based on these considerations, the elementary reaction steps are enlisted in Table 5.5. The list of the site coverage relations is shown in Table 5.6.

Table 5.3 Different possible rate determining steps for the individual main reactions

Reaction	Rate-Determining Step	Description
NO reduction by CO	$NO[S] + [S] \rightleftharpoons N[S] + O[S]$	Dissociation of adsorbed NO into N and O species
CO oxidation to CO_2	$CO + [S] \rightleftharpoons CO[S]$	Adsorption of CO
	$O_2 + 2[S] \rightleftharpoons 2O[S]$	Dissociative adsorption of O_2
	$CO[S] + O[S] \rightleftharpoons CO_2[S] + [S]$	Surface reaction between adsorbed CO and O species to form adsorbed CO_2 species
	$CO_2[S] \rightleftharpoons CO_2 + [S]$	Desorption of CO_2
NO oxidation to NO_2	$NO + [S] \rightleftharpoons NO[S]$	Adsorption of NO
	$O_2 + 2[S] \rightleftharpoons 2O[S]$	Dissociative adsorption of O_2
	$NO[S] + O[S] \rightleftharpoons NO_2[S] + [S]$	Surface reaction between adsorbed NO and O species to form adsorbed NO_2 species
	$NO_2[S] \rightleftharpoons NO_2 + [S]$	Desorption of NO_2

Step 1: Derivation of Site Coverage Relations

In the first step, the active site coverage by different reactants, products and reaction intermediates were expressed in terms of concentrations of the components in the product stream. For example, the fraction of the total number of active sites on the catalyst occupied by CO (θ_{CO}), can be derived in terms of partial pressure of CO in the product stream (P_{CO}) (refer Eq. (5.5)) by rearranging the equilibrium relation for CO adsorption as shown in Eq. (5.4). In Eq. (5.4) and (5.5), θ represents the fraction of the active sites on the catalyst that is vacant and K_i^{ads} represents the adsorption constant of component i. Similarly, the relation of θ_{NO} (refer Eq. (5.7)) and θ_{H_2O} (refer Eq. (5.9)) in terms of P_{NO} and P_{H_2O} were derived from their respective adsorption equilibrium (see Eq. (5.6) and Eq. (5.8)).

Table 5.4 List of different possible combinations of rate-determining steps

Form No.	NO reduction by CO	CO oxidation to CO_2	NO oxidation to NO_2
Form-1	$NO[S] + [S] \rightleftharpoons N[S] + O[S]$	$CO + [S] \rightleftharpoons CO[S]$	$NO + [S] \rightleftharpoons NO[S]$
Form-2	$NO[S] + [S] \rightleftharpoons N[S] + O[S]$	$CO + [S] \rightleftharpoons CO[S]$	$O_2 + 2[S] \rightleftharpoons 2O[S]$
Form-3	$NO[S] + [S] \rightleftharpoons N[S] + O[S]$	$CO + [S] \rightleftharpoons CO[S]$	$NO[S] + O[S] \rightleftharpoons NO_2[S] + [S]$
Form-4	$NO[S] + [S] \rightleftharpoons N[S] + O[S]$	$CO + [S] \rightleftharpoons CO[S]$	$NO_2[S] \rightleftharpoons NO_2 + [S]$
Form-5	$NO[S] + [S] \rightleftharpoons N[S] + O[S]$	$O_2 + 2[S] \rightleftharpoons 2O[S]$	$NO + [S] \rightleftharpoons NO[S]$
Form-6	$NO[S] + [S] \rightleftharpoons N[S] + O[S]$	$O_2 + 2[S] \rightleftharpoons 2O[S]$	$NO[S] + O[S] \rightleftharpoons NO_2[S] + [S]$
Form-7	$NO[S] + [S] \rightleftharpoons N[S] + O[S]$	$O_2 + 2[S] \rightleftharpoons 2O[S]$	$NO_2[S] \rightleftharpoons NO_2 + [S]$
Form-8	$NO[S] + [S] \rightleftharpoons N[S] + O[S]$	$CO[S] + O[S] \rightleftharpoons CO_2[S] + [S]$	$NO + [S] \rightleftharpoons NO[S]$
Form-9	$NO[S] + [S] \rightleftharpoons N[S] + O[S]$	$CO[S] + O[S] \rightleftharpoons CO_2[S] + [S]$	$O_2 + 2[S] \rightleftharpoons 2O[S]$
Form-10	$NO[S] + [S] \rightleftharpoons N[S] + O[S]$	$CO[S] + O[S] \rightleftharpoons CO_2[S] + [S]$	$NO[S] + O[S] \rightleftharpoons NO_2[S] + [S]$
Form-11	$NO[S] + [S] \rightleftharpoons N[S] + O[S]$	$CO[S] + O[S] \rightleftharpoons CO_2[S] + [S]$	$NO_2[S] \rightleftharpoons NO_2 + [S]$
Form-12	$NO[S] + [S] \rightleftharpoons N[S] + O[S]$	$CO_2[S] \rightleftharpoons CO_2 + [S]$	$NO + [S] \rightleftharpoons NO[S]$
Form-13	$NO[S] + [S] \rightleftharpoons N[S] + O[S]$	$CO_2[S] \rightleftharpoons CO_2 + [S]$	$O_2 + 2[S] \rightleftharpoons 2O[S]$
Form-14	$NO[S] + [S] \rightleftharpoons N[S] + O[S]$	$CO_2[S] \rightleftharpoons CO_2 + [S]$	$NO[S] + O[S] \rightleftharpoons NO_2[S] + [S]$

Form-15	$NO[S] + [S] \rightleftharpoons N[S] + O[S]$	$CO_2[S] \rightleftharpoons CO_2 + [S]$	$NO_2[S] \rightleftharpoons NO_2 + [S]$

Table 5.5 Elementary reaction steps for 'Form-10'

Type of Reaction	Elementary Step	Kinetic/Equilibrium Constant
Adsorption	$CO + [S] \rightleftharpoons CO[S]$	K_{CO}^{ads}
	$NO + [S] \rightleftharpoons NO[S]$	K_{NO}^{ads}
	$O_2 + 2[S] \rightleftharpoons 2O[S]$	$K_{O_2}^{ads}$
Surface Reactions	$NO[S] + [S] \rightleftharpoons N[S] + O[S]$	k_{CO-NO}^{f}, k_{CO-NO}^{b}
	$CO[S] + O[S] \rightleftharpoons CO_2[S] + [S]$	k_{CO-O}^{f}, k_{CO-O}^{b}
	$N[S] + N[S] \rightleftharpoons N_2[S] + [S]$	K_{N-N}^{eq}
	$NO[S] + O[S] \rightleftharpoons NO_2[S] + [S]$	k_{NO-O}^{f}, k_{NO-O}^{b}
Desorption	$CO_2[S] \rightleftharpoons CO_2 + [S]$	$K_{CO_2}^{des}$
	$NO_2[S] \rightleftharpoons NO_2 + [S]$	$K_{NO_2}^{des}$
	$N_2[S] \rightleftharpoons N_2 + [S]$	$K_{N_2}^{des}$
Inert	$H_2O + [S] \rightleftharpoons H_2O[S]$	$K_{H_2O}^{ads}$

$$K_{CO}^{ads} = \frac{\theta_{CO}}{P_{CO}\,\theta} \tag{5.4}$$

$$\theta_{CO} = K_{CO}^{ads} P_{CO}\,\theta \tag{5.5}$$

$$K_{NO}^{ads} = \frac{\theta_{NO}}{P_{NO}\,\theta} \tag{5.6}$$

$$\theta_{NO} = K_{NO}^{ads} P_{NO}\,\theta \tag{5.7}$$

$$K_{H_2O}^{ads} = \frac{\theta_{H_2O}}{P_{H_2O}\,\theta} \tag{5.8}$$

$$\theta_{H_2O} = K_{H_2O}^{ads} P_{H_2O}\,\theta \tag{5.9}$$

Unlike CO, NO and H_2O, O_2 undergoes dissociative adsorption on the catalytic surface (see Table 5.5). Therefore, the relation for O_2 adsorption at equilibrium and θ_O are derived as shown in Eq. (5.10) and Eq. (5.11) respectively.

$$\mathrm{K}_{\mathrm{O}_2}^{\mathrm{ads}} = \frac{{\theta_{\mathrm{O}_2}}^2}{\mathrm{P}_{\mathrm{O}_2}\,\theta^2} \tag{5.10}$$

$$\theta_{\mathrm{O}_2} = \sqrt{\mathrm{K}_{\mathrm{O}_2}^{\mathrm{ads}}\mathrm{P}_{\mathrm{O}_2}}\theta \tag{5.11}$$

Similar to the adsorption relation at equilibrium, the relations for desorption of N_2, NO_2 and CO_2 at equilibrium from the catalyst surface can be derived as shown in Eq. (5.12) - (5.14) and by rearrangement of these terms, relations for the respective site coverage can be derived as shown in Eq. (5.15) - (5.17).

$$\mathrm{K}_{\mathrm{N}_2}^{\mathrm{des}} = \frac{\mathrm{P}_{\mathrm{N}_2}\theta}{\theta_{\mathrm{N}_2}} \tag{5.12}$$

$$\mathrm{K}_{\mathrm{NO}_2}^{\mathrm{des}} = \frac{\mathrm{P}_{\mathrm{NO}_2}\theta}{\theta_{\mathrm{NO}_2}} \tag{5.13}$$

$$\mathrm{K}_{\mathrm{CO}_2}^{\mathrm{des}} = \frac{\mathrm{P}_{\mathrm{CO}_2}\theta}{\theta_{\mathrm{CO}_2}} \tag{5.14}$$

$$\theta_{\mathrm{N}_2} = \frac{\mathrm{P}_{\mathrm{N}_2}\theta}{\mathrm{K}_{\mathrm{N}_2}^{\mathrm{des}}} \tag{5.15}$$

$$\theta_{\mathrm{NO}_2} = \frac{\mathrm{P}_{\mathrm{NO}_2}\theta}{\mathrm{K}_{\mathrm{NO}_2}^{\mathrm{des}}} \tag{5.16}$$

$$\theta_{\mathrm{CO}_2} = \frac{\mathrm{P}_{\mathrm{CO}_2}\theta}{\mathrm{K}_{\mathrm{CO}_2}^{\mathrm{des}}} \tag{5.17}$$

Finally, the site coverage of reaction intermediates like N species can be derived from its surface reaction equilibrium i.e., reaction between two adsorbed N species to form adsorbed N_2 species (refer Table 5.5). The reaction equilibrium relation for this surface reaction was derived as shown in Eq. (5.18).

Upon substituting θ_{N_2} in Eq. (5.18) with the relation derived in Eq. (5.15) and rearranging the terms, a relation for the site coverage of N species (θ_N) in terms of P_{N_2} was established as shown in Eq. (5.19). Finally, all the site coverage relations derived here are enlisted in Table 5.6.

$$\mathrm{K}^{\mathrm{eq}}_{\mathrm{N-N}} = \frac{\theta_{\mathrm{N_2}}\ \theta}{{\theta_{\mathrm{N}}}^2} \tag{5.18}$$

$$\theta_{\mathrm{N}} = \sqrt{\frac{\mathrm{P_{N_2}}}{\mathrm{K}^{\mathrm{des}}_{\mathrm{N_2}}\mathrm{K}^{\mathrm{eq}}_{\mathrm{N-N}}}}\ \theta \tag{5.19}$$

Table 5.6 List of site coverage relations based on assumptions made for 'Form-10'

Elementary Step	Site Coverage Relation
$\mathrm{NO} + [\mathrm{S}] \rightleftharpoons \mathrm{NO[S]}$	$\theta_{\mathrm{NO}} = \mathrm{P_{NO}K^{ads}_{NO}}\theta$
$\mathrm{O_2} + 2[\mathrm{S}] \rightleftharpoons 2\mathrm{O[S]}$	$\theta_{\mathrm{O}} = \sqrt{\mathrm{K^{ads}_{O_2}\ P_{O_2}}}\ \theta$
$\mathrm{CO} + [\mathrm{S}] \rightleftharpoons \mathrm{CO[S]}$	$\theta_{\mathrm{CO}} = \mathrm{P_{CO}K^{ads}_{CO}}\theta$
$\mathrm{N[S]} + \mathrm{N[S]} \rightleftharpoons \mathrm{N_2[S]} + [\mathrm{S}]$	$\theta_{\mathrm{N}} = \sqrt{\frac{\mathrm{P_{N_2}}}{\mathrm{K^{des}_{N_2}K^{eq}_5}}}\,\theta$
$\mathrm{N_2[S]} \rightleftharpoons \mathrm{N_2} + [\mathrm{S}]$	$\theta_{\mathrm{N_2}} = \frac{\mathrm{P_{N_2}}\theta}{\mathrm{K^{des}_{N_2}}}$
$\mathrm{CO_2[S]} \rightleftharpoons \mathrm{CO_2} + [\mathrm{S}]$	$\theta_{\mathrm{CO_2}} = \frac{\mathrm{P_{CO_2}}\theta}{\mathrm{K^{des}_{CO_2}}}$
$\mathrm{NO_2[S]} \rightleftharpoons \mathrm{NO_2} + [\mathrm{S}]$	$\theta_{\mathrm{NO_2}} = \frac{\mathrm{P_{NO_2}}\theta}{\mathrm{K^{des}_{NO_2}}}$
$\mathrm{H_2O} + [\mathrm{S}] \rightleftharpoons \mathrm{H_2O[S]}$	$\theta_{\mathrm{H_2O}} = \mathrm{K^{ads}_{H_2O}\ P_{H_2O}}\,\theta$

Step 2: Active Site Balance

In LHHW kinetics, it is assumed that the number of active sites in the catalyst is constant throughout the reaction. Therefore, a site balance relation can be established as shown in Eq. (5.20). However, each of these site coverage terms can be substituted by their corresponding relation with partial pressures of reactant and product components in the reaction system. After this substitution,

the site balance expression evolves into Eq. (5.21). This expression can be used to derive the relation for the fraction of vacant sites (θ) in terms of partial pressures as shown in Eq. (5.22).

$$\theta + \theta_{CO} + \theta_{NO} + \theta_{N} + \theta_{O} + \theta_{CO_2} + \theta_{N_2} + \theta_{NO_2} + \theta_{H_2O} = 1 \tag{5.20}$$

$$\theta + \mathrm{K}_{\mathrm{CO}}^{\mathrm{ads}}\mathrm{P}_{\mathrm{CO}}\theta + \mathrm{K}_{\mathrm{NO}}^{\mathrm{ads}}\mathrm{P}_{\mathrm{NO}}\theta + \sqrt{\frac{\mathrm{P}_{\mathrm{N_2}}}{\mathrm{K}_{\mathrm{N_2}}^{\mathrm{des}}\mathrm{K}_{\mathrm{N-N}}^{\mathrm{eq}}}}\,\theta + \sqrt{\mathrm{K}_{\mathrm{O_2}}^{\mathrm{ads}}\mathrm{P}_{\mathrm{O_2}}}\theta + \frac{\mathrm{P}_{\mathrm{CO_2}}\theta}{\mathrm{K}_{\mathrm{CO_2}}^{\mathrm{des}}} + \frac{\mathrm{P}_{\mathrm{N_2}}\theta}{\mathrm{K}_{\mathrm{N_2}}^{\mathrm{des}}} + \frac{\mathrm{P}_{\mathrm{NO_2}}\theta}{\mathrm{K}_{\mathrm{NO_2}}^{\mathrm{des}}} + \mathrm{K}_{\mathrm{H_2O}}^{\mathrm{ads}}\mathrm{P}_{\mathrm{H_2O}}\,\theta = 1 \tag{5.21}$$

$$\theta = \frac{1}{\left(1 + \mathrm{K}_{\mathrm{CO}}^{\mathrm{ads}}\mathrm{P}_{\mathrm{CO}} + \mathrm{K}_{\mathrm{NO}}^{\mathrm{ads}}\mathrm{P}_{\mathrm{NO}} + \sqrt{\frac{\mathrm{P}_{\mathrm{N_2}}}{\mathrm{K}_{\mathrm{N_2}}^{\mathrm{des}}\mathrm{K}_{\mathrm{N-N}}^{\mathrm{eq}}}} + \sqrt{\mathrm{K}_{\mathrm{O_2}}^{\mathrm{ads}}\mathrm{P}_{\mathrm{O_2}}} + \frac{\mathrm{P}_{\mathrm{CO_2}}}{\mathrm{K}_{\mathrm{CO_2}}^{\mathrm{des}}} + \frac{\mathrm{P}_{\mathrm{N_2}}}{\mathrm{K}_{\mathrm{N_2}}^{\mathrm{des}}} + \frac{\mathrm{P}_{\mathrm{NO_2}}}{\mathrm{K}_{\mathrm{NO_2}}^{\mathrm{des}}} + \mathrm{K}_{\mathrm{H_2O}}^{\mathrm{ads}}\mathrm{P}_{\mathrm{H_2O}}\right)} \tag{5.22}$$

Step 3: Derivation of Reaction Rate Expressions

The reaction rate expressions are derived from the rate-limiting reactions. In this case, the expressions for the rate of conversion of CO into CO_2 (r_{CO_2}), rate of conversion of NO into N_2 (r_N) and rate of conversion of NO into NO_2 (r_{NO_2}) are shown in Eq. (5.23), Eq. (5.24) and Eq. (5.25) respectively. In these equations, the site coverage by different components (θ_i where i = reactant/intermediate/product component) and the fraction of vacant site (θ) can be substituted by their relations in terms of partial pressure of the components in the system as enlisted in Table 5.6. Therefore, the final form the reaction rate expressions are shown in Eq. (5.26) – Eq. (5.28).

$$\mathrm{r}_{\mathrm{CO_2}} = \mathrm{k}_{\mathrm{CO-O}}^{\mathrm{f}}\theta_{\mathrm{CO}}\theta_{\mathrm{O}} - \mathrm{k}_{\mathrm{CO-O}}^{\mathrm{b}}\theta_{\mathrm{CO_2}}\theta \tag{5.23}$$

$$\mathrm{r}_{\mathrm{N}} = \mathrm{k}_{\mathrm{CO-NO}}^{\mathrm{f}}\theta_{\mathrm{NO}}\theta - \mathrm{k}_{\mathrm{CO-NO}}^{\mathrm{b}}\theta_{\mathrm{N}}\theta_{\mathrm{O}} \tag{5.24}$$

$$r_{NO_2} = k^{f}_{NO-O}\theta_{NO}\theta_{O} - k^{b}_{NO-O}\theta_{NO_2}\theta \tag{5.25}$$

$$r_{CO_2} = \frac{\left(k^{f}_{CO-O}K^{ads}_{CO}\sqrt{K^{ads}_{O_2}\,P_{O_2}}P_{CO} - \frac{k^{b}_{CO-O}}{K^{des}_{CO_2}}P_{CO_2}\right)}{\left(1 + P_{CO}K^{ads}_{CO} + P_{NO}K^{ads}_{NO} + \sqrt{\frac{P_{N_2}}{K^{des}_{N_2}K^{eq}_{N-N}}} + \sqrt{K^{ads}_{O_2}\,P_{O_2}} + \frac{P_{CO_2}}{K^{des}_{CO_2}} + \frac{P_{N_2}}{K^{des}_{N_2}} + \frac{P_{NO_2}}{K^{des}_{NO_2}} + K^{ads}_{H_2O}\,P_{H_2O}\right)^2} \tag{5.26}$$

$$r_{N} = \frac{\left(k^{f}_{CO-NO}K^{ads}_{NO}P_{NO} - k^{b}_{CO-NO}\sqrt{\frac{K^{ads}_{O_2}}{K^{des}_{N_2}K^{eq}_{N-N}}}\,\sqrt{P_{N_2}P_{O_2}}\right)}{\left(1 + P_{CO}K^{ads}_{CO} + P_{NO}K^{ads}_{NO} + \sqrt{\frac{P_{N_2}}{K^{des}_{N_2}K^{eq}_{N-N}}} + \sqrt{K^{ads}_{O_2}\,P_{O_2}} + \frac{P_{CO_2}}{K^{des}_{CO_2}} + \frac{P_{N_2}}{K^{des}_{N_2}} + \frac{P_{NO_2}}{K^{des}_{NO_2}} + K^{ads}_{H_2O}\,P_{H_2O}\right)^2} \tag{5.27}$$

$$r_{NO_2} = \frac{\left(k^{f}_{NO-O}\sqrt{K^{ads}_{O_2}}K^{ads}_{NO}P_{NO}\sqrt{P_{O_2}} - \frac{k^{b}_{NO-O}}{K^{des}_{NO_2}}P_{NO_2}\right)}{\left(1 + P_{CO}K^{ads}_{CO} + P_{NO}K^{ads}_{NO} + \sqrt{\frac{P_{N_2}}{K^{des}_{N_2}K^{eq}_{N-N}}} + \sqrt{K^{ads}_{O_2}\,P_{O_2}} + \frac{P_{CO_2}}{K^{des}_{CO_2}} + \frac{P_{N_2}}{K^{des}_{N_2}} + \frac{P_{NO_2}}{K^{des}_{NO_2}} + K^{ads}_{H_2O}\,P_{H_2O}\right)^2} \tag{5.28}$$

In order to further simplify these reaction rate equations, the kinetic/adsorption/ desorption constants associated with each term in the rate expression can be clubbed together as a single term α_i where i = 1,2... n. Further, α_i is a function of reaction temperature T according to the Arrhenius relation as shown in Eq. (5.29). The pre-exponential factor A_i and activation energy (or heat of adsorption or desorption) Ea_i for each α_i term is unknown and therefore needs to be determined by regression. In this case, each set of reaction rate expressions has 28 (= 14 × 2) such unknown parameters in total.

The substitution of α_i terms with the function of A_1, Ea_1 and T ($f\left(A_i, Ea_i, T\right)$) for 'Form-10' reaction rate expressions are shown in Eq. (5.30) – Eq. (5.32).

$$\alpha_{\mathrm{i}} = \mathrm{A_i exp}\left(\frac{-\mathrm{Ea_i}}{\mathrm{RT}}\right) \tag{5.29}$$

$$\begin{aligned} \mathrm{r_N} = \frac{\left(\mathrm{f\left(A_1, Ea_1, T\right) P_{NO} - f\left(A_2, Ea_2, T\right)\ \sqrt{P_{N_2} P_{O_2}}}\right)}{\Bigg(1 + \mathrm{f\left(A_3, Ea_3, T\right) P_{CO} + f\left(A_4, Ea_4, T\right) P_{NO} + f\left(A_5, Ea_5, T\right)}\sqrt{\mathrm{P_{N_2}}} + \\ \mathrm{f\left(A_6, Ea_6, T\right)}\sqrt{\mathrm{P_{O_2}}}\ \mathrm{+ f\left(A_7, Ea_7, T\right) P_{CO_2} + f\left(A_8, Ea_8, T\right) P_{N_2}} \\ \mathrm{+ f\left(A_9, Ea_9, T\right) P_{NO_2} + f\left(A_{10}, Ea_{10}, T\right)\ P_{H_2O}}\Bigg)^2 \end{aligned} \tag{5.30}$$

$$\begin{aligned} \mathrm{r_{NO_2}} = \frac{\left(\mathrm{f\left(A_{11}, Ea_{11}, T\right) P_{NO}}\sqrt{\mathrm{P_{O_2}}} - \mathrm{f\left(A_{12}, Ea_{12}, T\right) P_{NO_2}}\right)}{\Bigg(1 + \mathrm{f\left(A_3, Ea_3, T\right) P_{CO} + f\left(A_4, Ea_4, T\right) P_{NO} + f\left(A_5, Ea_5, T\right)}\sqrt{\mathrm{P_{N_2}}} + \\ \mathrm{f\left(A_6, Ea_6, T\right)}\sqrt{\mathrm{P_{O_2}}}\ \mathrm{+ f\left(A_7, Ea_7, T\right) P_{CO_2} + f\left(A_8, Ea_8, T\right) P_{N_2}} \\ \mathrm{+ f\left(A_9, Ea_9, T\right) P_{NO_2} + f\left(A_{10}, Ea_{10}, T\right)\ P_{H_2O}}\Bigg)^2 \end{aligned} \tag{5.31}$$

$$\begin{aligned} \mathrm{r_{CO_2}} = \frac{\left(\mathrm{f\left(A_{13}, Ea_{13}, T\right)}\sqrt{\mathrm{P_{O_2}}}\mathrm{P_{CO} - f\left(A_{14}, Ea_{14}, T\right) P_{CO_2}}\right)}{\Bigg(1 + \mathrm{f\left(A_3, Ea_3, T\right) P_{CO} + f\left(A_4, Ea_4, T\right) P_{NO} + f\left(A_5, Ea_5, T\right)}\sqrt{\mathrm{P_{N_2}}} + \\ \mathrm{f\left(A_6, Ea_6, T\right)}\sqrt{\mathrm{P_{O_2}}}\ \mathrm{+ f\left(A_7, Ea_7, T\right) P_{CO_2} + f\left(A_8, Ea_8, T\right) P_{N_2}} \\ \mathrm{+ f\left(A_9, Ea_9, T\right) P_{NO_2} + f\left(A_{10}, Ea_{10}, T\right)\ P_{H_2O}}\Bigg)^2 \end{aligned} \tag{5.32}$$

5.3.4 Integral Packed-Bed Reactor (PBR) Model

For the determination of the unknown model parameters by regression, the mole balance equations for an integral steady-state one dimensional isothermal packed-bed reactor (PBR) model were considered. The mole balance equation

for steady-state PBR model is shown in Eq. (5.33) where F_i is the molar flow rate of component i (mol.s^{-1}), W is the catalyst weight (g) and r_i is reaction rate of component i (mol.s^{-1}.g^{-1}).

$$\frac{\mathrm{dF_i}}{\mathrm{dW}} = \mathrm{r_i} \tag{5.33}$$

It should be noted that for simplicity of the reactor model, temperature gradient and pressure drop across the reactor column have not been considered: reactor isothermal and isobaric. Further, to implement this integral reactor model, a system of differential equations was developed. The methodology followed in this work to determine the differential equations is according to that reported by Fogler et al. The authors suggest deriving the mole balance equations in terms of molar flow rates of the reaction components instead of molar conversions for multiple reaction systems.

Step 1: Mole Balance

Based on the mole balance equation for the PBR model (see Eq. (5.33)), the mole balance for the components of interest can be derived as shown in Eq. (5.34) – Eq. (5.38). In these equations, dF_i is the infinitesimal change in molar flow rate of the component i (mol.s^{-1}) for infinitesimal catalyst weight, dW (g) and r_i^{net} is the net reaction rate in terms of component i (mol.s^{-1}.g^{-1}).

$$\frac{\mathrm{dF_{CO_2}}}{\mathrm{dW}} = \mathrm{r_{CO_2}^{net}} \tag{5.34}$$

$$\frac{\mathrm{dF_{N_2}}}{\mathrm{dW}} = \mathrm{r_{N_2}^{net}} \tag{5.35}$$

$$\frac{\mathrm{dF_{NO_2}}}{\mathrm{dW}} = \mathrm{r_{NO_2}^{net}} \tag{5.36}$$

$$\frac{\mathrm{dF_{NO}}}{\mathrm{dW}} = \mathrm{r_{NO}^{net}} \tag{5.37}$$

$$\frac{\mathrm{dF_{CO}}}{\mathrm{dW}} = \mathrm{r_{CO}^{net}} \tag{5.38}$$

Step 2: Net Rate Laws

The net rate laws for each of the components are determined by respecting their stoichiometry in the corresponding reaction equations (refer Eq. (5.1)–(5.3)). The net rate laws for each of the components are shown in Eq. (5.39)– Eq. (5.43). In these equations, it should be noted that the negative sign indicates that the component is consumed in the system.

$$\mathrm{r}_{\mathrm{NO}}^{\mathrm{net}} = -\left(\mathrm{r}_{\mathrm{N}} + \mathrm{r}_{\mathrm{NO_2}}\right) \tag{5.39}$$

$$\mathrm{r}_{\mathrm{CO}}^{\mathrm{net}} = -\left(\mathrm{r}_{\mathrm{N}} + \mathrm{r}_{\mathrm{CO_2}}\right) \tag{5.40}$$

$$\mathrm{r}_{\mathrm{NO_2}}^{\mathrm{net}} = \mathrm{r}_{\mathrm{NO_2}} \tag{5.41}$$

$$\mathrm{r}_{\mathrm{N_2}}^{\mathrm{net}} = 0.5 \times \mathrm{r}_{\mathrm{N}} \tag{5.42}$$

$$\mathrm{r}_{\mathrm{CO_2}}^{\mathrm{net}} = \left(\mathrm{r}_{\mathrm{N}} + \mathrm{r}_{\mathrm{CO_2}}\right) \tag{5.43}$$

Step 3: Stoichiometry

The partial pressure of different components (P_i) at the reactor outlet can be determined by the ratio of the molar flow of the component i at the reactor outlet (F_i) to the total molar flow rate at the reactor outlet (F_T) multiplied by the total pressure of the reaction system (P_o) (see Eq. (5.44)). In this study, the reaction pressure is 1 bar. Moreover, F_T can be calculated by summing up the molar flow rates of the reaction components at the reactor outlet as shown in Eq. (5.45).

$$\mathrm{P_i} = \frac{\mathrm{F_i}}{\mathrm{F_T}} \times \mathrm{P_o} \tag{5.44}$$

$$\mathrm{F_T} = \sum_{\mathrm{i=1}}^{\mathrm{N_{comp}}} \mathrm{F_i} \tag{5.45}$$

where, $\mathrm{N_{comp}}$ = number of components in the reaction system

This system of differential equations was solved for different sets of experimental data and α_i values using for ODE solver in MATLAB 2020a software coupled with a parameter regression routine to determine the unknown α_i model parameters. The strategy for the parameter regression is discussed in the next section.

5.3.5 Parameter Regression

For the determination of the unknown model parameters, an objective function $(\mathrm{F_{obj}})$, sum of the square of difference between the experimental $(\mathrm{x_{i,j}}^{\mathrm{exp}})$ and calculated $(\mathrm{x_{i,j}}^{\mathrm{cal}})$ molar conversions for NO and CO (see Eq. (5.46)), was minimized. In this equation, N_{exp} represents the total number of sets of experimental data. Further, for the determination of the model parameters, the global optimization toolbox in MATLAB 2020a was utilized. According to the documentation of MATLAB, the general pattern search algorithm (the inbuilt routine is called '*patternsearch*') was preferred over other global optimization solvers.

$$\mathrm{F_{obj}} = \sum_{\mathrm{i=1}}^{2} \sum_{\mathrm{j=1}}^{\mathrm{N_{exp}}} \left(\mathrm{x_{i,j}}^{\mathrm{exp}} - \mathrm{x_{i,j}}^{\mathrm{cal}} \right)^2 \tag{5.46}$$

To perform this optimization, a MATLAB script file containing the commands to retrieve and store data in external Excel files, execute user-defined functions for objective function calculation and optimization solver. The workflow of this entire routine is shown in Figure 5.10. Moreover, the different parameters used for the optimization routine are enlisted in Table 5.7. The experimental dataset considered for the parameter regression was for the reaction temperature range of 200-400°C (this accounts for 70 sets of experimental data) because both NO and CO conversion activity was observed in this reaction temperature range. Moreover, the upper and lower bounds for the model parameters were assumed based on the kinetic data available for different reactions over catalysts with material composition similar to that considered in this thesis. Furthermore, the 'Mesh Tolerance' and 'Maximum Function Evaluations' in the solver options were altered from its default value to have more precise regressed

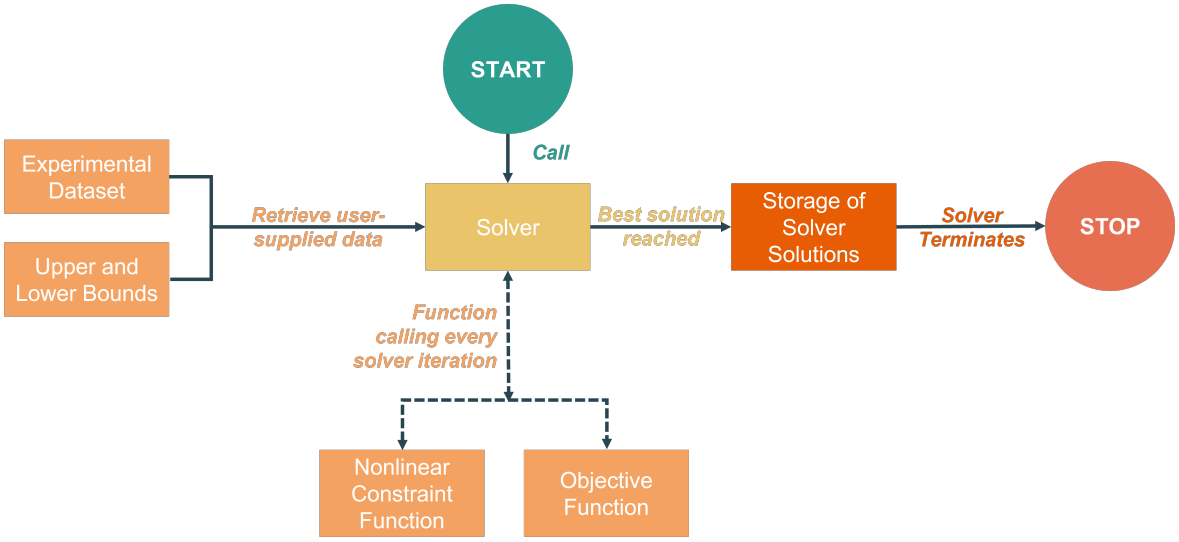

Figure 5.10 Workflow diagram for the parameter regression routine using MATLAB 2020a

value and increase the probability to achieve convergence respectively.

The regressions were performed for each of the kinetic model forms as enlisted in Table 5.4. The correlation between the experimental and calculated values for molar conversions of CO and NO (calculated by coefficient of

Table 5.7 Different parameters in the optimization routine

Parameter	Description
Experimental Dataset	Data for reaction temperature range 200-400°C
Parameter Bounds	Lower Bound: 1×10^{-30} Upper Bound:1×10^{3} (for pre-exponential factors A_i) and 1×10^{5} (for $\left(\frac{\text{activation energy (Ea)}}{\text{Gas constant (R)}}\right)$)
Number of parameters	28
Solver	patternsearch
Solver Options [a]	Mesh tolerance: 1×10^{-8} (default: 1×10^{-6}) Maximum function evaluations: 1×10^{6} (default: 2000 $\times$ number of parameters)

[a] The rest of the solver options are set to the default values. Therefore, these values are not mentioned in this table but can be found in the MATLAB 2020a documentation.

determination R^2: refer Eq. (5.47)) are enlisted in Table 5.7. The regression for Form 2, 5- 7, 13 and 15 could not be performed because the solver could not minimize the objective function further from the objective function value at the initial point. Therefore, correlation values for these forms of kinetic model were not considered and thus, are not mentioned in Table 5.7. From this table, it can be seen that Form-1, Form-10 and Form-12 have better fitting to the experimental molar conversion of CO and NO data than rest of the kinetic model forms. However, upon further investigation regarding the correlation between the experimental and calculated data for partial pressures of NO_2 and N_2, it was found that both Form-1 and Form-8 showed the best fitting among all the forms of kinetic models. Moreover, Form-1 showed better fitting to experimental data for CO conversion than Form-8 and therefore, Form-1 seems to be the choice of kinetic model. This means that both adsorption of CO and NO along with surface decomposition of NO into atomic N and O species are the rate-limiting steps in the reaction system.

$$R^2 = 1 - \frac{\sum_{i=1}^{N_{exp}} \left(x_i^{exp} - x_i^{cal}\right)^2}{\sum_{i=1}^{Nexp} \left(x_i^{exp} - \frac{1}{N_{exp}} \sum_{i=1}^{N_{exp}} x_i^{exp}\right)^2} \tag{5.47}$$

where,
x_i^{exp}, x_i^{cal} = experimental ('exp') and calculated ('cal') molar conversion values
N_{exp} = number of sets of experimental data

The reaction rate expression for the kinetic model Form-1 are shown in Eq. (5.48)– Eq. (5.50).The comparison between the calculated and experimental CO conversion and partial pressures of N_2 and NO_2 for Form-1 are shown in Figure 5.11. Moreover, the regressed values for the different model parameters are shown in Table 5.9. The solver assigned some model parameters, especially frequency coefficients (A_i), to the boundary values while the rest are regressed within the bounds to minimize the objective function (refer Eq. (5.46)).

Table 5.8 Coefficient of Determination (R^2) for different kinetic models

Kinetic Model Form	Correlation of Determination (R^2)			
	Conversion of NO (X_{NO})	Conversion of CO (X_{CO})	Partial Pressure	
			P_{N_2}	P_{NO_2}
Form-1	0.90	0.92	0.85	0.79
Form-3	0.89	0.91	0.20	0.79
Form-4	0.87	0.91	0.83	0.19
Form-8	0.85	0.89	0.75	0.83
Form-9	0.90	0.84	0.82	0.42
Form-10	0.90	0.93	0.07	0.82
Form-11	0.86	0.89	0.07	0.79
Form-12	0.90	0.93	0.46	0.85
Form-14	0.59	0.44	0.54	0.49

$$r_N = \frac{\left(f(A_1, Ea_1, T)\left(\frac{P_{NO_2}}{\sqrt{P_{O_2}}}\right) - f(A_2, Ea_2, T)\ \sqrt{P_{N_2}P_{O_2}}\right)}{\left(1 + f(A_3, Ea_3, T)\left(\frac{P_{CO_2}}{\sqrt{P_{O_2}}}\right) + f(A_4, Ea_4, T)\left(\frac{P_{NO_2}}{\sqrt{P_{O_2}}}\right) + f(A_5, Ea_5, T)\sqrt{P_{N_2}} + f(A_6, Ea_6, T)\sqrt{P_{O_2}} + f(A_7, Ea_7, T)P_{CO_2} + f(A_8, Ea_8, T)P_{N_2} + f(A_9, Ea_9, T)P_{NO_2} + f(A_{10}, Ea_{10}, T)\ P_{H_2O}\right)^2} \quad (5.48)$$

$$r_{NO_2} = \frac{\left(f(A_{11}, Ea_{11}, T)P_{NO} - f(A_{12}, Ea_{12}, T)\left(\frac{P_{NO_2}}{\sqrt{P_{O_2}}}\right)\right)}{\left(1 + f(A_3, Ea_3, T)\left(\frac{P_{CO_2}}{\sqrt{P_{O_2}}}\right) + f(A_4, Ea_4, T)\left(\frac{P_{NO_2}}{\sqrt{P_{O_2}}}\right) + f(A_5, Ea_5, T)\sqrt{P_{N_2}} + f(A_6, Ea_6, T)\sqrt{P_{O_2}} + f(A_7, Ea_7, T)P_{CO_2} + f(A_8, Ea_8, T)P_{N_2} + f(A_9, Ea_9, T)P_{NO_2} + f(A_{10}, Ea_{10}, T)\ P_{H_2O}\right)} \quad (5.49)$$

$$r_{CO_2} = \frac{\left(f(A_{13}, Ea_{13}, T)\, P_{CO} - f(A_{14}, Ea_{14}, T)\left(\frac{P_{CO_2}}{\sqrt{P_{O_2}}}\right)\right)}{\left(1 + f(A_3, Ea_3, T)\left(\frac{P_{CO_2}}{\sqrt{P_{O_2}}}\right) + f(A_4, Ea_4, T)\left(\frac{P_{NO_2}}{\sqrt{P_{O_2}}}\right) + f(A_5, Ea_5, T)\sqrt{P_{N_2}} + f(A_6, Ea_6, T)\sqrt{P_{O_2}} + f(A_7, Ea_7, T)\, P_{CO_2} + f(A_8, Ea_8, T)\, P_{N_2} + f(A_9, Ea_9, T)\, P_{NO_2} + f(A_{10}, Ea_{10}, T)\; P_{H_2O}\right)} \quad (5.50)$$

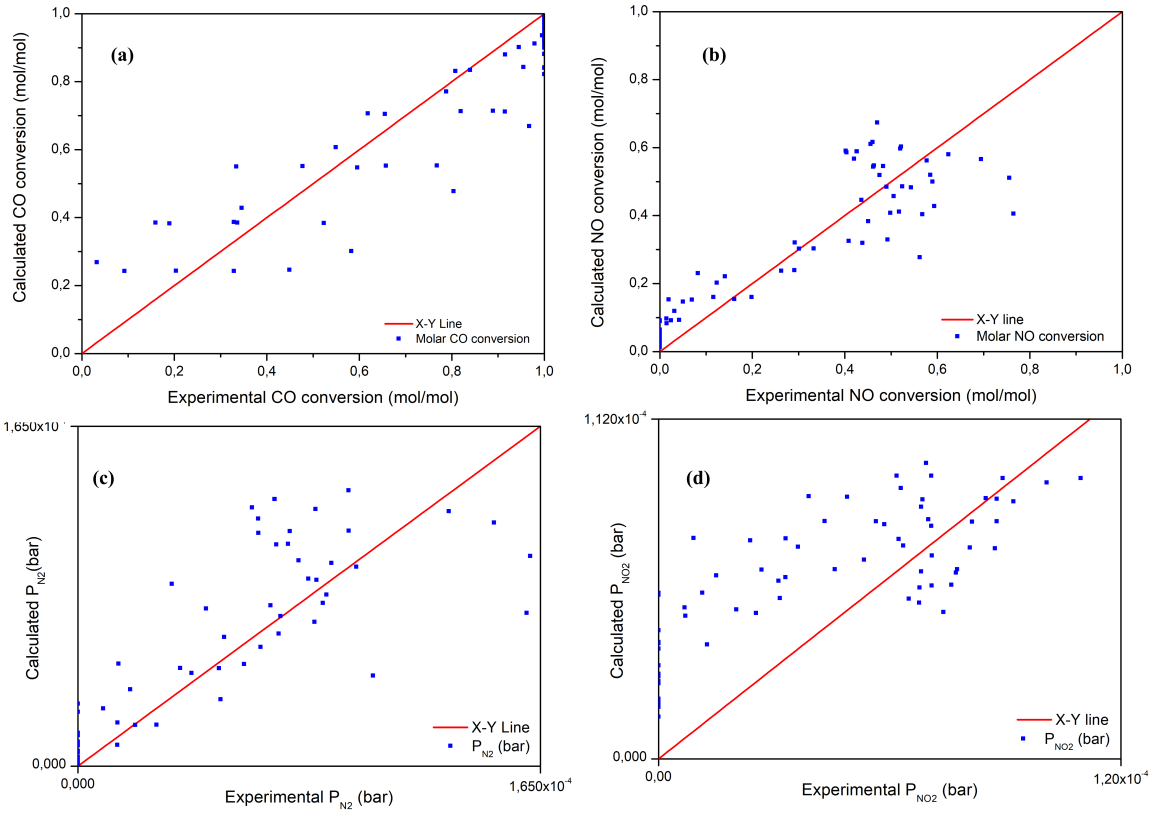

Figure 5.11 Correlation between the experimental and calculated values for (a) CO conversion (b) total NO conversion (c) Partial pressure of N_2 and (d) Partial pressure of NO_2 according to kinetic model Form-1

Table 5.9 Regressed values of model parameters for kinetic model Form-1.

Parameter	Regressed Value (unit)
A_1	9.99×10^2 ($bar^{0.5}$) [a]
Ea_1	63 ($kJ.mol^{-1}$)
A_2	4.80×10^2 (bar)
Ea_2	91 ($kJ.mol^{-1}$)
A_3	7.79×10^2 ($bar^{0.5}$)
Ea_3	776 ($kJ.mol^{-1}$)
A_4	1.3×10^2 ($bar^{0.5}$)
Ea_4	473 ($kJ.mol^{-1}$)
A_5	4.72×10^2 ($bar^{0.5}$)
Ea_5	554 ($kJ.mol^{-1}$)
A_6	9.99×10^2 ($bar^{0.5}$) [a]
Ea_6	48 ($kJ.mol^{-1}$)
A_7	9.99×10^2 ($bar^{0.5}$) [a]
Ea_7	47 ($kJ.mol^{-1}$)
A_8	9.99×10^2 ($bar^{0.5}$) [a]
Ea_8	11 ($kJ.mol^{-1}$)
A_9	9.97×10^2 ($bar^{0.5}$) [a]
Ea_9	585 ($kJ.mol^{-1}$)
A_{10}	6.54×10^2 ($bar^{0.5}$)
Ea_{10}	573 ($kJ.mol^{-1}$)

A_{11}	1×10^3 ($bar^{0.5}$) [a]
Ea_{11}	76 ($kJ.mol^{-1}$)
A_{12}	8.86×10^2 ($bar^{0.5}$)
Ea_{12}	72 ($kJ.mol^{-1}$)
A_{13}	9.75×10^2 ($bar^{0.5}$) [a]
Ea_{13}	54 ($kJ.mol^{-1}$)
A_{14}	7.85×10^2 ($bar^{0.5}$)
Ea_{14}	104 ($kJ.mol^{-1}$)

[a] These values are either near to or at the boundary values

In Figure 5.11 (a), it can be seen that the model shows a good fit to both the low (experimental $X_{CO} \leq 0.2$) and high (experimental $X_{CO} \geq 0.2$) the molar conversion of CO values. Moreover, in Figure 5.11 (b), it can be seen that the model shows a good fit to the molar conversion values for NO until experimental $X_{NO} = 0.6$. For experimental $X_{NO} \geq 0.6$, the model overestimates for some experimental points while underestimates for the others. Furthermore, in Figure 5.11 (c), the model shows a good estimation of the partial pressure of N_2 for experimental $P_{N_2} \leq 70$ ppm. For 70 ppm $\leq$ experimental $P_{N_2} \leq 130$ ppm and experimental $P_{N_2} \geq 130$ ppm, the model overestimates and underestimates the partial pressure values respectively. Finally, in Figure 5.11 (d), the model shows good estimation of experimental values for partial pressure of NO_2 (P_{NO_2}) for $P_{NO_2} \geq 100\text{ppm}$. However, the model overestimates the partial pressure values for $P_{NO_2} \leq 100\text{ppm}$. To improve the model response, additional adsorption isotherm measurements for certain reactant gases like CO, NO and CO_2 need to be performed to determine the corresponding pre-exponential factors and heat of adsorption over Co_4Cu_2Al-CO_2-400 catalyst. The results will decrease the number of model parameters to regress thereby improving the solver solution for the parameter values.

In Table 5.9, most of the activation energy terms are within the range of 0-110 $kJ.mol^{-1}$. However, certain activation energy terms like Ea_3 (related

to θ_{CO}), Ea_4 (related to θ_{NO}), Ea_5 (related to θ_{N}), Ea_9 (related to θ_{NO_2}) and Ea_{10}(related to θ_{H_2O}) have values higher than 500 kJ.mol^{-1} which is generally not the case for catalytic processes. Therefore, it is important to choose right boundary values for these parameters and re-run the objective function routine to obtain sensible values for all the model parameters, especially for the ones mentioned in this section.

5.4 Conclusion

In the first section of this chapter, the methodology of synthesis of the LDH form of the best performing catalyst, Co_4Cu_2Al-CO_2-400, was described and the synthesis protocol was compared with that at the small-scale. For the synthesis in the least number of batches so as to reduce the probability of change in the material properties, the concentration of material precursors and concentration of NaOH for the pH control of the resulting solution and their corresponding were adapted. Moreover, sample from each batch of synthesis was characterized under XRD and was found to be similar to each other indicating that no change in the material properties occurred between the two batches of syntheses. Furthermore, the material was shaped in the form of extrudes and dried for several days. These extrudes are planned to be used at a semi-pilot scale setup.

In the second section of this chapter, the influence of reactant gas composition at the reactor inlet on the corresponding catalytic performance was recorded. Only one gas component was varied at a time and the corresponding catalytic activity was recorded. The results showed that the catalytic activity varied with the change in the feed gas composition except for NO which was probably due to short range of variation in its concentration. Finally, a set of 133 experimental data was recorded in total which was used as the experimental dataset for the parameter regression in the kinetic model.

In the last section of this chapter, kinetic model based on LHHW kinetics was developed for the reaction system. Based on the different reaction mechanisms for this reaction system reported in the literature, 15 different sets of reaction rate expressions were derived. Moreover, 28 model parameters in each of the kinetic model form were determined by non-linear regression using general pattern search algorithm in MATLAB 2020a over a set of ordinary differ-

ential equations derived based on a one-dimensional isothermal packed-backed reactor model and 70 (out of 133) set of experimental data. Furthermore, the correlation between the experimental and calculated values of molar conversions of NO and CO and partial pressures of N_2 and NO_2, it was found that Form-1 i.e., adsorption steps of CO and NO and surface decomposition of NO into atomic N and O species as the rate-limiting steps, showed the best fitting to the experimental data. However, re-running the objective function routine with right boundary values for the parameters is recommended to obtain some sensible values for the model parameters which could possibly improve the fitting of the calculated values to the experimental values.

References

[1] D. Panayotov, L. Dimitrov, M. Khristova, L. Petrov, Reduction of nitric oxide with carbon monoxide on the surface of copper-containing catalysts based on aluminophosphates , silicoaluminosulphates and ZSM-5 zeolite, 6 (1995) 61–78.

[2] M. Fernandez-Garcia, M. Alvarez, I. Rodriguez-Ramos, A. Guerrero-Ruiz, G.L. Haller, New insights on the mechanism of the NO reduction with CO over alumina-supported copper catalysts, J. Phys. Chem. 99 (1995) 16380–16382. https://doi.org/10.1021/j100044a027.

[3] Y. Fu, Y. Tian, P. Lin, A low-temperature IR spectroscopic study of selective adsorption of NO and CO on CuO/γ-Al_2O_3, J. Catal. 132 (1991) 85–91. https://doi.org/10.1016/0021-9517(91)90249-4.

[4] W.N.R.W. Isahak, Z.A.C. Ramli, M.W. Ismail, K. Ismail, R.M. Yusop, M.W.M. Hisham, M.A. Yarmo, Adsorption-desorption of CO_2 on different type of copper oxides surfaces: Physical and chemical attractions studies, J. CO2 Util. 2 (2013) 8–15.
https://doi.org/10.1016/j.jcou.2013.06.002.

[5] L. Wang, X. Cheng, Z. Wang, C. Ma, Y. Qin, Investigation on Fe-Co binary metal oxides supported on activated semi-coke for NO reduction by CO, Appl. Catal. B Environ. 201 (2017) 636–651.
https://doi.org/10.1016/j.apcatb.2016.08.021.

[6] X. Cheng, X. Zhang, D. Su, Z. Wang, J. Chang, C. Ma, NO reduction by CO over copper catalyst supported on mixed CeO_2 and Fe_2O_3: Catalyst design and activity test, Appl. Catal. B Environ. 239 (2018) 485–501. https://doi.org/10.1016/j.apcatb.2018.08.054.

[7] M. Si, B. Shen, L. Liu, H. Zhang, W. Zhou, J. Wang, X. Zhang, Z. Zhang, C. Wu, Catalytic oxidation of NO over MnO: X-CoO_x/TiO_2 in the presence of a low ratio of O_3/NO: Activity and mechanism, RSC Adv. 10 (2020) 24493–24506. https://doi.org/10.1039/d0ra04129g.

[8] T.T. Yang, H.T. Bi, X. Cheng, Effects of O_2, CO_2 and H_2O on NO_x adsorption and selective catalytic reduction over Fe/ZSM-5, Appl. Catal. B Environ. 102 (2011) 163–171. https://doi.org/10.1016/j.apcatb.2010.11.038.

[9] H. Wang, S. Dong, Y. Qiao, Z. Qu, Effect of CO2 on the selective catalytic reduction of NO_x with NH_3 of $Fe_{0.4}Ce_{0.6}O_{2-\delta}$ catalyst: adsorption behavior, Surfaces and Interfaces. 24 (2021) 101118.
https://doi.org/10.1016/j.surfin.2021.101118.

[10] J. Akil, C. Ciotonea, S. Siffert, S. Royer, L. Pirault-Roy, R. Cousin, C. Poupin, NO reduction by CO under oxidative conditions over CoCuAl mixed oxides derived from hydrotalcite-like compounds: Effect of water, Catal. Today. (2021). https://doi.org/10.1016/j.cattod.2021.05.014.

[11] A. Prašnikar, A. Pavlišič, F. Ruiz-Zepeda, J. Kovač, B. Likozar, Mechanisms of Copper-Based Catalyst Deactivation during CO2 Reduction to Methanol, Ind. Eng. Chem. Res. 58 (2019) 13021–13029.
https://doi.org/10.1021/acs.iecr.9b01898.

[12] X. Cheng, L. Wang, Z. Wang, M. Zhang, C. Ma, Catalytic Performance of NO Reduction by CO over Activated Semicoke Supported Fe / Co Catalysts, Ind. Eng. Chem. Res. (2016). https://doi.org/10.1021/acs.iecr.6b00804.

[13] Z. Gholami, G. Luo, Low-temperature selective catalytic reduction of NO by CO in the presence of O_2 over Cu: Ce catalysts supported by multi-walled carbon nanotubes, Ind. Eng. Chem. Res. (2018).
https://doi.org/10.1021/acs.iecr.8b01343.

[14] B. Wen, M. He, E. Schrum, C. Li, NO reduction and CO oxidation over Cu/Ce/Mg/Al mixed oxide catalyst in FCC operation, J. Mol. Catal. A Chem. 180 (2002) 187–192. https://doi.org/10.1016/S1381-1169(01)00427-7.

Chapter 6

Perovskites: A Prospective Catalytic Material

Perovskites, in addition to the mixed oxides formed from the thermal treatment of parent LDHs, can be promising materials for the CO + NO reaction, particularly under industrial flue gas conditions. As a result, this chapter discusses perovskite materials as catalysts for NO reduction by CO reaction as a future promising material. Furthermore, this chapter discusses preliminary material characterisation and catalytic activity results for different perovskite materials.

6.1 General Introduction

Perovskites are oxides consisting of the structural formula ABO_3 (see Figure 6.1). It generally corresponds to the crystalline structure of $CaTiO_3$ [1]. The A and B in the ABO_3 structures can be lanthanides or alkaline and alkaline-earth metals and metallic cations with 3d, 4d and 5d configurations respectively [1,2]. In addition, it exists another structural phase represented as A_2BO_4 (see Figure 6.1), also known as Ruddlesden-Popper (RP) phases which are generally represented as $A_{n+1}B_nO_{3n+1}$ where n is the number of perovskite layers stacked along the crystallographic c axis [3]. Depending on the different valences of the A and B cations, perovskites with different charge distributions can be synthesized [2,3]. One of the major advantages of perovskites is the possibility to form a wide range of compositions by changing either A or B

cations and even substituting each cation with other cations of the same or different valences thereby altering the redox and acid-base properties of the materials which can be an important factor for certain catalytic applications like hydrocarbon oxidation [4–6], CO oxidation [4,6], VOC combustion [7,8], partial oxidation of methane [9,10] and decomposition of NO either directly [11,12] or selective catalytic reduction by hydrocarbons [13,14], H_2 [15,16] and CO [17,18]. Since the focus of this thesis is on NO_x reduction by CO, a brief discussion of the available reports for this reaction over perovskites as catalysts in the literature has been discussed in the next section.

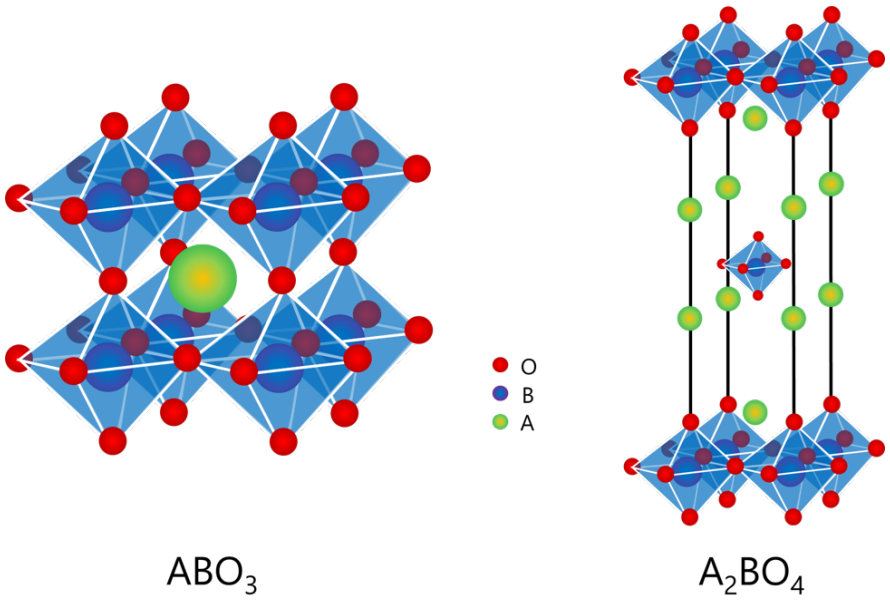

Figure 6.1 Crystal structure of perovskites and perovskite-like materials

6.2 Literature Studies: NO reduction by CO

Depending on the type of the A and B cations in the perovskite structure, the redox properties of the materials can be altered and therefore, can provide interesting NO_x reduction by CO activity. Some of the reported studies in the literature have been enlisted in Table 6.2. The effect of the material composition and the reaction gas composition on the NO-SCR by CO performance is discussed in the following sections.

6.2.1 Effect of Material Composition

The composition of the perovskite materials can be altered by changing the A and B cations resulting in materials with different redox behaviour and acid-base properties which can be crucial for the NO-SCR by CO reaction. More details about the effect of the alternation of A and/or B cations on the SCR performance are discussed below.

6.2.1.1 Effect of 'B' Cations

The B sites in the perovskites can be occupied by monovalent cations like Li, bivalent cations like Zn, Mg and Cu, trivalent cations like Ti and higher valence cations like Ru, Nb and Mo [2]. The type of the B cations in the perovskites significantly affects the NO-SCR activity. Zang et al. [19] compared NO reduction by CO activity over $LaCoO_3$ and $LaMnO_3$ perovskites. The authors reported that $LaCoO_3$ showed superior catalytic activity than $LaMnO_3$ sample. The formation of more oxygen vacant sites indicated by a broad O_2-TPD peak at $200 < T < 720°C$ which is attributed to the O_2 adsorbed on anion vacancies than $LaMnO_3$ which in contrary, had over stoichiometric oxygen (observed under O_2-TPD at 450-650°C) that accelerated NO and CO oxidation thereby affecting NO reduction activity. Similar studies were also reported by Zhu et al. [36] where the authors compared different $LaSrMO_4$ (M = Co, Ni and Cu) samples for CO + NO activity ($LaSrCuO_4 > LaSrNiO_4 > LaSrCoO_4$). The authors observed that the NO reduction performance of the samples is directly proportional to the concentration of non-stochiometric oxygen which in turn is inversely proportional to the average valence of the metal (Co, Ni or Cu).

Apart from the substitution of B cations by a single metal, more than one type of metal can occupy the B sites and can affect the catalytic performance of the resulting mixed oxides. Some studies like Wu et al. [18] and Tarjomannejad et al. [20] demonstrate the effect of the type of metal in partial B-site substitution on the catalytic performance while other studies like that of Zhang et al. [19] and Peter et al. [21] report the effect of extent of B-site substitution on the corresponding catalytic performance. Wu et al. [18] studied $LaM_{0.25}Co_{0.75}O_3$ (M = Cu, Mn, Fe) perovskites and compared their catalytic performance. For all samples, catalytic activity was improved by the substitution of the second active metal when compared with $LaCoO_3$ sample. The authors found that the

Cu-containing sample showed the best catalytic performance with 100% NO and CO conversion at 350°C and 300°C respectively (the order of NO and CO conversion activity: $LaCu_{0.25}Co_{0.75}O_3$ > $LaMn_{0.25}Co_{0.75}O_3$≈ $LaFe_{0.25}Co_{0.75}O_3$ > $LaCoO_3$). The formation of large amounts of oxygen vacant sites in the sample and improvement in the corresponding redox properties were considered to be crucial for the NO + CO activity. In a similar kind of study, Tarjomannejad et al. [20] report the comparison of catalytic activities of $LaCu_{0.7}B_{0.3}O_3$ (B = Mn, Fe, Co) perovskites. The authors observed that $LaCu_{0.7}Mn_{0.3}O_3$ showed the best catalytic activity with 88% CO conversion and 93% NO conversion at 350°C (catalytic activity trend: $LaCu_{0.7}Mn_{0.3}O_3$ > $LaCu_{0.7}Fe_{0.3}O_3$ > $LaCu_{0.7}Co_{0.3}O_3$). Like Wu et al. [18], the authors in this study concluded in addition to the deficiencies allowing the mobility of oxygen, the reducibility of the perovskite samples played an important role in the catalytic performance.

Further, Zhang et al. studied [19] the effect of Co/Cu and Mn/Cu atomic ratio in the $LaCo_{1-x}Cu_xO_3$ and $LaMn_{1-x}Cu_xO_3$ respectively on the corresponding NO-SCR by CO performance. The authors reported that the substitution of some Co and Mn atoms in the $LaCoO_3$ and $LaMnO_3$ perovskites by Cu improves the CO conversion activity, from 91% CO conversion at 500°C to complete CO conversion at 450°C for 20% of Cu substitution in $LaCoO_3$ sample while for La-Mn sample, the CO conversion improved from 70% at 500°C for $LaMnO_3$ to 90% at 500°C with 20% Cu substitution. Comparing the N_2 yield of the $LaCo_{1-x}Cu_xO_3$ and $LaMn_{1-x}Cu_xO_3$ samples, $LaCo_{0.8}Cu_{0.2}O_3$ showed the highest yield of 100% at 500°C while the worst yield was recorded to be 70% at 500°C for $LaMnO_3$. Increasing the Cu content from M/Cu = 0 to 0.2 (M = Co or Mn) in both the perovskites improved the catalytic activity significantly. The generation of oxygen vacant sites in the perovskites and enhancement in the lattice oxygen mobility in lanthanates by partial substitution of the B sites by Cu were considered as the reasons for their improved catalytic activities. Similar reports of enhancement in the catalytic activity by partial substitution of the B site metal species with Cu has also been reported by Peter et al. [21]. Here, the authors have used Fe-Cu-based perovskites for different Cu:Fe ratios (0 to 9) for assessing the catalytic reduction of NO by CO performance.

Table 6.1 Summary of literature studies on catalytic reduction of NO by CO over perovskite materials

Catalyst	NO	CO	Other Gases	GHSV	Peak CO Conversion	NO conversion			Ref
						Peak NO Conversion Yield (%)	Peak Temperature (°C)	N_2 Selectivity at Peak Temperature (%)	
$LaCu_{0.25}Co_{0.75}O_3$	5 vol%	10 vol%	He (rest)	36000 $ml.g^{-1}.h^{-1}$	55% at 300°C	100	400	100	[18]
$LaMn_{0.25}Co_{0.75}O_3$	5 vol%	10 vol%	He (rest)	36000 $ml.g^{-1}.h^{-1}$	55% at 450°C	100	500	100	[18]
$LaFe_{0.25}Co_{0.75}O_3$	5 vol%	10 vol%	He (rest)	36000 $ml.g^{-1}.h^{-1}$	55% at 450°C	100	500	100	[18]
$LaCe_{0.2}Co_{0.8}O_3$	5 vol%	10 vol%	He (rest)	36000 $ml.g^{-1}.h^{-1}$	55% at 550°C	100	600	100	[18]
$LaCo_{1-x}Cu_xO_3$	3000 ppm	3000 ppm	He (rest)	50000 h^{-1}	100% at 450°C for $LaCo_{0.8}Cu_{0.2}O_3$	100 for $LaCo_{0.8}Cu_{0.2}O_3$	450 for $LaCo_{0.8}Cu_{0.2}O_3$	100 for $LaCo_{0.8}Cu_{0.2}O_3$	[19]
$LaMn_{1-x}Cu_xO_3$	3000 ppm	3000 ppm	He (rest)	50000 h^{-1}	85% at 450°C for $LaMn_{0.8}Cu_{0.2}O_3$	85 for $LaMn_{0.8}Cu_{0.2}O_3$	450 for $LaMn_{0.8}Cu_{0.2}O_3$	100 for $LaMn_{0.8}Cu_{0.2}O_3$	[19]

$LaCu_{0.7}Mn_{0.3}O_3$	3000 ppm	3000 ppm	Ar (rest)	12000 h^{-1}	100% at 450°C	100	450	>99	[20]
$LaCu_{0.7}Fe_{0.3}O_3$	3000 ppm	3000 ppm	Ar (rest)	12000 h^{-1}	80% at 450°C	80	450	>99	[20]
$LaCu_{0.7}Co_{0.3}O_3$	3000 ppm	3000 ppm	Ar (rest)	12000 h^{-1}	75% at 450°C	100	450	>99	[20]
$La_{0.8}Rb_{0.2}Cu_{0.7}Mn_{0.3}O_3$	3000 ppm	3000 ppm	Ar (rest)	12000 h^{-1}	100% at 350°C	100	400	>99	[20]
$La_{0.8}Sr_{0.2}Cu_{0.7}Mn_{0.3}O_3$	3000 ppm	3000 ppm	Ar (rest)	12000 h^{-1}	100% at 350°C	100	400	>99	[20]
$La_{0.8}Cs_{0.2}Cu_{0.7}Mn_{0.3}O_3$	3000 ppm	3000 ppm	Ar (rest)	12000 h^{-1}	100% at 350°C	100	400	>99	[20]
$La_{0.8}Ba_{0.2}Cu_{0.7}Mn_{0.3}O_3$	3000 ppm	3000 ppm	Ar (rest)	12000 h^{-1}	100% at 350°C	100	400	>99	[20]
$La_2Cu_{1-x}Fe_xO_3$	2000 ppm	2000 ppm	He (rest)	101 h^{-1}	––	250×10^{-5} $mol.g^{-1}$ h^{-1}	350-400	––	[21]

$LnFeO_3$ (Ln = La, Pr-Tb, Dy-Yb, Y)	4000 ppm	4000 ppm	He (rest)	24000 h^{-1}	––	100 for $LaFeO_3$	400 for $LaFeO_3$	100	[22]
$La_{2-x}Sr_xCuO_4$	4000 ppm	4000 ppm	He (rest)	1.34 $g.s.cm^{-3}$	––	100 for $LaSrCuO_4$	550	100	[23]
$La_{2-x}Th_xCuO_4$	4000 ppm	4000 ppm	He (rest)	1.34 $g.s.cm^{-3}$	––	90 for $La_{1.6}Th_{0.4}CuO_4$	550	100	[23]
$La_{1-x}Sr_xFeO_3$	2 vol%	2 vol%	He (rest)	100 $cm^{-3}.min^{-1}$ through 200 mg catalyst	100% at 500°C for $La_{0.85}Sr_{0.15}FeO_3$	100 for $La_{0.85}Sr_{0.15}FeO_3$	500 for $La_{0.85}Sr_{0.15}FeO_3$	100 for $La_{0.85}Sr_{0.15}FeO_3$	[24]
$La_{0.8}Ce_{0.2}Cu_{0.4}Mn_{0.6}O_3$	1 vol%	1 vol%	He (rest)	20000 h^{-1}	––	100	250	96	[25]
$La_{0.8}Ce_{0.2}Ag_{0.4}Mn_{0.6}O_3$	1 vol%	1 vol%	He (rest)	20000 h^{-1}	––	99	450	68	[25]

$LaCo_{1-x}Cu_xO_3$	3000 ppm	3000 ppm	He (rest)	50000 h^{-1}	100% at 400°C for $LaCo_{0.8}Cu_{0.2}O_3$	100 for La $Co_{0.8}Cu_{0.2}O_3$	500 for $LaCo_{0.8}Cu_{0.2}O_3$	100 for La $Co_{0.8}Cu_{0.2}O_3$	[26]
$LaMn_{1-x}Cu_xO_3$	3000 ppm	3000 ppm	He (rest)	50000 h^{-1}	90% at 450°C for $LaMn_{0.8}Cu_{0.2}O_3$	90 for La $Mn_{0.8}Cu_{0.2}O_3$	500 for $LaMn_{0.8}Cu_{0.2}O_3$	100 for La $Mn_{0.8}Cu_{0.2}O_3$	[26]
$LaCu_{0.25}Co_{0.75}O_3$	5 vol%	10 vol%	Ar (rest)	60000 $ml.g^{-1}.h^{-1}$	55% at 350°C for sample calcined at 750°C	100 for for sample calcined at 750°C	350 for sample calcined at 750°C	100 for sample calcined at 750°C	[27]
$LaMnO_3$	2 vol%	2 vol%	He (rest)	100 $cm^3.min^{-1}$ through 200 mg of catalyst	80% at 500°C	90	500	100	[17]
$LaFeO_3$	2 vol%	2 vol%	He (rest)	100 $cm^3.min^{-1}$ through 200 mg of catalyst	80% at 450°C	90	450	100	[17]

$La_xCe_{1-x}FeO_3$	400 ppm	500 ppm	SO_2 (100 ppm), O_2 (3 vol%), H_2O (3 vol%) and N_2 (rest)	24000 h^{-1}	––	60 for $La_{0.6}Ce_{0.4}FeO_3$	500 for $La_{0.6}Ce_{0.4}FeO_3$	––	[28]
$La_xCe_{1-x}FeO_3$	400 ppm	500 ppm	SO_2 (100 ppm), and N_2 (rest)	24000 h^{-1}	––	75 for $La_{0.6}Ce_{0.4}FeO_3$	500 for $La_{0.6}Ce_{0.4}FeO_3$	––	[28]
$La_xCe_{1-x}FeO_3$	400 ppm	500 ppm	N_2 (rest)	24000 h^{-1}	––	90 for $La_{0.6}Ce_{0.4}FeO_3$	500 for $La_{0.6}Ce_{0.4}FeO_3$	80 for $La_{0.6}Ce_{0.4}FeO_3$	[28]
$La_{0.8}Ce_{0.2}Cu_{0.25}Co_{0.75}O_3$	5 vol%	10 vol%	He (rest)	60000 $ml.g^{-1}.h^{-1}$	45% at 350°C	100	400	100	[29]
$La_{0.8}Ce_{0.2}Mn_{0.25}Co_{0.75}O_3$	5 vol%	10 vol%	He (rest)	60000 $ml.g^{-1}.h^{-1}$	45% at 500°C	100	500	100	[29]
$La_{0.8}Ce_{0.2}Fe_{0.25}Co_{0.75}O_3$	5 vol%	10 vol%	He (rest)	60000 $ml.g^{-1}.h^{-1}$	45% at 500°C	100	500	100	[29]

$La_{0.8}Ce_{0.2}CoO_3$	5 vol%	10 vol%	He (rest)	60000 $ml.g^{-1}.h^{-1}$	45% at 550°C	100	550	100	[29]
$LaFe_{0.5}Co_{0.5}O_3$	3000 ppm	3000 ppm	Ar (rest)	12000 h^{-1}	75% at 500°C	80	450	90	[30]
$LaFe_{0.5}Cu_{0.5}O_3$	3000 ppm	3000 ppm	Ar (rest)	12000 h^{-1}	80% at 500°C	90	450	90	[30]
$LaFe_{0.5}Mn_{0.5}O_3$	3000 ppm	3000 ppm	Ar (rest)	12000 h^{-1}	90% at 500°C	100	450	90	[30]
$LaMn_{0.5}Co_{0.5}O_3$	3000 ppm	3000 ppm	Ar (rest)	12000 h^{-1}	90% at 450°C	100	450	95	[30]
$LaMn_{0.5}Cu_{0.5}O_3$	3000 ppm	3000 ppm	Ar (rest)	12000 h^{-1}	75% at 500°C	100	450	95	[30]
$LaNi_{0.5}Co_{0.5}O_3$	5 vol%	10 vol%	He (rest)	36000 $ml.g^{-1}.h^{-1}$	60% at 500°C	100	500	90	[31]
$LaNi_{0.5}Mn_{0.5}O_3$	5 vol%	10 vol%	He (rest)	36000 $ml.g^{-1}.h^{-1}$	60% at 500°C	90	500	90	[31]
$LaNi_{0.5}Cu_{0.5}O_3$	5 vol%	10 vol%	He (rest)	36000 $ml.g^{-1}.h^{-1}$	60% at 400°C	100	400	90	[31]

$La_{1-x}Sr_xMnO_3$	2 vol%	2 vol%	He (rest)	100 $cm^3.min^{-1}$ through 200 mg of catalyst	60% at 500°C for $LaMnO_3$	90 for $LaMnO_3$	500 for $LaMnO_3$	90 for for $LaMnO_3$	[31]
$La_{2-x}Sr_xNiO_4$	2 vol%	2 vol%	He (rest)	100 $cm^3.min^{-1}$ through 250 mg of catalyst	70% at 580°C for $La_{1.2}Sr_{0.75}NiO_4$	70 at 580°C for $La_{1.2}Sr_{0.75}NiO_4$	580 for $La_{1.2}Sr_{0.75}NiO_4$	––	[31]
$LaFe_{0.8}Cu_{0.2}O_3$	3000 ppm	3000 ppm	He (rest)	50000 h^{-1}	100% at 500°C	90	400-500	95 at 500°C	[34]
$LaFe_{0.97}Pd_{0.03}O_3$	3000 ppm	3000 ppm	He (rest)	50000 h^{-1}	100% at 500°C	95	350-550	100 at 500°C	[34]
$LaFe_{1-x}Co_xO_3$	5000 ppm	5000 ppm	He (rest)	15000 h^{-1}	100% at 500°C for x = 0 and 0.4	100 for x = 0 and 0.4	600°C for x = 0 and 0.4	100	[35]

The authors observed a synergistic effect between Cu and Fe and found that for the Cu:Fe ratio of 2.3, maximum NO conversion activity is achieved. The accessibility of metallic copper in the sample was considered to be a crucial factor in the NO reduction performance.

6.2.1.2 Effect of 'A' Cations

In addition to the B-site, the type of metals at the A-sites of the perovskites also affect the catalytic performance. Li et al. [22] studied the $LnFeO_3$ (Ln = light and median rare-earth elements: La, Pr-Tb and heavy rare-earth elements: Dy-Yb, Y) and compared their catalytic activities for NO + CO reaction. Out of these materials, $GdFeO_3$, $LaFeO_3$ and $NdFeO_3$ showed better NO conversion (100% at T > 350°C with N_2 selectivity of 100% for T > 400°C). The authors conclude that the difference in the catalytic activity was strongly correlated to the corresponding specific surface area. The light and median rare-earth metals at the A-sites produced perovskites with specific surface area higher than the heavy rare-earth metals and therefore, the former showed better NO and CO conversion than the latter.

Partial substitution of the metals at A site of the perovskite can generate structural defects thereby affecting the reducibility of the perovskites and subsequently, the catalytic performance. Tarjomannejad et al. [20] and Zhu et al. [23] studied this effect of partial substitution of metals in the A-site on the NO + CO activity. On one hand Tarjomannejad et al. [20] compared the catalytic activities of $La_{0.8}A_{0.2}Cu_{0.7}Mn_{0.3}O_3$ (A = Rb, Sr, Cs, Ba) perovskite samples and observed that $La_{0.8}Sr_{0.2}Cu_{0.7}Mn_{0.3}O_3$ showed the best catalytic activity of 93% CO conversion and 96% NO conversion (100% NO conversion was achieved at 375°C) at 350°C against 88% and 93% of CO and NO conversions at 350°C respectively for $LaCu_{0.7}Mn_{0.3}O_3$. Partial substitution of the metals at the A-site induced better reducibility and generated more oxygen vacant sites in the resulting perovskite samples which consequently, enhanced the catalytic performance of the samples. Moreover, the authors did not find a direct correlation between the catalytic activity and specific surface area of the samples as reported by Li et al. [22] for the study with different metals at the A-site of the perovskites. On the other hand, Zhu et al. [23] reported the difference in the catalytic activity for $La_{2-x}\ Sr_xCuO_4$ and $La_{2-x}Th_xCuO_4$ samples and observed that substitution of La by Sr^{2+} generated oxygen vacant sites while the substitution by Th^{2+}

generated Cu^{+} species in the samples. Moreover, the lattice oxygen mobility was found to be easier in case of Sr containing samples than in Th containing samples and therefore, the former samples showed higher catalytic activity than the latter.

Apart from the type of metal used for the partial substitution at the A-sites, the extent of substitution also plays an important role in determining the catalytic performance of the perovskites. Zhu et al. [23] studied the effect of extent of Sr and Th substitution at the A-sites of the $LaCuO_4$ perovskites on the NO + CO activity. The authors reported that increase in the La- substitution by Sr and Th improved the NO conversion activity over the corresponding perovskites materials. $LaSrCuO_4$ and $La_{0.6}Th_{0.4}CuO_4$ were found to have superior catalytic activity than the other Sr- and Th- containing samples. Finally, the authors concluded that the formation of oxygen vacant sites and ease of lattice-oxygen mobility are the crucial factors for the NO + CO activity. In another study, Leontiou et al. [24] studied the effect of degree of substitution of La by Sr in La-Sr-Fe perovskites on the NO reduction by CO activity. The authors reported that the maximum N_2O production and the corresponding reaction temperature decreased and increased respectively with the increase in the Sr content in the perovskite material. The authors explained this trend of catalytic activities at different degree of La substitution by Sr with the increase in the binding energy of oxygen with the increase in the Sr substitution thereby decreasing the ease of formation of oxygen vacant sites in the material and consequently, decreasing the catalytic activity.

6.2.2 Effect of Preparation Methods

6.2.2.1 Synthesis Protocol

The catalytic material synthesis protocol can greatly affect the specific surface area which is a crucial factor for the corresponding NO + CO performance. In this bibliographic study, 4 main synthesis routes have been reported by different authors: (1) conventional citrate method [35,37] (2) microemulsion [17,25] (3) sol-gel [25] (4) reactive grinding [26]. Schön et al. [37] prepared $La_{1-y}FeO_3$ perovskites by CCM for three-way catalysis and achieved a specific surface area in the range of 13 - 22 $m^2.g^{-1}$ while de Lima et al. prepared LaFeCo perovskites by CCM for NO reduction by CO reaction obtaining a specific surface area of

61 $m^2.g^{-1}$, higher than that reported by Schön et al. Further, He et al. [25] worked with two different synthesis methods: namely reverse microemulsion and sol-gel method for the synthesis of $La_{0.8}Ce_{0.2}B_{0.4}Mn_{0.6}O_3$ (B = Cu or Ag) perovskites. Aggregation of particles and formation of considerable amount of CeO_2 phase was noticed in case of the sol-gel method while uniform particle size distribution with comparatively less amount of CeO_2 formation was recorded for the reverse emulsification method. Moreover, reverse emulsification method of preparation increased the specific surface area from 5.7 to 14.2 $m^2.g^{-1}$ for $La_{0.8}Ce_{0.2}Cu_{0.4}Mn_{0.6}O_3$ and 13.9 to 17.9 $m^2.g^{-1}$ for $La_{0.8}Ce_{0.2}Ag_{0.4}Mn_{0.6}O_3$ against sol-gel mode of synthesis. This improvement in the specific surface area enhanced the NO reduction by CO activity of the catalytic samples since more amount of active surface species were exposed to the reactant gas mixture. Similar to the study reported by He et al. [25], Giannakas et al. [17] also synthesized their $LaMnO_3$ and $LaFeO_3$ perovskite materials by microemulsion method both in reverse and bicontinuous state. The former preparation protocol produced pure perovskites after calcination at 800°C with surface area higher and particle size smaller than the latter preparation protocol. Additionally, for comparison, the authors prepared the materials by ceramic method and this method generated particles of size 3 times larger and 50% lower specific surface area than the bicontinuous microemulsion method. Upon comparing the corresponding catalytic activities of these samples, the authors concluded that the materials prepared by microemulsion method were superior to that by the ceramic method. Unlike the previous studies, Zhang et al. [26] compared the catalytic activity of $La(Co, Mn)_{1-x}(Cu)_xO_3$ perovskites prepared by reactive grinding methodologies. The reactive grinding methodology yielded a specific surface area of 22-43 $m^2.g^{-1}$ against 2-5 $m^2.g^{-1}$ via ceramic method, 5-13 $m^2.g^{-1}$ via sol-gel and 14-25 $m^2.g^{-1}$ via reverse microemulsion as reported by He et al. [25] and Giannakas et al. [17]. Moreover, the crystalline size obtained by reactive grinding varied between 9-15 nm. However, the authors did not compare the catalytic activities based on the preparation methods for the perovskite samples.

6.2.2.2 Calcination Temperature

Generally, the increase in the calcination temperature increases the grain size and decreases the specific surface area of the perovskites which consequently

affects the catalytic activity. Wu et al [27] studied the effect of calcination temperature on the NO + CO activity with $LaCu_{0.25}Co_{0.75}O_3$ catalysts. Based on the NO conversion activity, the order was established as follow: $LaCu_{0.25}Co_{0.75}O_3$-750 > $LaCu_{0.25}Co_{0.75}O_3$-500 > $LaCu_{0.25}Co_{0.75}O_3$-250 > $LaCu_{0.25}Co_{0.75}O_3$-1000 (where the numbers after the catalyst name represents the calcination temperature in °C). In addition, the samples specific surface area decreased from 24 $m^2.g^{-1}$ to 3.8 $m^2.g^{-1}$, pore volume decreased from 0.12 to 0.01 $cm^3.g^{-1}$ and pore diameter from 20 to 410 nm with the increase in calcination temperature from 250°C to 1000°C. These changes can be attributed to the partial collapse of the material structure. However, no direct correlation was established with the calcination temperature and grain size. High reducibility and large amount of oxygen vacant sites were considered to be the main reason for the superior catalytic activity of La $Cu_{0.25}Co_{0.75}O_3$-750 sample.

6.2.3 Effect of Reactant Gas Composition

6.2.3.1 Effect of O_2

The effect of O_2 presence in the NO reduction by CO activity over perovskite-based catalysts have been scarcely reported in the literature. The major impact of the presence of O_2 in the reactant gas stream is the decrease in the amount of oxygen vacant sites in the perovskites and therefore promoting the formation of NO_2 instead of N_2. Furfori et al. [38] studied the NO_x reduction by H_2 in the presence and absence of 5 vol% O_2 over $La_{0.8}Sr_{0.2}Fe_{0.9}Pd_{0.1}O_3$. The authors reported that under '*no oxygen*' condition, 100% NO conversion to N_2 was achieved at a temperature of 200°C while in the presence of oxygen, this NO conversion to N_2 dropped to 50% at 150°C (peak NO reduction to N_2) and decreased upon further increase in the reaction temperature. Formation of NO_2 (peak selectivity of 15% at 300°C and NO:H_2 = 1:10) and N_2O (peak selectivity varying from 5-20% at 120-150°C depending on the NO:H_2 ratio) were detected in the presence of O_2 in the reaction system. Finally, the authors concluded that the O_2 occupied the active vacant sites in the catalyst and therefore, did not provide access for the decomposition of NO, an important step in the NO reduction to N_2. Similar detrimental effect of O_2 on the NO_x reduction over perovskite based catalysts has also been reported by Wu et al. [14] for NO_x reduction by C_3H_8 over $La_{1-x}Sr_xMnO_3$ catalysts, Zhang et al. for NO_x reduction by C_3H_6 over $LaFe_{0.97}Pd_{0.03}O_3$ [39] and $LaCo_{0.8}Cu_{0.2}O_3$ [40]. Unlike Furfori,

Wu and Zhang concluded that the consumption of the reductant by O_2 was the major reason for the decline in the NO_x conversion activity. However, the production of NO_2 has only been reported by Zhang et al. [39].

Furthermore, Zhang et al. [39,40] also reported the promotional effect of O_2 on NO_x reduction to N_2 due to the formation of nitrate, organo-nitrogen compounds and isocyanate species which are active intermediate species for N_2 formation. However, the concentration of O_2 in the reactant gas stream must be low in order to act as a promoter for the NO_x reduction, like certain studies have reported promotional effect of O_2 on the NO_x conversion to N_2. Nevertheless, no studies regarding the impact of O_2 on the NO reduction by CO has been reported in the literature.

6.2.3.2 Effect of H_2O

The presence of water in the reactant gas stream can have either promotional or detrimental effect on the NO_x reduction activity. Zhang et al. [41] studied the La(Co, Mn, Fe)$_{1-x}$(Cu, Pd)$_x$O$_3$ catalysts deactivation in the presence of 10 vol% H_2O for NO reduction by C_3H_6 and reported that the H_2O competes with O_2 and NO for the low-valence vacant sites in the catalyst and therefore, lowers the NO_x reduction activity. However, this effect is reversible, and the NO_x conversion activity is reinstated upon removal of H_2O from the reaction system. Similar observations were also reported by Wu et al. [42] where the authors introduced 10 vol% H_2O in the reaction mixture of NO and CO at a temperature of 300°C over $LaCu_{0.5}Mn_{0.5}O_3$ catalyst. Like Zhang et al. observations, Wu et al. also observed that upon removing the H_2O from the system, the NO_x conversion activity reached the level of initial dry reaction conditions.

The coexistence of CO and H_2O in the reactant gas mixture can also trigger the water-gas shift reaction which results in the formation of H_2, a reductant for NO conversion to N_2. Perovskites like $La_{0.7}Ce_{0.2}FeO_3$ [43] and $La_{1-y}Sr_yNi_xCo_{1-x}O_3$ [44] have shown appreciable water-gas shift reaction activity. Moreover, simultaneous reduction of NO_x by CO and H_2 produced from the water-gas shift reaction has been reported by Constantinou [45] and Mondragon et al. [46] over Pt-Rh/$La_{0.9}Sr_{0.1}MnO_3$ and $LaFe_{0.95-x}Co_xPd_{0.05}O_3$ catalysts respectively where the water splits into OH and H species ($H_2O_{ads} \rightarrow H_{ads} + OH_{ads}$) and the H species react with NO to form adsorbed N species (NO_{ads}

+ $H_{ads} \rightarrow N_{ads} + OH_{ads}$) which later react with another N species to form N_2 ($N_{ads} + N_{ads} \rightarrow N_{2,ads}$). Hence, water can inhibit or promote the NO_x reduction to N_2 activity over perovskites, similar to the behaviour reported for CoCu-Al based mixed oxide catalysts as discussed in the previous chapters of this thesis.

6.2.3.3 Effect of CO_2

Presence of CO_2 in the reaction gas stream reportedly inhibits the NO decomposition [13] and promotes/inhibits NO reduction by reductants like H_2 reactions [46,47]. The main reason for the inhibition is the adsorption of CO_2 on to specific surface oxygen species thereby reducing the number of active sites required for the NO adsorption. Mondragon et al. [46] studied the effect of CO_2 on two La-Fe-Co samples with different Co content and concluded that decreasing the Co content decreased the catalytic activity in general and in the presence of CO_2 (and H_2O since both these gases were added simultaneously) the sample with low Co content was the most affected catalyst with peak NO_x conversion decreased from 70% under CO_2-free condition to 55% in the presence of CO_2 and no considerable change in the N_2 selectivity at a reaction temperature of 200°C. Similar observations have also been reported by Tofan et al. [13] where the authors studied the effect of CO_2 content in the reactant gas feed on the direct decomposition of NO over $La_{0.87}Sr_{0.13}Mn_{0.2}Ni_{0.8}O_{3-\gamma}$, $La_{0.66}Sr_{0.34}Ni_{0.3}Co_{0.7}O_{3-\gamma}$ and $La_{0.85}Sr_{0.2}Cu_{0.15}Fe_{0.85}O_{3-\gamma}$ catalysts, and reported that the NO conversion is decreased with the increase in the CO_2 content up until 6 vol% and beyond this value, there is no further decline in the NO_x conversion. The authors finally concluded that the formation of stable carbonates at adsorption sites for NO was the reason for such a decline in the NO_x conversion activity.

However, in another study on $BaTi_{0.95}Pd_{0.05}O_3$ catalyst, Mondragon et al. [47] reported promotional effect of CO_2 along with H_2O in the NO_x reduction activity by H_2. The authors related this behaviour to the dissociation of water and its further participation in the NO_x reduction mechanism. Although there are studies regarding the influence of CO_2 on NO_x reduction reported in the literature, no study has been found so far for the NO reduction by CO and therefore, will be interesting to study.

6.2.3.4 Effect SO_2

The presence of SO_2 in the industrial flue gas emerge from the oxidation of sulphur containing fuels used in the industrial process and therefore, in

order to use perovskites as catalysts for NO_x reduction under industrial flue gas condition, it is important to assess the resistibility of the catalyst against SO_2. Certain studies like that reported by Qin et al. [28] over $La_xCe_{1-x}FeO_3$ catalyst showed considerable resistance to 100 ppm SO_2 and maintained NO_x conversion activity for over 270 minutes against the normal $LaFeO_3$ where the conversion decreased from 100% before the addition of SO_2 to 50% after the addition of SO_2. The formation of the irreversible sulphate species on the $LaFeO_3$ catalyst was the reason for the decline in its NO_x conversion activity. In case of the Ce-containing samples, the SO_2-TPD revealed that the catalysts do not interact to a large extent to SO_2 (the amount of SO_2 desorption was lower than $LaFeO_3$ sample) and therefore, the NO_x conversion activity was retained to a large extent upon introduction of SO_2 in the reactant gas mixture. The poisoning effect of SO_2 was also reported by Zhang et al. [48] over $LaFe_{0.8}Cu_{0.2}O_3$ catalyst for NO reduction by C_3H_6. The authors concluded that under low concentrations of SO_2 (< 20 ppm), the SO_2 adsorbs on the anionic vacancies of the perovskite whereas at high concentration (> 80 ppm) SO_2 reacts with the catalyst to form sulphate and sulphite species and this interaction is irreversible. Hence, it is important to utilise perovskites which show good resistance to SO_2 so that the NO reduction activity can be maintained for a long period of time.

6.3 CO + NO Reaction Under Industrial Flue Gas Conditions

To explore the feasibility of perovskite-based catalysts for NO reduction by CO under industrial flue gas conditions, different perovskite samples were tested both under wet and dry reaction conditions. The synthesis of these samples was performed via *CCM* route (detailed procedure of the synthesis protocol is mentioned in Chapter 3) at *Unité de Catalyse et de Chimie du Solide* (UCCS) Lab of *Université de Lille* (Lille, France). The material characterization and catalytic test results are discussed in the following sections.

6.3.1 $LaBO_3$ (B = Co, Mn and Fe) Perovskites

Based on the previous reports for NO reduction by CO over perovskites (see Table 6.1), three perovskite samples of the form $LaBO_3$ were considered where

B = Co, Mn and Fe. Various material characterization experiments like N_2-physisorption, X-Ray Diffraction and H_2-Temperature Programmed Reduction followed by catalytic tests under dry and wet reaction conditions for the $LaBO_3$ are discussed further in this section.

6.3.1.1 Material Characterization

X-Ray Diffraction (XRD)

The XRD analyses was used to determine the perovskite structure in the $LaBO_3$ samples. The diffractograms obtained from the XRD analyses for the different perovskite samples are shown in Figure 6.2. In this figure, α, β and γ peaks for $LaCoO_3$, $LaFeO_3$ and $LaMnO_3$ corresponds to the standard pattern of JCPDS-ICDD file nos. 00-048-0123, 01-075-0541 and 01-073-8342. Also, it can be concluded from the figure 6.2 that pure perovskite structures are formed for all the $LaBO_3$ samples after calcination at 600°C. However, presence of metal oxides outside the perovskite structure can be present in highly dispersed form which generally go undetected in the XRD analysis. In order to confirm the presence of these well dispersed species, surface characterization techniques

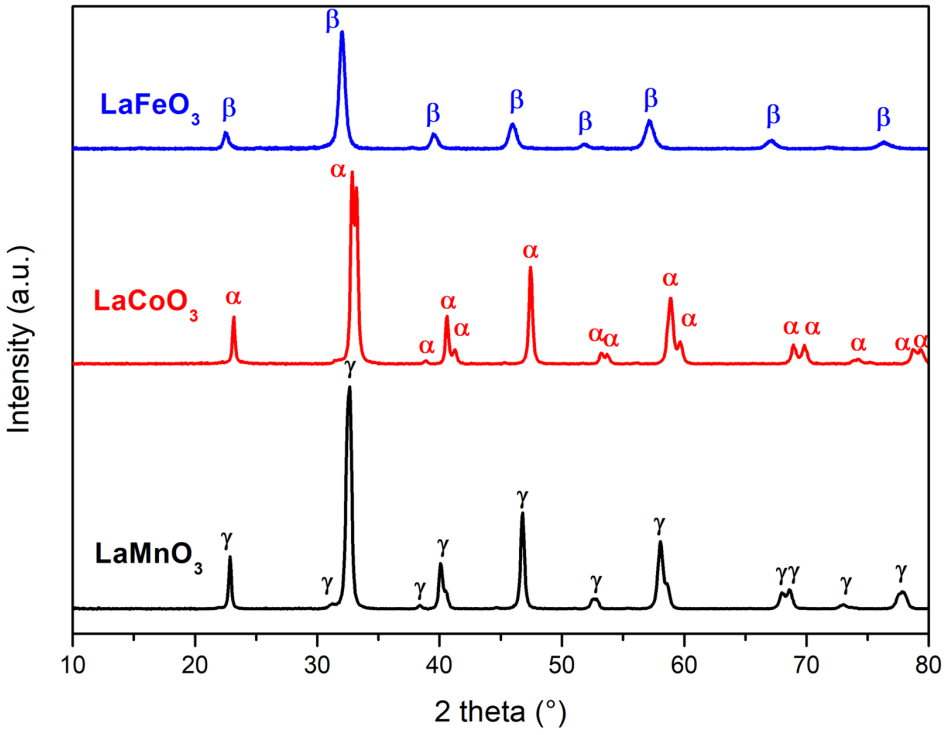

Figure 6.2 Diffractograms for different $LaBO_3$ samples: β = JCPDS 01-075-0541; α = JCPDS 048-0123 and γ = JCPDS 01-073-8342

like Raman Spectroscopy can be used.

N_2-Physisorption

N_2-Physisorption was used to determine the textural properties of the $LaBO_3$ samples. The specific surface area of the samples determined by B.E.T method are enlisted in Table 6.2. It can be seen that the specific surface areas of all the samples vary between 9-12 $m^2.g^{-1}$. This is probably because pure perovskite structures are formed at high reaction temperatures and long reaction time which result in grain growth and low specific surface area [2]. Clearly the type of metal at the B-site of the perovskite have no effect on the specific surface area of the resulting perovskite which is logical since the surface area of the perovskites is greatly influenced by the preparation method [2]. Moreover, no hysteresis loop was obtained during the N_2-physisorption (not shown here) on all the samples which is due to the absence of any pores in the material, thanks to the high calcination temperature during the synthesis that facilitated sintering of the particles.

Table 6.2 Specific surface area of $LaBO_3$ samples

$LaBO_3$ Sample	**Specific Surface Area[a] ($m^2.g^{-1}$)**
$LaFeO_3$	9
$LaMnO_3$	12.2
$LaCoO_3$	8.4

[a] measured by B.E.T. method

H_2-Temperature Programmed Reduction

Since redox property of the catalyst plays a crucial role in the catalytic activity especially for NO reduction by CO, the H_2-TPR analyses were conducted on the $LaBO_3$ samples. The temperature-reduction profile and the specific H_2 consumption for all the $LaBO_3$ samples are shown in Figure 6.3 and Table 6.3 respectively.

It can be seen from Figure 6.3 that only $LaCoO_3$ and $LaMnO_3$ samples show H_2 consumption peaks while $LaFeO_3$ shows no distinctive consumption peaks. For $LaCoO_3$, according to the literature [18,26,49] the low-temperature H_2 reduction peaks at 362°C and 404°C can be attributed to the reduction of Co^{3+} species into Co^{2+} species while the high-temperature reduction peak at

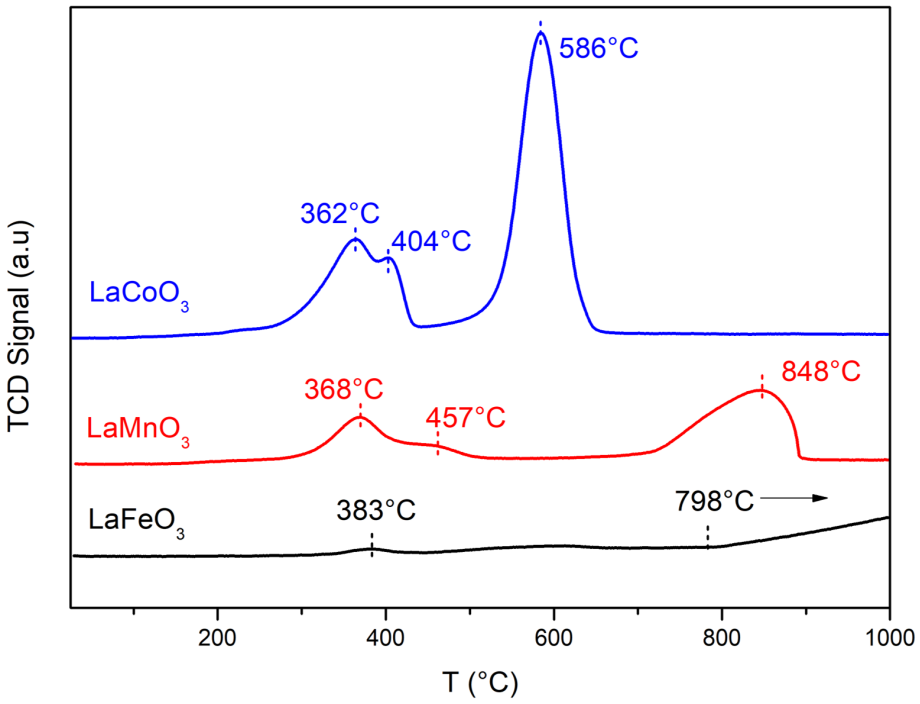

Figure 6.3 H_2-TPR profiles for $LaBO_3$ samples

586°C can be attributed to the reduction of Co^{2+} species into metallic Co species. Further, for $LaMnO_3$, according to the literature [26], the low temperature H_2 reduction peaks at 368°C and 457°C can be attributed to the reduction of Mn^{3+} species to Mn^{2+} species in the bulk while the reduction peak at 848°C can be attributed to the reduction of Mn^{2+} to metallic Mn species. However, certain studies in the literature [30,42] have attributed the reduction between 380-490°C to the reduction of Mn^{4+} to Mn^{3+} instead of Mn^{3+} to Mn^{2+} and the reduction peak beyond 850°C is attributed to the reduction of Mn^{3+} to Mn^{2+} instead of Mn^{3+} to metallic Mn [30,50]. Nevertheless, the reduction of Mn^{2+} to metallic Mn below 1000°C is unfeasible and therefore, the latter explanation should be considered regarding the reduction of different Mn species. Finally, for $LaFeO_3$, the low-temperature reduction peak at 383°C can be attributed to the reduction of easily reducible surface Fe^{3+} species into Fe^{2+}species [34]. However, certain studies attribute this low-temperature reduction peak to the easily reducible Fe^{4+} to Fe^{3+} species [51] but formation of Fe^{4+} species in case of $LaFeO_3$ is generally not observed and therefore, the possibility of existence of Fe^{4+} species in the sample can be neglected. Furthermore, another reduction zone is observed for T > 798°C and can be anticipated to have the peak beyond

Table 6.3 H_2 reduction peaks and specific H_2 consumption for $LaBO_3$ samples

Sample	Peak reduction temperature (°C)			Sp. H_2 Cons. ($mmol.g^{-1}$)
	1st Peak	2nd Peak	3rd Peak	
$LaCoO_3$	362	404	586	6.02
$LaMnO_3$	368	457	848	4.12
$LaFeO_3$	383	613	> 798	−−

[a] Specific H_2 Consumption

1000°C which is out of the operational range of the apparatus. Some studies [51,52] have attributed this incomplete reduction peak to the reduction of Fe^{2+} to metallic Fe species.

Furthermore, in Table 6.3, it can be seen that $LaCoO_3$ has the highest specific H_2 consumption followed by $LaMnO_3$ and the least is recorded for $LaFeO_3$. This indicates that $LaCoO_3$ has the greatest number of reducible species which can aid in superior catalytic activity.

6.3.1.2 Cataytic Activity Tests

$LaBO_3$ samples are further assessed for their NO reduction by CO performance under the industrial flue gas condition as utilized for the catalytic activity tests for CoCuAl mixed oxide samples discussed in Chapter 4 and 5. For the catalytic tests over these perovskite samples, 150 mg of the pelletized and sieved sample ($355 < \phi < 500$ μm) was diluted with SiC to obtain a GHSV of 22400 h^{-1}. The total flow rate of the reactant gas mixture used for the tests was 200 $ml.min^{-1}$ and the activity was measured in terms of light-off curves for range of 100-500°C of reaction temperatures. Finally, the catalytic activity of the samples was compared both under dry and wet reaction conditions as shown in Figure 6.4.

In Figure 6.4(a), the CO conversion activity for the perovskite samples under dry and wet reaction conditions are compared. Further, the temperature for 50% (T_{50}) and 90% (T_{90}) of CO conversion are enlisted in Table 6.4. Based on the T_{50} and T_{90} temperatures under dry reaction condition, the perovskite samples can be arranged in the following order: $LaMnO_3 > LaCoO_3 > LaFeO_3$. However, the difference between the CO conversion activity for $LaFeO_3$ and $LaCoO_3$ is very small. Upon introduction of water in the reactant feed mixture

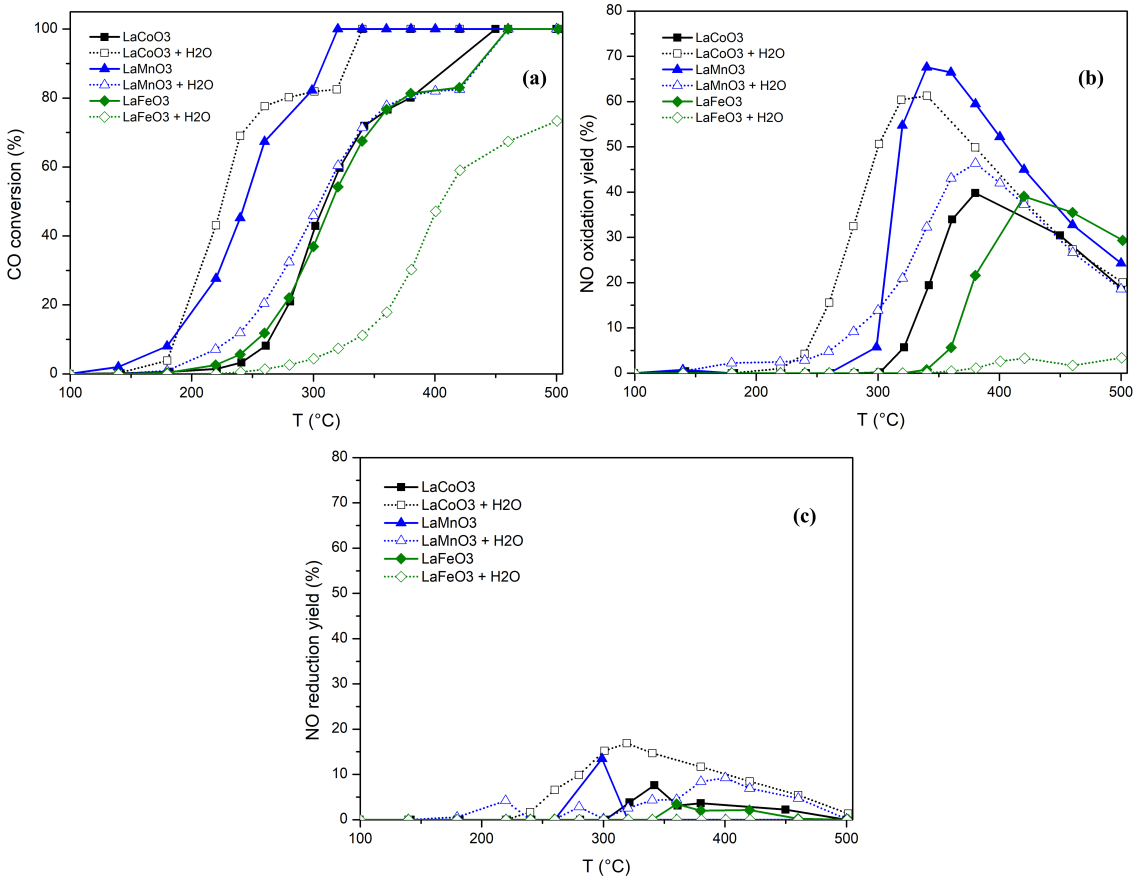

Figure 6.4 Catalytic activity over $LaBO_3$ perovskites under dry and wet (+H2O) reaction conditions: (a) CO conversion (b) NO oxidation yield and (c) NO reduction yield

i.e., wet reaction condition, the CO conversion is degraded for $LaFeO_3$ and $LaMnO_3$ indicated by the shift in the T_{50} and T_{90} temperatures to higher values (see Table 6.4). Moreover, the maximum CO conversion achieved over $LaFeO_3$ under wet reaction conditions is 73% at 500°C. Interestingly, the CO conversion activity of $LaCoO_3$ is improved under the wet reaction condition with T_{50} and T_{90} temperatures for CO conversion shifting towards low values (see Table 6.4).

Further, in Figure 6.4(b) and (c), the NO oxidation and NO reduction yield under the dry reaction conditions for the different perovskite samples can be arranged in the order as follows: $LaMnO_3$ > $LaCoO_3$ > $LaFeO_3$. However, under the wet reaction conditions, the trend changes and is as follows: $LaCoO_3$ > $LaMnO_3$ > $LaFeO_3$. Therefore, it can be considered that $LaMnO_3$ shows superior catalytic activity both in CO conversion and NO reduction/oxidation

Table 6.4 T_{50} and T_{90} temperatures for CO conversion over $LaBO_3$ perovskite samples

Sample	Dry reaction Conditions		Wet reaction Conditions	
	T_{50}(°C)	T_{90}(°C)	T_{50}(°C)	T_{90}(°C)
$LaFeO_3$	315	437	406	not achieved
$LaMnO_3$	244	308	306	437
$LaCoO_3$	310	415	226	329

than other perovskite samples under dry reaction conditions, while under wet reaction conditions $LaCoO_3$ shows the superior catalytic performance among all the samples. The poor catalytic activity of $LaFeO_3$ can be related to the poor reducibility of the active metal species in the material as observed from its corresponding TPR profile (see Figure 6.3) which is more pronounced under the wet reaction condition. Moreover, $LaMnO_3$ showed superior activity both in CO and NO conversion under dry reaction condition than $LaCoO_3$ even if the number of reducible species in the latter is higher than the former. This difference in the catalytic activity can be due to the higher specific surface area in $LaMnO_3$ than $LaCoO_3$ (see Table 6.2) but this correlation between specific surface area and catalytic activity alone is not valid for $LaFeO_3$ where even if $LaFeO_3$ has a higher specific surface area than $LaCoO_3$, it shows lower catalytic activity than $LaCoO_3$ both under dry and wet reaction conditions. The other properties that can affect the catalytic performance of $LaMnO_3$ and $LaCoO_3$ is the oxygen mobility in the material which depends on the metal-oxygen bond strength, concentration of oxygen vacancies and nature of oxygen sites [53]. This shows that the interaction between the reactants and the catalyst surface is not straight forward and therefore, further material characterization studies need to be performed. Nevertheless, the occurrence of water-gas shift like reaction over the $LaCoO_3$ sample cannot be ruled out which could explain the early CO oxidation and enhanced NO reduction yield under the wet reaction condition.

6.3.2 A-site Deficiency - $La_{0.85}CoO_3$

Certain studies have reported the enhancement in the catalytic activities by partial substitution of A cations either by another cation like Sr or Th [20,23] or generating deficient A-sites [37,54,55]. In either way, the perovskites with altered A sites have reportedly shown better reducibility [54], improved thermal

Table 6.5 Specific surface area for $LaCoO_3$ and $La_{0.85}CoO_3$ samples

Sample	Specific Surface Area[a] ($m^2.g^{-1}$)
$LaCoO_3$	8.4
$La_{0.85}CoO_3$	0.9

[a] measured by B.E.T. method

stability [54], increase in the number of oxygen vacant sites [56] and oxygen mobility in the material [54], which are considered to be crucial factors for catalytic performance. Since in the previous section, $LaCoO_3$ sample showed the best catalytic performance, a similar perovskite with La deficiency was therefore synthesized (named as '$La_{0.85}CoO_3$'). Results concerning the material characterization experiments and catalytic activity tests are discussed in the following parts in of this section.

6.3.2.1 Material Characterizations

N_2-Physisorption

The specific surface area calculated by the B.E.T. method for the $La_{0.85}CoO_3$ material is mentioned in Table 6.5. To determine the effect of A-site deficiency, the specific surface of $LaCoO_3$ is also mentioned in this table. It can be seen that with the deficient A-site, the specific surface area decreased drastically from 8.4 $m^2.g^{-1}$ to 0.9 $m^2.g^{-1}$. A decrease in the specific surface area indicates strong sintering of the particles in the material and can result in crystal growth [54]. Similar observations have also been reported by Wu et al [54] where the authors studied the change in the specific surface area of $La_{0.85}CoO_3$ (decrease from 4.6 to 2.4 m^2 g^{-1}) and $La_{0.85}Co_{0.8}Fe_{0.2}O_3$ (decrease from 4.5 to 2.4 m^2 g^{-1}) perovskites and concluded that the segregation of Co_3O_4 from the perovskite structure observed in La-deficient perovskites when compared with their La-sufficient counterpart can be correlated to this decrease in the specific surface area.

X-Ray Diffraction

The diffractogram for $La_{0.85}CoO_3$ is shown in Figure 6.5. For comparison, the diffractogram of $LaCoO_3$ is also included in this figure. It can be seen that upon reducing the La amount in the material, diffraction peaks corresponding to Co_3O_4 were observed for $La_{0.85}CoO_3$ sample. This indicates that not all the Co

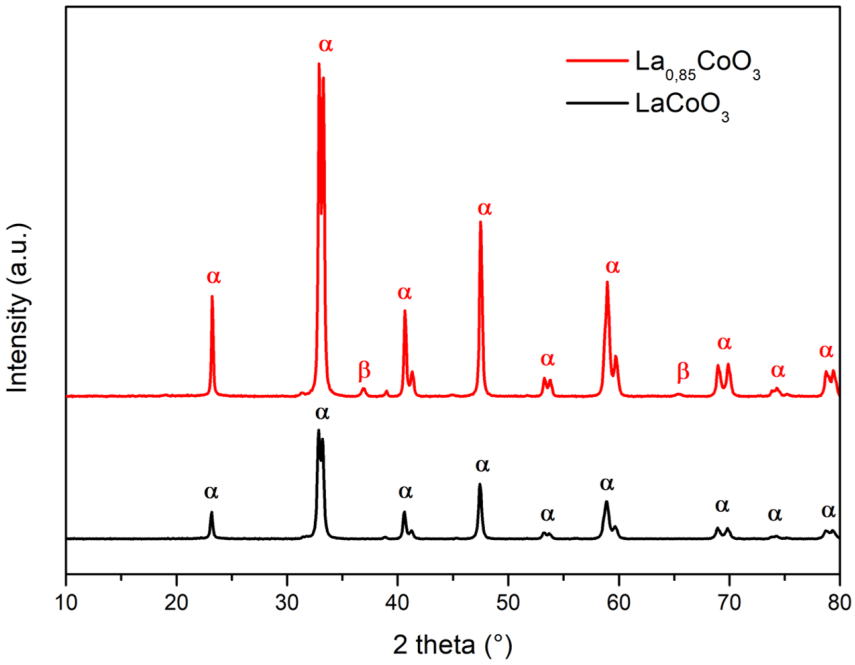

Figure 6.5 XRD analyses for $LaCoO_3$ and $La_{0.85}CoO_3$ (α = JCPDS 048-0123 and β = JCPDS 42-1467)

species went into the formation of perovskite structure. Similar observations were also reported by Wu et al [54] over $La_{0.85}CoO_3$ and $La_{0.85}Co_{0.8}Fe_{0.2}O_3$ catalysts and Schön et al [37] on $La_{1-y}FeO_3$ samples (in this case the segregated species was Fe_2O_3). They correlated this phenomenon with the drastic decrease in the specific surface area which is also evident in the current study (see Table 6.5).

H_2-TPR

To assess the reducibility of the materials, the H_2-TPR was conducted on the $La_{0.85}CoO_3$ sample and is shown in Figure 6.6. Again, for the comparison of the reducibility behaviour, the TPR profile for $LaCoO_3$ sample has also been shown in this figure. The different reduction peaks and specific H_2-consumption for the La-Co samples are enlisted in the Table 6.6.

As seen in Figure 6.6, the La-deficiency in the perovskites extracts the Co species from the perovskite structure and forms Co_3O_4. Reportedly, reduction of Co species in the Co_3O_4 structure is easier than in the perovskite structure [54]. This could explain the shift in the H_2 reduction peaks for $La_{0.85}CoO_3$ sample towards temperatures lower than what observed for $LaCoO_3$ sample. Moreover,

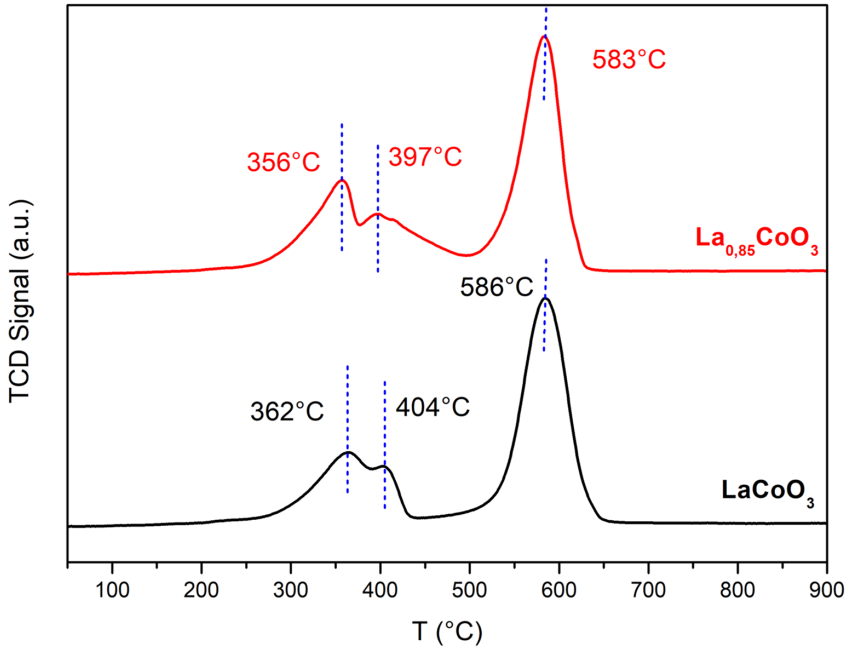

Figure 6.6 H_2-TPR analyses on $LaCoO_3$ and $La_{0.85}CoO_3$ samples

Table 6.6 H_2 reduction peaks and specific H_2 consumption for $La_{0.85}CoO_3$ and $LaCoO_3$ samples

Sample	Peak reduction temperature (°C)			Sp. H_2 Cons.[a] ($mmol.g^{-1}$)
	1st Peak	2nd Peak	3rd Peak	
$LaCoO_3$	362	404	586	6.02
$La_{0.85}CoO_3$	356	397	583	6.90

[a] Specific H_2 Consumption

the reduction peaks between 300-400°C is well separated in case of $La_{0.85}CoO_3$ than in case of $LaCoO_3$. Wu et al. [54] also observed such a difference in the TPR profiles for their $LaCoO_3$ and $La_{0.85}CoO_3$ samples. They attributed such a phenomenon reduction of Co^{3+} to metallic Co proceeds at low temperature from 350°C and involves two reduction peaks followed by the reduction of Co^{3+} species in the perovskite structure to Co^{2+} species. This segregation may have also led to a greater number of reducible species as evident from difference in the specific H_2 consumption data (see Table 6.6).

6.3.2.2 Catalytic Activity

The catalytic performance of the $LaCoO_3$ and $La_{0.85}CoO_3$ has been compared and shown in Figure 6.7. The discussions over the CO and NO conversion

activities under the dry and wet reaction conditions are discussed individually in the following sections.

In Figure 6.7 (a), the CO conversion activity for $LaCoO_3$ and $La_{0.85}CoO_3$ are compared. The corresponding T_{50} and T_{90} temperatures for CO conversions are enlisted in Table 6.7. It can be seen for the figure that decreasing the amount of La in the perovskite sample improved the CO conversion activity under dry reaction condition. However, under the wet reaction condition, there was no change in the T_{50} temperatures for CO conversion in both the samples whereas the T_{90} temperature for $La_{0.85}CoO_3$ shifted towards higher temperatures than that for $LaCoO_3$ sample (see Table 6.7). CO conversion activity was independent of the amount of La in the sample. An improvement in the CO oxidation activity due to La-deficiency in the perovskite samples has also been reported by Schön et al [37] over $La_{1-y}FeO_3$ perovskites under lean

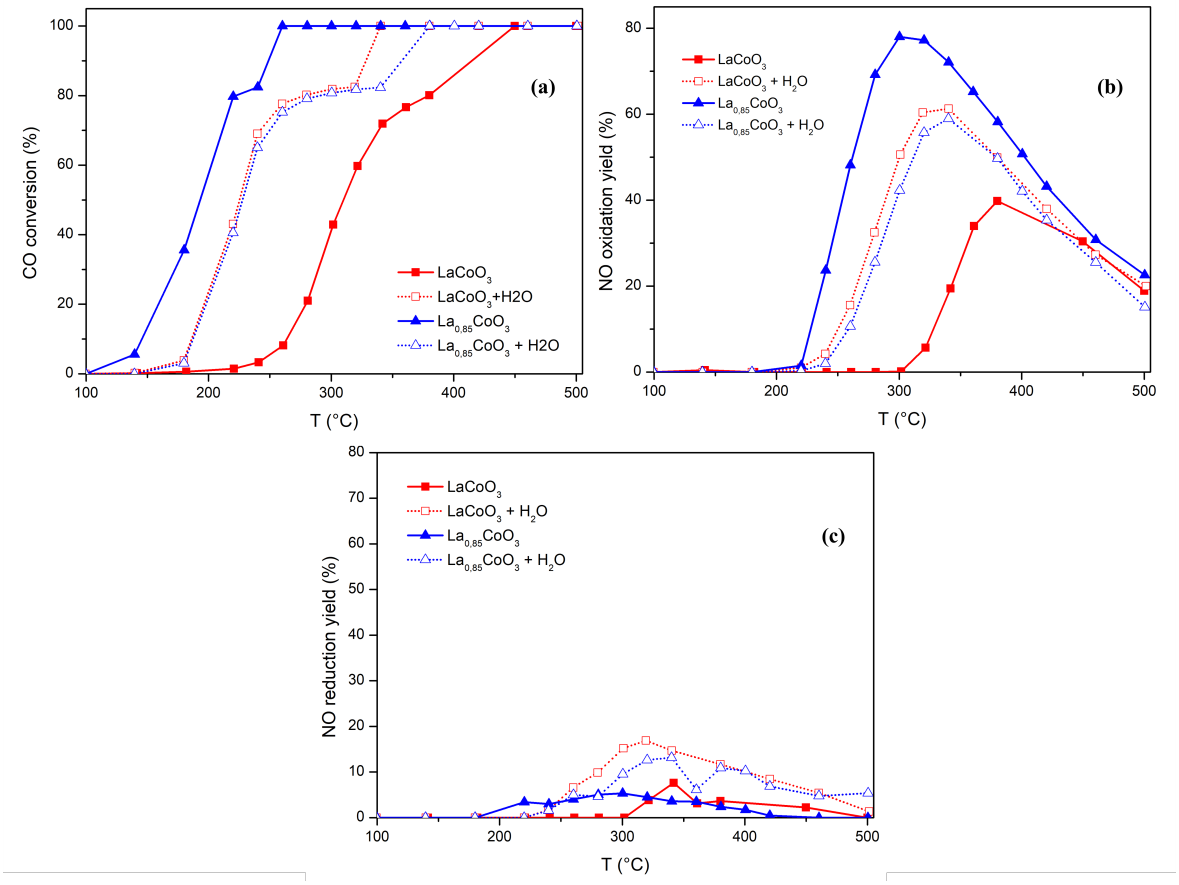

Figure 6.7 Comparison of catalytic activities of $LaCoO_3$ and $La_{0.85}CoO_3$ based on (a) CO conversion (%), (b) NO oxidation yield (%) and (c) NO reduction yield (%)

Table 6.7 T_{50} and T_{90} temperatures for CO conversion over $LaCoO_3$ and $La_{0.85}CoO_3$perovskite samples

Sample	Dry reaction Conditions		Wet reaction Conditions	
	T_{50}(°C)	T_{90}(°C)	T_{50}(°C)	T_{90}(°C)
$LaCoO_3$	310	415	226	329
$La_{0.85}CoO_3$	193	249	228	369

and rich auto-exhaust gas condition. The authors attributed this increase in the catalytic activity with degree of La-deficiency to the strong interaction between the Fe_2O_3 and perovskite structures and improved concentration of active Fe species on the catalyst surface due to La deficiency. In the present study, active Co species may have been increased in the catalyst surface due to the lowering of La content in the perovskite and therefore, have led to enhancement in the CO oxidation to CO_2. However, the delay in the CO conversions under the wet reaction condition for $La_{0.85}CoO_3$ indicates that H_2O species occupied the active sites in the catalyst thereby leaving a smaller number of sites for CO adsorption and subsequently conversion into CO_2.

In Figure 6.7(b), it can be seen that upon decreasing the La content in the perovskite, the NO oxidation yield increases under the dry reaction condition but under the wet reaction condition, no considerable difference is observed. Previous reports in the literature demonstrate that decreasing the La-content in the perovskite increases the oxygen vacant sites and oxygen mobility in the material [54,56]. Due to the excess amount of O_2 in the reactant gas mixture, these oxygen vacant sites can be occupied by the O_2 in the gas phase [57] and therefore, do not provide a lot of vacant sites active for NO decomposition reaction [38]. These filled oxygen sites can eventually react with NO species generally adsorbed on the B cations and form NO_2 [58]. Moreover, the presence of Co_3O_4 species segregated from the perovskite structure in the $La_{0.85}CoO_3$ sample (confirmed by XRD, see Figure 6.5) can also facilitate the NO oxidation reaction [59]. These two mechanisms may have taken place simultaneously and could possibly explain the increase in NO_2 formation over the La deficient perovskite. However, under the wet reaction condition, H_2O, O_2 and NO compete for these oxygen vacant sites and therefore, decreases the NO oxidation reaction.

Furthermore, under the wet reaction conditions (see Figure 6.7(c)), the NO reduction yield was observed to be higher than that under the dry reaction condition for both the La-Co samples. It can be possibly explained by the dissociation of adsorbed H_2O species into H and OH species and its subsequent reaction with the adsorbed NO species to form N species, an important intermediate for the N_2 formation [45,46]. Upon comparing the NO reduction yield for $La_{0.85}CoO_3$ with $LaCoO_3$, it can be observed that the NO reduction yield for $La_{0.85}CoO_3$ sample is lower than that of the $LaCoO_3$ sample both under dry and wet reaction condition even if more oxygen vacant sites and better oxygen mobility are expected in the former than in the latter sample. This could be explained by the low specific surface area of $La_{0.85}CoO_3$ which may have led to the inaccessible active sites thereby degrading the catalytic performance [37].

6.3.3 B site Substitution - $La_{0.85}Co_{1-x}Cu_xO_3$

As seen in bibliographic review, the degree of substitution of B site metal cation by other cations can improve the catalytic activity of NO reduction by CO because of the increase in the number of oxygen vacant sites and enhanced lattice oxygen mobility in the material. Therefore, to assess the effect of degree of B site substitution on the NO reduction by CO activity under the industrial flue gas condition $La_{0.85}Co_{1-x}Cu_xO_3$ ($0 < x < 0.25$) perovskite samples were synthesized and tested for their material properties and catalytic performance. The results for the material characterization and catalytic activity studies are discussed in this section.

6.3.3.1 Material Characterization

N_2-Physisorption

N_2-physisorption was performed on the $La_{0.85}Co_{1-x}Cu_xO_3$ samples to determine the corresponding specific surface area. The specific surface areas of these samples along with $La_{0.85}CoO_3$ (for comparison) are enlisted in Table 6.8. It can be seen that the specific surface area of the perovskite increases with the increase in Cu substitution at the B-site but only until $x = 0.2$. All the $La_{0.85}Co_{1-x}Cu_xO_3$ samples show a specific surface area between 8-11 $m^2.g^{-1}$ except for $La_{0.85}CoO_3$ which has a specific surface area below 1 $m^2.g^{-1}$. An increase in the specific surface by partial substitution of B-site cation has already been reported by Zhang et al. [19] on $LaMn_{1-x}Cu_xO_3$ and Peter et al. [21] on

$La_2Cu_{1-x}Fe_xO_4$ perovskites. However, increase in degree of B-site substitution does not necessarily increase the specific surface as observed by Zhang et al. [41] and Wu et al. [54] for $LaCo_{0.8}Cu_{0.2}O_3$ and $La_{0.8}Co_{0.8}Fe_{0.2}O_3$ perovskites respectively. However, none of the authors have discussed this effect of B-site substitution on specific surface area of the perovskite material.

Table 6.8 Specific surface area for $La_{0.85}Co_{1-x}Cu_xO_3$ samples

Sample	Specific Surface Area ($m^2.g^{-1}$)[a]
$La_{0.85}CoO_3$	0.9
$La_{0.85}Co_{0.9}Cu_{0.1}O_3$	8.0
$La_{0.85}Co_{0.8}Cu_{0.2}O_3$	10.7
$La_{0.85}Co_{0.75}Cu_{0.25}O_3$	9.4

[a] measured by B.E.T. method

X-ray Diffraction (XRD)

The comparison of the diffractograms obtained from the XRD analyses of $La_{0.85}Co_{1-x}Cu_xO_3$ are shown in Figure 6.8. In Figure 6.8 (a), it can be seen that all the samples have typical perovskites structures after the calcination. Upon further investigation of the diffractograms between the 35-40° (see Figure 6.8), it was observed that the diffraction peaks attributed to Co_3O_4 vanished upon partial substitution of Co in the perovskites and no peaks corresponding to copper oxide species are observed on any of the samples. This indicates that both Cu and Co are well integrated into the perovskite structure. Moreover, in Figure 6.8 (c), it can be seen that the crystallographic structure of the perovskite changed from rhombohedral (identified by the doublet diffraction peak) to orthorhombic with the increase in the degree of Co substitution by Cu in the perovskite. Similar change in the crystallographic structure of perovskite upon partial substitution of B site cation have been reported by Dinamarca et al. [56] and Mota et al. [60] on $LaMn_{1-x}Co_xO_3$ and $LaCo_{1-x}Ru_xO_3$ perovskites respectively. Mota et al. [60] explained in their study that the decrease in the tolerance factor from 1 is generally recorded for different degree of substitution of Ru in $LaCoO_3$ perovskite which results in the distortion of its rhombohedral structure and moves towards structure with lower coordination number for A cation.

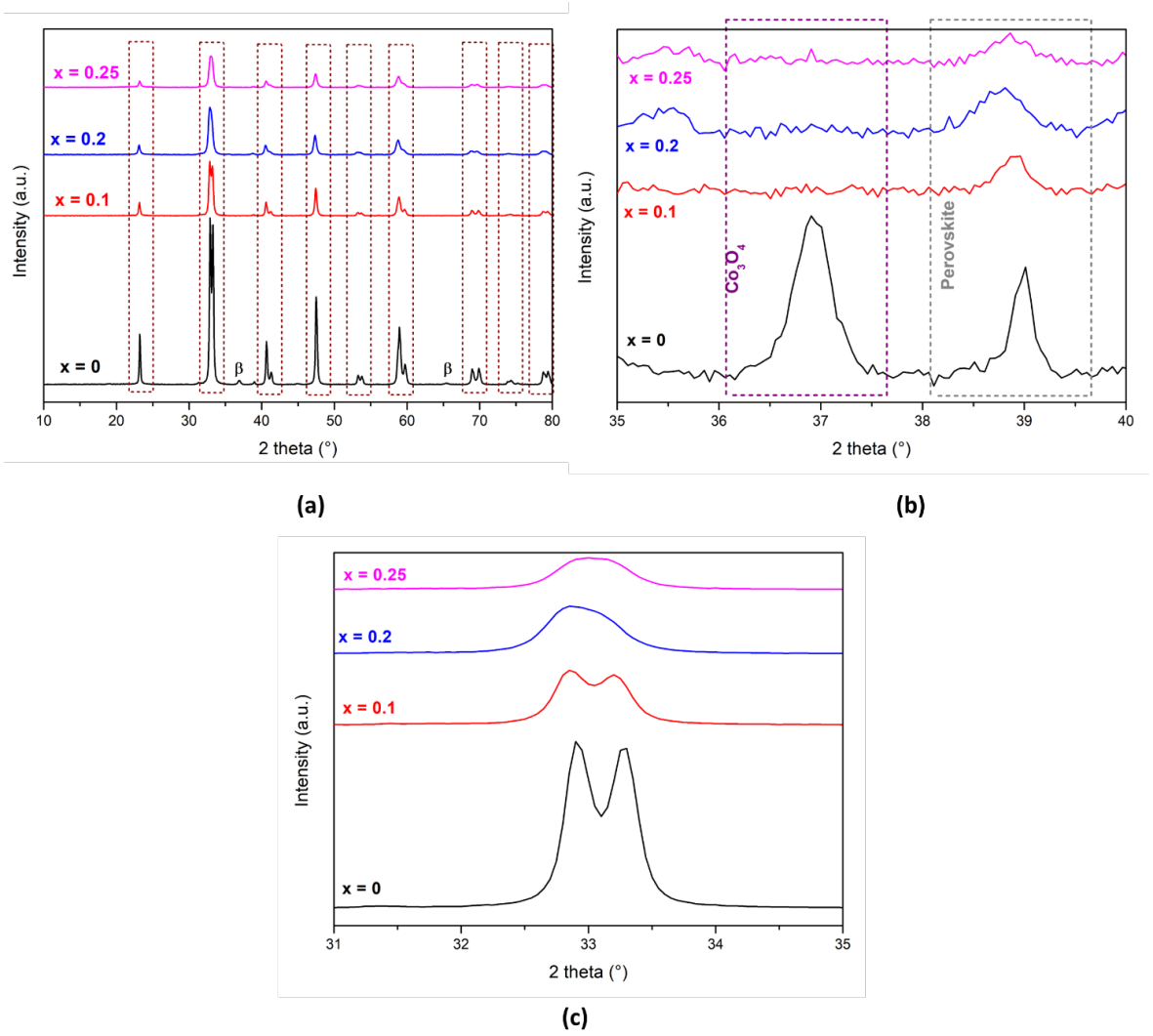

Figure 6.8 XRD analyses on the $La_{0.85}Co_{1-x}Cu_xO_3$ sample and the comparison of diffractograms between (a) 10-80°, (b) 35-40° and (c) 30-35° diffractograms

H_2-TPR

The reducibility of the different $La_{0.85}Co_{1-x}Cu_xO_3$ samples are assessed by H_2-TPR analysis and the results are shown in Figure 6.9. Moreover, the reduction temperatures for the different H_2 reduction peaks and specific H_2 consumption values are enlisted in Table 6.9. From Figure 6.9, it can be concluded that inclusion of Cu into the perovskite improves the reducibility of the active species indicated by the shift in the reduction peaks to the low temperatures for $0.1 \leq x \leq 0.25$ samples when compared with $x = 0$ sample. Also, it can be seen that $La_{0.85}Co_{0.9}Cu_{0.1}O_3$ sample shows 4 different H_2 reduction peaks while only two reduction peaks are recorded for $La_{0.85}Co_{0.8}Cu_{0.2}O_3$ and $La_{0.85}Co_{0.25}Cu_{0.15}O_3$

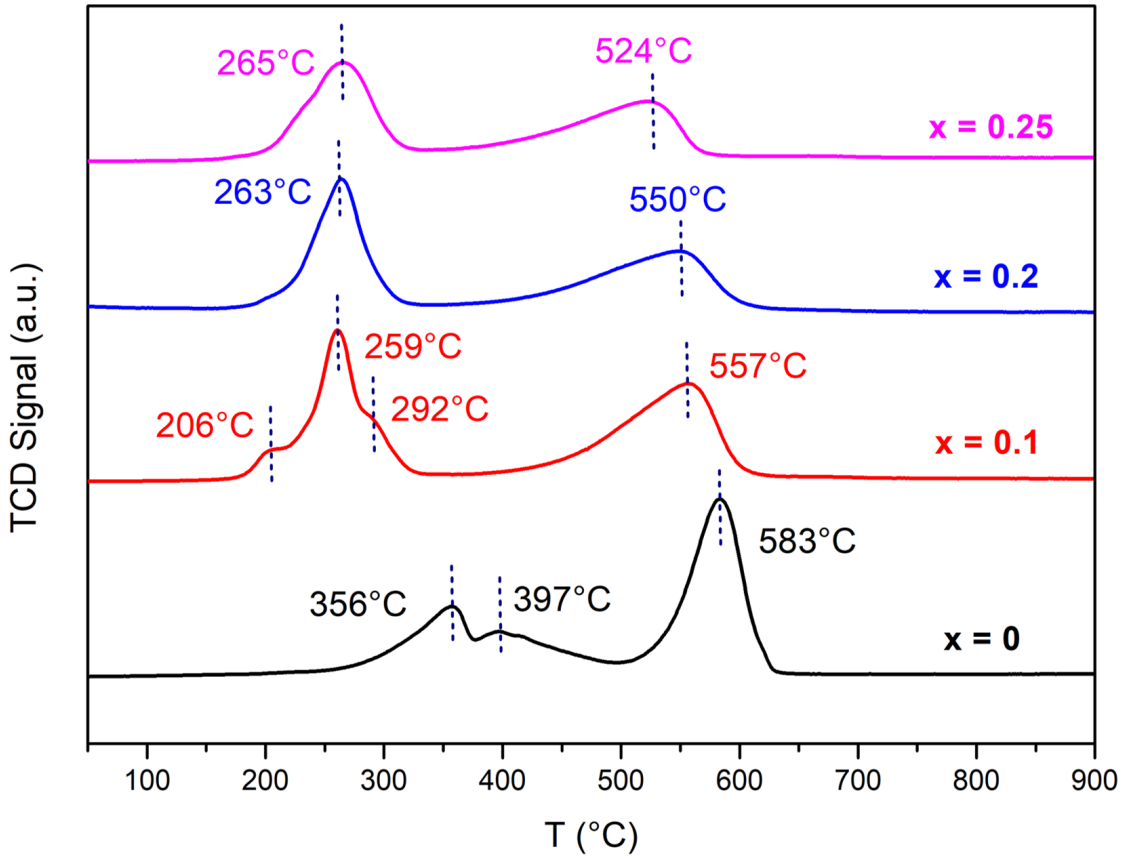

Figure 6.9 H_2-TPR analysis of $La_{0.85}Co_{1-x}Cu_xO_3$ samples

samples. The low temperature reduction peaks between 200-35O°C can be attributed to the reduction of Cu^{2+} species into metallic Cu and Co^{3+} species into Co^{2+} species simultaneously [20,40]. Moreover, the reduction peak between 500-600°C can be attributed to the reduction of Co^{2+} into metallic Co respectively [40]. Interestingly, the shoulder reduction peaks at 206°C and 292°C observed for x = 0.1 sample vanishes with the further increase in the degree of Cu substitution at the B-site of the perovskite. Similar observations were reported by Zhou et al. [61]. Upon combining TPR and XPS analyses on the samples, the authors concluded that the enrichment of CuO species on the surface with the degree of substitution of Cu at the B-site resulted in the single H_2 reduction peak at 260-280°C which is attributed to the reduction of Cu^{2+} species into metallic Cu [61]. Furthermore, upon comparing this phenomenon to the corresponding specific H_2 consumption in this study (see Table 6.9), it can be hypothesized that the copper species in samples with x > 0 are arranged

Table 6.9 H_2 reduction peaks and specific H_2 consumption for $La_{0.85}Co_{1-x}Cu_xO_3$ samples

Sample	Peak reduction temperature (°C)				Sp. H_2 Cons.[a] ($mmol.g^{-1}$)
	1st Peak	2nd Peak	3rd Peak	4th Peak	
$La_{0.85}CoO_3$	356	397	583	––	6.02
$La_{0.85}Co_{0.9}Cu_{0.1}O_3$	206	259	292	557	7.81
$La_{0.85}Co_{0.8}Cu_{0.2}O_3$	263	550	––	––	7.35
$La_{0.85}Co_{0.75}Cu_{0.25}O_3$	265	524	––	––	6.54

(a) Specific H_2 Consumption

in different coordination environments for different degree of substitution which affects the reducibility of the active metal species in the corresponding perovskite samples [60,62]. Moreover, from the XRD analyses shown in Figure 6.8, a change in the crystallographic structure of the perovskite is observed for $x > 0.1$ which further supports this hypothesis [60]. However, characterization methods like XANES or XPS need to be performed to understand the coordinate environment of the active species on the catalyst surface.

6.3.3.2 Catalytic Activity

A comparison of catalytic performances among different $La_{0.85}Co_{1-x}Cu_xO_3$ are shown in the Figure 6.10. In Figure 6.10 (a), CO conversion activity of $La_{0.85}Co_{1-x}Cu_xO_3$ samples are compared. It can be seen that increase in the Cu content in the $La_{0.85}Co_{1-x}Cu_xO_3$ delays the CO conversion activity both under dry and wet reaction conditions. However, no appreciable difference in CO conversion activity can be observed between $x = 0$ and $x = 0.2$ under dry reaction condition and $x = 0.1$ and $x = 0.2$ under the wet reaction condition. Comparing the CO conversion activity of the samples to their corresponding specific surface area (refer Table 6.8) and reducibility (refer Figure 6.9 and Table 6.9), no correlation can be derived implying that specific surface area and reducibility of active metal species in the sample are not decisive factors for the catalytic activity of these samples. In the literature for NO reduction by CO over perovskite studies, the surface metal composition and presence of oxygen vacant sites have been considered to be the important factors for NO reduction by CO reaction which can be determined by X-ray Photoelectron Spectroscopy (XPS) technique of material characterization [18,37,55,56]. Moreover, presence of water in the reaction system delays the CO conversion activity which can be

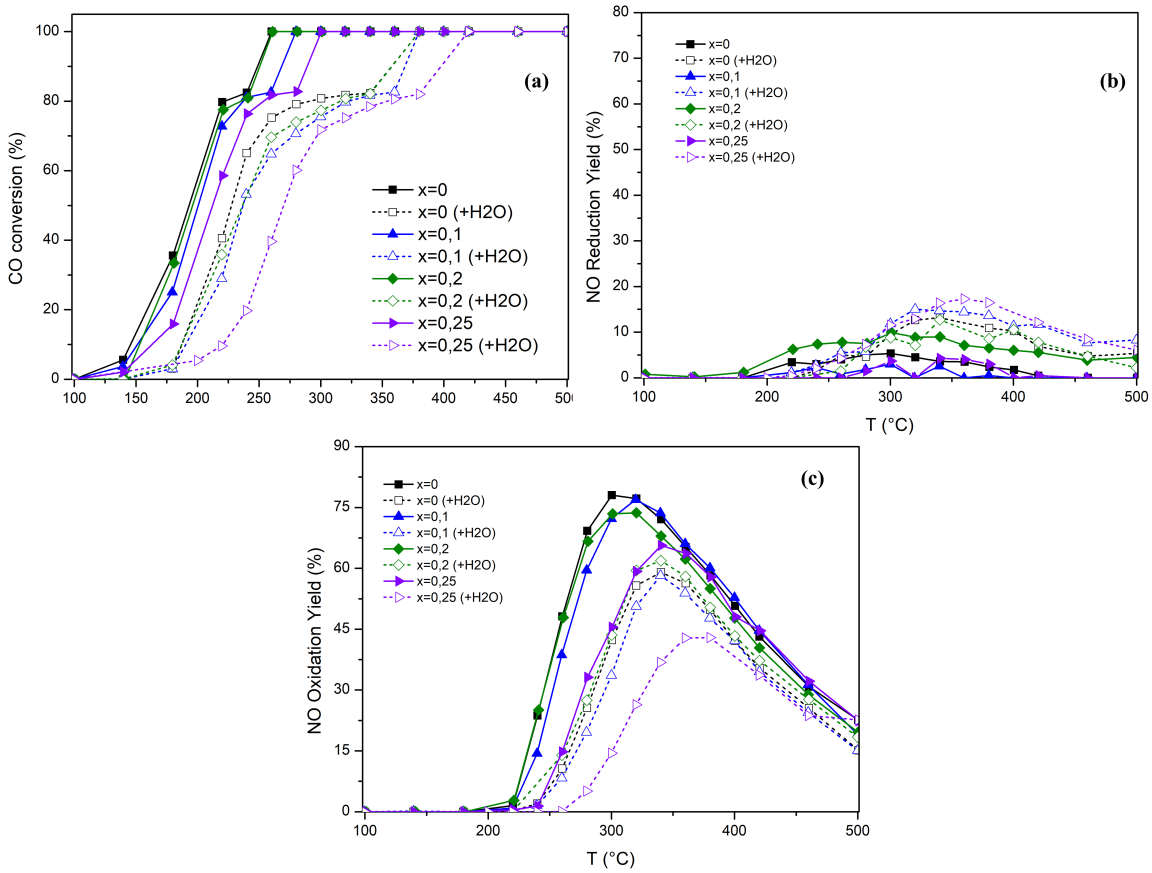

Figure 6.10 CO and NO conversions for $La_{0.85}Co_{1-x}Cu_xO_3$ perovskite samples (a) CO conversion (b) NO reduction yield and (c) NO oxidation yield

attributed to the competition between the CO and H_2O for the common active sites in the catalyst samples [63].

In Figure 6.10 (b) and (c), NO oxidation and reduction yield over the $La_{0.85}Co_{1-x}Cu_xO_3$ samples under dry and wet reaction conditions are compared. Under dry reaction conditions, the NO reduction yield for the $La_{0.85}Co_{1-x}Cu_xO_3$ samples are below 5% except for the sample with x = 0.25, where the NO reduction yield reached a maximum value of 10%. Further, under the wet reaction conditions, the NO reduction yield for all the samples increased considerably implying the occurrence of water-gas shift like reaction. However, under the wet reaction condition, sample with x = 0.25 showed the highest NO reduction yield of 17% followed by x = 0.1, 0.2 and 0 samples. Additionally, upon comparing the NO oxidation yield over the $La_{0.85}Co_{1-x}Cu_xO_3$ samples (refer Figure 6.10 (c), interestingly, x = 0.25 sample showed the lowest value among

all the samples both under dry and wet reaction conditions. Moreover, the samples other than x = 0.25 showed similar NO oxidation activity both under wet and dry reaction conditions. Furthermore, presence of water decreases the NO oxidation yield and shifts the NO oxidation yield peak to temperatures higher than that under the dry reaction conditions. This can probably be explained by the formation of hydroxyl species from the dissociation of water competing with O_2 for the common oxygen vacant sites on the catalyst surface and simultaneously competing with NO for the common metal active sites on the catalyst [41]. Moreover, the enhancement in NO reduction activity under wet reaction condition can be attributed to the NO dissociation facilitated by the H species formed from the dissociation of the adsorbed H_2O species on the catalyst surface [46].

6.4 Conclusion

In conclusion, perovskite-based materials are active for the NO reduction by CO under industrial flue gas condition i.e., oxidative, and wet conditions. To explore the potential metal composition, firstly, different B-site cations like Co, Mn and Fe in $LaBO_3$ were synthesized, characterized and tested for the catalytic performance. $LaCoO_3$ showed superior catalytic activity among the different $LaBO_3$ samples. Secondly, the effect of A-site deficiency on the catalytic activity was studied over $La_{0.85}CoO_3$ and was compared with the $LaCoO_3$ sample. It was observed that decreasing the La content changes the material properties drastically and enhances the CO and NO oxidation activity but lowers the NO reduction activity. Thirdly, the effect of different degrees of partial substitution of B-site cation i.e., Co was studied. NO correlation between the specific surface area, reducibility of active metal species in the sample and the catalytic performance was established. It was concluded that presence of different number of oxygen vacant sites and different surface metal composition of the perovskites can be the reason for the difference in their corresponding catalytic activities. Therefore, material characterization techniques like XPS are required to be performed in order to better understand this difference in the catalytic performance and postulate the underlying reaction mechanism.

References

[1] P.C. Reshmi Varma, Low-dimensional perovskites, Elsevier Inc., 2018. doi:10.1016/B978-0-12-812915-9.00007-1.

[2] S. Royer, D. Duprez, F. Can, X. Courtois, C. Batiot-Dupeyrat, S. Laassiri, H. Alamdari, Perovskites as substitutes of noble metals for heterogeneous catalysis: Dream or reality, Chem. Rev. 114 (2014) 10292–10368. doi:10.1021/cr500032a.

[3] G. Nirala, D. Yadav, S. Upadhyay, Ruddlesden-Popper phase A2BO4 oxides: Recent studies on structure, electrical, dielectric, and optical properties, J. Adv. Ceram. 9 (2020) 129–148. doi:10.1007/s40145-020-0365-x.

[4] S. Royer, C. Ayrault, C. Carnevillier, F. Epron, P. Marécot, D. Duprez, Enthalpy recovery of gases issued from H_2 production processes: Activity and stability of oxide and noble metal catalysts in oxidation reaction under highly severe conditions, Catal. Today. 117 (2006) 543–548. doi:10.1016/j.cattod.2006.06.023.

[5] C. Oliva, M. Allieta, M. Scavini, C. Biffi, I. Rossetti, L. Forni, D. Chimica, V.C. Golgi, Electron Paramagnetic Resonance Analysis of La, Inorg. Chem. 51 (2012) 8433-8440.

[6] P. Esmaeilnejad-Ahranjani, A. Khodadadi, H. Ziaei-Azad, Y. Mortazavi, Effects of excess manganese in lanthanum manganite perovskite on lowering oxidation light-off temperature for automotive exhaust gas pollutants, Chem. Eng. J. 169 (2011) 282–289. doi:10.1016/j.cej.2011.02.062.

[7] Y. Gu, Y. Yang, Y. Qiu, K. Sun, X. Xu, $LaMn_{1-x}Cu_xO_3$ Perovskite Catalysts Prepared for Volatile Organic Compounds Combustion, Asian J. Chem. 23 (2011) 1247–1251.

[8] J. Niu, J. Deng, W. Liu, L. Zhang, G. Wang, H. Dai, H. He, X. Zi, Nanosized perovskite-type oxides $La_{1-x}Sr_xMO_{3-\delta}$ (M = Co, Mn; x = 0, 0.4) for the catalytic removal of ethylacetate, Catal. Today. 126 (2007) 420–429. doi:10.1016/j.cattod.2007.06.027.

[9] O. Mihai, D. Chen, A. Holmen, Chemical looping methane partial oxidation: The effect of the crystal size and O content of $LaFeO_3$, J. Catal. 293 (2012) 175–185. doi:10.1016/j.jcat.2012.06.022.

[10] K. Heitnes, S. Lindberg, O.A. Rokstad, A. Holmen, Catalytic partial oxidation of methane to synthesis gas using monolithic reactors, Catal. Today. 21 (1994) 471–480. doi:10.1016/0920-5861(94)80169-X.

[11] J. Zhu, D. Xiao, J. Li, X. Yang, Y. Wu, Kinetics and mechanism of NO decomposition over $La_{0.4}Sr_{0.6}Mn_{0.8}Ni_{0.2}O_3$ perovskite-type oxides, J. Mol. Catal. A Chem. 236 (2005) 182–186. doi:10.1016/j.molcata.2005.04.018.

[12] J. Zhu, X. Yang, X. Xu, K. Wei, Erratum: Active site structure of NO decomposition on perovskite(-like) oxides: An investigation from experiment and density functional theory (J. Phys. Chem. C (2007) 111C (16838) 10.1021/jp9076596), J. Phys. Chem. C. 113 (2009) 16838. doi:10.1021/jp9076596.

[13] C. Tofan, D. Klvana, J. Kirchnerova, Decomposition of nitric oxide over perovskite oxide catalysts: Effect of CO_2, H_2O and CH_4, Appl. Catal. B Environ. 36 (2002) 311–323. doi:10.1016/S0926-3373(01)00312-5.

[14] X. Wu, L. Xu, D. Weng, The NO selective reduction on the $La_{1-x}Sr_xMnO_3$ catalysts, Catal. Today. 90 (2004) 199–206. doi:10.1016/j.cattod.2004.04.027.

[15] H.H. Tseng, H.Y. Lin, Y.F. Kuo, Y.T. Su, Synthesis, characterization, and promoter effect of Cu-Zn/γ-Al_2O_3 catalysts on NO reduction with CO, Chem. Eng. J. 160 (2010) 13–19.
doi:10.1016/j.cej.2010.02.039.

[16] I. Twagirashema, M. Frere, L. Gengembre, C. Dujardin, P. Granger, Structural regeneration of $LaCoO_3$ perovskite-based catalysts during the NO + H_2 + O_2 reactions, Top. Catal. 42–43 (2007) 171–176. doi:10.1007/s11244-007-0173-3.

[17] A.E. Giannakas, A.K. Ladavos, P.J. Pomonis, Preparation, characterization and investigation of catalytic activity for NO + CO reaction of $LaMnO_3$ and $LaFeO_3$ perovskites prepared via microemulsion method, Appl. Catal. B Environ. 49 (2004) 147–158.
doi:10.1016/j.apcatb.2003.12.002.

[18] Y. Wu, L. Li, B. Chu, Y. Yi, Z. Qin, M. Fan, Q. Qin, H. He, L. Zhang, L. Dong, B. Li, L. Dong, Catalytic reduction of NO by CO over B−site partially substituted $LaM_{0.25}Co_{0.75}O_3$ (M=Cu, Mn, Fe) perovskite oxide catalysts: The correlation between physicochemical properties and catalytic performance, Appl. Catal. A Gen. 568 (2018) 43–53.
doi:10.1016/j.apcata.2018.09.022.

[19] R. Zhang, A. Villanueva, H. Alamdari, S. Kaliaguine, Reduction of NO by CO over nanoscale $LaCo_{1-x}Cu_xO_3$ and $LaMn_{1-x}Cu_xO_3$ perovskites, J. Mol. Catal. A Chem. 258 (2006) 22–34. doi:10.1016/j.molcata.2006.05.008.

[20] A. Tarjomannejad, A. Niaei, M.J.I. Gómez, A. Farzi, D. Salari, V. Albaladejo-Fuentes, NO + CO reaction over $LaCu0_{0.7}B_{0.3}O_3$ (B = Mn, Fe, Co) and $La_{0.8}A_{0.2}$ $Cu_{0.7}Mn_{0.3}$ O_3 (A = Rb, Sr, Cs, Ba) perovskite-type catalysts, J. Therm. Anal. Calorim. 129 (2017) 671–680. doi:10.1007/s10973-017-6264-x.

[21] S.D. Peter, E. Garbowski, V. Perrichon, B. Pommier, M. Primet, Activity enhancement of mixed lanthanum-copper-iron-perovskites in the CO+NO reaction, Appl. Catal. A Gen. 205 (2001) 147–158. doi:10.1016/S0926-860X(00)00551-2.

[22] X. Li, C. Tang, M. Ai, L. Dong, Z. Xu, Controllable synthesis of pure-phase rare-earth orthoferrites hollow spheres with a porous shell and their catalytic performance for the CO + NO reaction, Chem. Mater. 22 (2010) 4879–4889. doi:10.1021/cm101419w.

[23] Z. Zhao, X. Yang, Y. Wu, Characterization and catalytic behavior of $La_{2-x}(Sr, Th)_xCuO_{4\pm\lambda}$ in reaction NO + CO, Sci. China, Ser. B Chem. 40 (1997) 464–474. doi:10.1007/BF02875414.

[24] A.A. Leontiou, A.K. Ladavos, P.J. Pomonis, Catalytic NO reduction with CO on
$La_{1-x}Sr_x(Fe^{3+}/Fe^{4+})O_{3\pm\delta}$ perovskite-type mixed oxides (x = 0.00, 0.15, 0.30, 0.40, 0.60, 0.70, 0.80, and 0.90), Appl. Catal. A Gen. 241 (2003) 133–141. doi:10.1016/S0926-860X(02)00457-X.

[25] H. He, M. Liu, H. Dai, W. Qiu, X. Zi, An investigation of NO/CO reaction over perovskite-type oxide $La_{0.8}Ce_{0.2}B_{0.4}Mn_{0.6}O_3$ (B = Cu or Ag) catalysts synthesized by reverse microemulsion, Catal. Today. 126 (2007) 290–295. doi:10.1016/j.cattod.2007.06.004.

[26] R. Zhang, W. Yang, J. Xue, B. Chen, Role of structural deficiency of nanoscaled perovskites prepared by reactive grinding on the catalytic purification of exhaust pollutants, Int. J. Chem. React. Eng. 7 (2009). doi:10.2202/1542-6580.1875.

[27] Y. Wu, B. Chu, M. Zhang, Y. Yi, L. Dong, M. Fan, G. Jin, L. Zhang, B. Li, Influence of calcination temperature on the catalytic properties of $LaCu_{0.25}Co_{0.75}O_3$

catalysts in NO_x reduction, Appl. Surf. Sci. 481 (2019) 1277–1286. doi:10.1016/j.apsusc.2019.03.263.

[28] Y. Qin, L. Sun, D. Zhang, L. Huang, Role of ceria in the improvement of SO_2 resistance of $La_xCe_{1-x}FeO_3$ catalysts for catalytic reduction of NO with CO, Catal. Commun. 79 (2016) 53–57. doi:10.1016/j.catcom.2016.03.005.

[29] Y. Wu, G. Li, B. Chu, L. Dong, Z. Tong, H. He, L. Zhang, M. Fan, B. Li, L. Dong, NO Reduction by CO over Highly Active and Stable Perovskite Oxide Catalysts $La_{0.8}Ce_{0.2}M_{0.25}Co_{0.75}O_3$ (M = Cu, Mn, Fe): Effect of the Role in B Site, Ind. Eng. Chem. Res. 57 (2018) 15670–15682. doi:10.1021/acs.iecr.8b04214.

[30] A. Tarjomannejad, A. Farzi, A. Niaei, D. Salari, NO reduction by CO over $LaB_{0.5}B_{0.5}O_3$ (B = Fe, Mn, B=Fe, Mn, Co, Cu) perovskite catalysts, an experimental and kinetic study, J. Taiwan Inst. Chem. Eng. 78 (2017) 200–211. doi:10.1016/j.jtice.2017.05.034.

[31] Y. Yi, H. Liu, B. Chu, Z. Qin, L. Dong, H. He, C. Tang, M. Fan, L. Bin, Catalytic removal NO by CO over $LaNi_{0.5}M_{0.53}$ (M=Co, Mn, Cu) perovskite oxide catalysts: Tune surface chemical composition to improve N_2 selectivity, Chem. Eng. J. 369 (2019) 511–521. doi:10.1016/j.cej.2019.03.066.

[32] A.A. Leontiou, A.K. Ladavos, G.S. Armatas, P.N. Trikalitis, P.J. Pomonis, Kinetics investigation of NO + CO reaction on La-Sr-Mn-O perovskite-type mixed oxides, Appl. Catal. A Gen. 263 (2004) 227–239. doi:10.1016/j.apcata.2003.12.017.

[33] A.K. Ladavos, P.J. Pomonis, Mechanistic aspects of NO+CO reaction on $La_{2-x}Sr_xNiO_{4-\delta}$ (x=0.00–1.50) perovskite-type oxides, Appl. Catal. A Gen. 165 (1997) 73–85. doi:10.1016/s0926-860x(97)00192-0.

[34] R. Zhang, H. Alamdari, S. Kaliaguine, Fe-based perovskites substituted by copper and palladium for NO + CO reaction, J. Catal. 242 (2006) 241–253. doi:10.1016/j.jcat.2006.05.033.

[35] R.K.C. de Lima, M.S. Batista, M. Wallau, E.A. Sanches, Y.P. Mascarenhas, E.A. Urquieta-González, High specific surface area LaFeCo perovskites-Synthesis by nanocasting and catalytic behavior in the reduction of NO with CO, Appl. Catal. B Environ. 90 (2009) 441–450. doi:10.1016/j.apcatb.2009.04.004.

[36] J. Zhu, Z. Zhao, D. Xiao, J. Li, X. Yang, Y. Wu, Application of cyclic voltammetry in heterogeneous catalysis: NO decomposition and reduction, Electrochem. Commun. 7 (2005) 58–61. doi:10.1016/j.elecom.2004.11.005.

[37] A. Schön, C. Dujardin, J.P. Dacquin, P. Granger, Enhancing catalytic activity of perovskite-based catalysts in three-way catalysis by surface composition optimisation, Catal. Today. 258 (2015) 543–548. doi:10.1016/j.cattod.2014.11.002.

[38] S. Furfori, N. Russo, D. Fino, G. Saracco, V. Specchia, NO SCR reduction by hydrogen generated in line on perovskite-type catalysts for automotive diesel exhaust gas treatment, Chem. Eng. Sci. 65 (2010) 120–127. doi:10.1016/j.ces.2009.01.065.

[39] R. Zhang, A. Villanueva, H. Alamdari, S. Kaliaguine, Cu- and Pd-substituted nanoscale Fe-based perovskites for selective catalytic reduction of NO by propene, J. Catal. 237 (2006) 368–380. doi:10.1016/j.jcat.2005.11.019.

[40] R. Zhang, A. Villanueva, H. Alamdari, S. Kaliaguine, Catalytic reduction of NO by propene over $LaCo_{1-x}Cu_xO_3$ perovskites synthesized by reactive grinding, Appl. Catal. B Environ. 64 (2006) 220–233. doi:10.1016/j.apcatb.2005.10.028.

[41] R. Zhang, H. Alamdari, S. Kaliaguine, Water vapor sensitivity of nanos-

ized La(Co, Mn, Fe)$_{1-x}$(Cu, Pd)$_x$O$_3$ perovskites during NO reduction by C_3H_6 in the presence of oxygen, Appl. Catal. B Environ. 72 (2007) 331–341. doi:10.1016/j.apcatb.2006.10.025.

[42] Y. Wu, H. Liu, G. Li, L. Jin, X. Li, X. Ou, L. Dong, G. Jin, B. Li, Tuning composition on B sites of $LaM_{0.5}Mn_{0.5}O_{0.3}$ (M = Cu, Co, Fe, Ni, Cr) perovskite catalysts in NO_x efficient reduction, Appl. Surf. Sci. 508 (2020). doi:10.1016/j.apsusc.2019.145158.

[43] S.S. Hla, Y. Sun, G.J. Duffy, L.D. Morpeth, A. Ilyushechkin, A. Cousins, D.G. Roberts, J.H. Edwards, Kinetics of the water-gas shift reaction over a $La_{0.7}Ce_{0.2}FeO_3$ perovskite-like catalyst using simulated coal-derived syngas at high temperature, Int. J. Hydrogen Energy. 36 (2011) 518–527. doi:10.1016/j.ijhydene.2010.10.015.

[44] S.S. Maluf, E.Y. Tanabe, P.A.P. Nascente, E.M. Assaf, Study of water-gas-shift reaction over $La_{1-y}Sr_yNi_xCo_{1-x}O_3$ perovskite as precursors, Top. Catal. 54 (2011) 210–218. doi:10.1007/s11244-011-9654-5.

[45] C. Constantinou, W. Li, G. Qi, W.S. Epling, NO_x storage and reduction over a perovskite-based lean NO_x trap catalyst, Appl. Catal. B Environ. 134–135 (2013) 66–74.
doi:10.1016/j.apcatb.2012.12.034.

[46] G.C. Mondragón Rodríguez, B. Saruhan, Effect of Fe/Co-ratio on the phase composition of Pd-integrated perovskites and its H_2-SCR of NO_x performance, Appl. Catal. B Environ. 93 (2010) 304–313. doi:10.1016/j.apcatb.2009.10.004.

[47] G.C. Mondragón Rodríguez, K. Kelm, B. Saruhan, H_2-selective catalytic reduction of NO_x activity and microstructural analysis of new $BaTi_{0.95}Pd_{0.05}O_3$ catalyst, Appl. Catal. A Gen. 387 (2010) 173–184.
doi:10.1016/j.apcata.2010.08.012.

[48] R. Zhang, H. Alamdari, S. Kaliaguine, SO_2 poisoning of $LaFe_{0.8}Cu_{0.2}O_{0.3}$ perovskite prepared by reactive grinding during NO reduction by C_3H_6, Appl. Catal. A Gen. 340 (2008) 140–151. doi:10.1016/j.apcata.2008.02.028.

[49] S. Wang, P. Xiao, X. Xu, H. Bi, X. Liu, J. Zhu, Catalytic CO oxidation and CO+NO reduction conducted on La-Co-O composites: The synergistic effects between Co_3O_4 and $LaCoO_3$, Catal. Today. (2020) 1–7. doi:10.1016/j.cattod.2020.05.035.

[50] M. Abdolrahmani, M. Parvari, M. Habibpoor, Effect of copper substitution and preparation methods on the $LaMnO_{\pm\delta}$ structure and catalysis of methane combustion and CO oxidation, Cuihua Xuebao/Chinese J. Catal. 31 (2010) 394–403. doi:10.1016/S1872-2067(09)60059-0.

[51] B. Heidinger, S. Royer, H. Alamdari, J.M. Giraudon, J.F. Lamonier, Reactive grinding synthesis of $LaBO_3$ (B: Mn, Fe) perovskite; properties for toluene total oxidation, Catalysts. 9 (2019) 1–18. doi:10.3390/catal9080633.

[52] B. Kucharczyk, K. Adamska, W. Tylus, W. Miśta, B. Szczygieł, J. Winiarski, Effect of Silver Addition to $LaFeO_3$ Perovskite on the Activity of Monolithic $La_{1-x}Ag_xFeO_3$ Perovskite Catalysts in Methane Hexane Oxidation, Catal. Letters. 149 (2019) 1919–1933. doi:10.1007/s10562-019-02779-7.

[53] H. Chang, E. Bjørgum, O. Mihai, J. Yang, H.L. Lein, T. Grande, S. Raaen, Y.A. Zhu, A. Holmen, D. Chen, Effects of Oxygen Mobility in La-Fe-Based Perovskites on the Catalytic Activity and Selectivity of Methane Oxidation, ACS Catal. 10 (2020) 3707–3719. doi:10.1021/acscatal.9b05154.

[54] Y. Wu, X. Ni, A. Beaurain, C. Dujardin, P. Granger, Stoichiometric and non-stoichiometric perovskite-based catalysts: Consequences on surface properties and on catalytic performances in the decomposition of N_2O from nitric acid

plants, Appl. Catal. B Environ. 125 (2012) 149–157. doi:10.1016/j.apcatb.2012.05.033.

[55] A. Schön, J.P. Dacquin, P. Granger, C. Dujardin, Non stoichiometric $La_{1-y}FeO_3$ perovskite-based catalysts as alternative to commercial three-way-catalysts? – Impact of Cu and Rh doping, Appl. Catal. B Environ. 223 (2018) 167–176. doi:10.1016/j.apcatb.2017.06.026.

[56] R. Dinamarca, X. Garcia, R. Jimenez, J.L.G. Fierro, G. Pecchi, Effect of A-site deficiency in $LaMn_{0.9}Co_{0.1}O_3$ perovskites on their catalytic performance for soot combustion, Mater. Res. Bull. 81 (2016) 134–141. doi:10.1016/j.materresbull.2016.05.007.

[57] J. Yang, S. Hu, Y. Fang, S. Hoang, L. Li, W. Yang, Z. Liang, J. Wu, J. Hu, W. Xiao, C. Pan, Z. Luo, J. Ding, L. Zhang, Y. Guo, Oxygen vacancy promoted $_2$ activation over perovskite oxide for low-temperature CO oxidation, ACS Catal. 9 (2019) 9751–9763. doi:10.1021/acscatal.9b02408.

[58] J. Liu, Z. Zhao, C.M. Xu, A.J. Duan, G.Y. Jiang, The structures, adsorption characteristics of La-Rb-Cu-O perovskite-like complex oxides, and their catalytic performances for the simultaneous removal of nitrogen oxides and diesel soot, J. Phys. Chem. C. 112 (2008) 5930–5941. doi:10.1021/jp709640f.

[59] L. Ma, W. Zhang, Y.G. Wang, X. Chen, W. Yu, K. Sun, H. Sun, J. Li, J.W. Schwank, Catalytic performance and reaction mechanism of NO oxidation over Co_3O_4 catalysts, Appl. Catal. B Environ. 267 (2020) 118371. doi:10.1016/j.apcatb.2019.118371.

[60] N. Mota, R.M. Navarro, M.C. Alvarez-Galvan, S.M. Al-Zahrani, J.L.G. Fierro, Hydrogen production by reforming of diesel fuel over catalysts derived from $LaCo_{1-x}Ru_xO_3$ perovskites: Effect of the partial substitution of Co by Ru (x = 0.01-0.1), J. Power Sources. 196 (2011) 9087–9095.

doi:10.1016/j.jpowsour.2010.11.143.

[61] C. Zhou, X. Liu, C. Wu, Y. Wen, Y. Xue, R. Chen, Z. Zhang, B. Shan, H. Yin, W.G. Wang, NO oxidation catalysis on copper doped hexagonal phase $LaCoO_3$: A combined experimental and theoretical study, Phys. Chem. Chem. Phys. 16 (2014) 5106–5112. doi:10.1039/c3cp54963a.

[62] L. Huang, M. Bassir, S. Kaliaguine, Reducibility of Co^{3+} in perovskite-type $LaCoO_3$ and promotion of copper on the reduction of Co^{3+} in perovskite-type oxides, Appl. Surf. Sci. 243 (2005) 360–375. doi:10.1016/j.apsusc.2004.09.079.

[63] X. Yan, Q. Huang, B. Li, X. Xu, Y. Chen, S. Zhu, S. Shen, Catalytic performance of $LaCo_{0.5}M_{0.5}O_3$ (M=Mn, Cr, Fe, Ni, Cu) perovskite-type oxides and $LaCo_{0.5}Mn_{0.5}O_3$ supported on cordierite for CO oxidation, J. Ind. Eng. Chem. 19 (2013) 561–565.
doi:10.1016/j.jiec.2012.09.026.

Chapter 7

General Conclusions and Perspectives

General Conclusions

The objective of this thesis was to develop a catalytic material that is economically feasible, stable under reaction condition and demonstrates a high NO reduction activity. In this thesis, transition metal oxide-based materials were synthesized because of their competitive cost and comparable catalytic activity as compared to precious metal based catalytic materials. Different mixed oxides were synthesized via Layered Double Hydroxide (LDH) route, characterized for determination of various material properties and assessed for catalytic activity.

Based on the extensive bibliographic study, copper was chosen as the starting active metal for the NO reduction reaction. Copper-Aluminium mixed oxides were synthesized by thermal treatment of its parent LDH under the flow of different treatment gases: 1 vol% CO/He (CuAl-CO/He), air (CuAl-air), He (CuAl-He) and CO_2 (CuAl-CO_2).

- These mixed oxide samples showed similar textural properties and specific surface area except for the CuAl-CO/He sample because of strong reduction of copper species under the flow of CO/He gas mixture.
- Interestingly, CuAl-air, CuAl-He and CuAl-CO_2 treated samples showed sim-

ilar composition under XRD and specific surface area under N_2-physisorption but different catalytic activity, specifically for CuAl-CO_2.

- Catalytic tests were performed under dry and wet reaction conditions. CuAl-CO_2 was the only sample that showed NO reduction activity under dry reaction condition while all the other CuAl mixed oxides showed NO reduction activity only under wet reaction condition. TGA and FTIR analyses indicated that CO_2-treatment of CuAl LDH led to the formation of stable bidentate and/or polydentate carbonates, which were active species for NO reduction reaction. However, the formation of additional carbonate species occupied the active sites for NO adsorption in the catalyst as a result of which total NO conversion yield was lower for CuAl-CO_2 than CuAl-air and CuAl-He.

Hence, from these studies, it was concluded that CO_2 treatment of CuAl LDH can improve the catalytic performance for NO reduction by CO, especially under dry reaction condition and therefore, this treatment method was followed to synthesize mixed oxides further in this study.

Literature reports have shown that presence of a secondary active metal can improve the catalytic performance especially for NO reduction by CO reaction. In this study, Co was selected as the secondary active metal in the mixed metal oxide material. To investigate the effect of Co content on the corresponding catalytic performance, mixed metal oxides with different Cu/Co ratios were synthesized by thermal treatment of corresponding parent LDH under the flow of CO_2 at 500°C.

- Upon comparing the CO oxidation activity under wet reaction conditions for different CoCuAl samples, the samples showed the following trend: $Co_6Al \sim Co_4Cu_2Al > Co_2Cu_4Al > Cu_6Al$. Moreover, same trend was observed for the NO conversion activity.
- The reaction temperature for NO reduction activity was found to shift to lower values upon increasing the Co content in the mixed oxides. However, NO oxidation yield varied between 23-29% and established no correlation to the Co content in the mixed oxide.
- Upon comparing the TPR profile for Cu_6Al and Co_4Cu_2Al revealed that the

latter has more reducible species than the former which was considered to be reason for superior catalytic activity.

Based on the observed catalytic performance under wet reaction conditions, Co_4Cu_2Al mixed oxide sample was considered for further studies. This was because Co_6Al and Co_4Cu_2Al samples showed similar catalytic activity, Co is a more expensive metal than Cu so lowering the Co content will lower the cost of the catalyst (one of the main objective of this thesis) and Co_4Cu_2Al mixed oxide formed sinter-resistant spinel structure due to interaction between Co and Cu species.

Furthermore, a study to investigate the optimal thermal treatment temperature for the mixed metal oxide synthesis was performed where samples of Co_4Cu_2Al mixed oxides were derived by thermal treatment of parent LDH under the flow of CO_2 and at different treatment temperatures (T = 350, 400, 450 and 500°C). It was observed that treatment temperature had no effect on the specific surface area and pore diameter of the corresponding mixed oxides. However, XRD analyses showed that with the increase in the treatment temperature, the crystallinity of corresponding mixed oxides increased. Moreover, upon comparing the catalytic activity of the different mixed oxide sample treated at different temperatures and under wet reaction conditions, no appreciable change was observed in the CO oxidation activity of mixed oxides. However, considerable change in the NO conversion activity was observed. The NO conversion was improved from 17% to 87% with decrease in the treatment temperature from 500°C to 350°C and N_2 selectivity was improved when the treatment temperature was increased from 350°C to 400°C and then it decreased to 77% and 79% for samples treated at 450°C and 500°C respectively. The presence of different amount of carbonate species in the mixed oxides due to different treatment temperatures was considered to be the reason for the difference in the NO conversion activity. Hence, Co_4Cu_2Al mixed oxide treated under the flow of CO_2 and at 400°C (termed as 'Co_4Cu_2Al-400-CO_2') was scouted for the stability tests and further for large-scale synthesis to perform the semi-pilot scale tests.

Additionally, a study regarding stability of catalytic performance under the industrial flue gas conditions was performed on Co_4Cu_2Al-400-CO_2. For

this, the sample was subjected to 6 cycles of light-off between 50 and 400°C of reaction temperatures. It was observed that on one hand, the T_{90} for CO conversion increased from 250°C in the 1st cycle to 280°C in the 5th cycle and remained constant until the 6th light-off cycle while on the other hand, the NO reduction yield decreased from 38% in the 1st cycle to 32% in the 3rd cycle and thereafter, no appreciable change in the NO oxidation yield with the light-off cycles was observed. These results indicated that the material was considerably stable under the reaction conditions. Furthermore, the catalytic activity of Co_4Cu_2Al-400-CO_2 was compared with commercially available 1 wt% Pt/Al_2O_3 and 1 wt% Pt/CeO_2. It was observed that Co_4Cu_2Al-400-CO_2 showed higher NO reduction activity but slower CO conversion to CO_2 than the Pt-containing samples.

Apart from the effect of the material composition and treatment temperature used in the catalytic material synthesis, the effect of reactant gas composition on the NO reduction activity was also studied. For this, the content of each of the gas components were altered in the reactant gas mixture and the corresponding effect on the catalytic activity was recorded.

- Effect of CO content: The CO content in the feed gas mixture was increased from 0.13 vol% to 0.5 vol%. Increasing the CO content delayed CO conversion to CO_2 and NO reduction with decrease in NO oxidation yield and no change in maximum NO reduction yield. These observations implied the occurrence of CO poisoning.
- Effect of NO content: The NO content in the feed gas mixture was decreased from 475 ppm to 300 ppm. No appreciable change in the catalytic activity was observed.
- Effect of CO_2: The CO_2 content in the feed gas mixture was increased from 20.4 vol% to 60 vol%. Increase in the CO_2 content, slight delay in NO reduction with no change in maximum NO reduction yield while no appreciable change in CO conversion activity and considerable decrease in the NO oxidation yield were observed. Competitive adsorption between NO and CO_2 for the common active sites in the catalyst was considered to be the possible reason for such a behaviour.

- Effect of H_2O content: The water content in the feed gas mixture was decreased from 8.2 vol% to 0 vol% (dry reaction condition). It was observed that presence of water delayed NO and CO conversion, decreased NO reduction yield, and increased NO oxidation yield. This behaviour implied that H_2O competes with other reactants for the common active sites in the catalyst.

Along with reactant gas composition, the effect of catalyst weight in the reactor on the catalytic performance was also studies. For this, the catalyst weight was increased from 150 mg to 762 mg with no change in the GHSV. The catalytic activity improved expectedly with the increase in the catalyst weight which due to the presence of a greater number of reaction active sites in the reactor.

Furthermore, a kinetic model was developed for the reaction system using Langmuir Hinshelwood Hougen Watson (LHHW) kinetics. For this model, 15 different sets of reaction rate expressions (each set consisted of the reaction rate equation for CO conversion to CO_2, NO conversion to N_2 and NO conversion to NO_2) based on different possible elementary reaction steps as rate-determining. The kinetic, adsorption and desorption constants used in these expressions varied with temperature according to the Arrhenius relation and therefore, each set of these reaction rate expressions consisted of 28 unknown parameters that were required to be determined. 70 sets of experimental data obtained from the tests to investigate the effect of reactant gas composition and catalyst weight on the catalytic activity were utilised for the parameter regression. Only the set of experimental data where NO conversion activity was recorded were considered for the parameter regression. Solvers available in the Global Optimisation Toolbox of MATLAB 2020a software were used for the parameter regression and their ability to minimize the error between the calculated and experimental values was assessed. It was found that the model form with adsorption of CO and NO and dissociation of adsorbed NO into adsorbed N and O species as rate-determining steps fitted the experimental data the best.

Finally, an extensive bibliographic study was performed for perovskites as potential catalytic material for NO reduction by CO. In this thesis, preliminary studies on different perovskites were studied and their catalytic activity under

industrial flue gas conditions were assessed.

- Firstly, $LaBO_3$ (where B = Co, Fe and Mn) were first synthesized by conventional citrate route and calcined at 600°C under air. XRD analyses of the samples showed that only perovskite structure was formed after the calcination step and no secondary oxide phases were observed. Moreover, the specific surface area of these perovskites varied between 9-12 $m^2.g^{-1}$ which was 10 times lower than that obtained for Co_4Cu_2Al-400-CO_2 sample. Out of these samples, $LaCoO_3$ showed superior catalytic activity than the rest both under wet and dry reaction conditions. However, the maximum NO reduction yield for $LaCoO_3$ was found to be 20% which is almost half of that observed for Co_4Cu_2Al-400-CO_2 sample.
- Further, the influence of La content in the perovskite on the catalytic performance was studied using Co as the B-site cation. On one hand upon decreasing the La content (La/Co ratio decreased from 1 to 0.85), the specific surface area decreased drastically, from 8.4 $m^2.g^{-1}$1 to 0.9 $m^2.g^{-1}$ while on the other hand, XRD analysis of the $La_{0.85}CoO_3$ revealed that Co_3O_4 was formed along with perovskite structure which also led to the higher specific H_2 consumption during the TPR analysis than $LaCoO_3$ sample. Moreover, upon comparing the catalytic activity of $La_{0.85}CoO_3$ with that of $LaCoO_3$, it was observed that CO conversion to CO_2 and NO oxidation to NO_2 was higher in case $La_{0.85}CoO_3$ than $LaCoO_3$ under dry reaction conditions but, under the wet reaction conditions, both of these conversion activities were similar except for the T_{90} temperatures for CO conversion which increased by 40°C under wet reaction conditions. For NO reduction activity over both the catalysts, the yield was found to be less than 20% both under the dry and wet reaction condition and no noticeable improvement in the reduction activity due to the decrease in the La content was observed. Therefore, it was concluded that decreasing the La content did not improve the NO reduction activity.
- In addition to the studies regarding type of B-site cation and La content, the influence of partial B-site substitution in the perovskite on the catalytic performance was also studied. For these studies, Cu was considered as the secondary B-site cation along with Co and low La content in the perovskite

samples. Samples with x = 0.1, 0.2 and 0.25 (x in $La_{0.85}Co_{1-x}Cu_xO_3$) were synthesized and calcined under air at 600°C. The partial substitution of B-site improved the specific surface area only until x= 0.2 and then it decreased slightly at x = 0.25. Distortion of the rhombohedral structure of perovskite was observed for x = 0.2 and x = 0.25 in the XRD analysis. Moreover, H_2-TPR analysis revealed that the inclusion of Cu in the perovskite structure shifted the first reduction peak to lower temperatures and increased the specific H_2 consumption only for x = 0.1 and further increase in Cu substitution decreased the specific H_2 consumption values. Change in the coordination environment with the increase of Cu substitution could be the reason for such a behaviour. Furthermore, the catalytic activity for these $La_{0.85}Co_{1-x}Cu_xO_3$ samples were compared under dry and wet reaction conditions. It was observed that sample with x = 0.25 showed superior catalytic activity both under the wet and dry reaction conditions. For all the catalysts, CO conversion was delayed, NO oxidation yield was decreased, and NO reduction yield was slightly increased upon introduction of water in the reactant feed mixture. However, the NO reduction yield remained below 20% for all the samples. With respect to the catalytic performance of $La_{0.85}Co_{1-x}Cu_xO_3$, no clear correlation among the reducibility of active metal species, specific surface area and catalytic activity could be established. Hence, other material characterization techniques like XPS can be used to determine the surface metal species and concentration of oxygen vacant sites in the samples which can consequently explain the different catalytic behaviour.

Perspectives

The results in this thesis showed that CO can be a good reductant for NO under industrial flue gas condition and over cobalt-copper based materials as catalyst. However, a maximum NO reduction activity of 40% was achieved (considering N_2 as the gas vector). Nevertheless, this study opens the possibility of using transition-metal based catalysts for NO reduction under industrial flue gas conditions.

In this study, Co_4Cu_2Al mixed oxides were synthesized at different treatment temperatures which resulted in different catalytic activities. The

presence of different concentration of carbonates in the mixed oxide sample can be one of the plausible reasons for such a catalytic behaviour. However, it is important to quantify the type of carbonate species (such as monodentate or bidentate carbonates) present in the samples via techniques like Raman Spectroscopy and compare their acido-basicity properties determined through CO_2 or NH_3-TPD to fully understand their corresponding catalytic behaviour. Moreover, the Co_4Cu_2Al synthesized on a large-scale should be tested on the semi-pilot test setup which is currently under development in the UMONS lab. The results from this setup should be compared with that from the lab-scale tests to visualize the effect of scaling up on the catalytic activity.

Regarding the catalyst development, the effect of treatment gas other than CO_2 on the catalytic activity of different Co-Cu mixed oxide samples have not been studied. Therefore, it is important to perform a Design of Experiments (DoE) to develop different Co-Cu mixed oxides treated under different treatment gases and compare their catalytic performance. Moreover, literature studies have shown that redox treatment can introduce certain metal species in the catalyst that are active for the CO + NO reaction. Therefore, it will be interesting to investigate the influence of redox treatment of the mixed metal oxides on their corresponding catalytic performance, especially NO reduction to N_2.

The other aspect that can be studied is the use of different acidic promoters like Ce and Zr basic promoters like Mg and alkali metal promoters like K in the catalytic materials and their effect on the corresponding catalytic performance. Ce and Zr are known for their outstanding oxygen storage capacity and redox properties which can be a benefit for the active metals while Mg can improve the dispersion of active metal in the material and the active metal interaction with other promoter metals which can improve the catalytic activity and K can improve the adsorption of reactant molecules and therefore, enhance the probability of surface reaction.

In the final chapter of this thesis, it was demonstrated that perovskite materials are also active for NO reduction by CO under industrial flue gas conditions. Copper seems to be active for the NO reduction reaction under these conditions and therefore, can be used as the secondary active metal in

the perovskite by partially substituting different B-site cation like Fe and Mn and the influence of degree of substitution on their catalytic performances can be investigated. Moreover, surface characterization techniques like XPS can be used to determine the material composition at the catalyst surface and the concentration of oxygen vacant sites on the catalyst, both of which are important factors influencing the catalytic materials. Furthermore, the effect of inclusion of low concentration of precious metals from the PGMs like Pt, Pd and/or Rh on the catalytic activity can also be investigated. Such studies with perovskites as catalyst under industrial flue gas conditions have been scarcely reported in the literature and therefore, these studies can provide novel results.

In this thesis, the kinetic model is developed for the reaction system considering one type of active site in the catalytic material. However, in case of binary metal oxide catalysts, more than one type of active sites is expected. Therefore, the current kinetic model can be further developed to include dual site mechanism considering different active sites for adsorption of various reactant molecules. Further, catalytic tests with different GHSVs can also be performed and the results can be used for parameter regression of the kinetic model. Moreover, the kinetic model developed in this thesis do not follow the template for LHHW kinetics recommended in Aspen Plus and therefore, a FORTRAN routine need to be developed that utilises the user-defined kinetics and simulated using the RPLUG reactor available in the software. Finally, the kinetic model previously developed can be extended for the perovskite-based materials as well.

Appendix A: Supplementary Material Characterization Results

N_2-Physisorption: Pore Size Distribution

The pore size distribution was calculated by applying the Barrett-Joyner-Halenda (BJH) method on the desorption branch. The distribution is shown in Figure A.1.

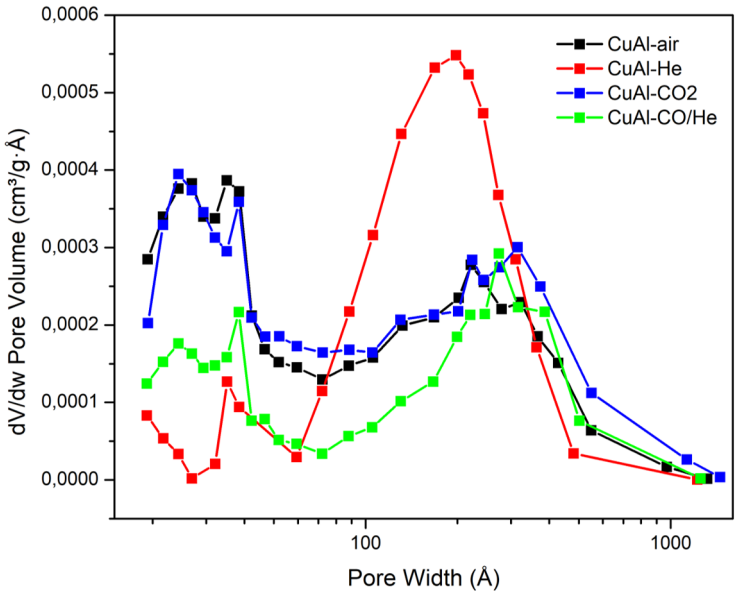

Figure A.1 Pore size distribution of the CuAl-X mixed oxide material samples

NO Reduction and Oxidation Yield for CuAl-X samples

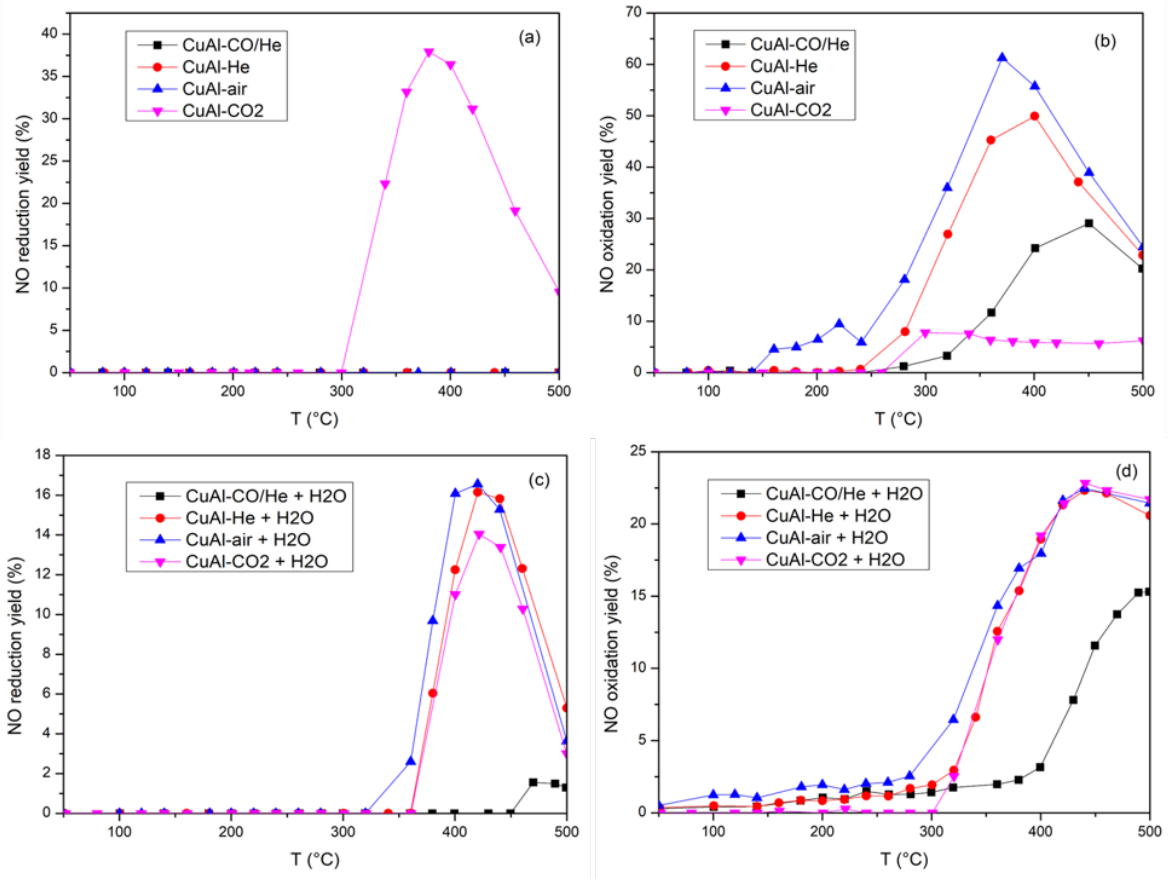

Figure A.2 NO conversion activity for CuAl-X under dry and wet reaction conditions: (a) NO reduction yield under dry reaction condition, (b) NO oxidation yield under dry reaction condition, (c) NO reduction yield under wet reaction condition and (d) NO oxidation yield for the wet reaction condition

The NO reduction and oxidation yield for CuAl-X samples are shown in the Figure A.2. It can be seen that NO reduction activity is observed only for CuAl-CO_2 sample under the dry reaction condition while under the wet reaction condition, all the samples show NO reduction activity. Moreover, NO oxidation activity is observed for all the CuAl-X both under the dry and wet reaction conditions.

Appendix B: MATLAB Script for Parameter Regression

This appendix contains the MATLAB script files used for the parameter regression routine. The script files contains the equations concerning the kinetic model form 1.

Script for Global Optimization Routine

Importing the experimental data

```
expt_data = table2array(readtable('Expt_Data_25122022.xlsx', 'Sheet', 'Sheet3', 'Range', 'A2:P75')) ; % returns a matrix of data
warning('off') % To suppress the warning messages
```

The lower and Upper Bound of the Parameters to be regressed

```
lb = 1e-30*ones(28,1); % lower bound
ub = zeros(28,1);% upper bound
for i = 1:28
if rem(i,2)==0
ub(i,1) = 1e5; % upper bound for Ea/R terms
else
ub(i,1) = 1e3; % upper bound for A terms
end end
```

Initial value of parameters

```
x0 = lb + rand(size(lb)).*(ub - lb); % Generates random initial points between lower and upper bound
```

PATTERNSEARCH

```
% Solver Options
options = optimoptions('patternsearch','PlotFcn','psplotbestf','UseParallel','Always',
'MeshTolerance',1e-8,'OutputFcn',@custom,'MaxFunctionEvaluations',1e6);

objfun = @(K)objfun_pfr_v3_f1(expt_data,K); % Assigning objective function
to a variable name 'objfun'

% Storing the solutions
j = 1; % Initialization to be used for data storage
[x, fval, exitflag, output] = patternsearch(objfun,x0,[ ],[ ],[ ],[ ],lb,ub,
@(K)nonlcon_%form1(expt_data,K),options);
writematrix(fval,'xvalues_27122022.xlsx','Sheet','Sheet8','Range',sprintf('A%d',
j+1));
writematrix(exitflag,'xvalues_27122022.xlsx','Sheet','Sheet8','Range',sprintf('B%d',
j+1));
writematrix(x','xvalues_27122022.xlsx','Sheet','Sheet8','Range',sprintf('C%d:AD%d',
j+1, j+1));
```

Script for Nonlinear Constraints Function

```
function [c,ceq] = nonlcon_form1(expt_data,K)
% Fuction definition:
% expt_data = experimental dataset
% K = Set of model parameters to be regressed
```

Partial pressure (= volume fraction) of NO and CO at the reactor inlet

```
PP_CO_in = expt_data(:,15);
PP_NO_in = expt_data(:,13);
PP_CO2_in = expt_data(:,16);
```

Initial Partial Pressures of the Gas Components

```
PP_NO2_in = zeros(size(expt_data,1),1);
```

```
PP_N2_in = zeros(size(expt_data,1),1);
PP_H2O_in = expt_data(:,7);
PP_O2_in = expt_data(:,4);
PP_He_in = (1 - (PP_NO_in + PP_CO_in + PP_N2_in + PP_CO2_in + PP_O2_in
+ PP_NO2_in + PP_H2O_in));


P_tot = 101325 ; % Total Reaction Pressure, unit = N/m_2
F_vol = 200; % Total volumetric flow rate at the inlet, unit = ml_N/min
F0 = P_tot*(F_vol*1e-6)/(8.3145*298*60); % Total molar flow rate at the
inlet, unit = mol/s
```

Reaction Temperature

```
T = expt_data(:,1); % Reaction temperature, K
F_cal = zeros(size(expt_data,1),5); % Initialisation of the calculated conversion
values matrix
for i = 1:size(expt_data,1)
Fin(1) = F0 .* PP_NO_in(i,1);
Fin(2) = F0 .* PP_CO_in(i,1);
Fin(3) = F0 .* PP_N2_in(i,1);
Fin(4) = F0 .* PP_CO2_in(i,1);
Fin(5) = F0 .* PP_O2_in(i,1);
Fin(6) = F0 .* PP_NO2_in(i,1);
Fin(7) = F0 .* PP_H2O_in(i,1);
Fin(8) = F0 .* PP_He_in(i,1);
wspan = [0, expt_data(i,12)];
T_K = T(i,1); % assigning the temperature data for each row of experimental
data set
% Using ODE solver to solve the system of ODEs
[w, F] = ode15s(@(w,F)pfr_model_v3_f1(w,F,T_K,K,Fin),wspan,
[]Fin(1), Fin(2), Fin(3), Fin(4), Fin(6)]);
F_cal(i,:) = F(size(w,1),:); % Assigning the outlet molar flow rate of all the
components to
variable F_cal end
c = -F_cal ; % Molar flow rates need to be positive F_cal ge0 or -F_cal le 0
```

```
ceq = [];
end
```

Script for Objective Function Definition

```
function y = objfun_pfr_v3_f1(expt_data,K)

Partial pressure (= volume fraction) of NO and CO at the reactor inlet
PP_CO_in = expt_data(:,15);
PP_NO_in = expt_data(:,13);
PP_CO2_in = expt_data(:,16);


Initial Partial Pressures of the Gas Components
PP_NO2_in = zeros(size(expt_data,1),1); % Partial pressure of NO2 at the inlet
PP_N2_in = zeros(size(expt_data,1),1); % Partial pressure of N2 at the inlet
PP_H2O_in = expt_data(:,7); % Partial pressure of H2O at the inlet
PP_O2_in = expt_data(:,4); % Partial pressure of O2 at the inlet
PP_He_in = (1 - (PP_NO_in + PP_CO_in + PP_N2_in + PP_CO2_in + PP_O2_in
+ PP_NO2_in + PP_H2O_in)); % Partial pressure of He calculated from the
partial pressures from all other components


P_tot = 101325 ; % Total pressure in the reactor, unit = N/m_2
F_vol = 200; % Total Volumetric flow rate, unit = ml_N/min
F0 = P_tot*(F_vol*1e-6)/(8.3145*298*60); % Converting volumetric flow rate
to total molar flow rate, unit = mol/s


Reaction Temperature
T = expt_data(:,1);


ODE Integration
X_CO2_cal = zeros(size(expt_data,1),1); % Initialisation of the calculated con-
version values matrix
P_N2_cal = zeros(size(expt_data,1),1);
P_NO2_cal = zeros(size(expt_data,1),1);
```

```
Y_N2_cal = zeros(size(expt_data,1),1);
Y_NO2_cal = zeros(size(expt_data,1),1);
```

A FOR loop is used to determine the molar conversions for NO (into N2 and NO2) and CO (into CO2) for each set of experimental data

```
for i = 1:size(expt_data,1)
Fin(1) = F0 .* PP_NO_in(i,1);
Fin(2) = F0 .* PP_CO_in(i,1);
Fin(3) = F0 .* PP_N2_in(i,1);
Fin(4) = F0 .* PP_CO2_in(i,1);
Fin(5) = F0 .* PP_O2_in(i,1);
Fin(6) = F0 .* PP_O2_in(i,1);
Fin(7) = F0 .* PP_H2O_in(i,1);
Fin(8) = F0 .* PP_He_in(i,1);
wspan = [0, expt_data(i,12)];
T_K = T(i,1);

% Using ODE solver
[w, F] = ode15s(@(w,F)pfr_model_v3_f1(w,F,T_

P_N2_cal(i,1) = F(size(w,1),3)./(F(size(w,1),1)+F(size(w,1),2)+F(size(w,1),3)
+F(size(w,1),4)+F(size(w,1),5)+Fin(5)+Fin(7)+Fin(8));
P_NO2_cal(i,1) = F(size(w,1),5)./(F(size(w,1),1)+F(size(w,1),2)+F(size(w,1),3)
+F(size(w,1),4)+F(size(w,1),5)+Fin(5)+Fin(7)+Fin(8));

Y_N2_cal(i,1) = P_N2_cal(i,1)./PP_NO_in(i,1);
Y_NO2_cal(i,1) = P_NO2_cal(i,1)./PP_NO_in(i,1);

X_CO_cal(i,1) = (Fin(2) - F(size(w,1),2))./Fin(2); % Calculated CO conversion
% (Not shown here but NO conversion can be calculated same as CO % conver-
sion)
end
```

Objective Function

```
% Initialisation of variables to avoid computational time
Y_N2_exp = zeros(size(expt_data,1),1); % Experimental values of NO reduction to N2 yield
Y_NO2_exp = zeros(size(expt_data,1),1); % Experimental values of NO oxidation to NO2 yield
X_CO2_exp = zeros(size(expt_data,1),1); % Experimental values of CO oxidation to CO2 yield


Y_N2_exp(:,1) = expt_data(:,10);
Y_NO2_exp(:,1) = expt_data(:,9);
X_CO2_exp(:,1) = expt_data(:,11);
```

Objective function: error between experimental and calculated values

```
y_err(1) = sum((X_CO2_cal(:,1) - X_CO2_exp).^2);
y_err(2) = sum((Y_N2_cal(:,1) - Y_N2_exp).^2);
y_err(3) = sum((Y_NO2_cal(:,1) - Y_NO2_exp).^2);
```

Sum of the errors between experimental and calculated values

```
y = sum(y_err);
end
```

This is the system of ODE functions

```
function dFdW = pfr_model_v3_f1(w,F,T,K,Fin,i)
% w = weight of the catalyst, g
% F = molar flow rate of the reactant and product components in the product stream i.e. outlet of the reactor, mol/s


% T = Reaction temperature, K
% K = array of unknown parameters that need to be regressed
% Fin = inlet flow rates of different reactant components
```

Intitialisation of output parameter of this script function

```
dFdW = zeros(5,1); % column vector
```

Nomenclature of outlet flow rates of different reactant and product components

```
% F(1) = F_NO; % Molar flow rate of NO, mol/s
% F(2) = F_CO; % Molar flow rate of CO, mol/s
% F(3) = F_N2; % Molar flow rate of N2, mol/s
% F(4) = F_CO2; % Molar flow rate of CO2, mol/s
% F_O2 = Fin(5); % Molar flow rate of O2, mol/s . Since, O2 is in excess, the inlet and outlet molar flow rate is the same
% F(5) = F_NO2; % Molar flow rate of NO2, mol/s
% F_H2O = Fin(7); % Molar flow rate of H2O, mol/s . Since H2O is in excess, the inlet and the outlet molar flow rates are same
% F_He = Fin(8); % Molar flow rate of He (inert component), mol/s . Since He is an inert component and doesnot participate in the reaction, the inlet and the outlet molar flow rates are the same.
```

Total flow rate at the outlet of the reactor

```
FT = F(1) + F(2) + F(3) + F(4) + Fin(5) + F(5) + Fin(7) + Fin(8);
```

Assigning the different flow rate components to an array 'A'

```
A = zeros(8,1); % Initialization
A(1) = T; % Reaction temperature, K
```

```
% To avoid calculating complex number, the partial pressures need to be positive. Theerfore, when the F(i)/FT < 0, the partial pressure of the component i is assigned zero
```

```
% The partial pressures are in bar
```

```
% Partial Pressure of NO
if (F(1)/FT) >=0
A(2) = F(1)./FT;
else
A(2) = 0;
F(1) = 0;
end

% Partial Pressure of CO
if (F(2)/FT) >=0
A(3) = F(2)./FT;
else
A(3) = 0;
F(2) = 0;
end

% Partial Pressure of N2
if (F(3)/FT) >=0
A(5) = F(3)./FT;
else
A(5) = 0;
F(3) = 0;
end

% Partial Pressure of CO2
if (F(4)/FT) >=0
A(6) = F(4)./FT;
else
A(6) = 0;
F(4) = 0;
end

A(4) = Fin(5)./FT; % Partial Pressure of O2
```

```
% Partial Pressure of NO2
if (F(5)/FT) >=0
A(8) = F(5)./FT;
else
A(8) = 0;
F(5) = 0;
end

A(7) = Fin(7)./FT; % Partial Pressure of H2O
```

Calculation of reaction rate

```
r_N2 = rate_N_form1(A,K); % rate of conversion of NO to N2
r_NO2 = rate_NO2_form1(A,K); % rate of conversion of NO to NO2
r_CO2 = rate_CO2_form1(A,K); % rate of conversion of CO to CO2
```

Mole balance equations for a Packed Bed Reactor

```
dFdW_NO = -((r_N2) + (r_NO2));
dFd_CO = -((r_N2) + (r_CO2));
dFdW_N2 = 0.5 .* (r_N2) ;
dFdW_CO2 = ((r_N2) + (r_CO2));
dFdW_NO2 = (r_NO2);
```

Assigning the change of molar flow rate w.r.t. to catalyst weight to the output of this function

```
dFdW(1) = dFdW_NO;
dFdW(2) = dFdW_CO;
dFdW(3) = dFdW_N2;
dFdW(4) = dFdW_CO2;
dFdW(5) = dFdW_NO2;
end
```

Reaction Rate Expressions for Form-1

Reaction rate for NO reduction (r_N)

```
function rate = rate_N _form1(A,K)
% A = experimental dataset in terms of partial pressures of different gas components


T = A(1); % Reaction temperature in K
P_NO = A(2); % Partial pressure of NO at the outlet
P_CO = A(3); % Partial pressure of CO at the outlet
P_O2 = A(4); % Partial pressure of O2 at the outlet
P_N2 = A(5); % Partial pressure of N2 at the outlet
P_CO2 = A(6);% Partial Pressure of CO2 at the outlet
P_H2O = A(7); % Partial pressure of H2O at the outlet
P_NO2 = A(8); % Partial pressure of NO2 at the outlet


% K = array of unknown parameters i.e. pre-exponential factor and activation energy/R (R = universal gas constant)


rate = ((K(1).*exp(-K(2)./T).*(P_NO2./(P_O2).^0.5) - K(3).*exp(-K(4)./T).*(P_N2
.*
P_O2).^0.5)./ ...
( 1 + ... K(5).*exp(-K(6)./T).*(P_CO2./(P_O2).^0.5)...
+ K(7).*exp(-K(8)./T).*(P_NO2./(P_O2).^0.5)...
+ K(9).*exp(-K(10)./T).*(P_N2).^0.5 ...
+ K(11).*exp(-K(12)./T).*(P_O2).^0.5 ...
+ K(13).*exp(-K(14)./T).*P_CO2 ...
+ K(15).*exp(-K(16)./T).*P_N2 ...
+ K(17).*exp(-K(18)./T).*P_NO2 ...
+ K(19).*exp(-K(20)./T).*P_H2O ...
).^2 ...
);
end
```

Reaction rate for CO oxidation (r_{CO2})

```
function rate = rate_CO2 _form1(A,K)
% A = experimental dataset in terms of partial pressures of different gas components


T = A(1); % Reaction temperature in K
P_NO = A(2); % Partial pressure of NO at the outlet
P_CO = A(3); % Partial pressure of CO at the outlet
P_O2 = A(4); % Partial pressure of O2 at the outlet
P_N2 = A(5); % Partial pressure of N2 at the outlet
P_CO2 = A(6);% Partial Pressure of CO2 at the outlet
P_H2O = A(7); % Partial pressure of H2O at the outlet
P_NO2 = A(8); % Partial pressure of NO2 at the outlet


% K = array of unknown parameters i.e. pre-exponential factor and activation energy/R (R = universal gas constant)


rate = ((K(25).*exp(-K(26)./T).*P_CO - K(27).*exp(-K(28)./T).*
(P_CO2./(P_O2).^0.5))./ ...
( 1 + ... K(5).*exp(-K(6)./T).*(P_CO2./(P_O2).^0.5)...
+ K(7).*exp(-K(8)./T).*(P_NO2./(P_O2).^0.5)...
+ K(9).*exp(-K(10)./T).*(P_N2).^0.5 ...
+ K(11).*exp(-K(12)./T).*(P_O2).^0.5 ...
+ K(13).*exp(-K(14)./T).*P_CO2 ...
+ K(15).*exp(-K(16)./T).*P_N2 ...
+ K(17).*exp(-K(18)./T).*P_NO2 ...
+ K(19).*exp(-K(20)./T).*P_H2O ...
).^2 ...
);
end
```

Reaction rate for NO oxidation (r_{NO2})

```
function rate = rate_NO2 _form1(A,K)
% A = experimental dataset in terms of partial pressures of different gas components


T = A(1); % Reaction temperature in K
P_NO = A(2); % Partial pressure of NO at the outlet
P_CO = A(3); % Partial pressure of CO at the outlet
P_O2 = A(4); % Partial pressure of O2 at the outlet
P_N2 = A(5); % Partial pressure of N2 at the outlet
P_CO2 = A(6);% Partial Pressure of CO2 at the outlet
P_H2O = A(7); % Partial pressure of H2O at the outlet
P_NO2 = A(8); % Partial pressure of NO2 at the outlet


% K = array of unknown parameters i.e. pre-exponential factor and activation energy/R (R = universal gas constant)


rate = ((K(21)*exp(-K(22)./T).*P_NO - K(23)*exp(-K(24)./T).*
(P_NO2./(P_O2).^0.5))./ ...
( 1 + ... K(5).*exp(-K(6)./T).*(P_CO2./(P_O2).^0.5)...
+ K(7).*exp(-K(8)./T).*(P_NO2./(P_O2).^0.5)...
+ K(9).*exp(-K(10)./T).*(P_N2).^0.5 ...
+ K(11).*exp(-K(12)./T).*(P_O2).^0.5 ...
+ K(13).*exp(-K(14)./T).*P_CO2 ...
+ K(15).*exp(-K(16)./T).*P_N2 ...
+ K(17).*exp(-K(18)./T).*P_NO2 ...
+ K(19).*exp(-K(20)./T).*P_H2O ...
).^2 ...
);
end
```

Appendix C: Reaction Rate Expressions for Different Kinetic Models

This appendix contains the final expressions for the rates of CO conversion to CO_2, NO oxidation to NO_2, and NO reduction to N_2 for various kinetic models. As described in Chapter 5, a similar procedure was utilized to derive the reaction rate expressions for each kinetic model. In addition, the reaction rate expressions for forms 1 and 10 have already been presented in Chapter 5; thus, a set of rate-determining steps and reaction rate expressions for all other forms kinetic models have been presented here.

Kinetic Model Form 2

$$r_{CO_2} = \frac{\left(k_{CO}^{ads} P_{CO} - \left(\frac{k_{CO}^{des} K_{NO-O}^{eq} K_{NO_2}^{des} K_{NO}^{ads}}{K_{CO-O}^{eq} K_{CO_2}^{des}}\right) \frac{P_{CO_2} P_{NO}}{P_{NO_2}}\right)}{\left(1 + \left(\frac{k_{CO}^{des} K_{NO-O}^{eq} K_{NO_2}^{des} K_{NO}^{ads}}{K_{CO-O}^{eq} K_{CO_2}^{des}}\right) \frac{P_{CO_2} P_{NO}}{P_{NO_2}} + K_{NO}^{ads} P_{NO} + \sqrt{\frac{P_{N_2}}{K_{N_2} K_{N-N}^{eq}}} + \left(\frac{1}{K_{NO-O}^{eq} K_{NO_2}^{des} K_{NO}^{ads}}\right) \frac{P_{NO_2}}{P_{NO}} + \frac{P_{CO_2}}{K_{CO_2}^{des}} + \frac{P_{N_2}}{K_{N_2}^{des}} + \frac{P_{NO_2}}{K_{NO_2}^{des}} + K_{H_2O}^{ads} P_{H_2O}\right)^2} \quad \text{(C1)}$$

Table C1 Elementary reaction steps for 'Form-2'

Type of Reaction	Elementary Step	Kinetic/Equilibrium Constant
Adsorption	$CO + [S] \rightleftharpoons CO[S]$	k^{ads}_{CO}, k^{des}_{CO}
	$NO + [S] \rightleftharpoons NO[S]$	K^{ads}_{NO}
	$O_2 + 2[S] \rightleftharpoons 2O[S]$	$k^{ads}_{O_2}$, $k^{des}_{O_2}$
Surface Reactions	$NO[S] + [S] \rightleftharpoons N[S] + O[S]$	k^{f}_{CO-NO}, k^{b}_{CO-NO}
	$CO[S] + O[S] \rightleftharpoons CO_2[S] + [S]$	K^{eq}_{CO-O}
	$N[S] + N[S] \rightleftharpoons N_2[S] + [S]$	K^{eq}_{N-N}
	$NO[S] + O[S] \rightleftharpoons NO_2[S] + [S]$	K^{eq}_{NO-O}
Desorption	$CO_2[S] \rightleftharpoons CO_2 + [S]$	$K^{des}_{CO_2}$
	$NO_2[S] \rightleftharpoons NO_2 + [S]$	$K^{des}_{NO_2}$
	$N_2[S] \rightleftharpoons N_2 + [S]$	$K^{des}_{N_2}$
Inert	$H_2O + [S] \rightleftharpoons H_2O[S]$	$K^{ads}_{H_2O}$

$$r_N = \frac{\left(k^{f}_{CO-NO} P_{NO} K^{ads}_{NO} - k^{b}_{CO-NO} \left(\frac{1}{\sqrt{K^{des}_{N_2} K^{eq}_{N-N}}\, K^{eq}_{NO-O}\, K^{des}_{NO_2} K^{ads}_{NO}}\right)\left(\frac{P_{NO_2}\sqrt{P_{N_2}}}{P_{NO}}\right)\right)}{\left(1 + \left(1 + \left(\frac{k^{des}_{CO} K^{eq}_{NO-O} K^{des}_{NO_2} K^{ads}_{NO}}{K^{eq}_{CO-O} K^{des}_{CO_2}}\right)\frac{P_{CO_2} P_{NO}}{P_{NO_2}} + K^{ads}_{NO} P_{NO}\right.\right.\right.} \\ \left.\left.\left. + \sqrt{\frac{P_{N_2}}{K_{N_2} K^{eq}_{N-N}}} + \left(\frac{1}{K^{eq}_{NO-O} K^{des}_{NO_2} K^{ads}_{NO}}\right)\frac{P_{NO_2}}{P_{NO}} + \frac{P_{CO_2}}{K^{des}_{CO_2}} + \frac{P_{N_2}}{K^{des}_{N_2}}\right.\right.\right. \\ \left.\left.\left. + \frac{P_{NO_2}}{K^{des}_{NO_2}} + K^{ads}_{H_2O} P_{H_2O}\right)^2\right.} \quad \text{(C2)}$$

$$r_{NO_2} = \frac{\left(k^{ads}_{O_2} P_{O_2} - k^{des}_{O_2}\left[\left(\frac{1}{K^{eq}_{NO-O}\ K^{des}_{NO_2} K^{ads}_{NO}}\right)\left(\frac{P_{NO_2}}{P_{NO}}\right)\right]^2\right)}{\left(1 + \left(1 + \left(\frac{k^{des}_{CO} K^{eq}_{NO-O} K^{des}_{NO_2} K^{ads}_{NO}}{K^{eq}_{CO-O} K^{des}_{CO_2}}\right)\frac{P_{CO_2} P_{NO}}{P_{NO_2}}\ + K^{ads}_{NO} P_{NO} + \sqrt{\frac{P_{N_2}}{K_{N_2} K^{eq}_{N-N}}} + \left(\frac{1}{K^{eq}_{NO-O} K^{des}_{NO_2} K^{ads}_{NO}}\right)\frac{P_{NO_2}}{P_{NO}}\ + \frac{P_{CO_2}}{K^{des}_{CO_2}} + \frac{P_{N_2}}{K^{des}_{N_2}} + \frac{P_{NO_2}}{K^{des}_{NO_2}} + K^{ads}_{H_2O} P_{H_2O}\right)^2} \quad \text{(C3)}$$

Kinetic Model Form 3

$$r_{CO_2} = \frac{\left(k^{ads}_{CO} P_{CO} - \frac{k^{des}_{CO}}{K^{des}_{CO_2}\ K^{eq}_{CO-O}\sqrt{K^{ads}_{O_2}}}\left(\frac{P_{CO_2}}{\sqrt{P_{O_2}}}\right)\right)}{\left(1 + \frac{1}{K^{des}_{CO_2}\ K^{eq}_{CO-O}\sqrt{K^{ads}_{O_2}}}\left(\frac{P_{CO_2}}{\sqrt{P_{O_2}}}\right) + P_{NO} K^{ads}_{NO} + \sqrt{\frac{P_{N_2}}{K^{des}_{N_2} K^{eq}_{N-N}}} + \sqrt{K^{ads}_{O_2}\ P_{O_2}}\ + \frac{P_{CO_2}}{K^{des}_{CO_2}} + \frac{P_{N_2}}{K^{des}_{N_2}} + \frac{P_{NO_2}}{K^{des}_{NO_2}} + K^{ads}_{H_2O}\ P_{H_2O}\right)} + \quad \text{(C4)}$$

$$r_N = \frac{\left(k^{f}_{CO-NO} K^{ads}_{NO} P_{NO} - k^{b}_{CO-NO}\sqrt{\frac{K^{ads}_{O_2}}{K^{des}_{N_2} K^{eq}_{N-N}}}\ \sqrt{P_{N_2} P_{O_2}}\right)}{\left(1 + \frac{1}{K^{des}_{CO_2}\ K^{eq}_{CO-O}\sqrt{K^{ads}_{O_2}}}\left(\frac{P_{CO_2}}{\sqrt{P_{O_2}}}\right) + P_{NO} K^{ads}_{NO} + \sqrt{\frac{P_{N_2}}{K^{des}_{N_2} K^{eq}_{N-N}}} + \sqrt{K^{ads}_{O_2}\ P_{O_2}}\ + \frac{P_{CO_2}}{K^{des}_{CO_2}} + \frac{P_{N_2}}{K^{des}_{N_2}} + \frac{P_{NO_2}}{K^{des}_{NO_2}} + K^{ads}_{H_2O}\ P_{H_2O}\right)^2} + \quad \text{(C5)}$$

Table C2 Elementary reaction steps for 'Form-3'

Type of Reaction	Elementary Step	Kinetic/Equilibrium Constant
Adsorption	$CO + [S] \rightleftharpoons CO[S]$	k^{ads}_{CO}, k^{des}_{CO}
	$NO + [S] \rightleftharpoons NO[S]$	K^{ads}_{NO}
	$O_2 + 2[S] \rightleftharpoons 2O[S]$	$K^{ads}_{O_2}$
Surface Reactions	$NO[S] + [S] \rightleftharpoons N[S] + O[S]$	k^{f}_{CO-NO}, k^{b}_{CO-NO}
	$CO[S] + O[S] \rightleftharpoons CO_2[S] + [S]$	K^{eq}_{CO-O}
	$N[S] + N[S] \rightleftharpoons N_2[S] + [S]$	K^{eq}_{N-N}
	$NO[S] + O[S] \rightleftharpoons NO_2[S] + [S]$	k^{f}_{NO-O},k^{b}_{NO-O}
Desorption	$CO_2[S] \rightleftharpoons CO_2 + [S]$	$K^{des}_{CO_2}$
	$NO_2[S] \rightleftharpoons NO_2 + [S]$	$K^{des}_{NO_2}$
	$N_2[S] \rightleftharpoons N_2 + [S]$	$K^{des}_{N_2}$
Inert	$H_2O + [S] \rightleftharpoons H_2O[S]$	$K^{ads}_{H_2O}$

$$r_{NO_2} = \frac{\left(k^{f}_{NO-O}\sqrt{K^{ads}_{O_2}}K^{ads}_{NO}P_{NO}\sqrt{P_{O_2}} - \frac{k^{b}_{NO-O}}{K^{des}_{NO_2}}P_{NO_2}\right)}{\left(1 + \frac{1}{K^{des}_{CO_2}\ K^{eq}_{CO-O}\sqrt{K^{ads}_{O_2}}}\left(\frac{P_{CO_2}}{\sqrt{P_{O_2}}}\right) + P_{NO}K^{ads}_{NO} + \sqrt{\frac{P_{N_2}}{K^{des}_{N_2}K^{eq}_{N-N}}}\right.} + \\ \left. \sqrt{K^{ads}_{O_2}\ P_{O_2}} + \frac{P_{CO_2}}{K^{des}_{CO_2}} + \frac{P_{N_2}}{K^{des}_{N_2}} + \frac{P_{NO_2}}{K^{des}_{NO_2}} + K^{ads}_{H_2O}\ P_{H_2O}\right)^2 \quad \text{(C6)}$$

Kinetic Model Form 4

$$r_{CO_2} = \frac{\left(k^{ads}_{CO}P_{CO} - \frac{k^{des}_{CO}}{K^{des}_{CO_2}\ K^{eq}_{CO-O}\sqrt{K^{ads}_{O_2}}}\left(\frac{P_{CO_2}}{\sqrt{P_{O_2}}}\right)\right)}{\left(1 + \frac{1}{K^{des}_{CO_2}\ K^{eq}_{CO-O}\sqrt{K^{ads}_{O_2}}}\left(\frac{P_{CO_2}}{\sqrt{P_{O_2}}}\right) + P_{NO}K^{ads}_{NO} + \sqrt{\frac{P_{N_2}}{K^{des}_{N_2}K^{eq}_{N-N}}}\right.} + \\ \left. \sqrt{K^{ads}_{O_2}\ P_{O_2}} + \frac{P_{CO_2}}{K^{des}_{CO_2}} + \frac{P_{N_2}}{K^{des}_{N_2}} + K^{eq}_{NO-O}K^{ads}_{NO}\sqrt{K^{ads}_{O_2}\ P_{O_2}}P_{NO} + K^{ads}_{H_2O}\ P_{H_2O}\right) \quad \text{(C7)}$$

Table C3 Elementary reaction steps for 'Form-4'

Type of Reaction	Elementary Step	Kinetic/Equilibrium Constant
Adsorption	$CO + [S] \rightleftharpoons CO[S]$	k^{ads}_{CO}, k^{des}_{CO}
	$NO + [S] \rightleftharpoons NO[S]$	K^{ads}_{NO}
	$O_2 + 2[S] \rightleftharpoons 2O[S]$	$K^{ads}_{O_2}$
Surface Reactions	$NO[S] + [S] \rightleftharpoons N[S] + O[S]$	k^{f}_{CO-NO}, k^{b}_{CO-NO}
	$CO[S] + O[S] \rightleftharpoons CO_2[S] + [S]$	K^{eq}_{CO-O}
	$N[S] + N[S] \rightleftharpoons N_2[S] + [S]$	K^{eq}_{N-N}
	$NO[S] + O[S] \rightleftharpoons NO_2[S] + [S]$	K^{eq}_{NO-O}
Desorption	$CO_2[S] \rightleftharpoons CO_2 + [S]$	$K^{des}_{CO_2}$
	$NO_2[S] \rightleftharpoons NO_2 + [S]$	$k^{f}_{NO_2}$, $k^{b}_{NO_2}$
	$N_2[S] \rightleftharpoons N_2 + [S]$	$K^{des}_{N_2}$
Inert	$H_2O + [S] \rightleftharpoons H_2O[S]$	$K^{ads}_{H_2O}$

$$r_N = \frac{\left(k^{f}_{CO-NO}K^{ads}_{NO}P_{NO} - k^{b}_{CO-NO}\sqrt{\frac{K^{ads}_{O_2}}{K^{des}_{N_2}K^{eq}_{N-N}}}\sqrt{P_{N_2}P_{O_2}}\right)}{\left(1 + \frac{1}{K^{des}_{CO_2}\ K^{eq}_{CO-O}\sqrt{K^{ads}_{O_2}}}\left(\frac{P_{CO_2}}{\sqrt{P_{O_2}}}\right) + P_{NO}K^{ads}_{NO} + \sqrt{\frac{P_{N_2}}{K^{des}_{N_2}K^{eq}_{N-N}}}\right.+}$$
$$\left.\sqrt{K^{ads}_{O_2}\ P_{O_2}}\ + \frac{P_{CO_2}}{K^{des}_{CO_2}} + \frac{P_{N_2}}{K^{des}_{N_2}} + K^{eq}_{NO-O}K^{ads}_{NO}\sqrt{K^{ads}_{O_2}\ P_{O_2}}P_{NO} + K^{ads}_{H_2O}\ P_{H_2O}\right)^2 \quad \text{(C8)}$$

$$r_{NO_2} = \frac{\left(k^{ads}_{NO_2}K^{eq}_{NO-O}K^{ads}_{NO}\sqrt{K^{ads}_{O_2}\ P_{O_2}}P_{NO} - k^{des}_{NO_2}P_{NO_2}\right)}{\left(1 + \frac{1}{K^{des}_{CO_2}\ K^{eq}_{CO-O}\sqrt{K^{ads}_{O_2}}}\left(\frac{P_{CO_2}}{\sqrt{P_{O_2}}}\right) + P_{NO}K^{ads}_{NO} + \sqrt{\frac{P_{N_2}}{K^{des}_{N_2}K^{eq}_{N-N}}}\right.+}$$
$$\left.\sqrt{K^{ads}_{O_2}\ P_{O_2}}\ + \frac{P_{CO_2}}{K^{des}_{CO_2}} + \frac{P_{N_2}}{K^{des}_{N_2}} + K^{eq}_{NO-O}K^{ads}_{NO}\sqrt{K^{ads}_{O_2}\ P_{O_2}}P_{NO} + K^{ads}_{H_2O}\ P_{H_2O}\right) \quad \text{(C9)}$$

Kinetic Model Form 5

$$r_{CO_2} = \frac{\left(k_{O_2}^{ads} P_{O_2} - \left(\frac{k_{O_2}^{des}}{\left[K_{CO-O}^{eq}\ K_{CO_2}^{des} K_{CO}^{ads}\right]^2}\right)\left(\frac{P_{CO_2}}{P_{CO}}\right)^2\right)}{\left(1 + P_{CO}K_{CO}^{ads} + \left(\frac{K_{CO-O}^{eq} K_{CO_2}^{des} K_{CO}^{ads}}{K_{NO-O}^{eq} K_{NO_2}^{des}}\right)\left(\frac{P_{NO_2} P_{CO}}{P_{CO_2}}\right) + \sqrt{\frac{P_{N_2}}{K_{N_2}^{des} K_{N-N}^{eq}}} + \left(\frac{1}{K_{CO-O}^{eq}\ K_{CO_2}^{des} K_{CO}^{ads}}\right)\left(\frac{P_{CO_2}}{P_{CO}}\right) + \frac{P_{CO_2}}{K_{CO_2}^{des}} + \frac{P_{N_2}}{K_{N_2}^{des}} + \frac{P_{NO_2}}{K_{NO_2}^{des}} + K_{H_2O}^{ads}\ P_{H_2O}\right)^2} \quad \text{(C10)}$$

Table C4 Elementary reaction steps for 'Form-5'

Type of Reaction	Elementary Step	Kinetic/Equilibrium Constant
Adsorption	$CO + [S] \rightleftharpoons CO[S]$	K_{CO}^{ads}
	$NO + [S] \rightleftharpoons NO[S]$	k_{NO}^{ads}, k_{NO}^{des}
	$O_2 + 2[S] \rightleftharpoons 2O[S]$	$k_{O_2}^{ads}$, $k_{O_2}^{des}$
Surface Reactions	$NO[S] + [S] \rightleftharpoons N[S] + O[S]$	k_{CO-NO}^{f}, k_{CO-NO}^{b}
	$CO[S] + O[S] \rightleftharpoons CO_2[S] + [S]$	K_{CO-O}^{eq}
	$N[S] + N[S] \rightleftharpoons N_2[S] + [S]$	K_{N-N}^{eq}
	$NO[S] + O[S] \rightleftharpoons NO_2[S] + [S]$	K_{NO-O}^{eq}
Desorption	$CO_2[S] \rightleftharpoons CO_2 + [S]$	$K_{CO_2}^{des}$
	$NO_2[S] \rightleftharpoons NO_2 + [S]$	$k_{NO_2}^{f}$, $k_{NO_2}^{b}$
	$N_2[S] \rightleftharpoons N_2 + [S]$	$K_{N_2}^{des}$
Inert	$H_2O + [S] \rightleftharpoons H_2O[S]$	$K_{H_2O}^{ads}$

$$r_N = \frac{\left(k^f_{CO-NO}\left(\frac{K^{eq}_{CO-O}K^{des}_{CO_2}K^{ads}_{CO}}{K^{eq}_{NO-O}K^{des}_{NO_2}}\right)\left(\frac{P_{NO_2}P_{CO}}{P_{CO_2}}\right) - \left(\frac{k^b_{CO-NO}}{K^{eq}_{CO-O}\ K^{des}_{CO_2}K^{ads}_{CO}\sqrt{K^{des}_{N_2}K^{eq}_{N-N}}}\right)\left(\frac{P_{CO_2}\sqrt{P_{N_2}}}{P_{CO}}\right)\right)}{\left(1 + P_{CO}K^{ads}_{CO} + \left(\frac{K^{eq}_{CO-O}K^{des}_{CO_2}K^{ads}_{CO}}{K^{eq}_{NO-O}K^{des}_{NO_2}}\right)\left(\frac{P_{NO_2}P_{CO}}{P_{CO_2}}\right) + \sqrt{\frac{P_{N_2}}{K^{des}_{N_2}K^{eq}_{N-N}}} + \left(\frac{1}{K^{eq}_{CO-O}\ K^{des}_{CO_2}K^{ads}_{CO}}\right)\left(\frac{P_{CO_2}}{P_{CO}}\right) + \frac{P_{CO_2}}{K^{des}_{CO_2}} + \frac{P_{N_2}}{K^{des}_{N_2}} + \frac{P_{NO_2}}{K^{des}_{NO_2}} + K^{ads}_{H_2O}\ P_{H_2O}\right)^2} \quad \text{(C11)}$$

$$r_{NO_2} = \frac{\left(k^{ads}_{NO}P_{NO} - k^{des}_{NO}\left(\frac{K^{eq}_{CO-O}K^{des}_{CO_2}K^{ads}_{CO}}{K^{eq}_{NO-O}K^{des}_{NO_2}}\right)\left(\frac{P_{NO_2}P_{CO}}{P_{CO_2}}\right)\right)}{\left(1 + P_{CO}K^{ads}_{CO} + \left(\frac{K^{eq}_{CO-O}K^{des}_{CO_2}K^{ads}_{CO}}{K^{eq}_{NO-O}K^{des}_{NO_2}}\right)\left(\frac{P_{NO_2}P_{CO}}{P_{CO_2}}\right) + \sqrt{\frac{P_{N_2}}{K^{des}_{N_2}K^{eq}_{N-N}}} + \left(\frac{1}{K^{eq}_{CO-O}\ K^{des}_{CO_2}K^{ads}_{CO}}\right)\left(\frac{P_{CO_2}}{P_{CO}}\right) + \frac{P_{CO_2}}{K^{des}_{CO_2}} + \frac{P_{N_2}}{K^{des}_{N_2}} + \frac{P_{NO_2}}{K^{des}_{NO_2}} + K^{ads}_{H_2O}\ P_{H_2O}\right)} \quad \text{(C12)}$$

Kinetic Model Form 6

$$r_{CO_2} = \frac{\left(k^{ads}_{O_2}P_{O_2} - \left(\frac{k^{des}_{O_2}}{\left[K^{eq}_{CO-O}\ K^{des}_{CO_2}K^{ads}_{CO}\right]^2}\right)\left(\frac{P_{CO_2}}{P_{CO}}\right)^2\right)}{\left(1 + P_{CO}K^{ads}_{CO} + P_{NO}K^{ads}_{NO} + \sqrt{\frac{P_{N_2}}{K^{des}_{N_2}K^{eq}_{N-N}}} + \left(\frac{1}{K^{eq}_{CO-O}\ K^{des}_{CO_2}K^{ads}_{CO}}\right)\left(\frac{P_{CO_2}}{P_{CO}}\right) + \frac{P_{CO_2}}{K^{des}_{CO_2}} + \frac{P_{N_2}}{K^{des}_{N_2}} + \frac{P_{NO_2}}{K^{des}_{NO_2}} + K^{ads}_{H_2O}\ P_{H_2O}\right)^2} \quad \text{(C13)}$$

Table C5 Elementary reaction steps for 'Form-6'

Type of Reaction	Elementary Step	Kinetic/Equilibrium Constant
Adsorption	$CO + [S] \rightleftharpoons CO[S]$	K_{CO}^{ads}
	$NO + [S] \rightleftharpoons NO[S]$	K_{NO}^{ads}
	$O_2 + 2[S] \rightleftharpoons 2O[S]$	$k_{O_2}^{ads}$, $k_{O_2}^{des}$
Surface Reactions	$NO[S] + [S] \rightleftharpoons N[S] + O[S]$	k_{CO-NO}^{f}, k_{CO-NO}^{b}
	$CO[S] + O[S] \rightleftharpoons CO_2[S] + [S]$	K_{CO-O}^{eq}
	$N[S] + N[S] \rightleftharpoons N_2[S] + [S]$	K_{N-N}^{eq}
	$NO[S] + O[S] \rightleftharpoons NO_2[S] + [S]$	k_{NO-O}^{f}, k_{NO-O}^{b}
Desorption	$CO_2[S] \rightleftharpoons CO_2 + [S]$	$K_{CO_2}^{des}$
	$NO_2[S] \rightleftharpoons NO_2 + [S]$	$K_{NO_2}^{des}$
	$N_2[S] \rightleftharpoons N_2 + [S]$	$K_{N_2}^{des}$
Inert	$H_2O + [S] \rightleftharpoons H_2O[S]$	$K_{H_2O}^{ads}$

$$r_N = \frac{\left(k_{CO-NO}^{f} P_{NO} K_{NO}^{ads} - \left(\frac{k_{CO-NO}^{b}}{\sqrt{K_{N_2}^{des} K_{N-N}^{eq}} K_{CO-O}^{eq}\ K_{CO_2}^{des} K_{CO}^{ads}}\right)\left(\frac{P_{CO_2}\sqrt{P_{N_2}}}{P_{CO}}\right)\right)}{\left(1 + P_{CO} K_{CO}^{ads} + P_{NO} K_{NO}^{ads} + \sqrt{\frac{P_{N_2}}{K_{N_2}^{des} K_{N-N}^{eq}}} + \left(\frac{1}{K_{CO-O}^{eq}\ K_{CO_2}^{des} K_{CO}^{ads}}\right)\left(\frac{P_{CO_2}}{P_{CO}}\right) + \frac{P_{CO_2}}{K_{CO_2}^{des}} + \frac{P_{N_2}}{K_{N_2}^{des}} + \frac{P_{NO_2}}{K_{NO_2}^{des}} + K_{H_2O}^{ads}\ P_{H_2O}\right)^2} \quad \text{(C14)}$$

$$r_{NO_2} = \frac{\left(\left(\frac{k^{f}_{NO-O} K^{ads}_{NO}}{K^{eq}_{CO-O}\ K^{des}_{CO_2} K^{ads}_{CO}}\right)\left(\frac{P_{CO_2} P_{NO}}{P_{CO}}\right) - \frac{k^{b}_{NO-O}}{K^{des}_{NO_2}} P_{NO_2}\right)}{\left(1 + P_{CO} K^{ads}_{CO} + P_{NO} K^{ads}_{NO} + \sqrt{\frac{P_{N_2}}{K^{des}_{N_2} K^{eq}_{N-N}}} + \left(\frac{1}{K^{eq}_{CO-O}\ K^{des}_{CO_2} K^{ads}_{CO}}\right)\left(\frac{P_{CO_2}}{P_{CO}}\right) + \frac{P_{CO_2}}{K^{des}_{CO_2}} + \frac{P_{N_2}}{K^{des}_{N_2}} + \frac{P_{NO_2}}{K^{des}_{NO_2}} + K^{ads}_{H_2O}\ P_{H_2O}\right)^2} \quad \text{(C15)}$$

Kinetic Model Form 7

$$r_{CO_2} = \frac{\left(k^{ads}_{O_2} P_{O_2} - \left(\frac{k^{des}_{O_2}}{\left[K^{eq}_{CO-O}\ K^{des}_{CO_2} K^{ads}_{CO}\right]^2}\right)\left(\frac{P_{CO_2}}{P_{CO}}\right)^2\right)}{\left(1 + P_{CO} K^{ads}_{CO} + P_{NO} K^{ads}_{NO} + \sqrt{\frac{P_{N_2}}{K^{des}_{N_2} K^{eq}_{N-N}}} + \left(\frac{1}{K^{eq}_{CO-O}\ K^{des}_{CO_2} K^{ads}_{CO}}\right)\left(\frac{P_{CO_2}}{P_{CO}}\right) + \frac{P_{CO_2}}{K^{des}_{CO_2}} + \frac{P_{N_2}}{K^{des}_{N_2}} + \left(\frac{K^{eq}_{NO-O}\ K^{ads}_{NO}}{K^{eq}_{CO-O}\ K^{des}_{CO_2} K^{ads}_{CO}}\right)\left(\frac{P_{CO_2}\ P_{NO}}{P_{CO}}\right) + K^{ads}_{H_2O}\ P_{H_2O}\right)^2} \quad \text{(C16)}$$

$$r_{N} = \frac{\left(k^{f}_{CO-NO} P_{NO} K^{ads}_{NO} - \left(\frac{k^{b}_{CO-NO}}{\sqrt{K^{des}_{N_2} K^{eq}_{N-N}} K^{eq}_{CO-O}\ K^{des}_{CO_2} K^{ads}_{CO}}\right)\left(\frac{P_{CO_2}\sqrt{P_{N_2}}}{P_{CO}}\right)\right)}{\left(1 + P_{CO} K^{ads}_{CO} + P_{NO} K^{ads}_{NO} + \sqrt{\frac{P_{N_2}}{K^{des}_{N_2} K^{eq}_{N-N}}} + \left(\frac{1}{K^{eq}_{CO-O}\ K^{des}_{CO_2} K^{ads}_{CO}}\right)\left(\frac{P_{CO_2}}{P_{CO}}\right) + \frac{P_{CO_2}}{K^{des}_{CO_2}} + \frac{P_{N_2}}{K^{des}_{N_2}} + \left(\frac{K^{eq}_{NO-O}\ K^{ads}_{NO}}{K^{eq}_{CO-O}\ K^{des}_{CO_2} K^{ads}_{CO}}\right)\left(\frac{P_{CO_2}\ P_{NO}}{P_{CO}}\right) + K^{ads}_{H_2O}\ P_{H_2O}\right)^2} \quad \text{(C17)}$$

Table C6 Elementary reaction steps for 'Form-7'

Type of Reaction	Elementary Step	Kinetic/Equilibrium Constant
Adsorption	$CO + [S] \rightleftharpoons CO[S]$	K_{CO}^{ads}
	$NO + [S] \rightleftharpoons NO[S]$	K_{NO}^{ads}
	$O_2 + 2[S] \rightleftharpoons 2O[S]$	$k_{O_2}^{ads}$, $k_{O_2}^{des}$
Surface Reactions	$NO[S] + [S] \rightleftharpoons N[S] + O[S]$	k_{CO-NO}^{f}, k_{CO-NO}^{b}
	$CO[S] + O[S] \rightleftharpoons CO_2[S] + [S]$	K_{CO-O}^{eq}
	$N[S] + N[S] \rightleftharpoons N_2[S] + [S]$	K_{N-N}^{eq}
	$NO[S] + O[S] \rightleftharpoons NO_2[S] + [S]$	K_{NO-O}^{eq}
Desorption	$CO_2[S] \rightleftharpoons CO_2 + [S]$	$K_{CO_2}^{des}$
	$NO_2[S] \rightleftharpoons NO_2 + [S]$	$k_{NO_2}^{ads}$, $k_{NO_2}^{des}$
	$N_2[S] \rightleftharpoons N_2 + [S]$	$K_{N_2}^{des}$
Inert	$H_2O + [S] \rightleftharpoons H_2O[S]$	$K_{H_2O}^{ads}$

$$r_{NO_2} = \frac{\left(\left(\frac{k_{NO_2}^{ads} K_{NO-O}^{eq} K_{NO}^{ads}}{K_{CO-O}^{eq} K_{CO_2}^{des} K_{CO}^{ads}}\right)\left(\frac{P_{CO_2} P_{NO}}{P_{CO}}\right) - k_{NO_2}^{des} P_{NO_2}\right)}{\left(1 + P_{CO} K_{CO}^{ads} + P_{NO} K_{NO}^{ads} + \sqrt{\frac{P_{N_2}}{K_{N_2}^{des} K_{N-N}^{eq}}} + \left(\frac{1}{K_{CO-O}^{eq} K_{CO_2}^{des} K_{CO}^{ads}}\right)\left(\frac{P_{CO_2}}{P_{CO}}\right) + \frac{P_{CO_2}}{K_{CO_2}^{des}} + \frac{P_{N_2}}{K_{N_2}^{des}} + \left(\frac{K_{NO-O}^{eq} K_{NO}^{ads}}{K_{CO-O}^{eq} K_{CO_2}^{des} K_{CO}^{ads}}\right)\left(\frac{P_{CO_2} P_{NO}}{P_{CO}}\right) + K_{H_2O}^{ads} P_{H_2O}\right)} \quad \text{(C18)}$$

Kinetic Model Form 8

$$r_{CO_2} = \frac{\left(k^{f}_{CO-O} K^{ads}_{CO} \sqrt{K^{ads}_{O_2}\, P_{O_2}}\, P_{CO} - k^{b}_{CO-O} \frac{P_{CO_2}}{K^{des}_{CO_2}}\right)}{\left(1 + P_{CO} K^{ads}_{CO} + \frac{1}{K^{des}_{NO_2}\, K^{eq}_{NO-O} \sqrt{K^{ads}_{O_2}}} \left(\frac{P_{NO_2}}{\sqrt{P_{O_2}}}\right) + \sqrt{\frac{P_{N_2}}{K^{des}_{N_2} K^{eq}_{N-N}}} + \sqrt{K^{ads}_{O_2}\, P_{O_2}} + \frac{P_{CO_2}}{K^{des}_{CO_2}} + \frac{P_{N_2}}{K^{des}_{N_2}} + \frac{P_{NO_2}}{K^{des}_{NO_2}} + K^{ads}_{H_2O}\, P_{H_2O}\right)^2} \quad \text{(C19)}$$

$$r_N = \frac{\left(\frac{k^{f}_{CO-NO}}{K^{des}_{NO_2}\, K^{eq}_{NO-O} \sqrt{K^{ads}_{O_2}}} \left(\frac{P_{NO_2}}{\sqrt{P_{O_2}}}\right) - k^{b}_{CO-NO} \sqrt{\frac{K^{ads}_{O_2}}{K^{des}_{N_2} K^{eq}_{N-N}}} \sqrt{P_{N_2} P_{O_2}}\right)}{\left(1 + P_{CO} K^{ads}_{CO} + \frac{1}{K^{des}_{NO_2}\, K^{eq}_{NO-O} \sqrt{K^{ads}_{O_2}}} \left(\frac{P_{NO_2}}{\sqrt{P_{O_2}}}\right) + \sqrt{\frac{P_{N_2}}{K^{des}_{N_2} K^{eq}_{N-N}}} + \sqrt{K^{ads}_{O_2}\, P_{O_2}} + \frac{P_{CO_2}}{K^{des}_{CO_2}} + \frac{P_{N_2}}{K^{des}_{N_2}} + \frac{P_{NO_2}}{K^{des}_{NO_2}} + K^{ads}_{H_2O}\, P_{H_2O}\right)^2} \quad \text{(C20)}$$

Table C7 Elementary reaction steps for 'Form-8'

Type of Reaction	Elementary Step	Kinetic/Equilibrium Constant
Adsorption	$CO + [S] \rightleftharpoons CO[S]$	K^{ads}_{CO}
	$NO + [S] \rightleftharpoons NO[S]$	k^{ads}_{NO}, k^{des}_{NO}
	$O_2 + 2[S] \rightleftharpoons 2O[S]$	$K^{ads}_{O_2}$
Surface Reactions	$NO[S] + [S] \rightleftharpoons N[S] + O[S]$	k^{f}_{CO-NO}, k^{b}_{CO-NO}
	$CO[S] + O[S] \rightleftharpoons CO_2[S] + [S]$	k^{f}_{CO-O}, k^{b}_{CO-O}
	$N[S] + N[S] \rightleftharpoons N_2[S] + [S]$	K^{eq}_{N-N}
	$NO[S] + O[S] \rightleftharpoons NO_2[S] + [S]$	K^{eq}_{NO-O}
Desorption	$CO_2[S] \rightleftharpoons CO_2 + [S]$	$K^{des}_{CO_2}$
	$NO_2[S] \rightleftharpoons NO_2 + [S]$	$K^{des}_{NO_2}$
	$N_2[S] \rightleftharpoons N_2 + [S]$	$K^{des}_{N_2}$
Inert	$H_2O + [S] \rightleftharpoons H_2O[S]$	$K^{ads}_{H_2O}$

$$r_{NO_2} = \frac{\left(k_{NO}^{ads} P_{NO} - \frac{k_{NO}^{des}}{K_{NO_2}^{des}\ K_{NO-O}^{eq}\sqrt{K_{O_2}^{ads}}}\left(\frac{P_{NO_2}}{\sqrt{P_{O_2}}}\right)\right)}{\left(1 + P_{CO}K_{CO}^{ads} + \frac{1}{K_{NO_2}^{des}\ K_{NO-O}^{eq}\sqrt{K_{O_2}^{ads}}}\left(\frac{P_{NO_2}}{\sqrt{P_{O_2}}}\right)\right.}$$
$$\left. + \sqrt{\frac{P_{N_2}}{K_{N_2}^{des}K_{N-N}^{eq}}} + \sqrt{K_{O_2}^{ads}\ P_{O_2}} + \frac{P_{CO_2}}{K_{CO_2}^{des}} + \frac{P_{N_2}}{K_{N_2}^{des}} + \frac{P_{NO_2}}{K_{NO_2}^{des}} + K_{H_2O}^{ads}\ P_{H_2O}\right)^2 \quad \text{(C21)}$$

Kinetic Model Form 9

$$r_{CO_2} = \frac{\left(\left(\frac{k_{CO-O}^{f}K_{CO}^{ads}}{K_{NO-O}^{eq}\ K_{NO_2}^{des}K_{NO}^{ads}}\right)\left(\frac{P_{NO_2}P_{CO}}{P_{NO}}\right) - k_{CO-O}^{b}\frac{P_{CO_2}}{K_{CO_2}^{des}}\right)}{\left(1 + P_{CO}K_{CO}^{ads} + P_{NO}K_{NO}^{ads}\right.}$$
$$\left. + \sqrt{\frac{P_{N_2}}{K_{N_2}^{des}K_{N-N}^{eq}}} + \left(\frac{1}{K_{NO-O}^{eq}\ K_{NO_2}^{des}K_{NO}^{ads}}\right)\left(\frac{P_{NO_2}}{P_{NO}}\right) + \frac{P_{CO_2}}{K_{CO_2}^{des}}\right.$$
$$\left. + \frac{P_{N_2}}{K_{N_2}^{des}} + \frac{P_{NO_2}}{K_{NO_2}^{des}} + K_{H_2O}^{ads}\ P_{H_2O}\right)^2 \quad \text{(C22)}$$

$$r_N = \frac{\left(k_{CO-NO}^{f}P_{NO}K_{NO}^{ads} - k_{CO-NO}^{b}\ \left(\frac{1}{\sqrt{K_{N_2}^{des}K_{N-N}^{eq}}K_{NO-O}^{eq}\ K_{NO_2}^{des}K_{NO}^{ads}}\right)\left(\frac{P_{NO_2}\sqrt{P_{N_2}}}{P_{NO}}\right)\right)}{\left(1 + P_{CO}K_{CO}^{ads} + P_{NO}K_{NO}^{ads}\right.}$$
$$\left. + \sqrt{\frac{P_{N_2}}{K_{N_2}^{des}K_{N-N}^{eq}}} + \left(\frac{1}{K_{NO-O}^{eq}\ K_{NO_2}^{des}K_{NO}^{ads}}\right)\left(\frac{P_{NO_2}}{P_{NO}}\right) + \frac{P_{CO_2}}{K_{CO_2}^{des}}\right.$$
$$\left. + \frac{P_{N_2}}{K_{N_2}^{des}} + \frac{P_{NO_2}}{K_{NO_2}^{des}} + K_{H_2O}^{ads}\ P_{H_2O}\right)^2 \quad \text{(C23)}$$

Table C8 Elementary reaction steps for 'Form-9'

Type of Reaction	Elementary Step	Kinetic/Equilibrium Constant
Adsorption	$CO + [S] \rightleftharpoons CO[S]$	K_{CO}^{ads}
	$NO + [S] \rightleftharpoons NO[S]$	K_{NO}^{ads}
	$O_2 + 2[S] \rightleftharpoons 2O[S]$	$k_{O_2}^{ads}$, $k_{O_2}^{des}$
Surface Reactions	$NO[S] + [S] \rightleftharpoons N[S] + O[S]$	k_{CO-NO}^{f}, k_{CO-NO}^{b}
	$CO[S] + O[S] \rightleftharpoons CO_2[S] + [S]$	k_{CO-O}^{f}, k_{CO-O}^{b}
	$N[S] + N[S] \rightleftharpoons N_2[S] + [S]$	K_{N-N}^{eq}
	$NO[S] + O[S] \rightleftharpoons NO_2[S] + [S]$	K_{NO-O}^{eq}
Desorption	$CO_2[S] \rightleftharpoons CO_2 + [S]$	$K_{CO_2}^{des}$
	$NO_2[S] \rightleftharpoons NO_2 + [S]$	$K_{NO_2}^{des}$
	$N_2[S] \rightleftharpoons N_2 + [S]$	$K_{N_2}^{des}$
Inert	$H_2O + [S] \rightleftharpoons H_2O[S]$	$K_{H_2O}^{ads}$

$$r_{NO_2} = \frac{\left(k_{O_2}^{ads} P_{O_2} - k_{O_2}^{des}\left[\left(\frac{1}{K_{NO-O}^{eq}\, K_{NO_2}^{des} K_{NO}^{ads}}\right)\left(\frac{P_{NO_2}}{P_{NO}}\right)\right]^2\right)}{\left(1 + P_{CO}K_{CO}^{ads} + P_{NO}K_{NO}^{ads} + \sqrt{\frac{P_{N_2}}{K_{N_2}^{des}K_{N-N}^{eq}}} + \left(\frac{1}{K_{NO-O}^{eq}\, K_{NO_2}^{des} K_{NO}^{ads}}\right)\left(\frac{P_{NO_2}}{P_{NO}}\right) + \frac{P_{CO_2}}{K_{CO_2}^{des}} + \frac{P_{N_2}}{K_{N_2}^{des}} + \frac{P_{NO_2}}{K_{NO_2}^{des}} + K_{H_2O}^{ads}\, P_{H_2O}\right)^2} \quad \text{(C24)}$$

Kinetic Model Form 11

$$r_{CO_2} = \frac{\left(k^f_{CO-O} K^{ads}_{CO} \sqrt{K^{ads}_{O_2}\ P_{O_2}} P_{CO} - \frac{k^b_{CO-O}}{K^{des}_{CO_2}} P_{CO_2}\right)}{\left(1 + P_{CO} K^{ads}_{CO} + P_{NO} K^{ads}_{NO} + \sqrt{\frac{P_{N_2}}{K^{des}_{N_2} K^{eq}_{N-N}}} + \sqrt{K^{ads}_{O_2}\ P_{O_2}} + \frac{P_{CO_2}}{K^{des}_{CO_2}} + \frac{P_{N_2}}{K^{des}_{N_2}} + K^{eq}_{NO-O} K^{ads}_{NO} \sqrt{K^{ads}_{O_2}\ P_{O_2}} P_{NO} + K^{ads}_{H_2O}\ P_{H_2O}\right)^2} \quad \text{(C25)}$$

$$r_N = \frac{\left(k^f_{CO-NO} K^{ads}_{NO} P_{NO} - k^b_{CO-NO} \sqrt{\frac{K^{ads}_{O_2}}{K^{des}_{N_2} K N-N^{eq}}}\ \sqrt{P_{N_2} P_{O_2}}\right)}{\left(1 + P_{CO} K^{ads}_{CO} + P_{NO} K^{ads}_{NO} + \sqrt{\frac{P_{N_2}}{K^{des}_{N_2} K^{eq}_{N-N}}} + \sqrt{K^{ads}_{O_2}\ P_{O_2}} + \frac{P_{CO_2}}{K^{des}_{CO_2}} + \frac{P_{N_2}}{K^{des}_{N_2}} + K^{eq}_{NO-O} K^{ads}_{NO} \sqrt{K^{ads}_{O_2}\ P_{O_2}} P_{NO} + K^{ads}_{H_2O}\ P_{H_2O}\right)^2} \quad \text{(C26)}$$

Table C9 Elementary reaction steps for 'Form-11'

Type of Reaction	Elementary Step	Kinetic/Equilibrium Constant
Adsorption	$CO + [S] \rightleftharpoons CO[S]$	K^{ads}_{CO}
	$NO + [S] \rightleftharpoons NO[S]$	K^{ads}_{NO}
	$O_2 + 2[S] \rightleftharpoons 2O[S]$	$K^{ads}_{O_2}$
Surface Reactions	$NO[S] + [S] \rightleftharpoons N[S] + O[S]$	k^f_{CO-NO}, k^b_{CO-NO}
	$CO[S] + O[S] \rightleftharpoons CO_2[S] + [S]$	k^f_{CO-O}, k^b_{CO-O}
	$N[S] + N[S] \rightleftharpoons N_2[S] + [S]$	K^{eq}_{N-N}
	$NO[S] + O[S] \rightleftharpoons NO_2[S] + [S]$	K^{eq}_{NO-O}
Desorption	$CO_2[S] \rightleftharpoons CO_2 + [S]$	$K^{des}_{CO_2}$
	$NO_2[S] \rightleftharpoons NO_2 + [S]$	$k^{ads}_{NO_2}$, $k^{des}_{NO_2}$
	$N_2[S] \rightleftharpoons N_2 + [S]$	$K^{des}_{N_2}$
Inert	$H_2O + [S] \rightleftharpoons H_2O[S]$	$K^{ads}_{H_2O}$

$$r_{NO_2} = \frac{\left(k^{ads}_{NO_2} K^{eq}_{NO-O} K^{ads}_{NO} \sqrt{K^{ads}_{O_2}\ P_{O_2}} P_{NO} - k^{des}_{NO_2} P_{NO_2}\right)}{\left(1 + P_{CO} K^{ads}_{CO} + P_{NO} K^{ads}_{NO} + \sqrt{\frac{P_{N_2}}{K^{des}_{N_2} K^{eq}_{N-N}}} + \right.}$$

$$\left. \sqrt{K^{ads}_{O_2}\ P_{O_2}} + \frac{P_{CO_2}}{K^{des}_{CO_2}} + \frac{P_{N_2}}{K^{des}_{N_2}} + K^{eq}_{NO-O} K^{ads}_{NO} \sqrt{K^{ads}_{O_2}\ P_{O_2}} P_{NO} + K^{ads}_{H_2O}\ P_{H_2O} \right)^2 \quad \text{(C27)}$$

Kinetic Model Form 12

$$r_{CO_2} = \frac{\left(k^{ads}_{CO_2} K^{eq}_{CO-O} K^{ads}_{CO} \sqrt{K^{ads}_{O_2}\ P_{O_2}} P_{CO} - k^{des}_{CO_2} P_{CO_2}\right)}{\left(1 + P_{CO} K^{ads}_{CO} + \frac{1}{K^{des}_{NO_2}\ K^{eq}_{NO-O} \sqrt{K^{ads}_{O_2}}} \left(\frac{P_{NO_2}}{\sqrt{P_{O_2}}}\right) \right.}$$

$$\left. + \sqrt{\frac{P_{N_2}}{K^{des}_{N_2} K^{eq}_{N-N}}} + \sqrt{K^{ads}_{O_2}\ P_{O_2}} + K^{eq}_{CO-O} K^{ads}_{CO} \sqrt{K^{ads}_{O_2}\ P_{O_2}} P_{CO} \right.$$

$$\left. + \frac{P_{N_2}}{K^{des}_{N_2}} + \frac{P_{NO_2}}{K^{des}_{NO_2}} + K^{ads}_{H_2O}\ P_{H_2O} \right)^2 \quad \text{(C28)}$$

$$r_N = \frac{\left(\frac{k^{f}_{CO-NO}}{K^{des}_{NO_2}\ K^{eq}_{NO-O} \sqrt{K^{ads}_{O_2}}} \left(\frac{P_{NO_2}}{\sqrt{P_{O_2}}}\right) - k^{b}_{CO-NO} \sqrt{\frac{K^{ads}_{O_2}}{K^{des}_{N_2} K^{eq}_{N-N}}} \sqrt{P_{N_2} P_{O_2}}\right)}{\left(1 + P_{CO} K^{ads}_{CO} + \frac{1}{K^{des}_{NO_2}\ K^{eq}_{NO-O} \sqrt{K^{ads}_{O_2}}} \left(\frac{P_{NO_2}}{\sqrt{P_{O_2}}}\right) \right.}$$

$$\left. + \sqrt{\frac{P_{N_2}}{K^{des}_{N_2} K^{eq}_{N-N}}} + \sqrt{K^{ads}_{O_2}\ P_{O_2}} + K^{eq}_{CO-O} K^{ads}_{CO} \sqrt{K^{ads}_{O_2}\ P_{O_2}} P_{CO} \right.$$

$$\left. + \frac{P_{N_2}}{K^{des}_{N_2}} + \frac{P_{NO_2}}{K^{des}_{NO_2}} + K^{ads}_{H_2O}\ P_{H_2O} \right)^2 \quad \text{(C29)}$$

Table C10 Elementary reaction steps for 'Form-12'

Type of Reaction	Elementary Step	Kinetic/Equilibrium Constant
Adsorption	$CO + [S] \rightleftharpoons CO[S]$	K_{CO}^{ads}
	$NO + [S] \rightleftharpoons NO[S]$	k_{NO}^{ads}, k_{NO}^{des}
	$O_2 + 2[S] \rightleftharpoons 2O[S]$	$K_{O_2}^{ads}$
Surface Reactions	$NO[S] + [S] \rightleftharpoons N[S] + O[S]$	k_{CO-NO}^{f}, k_{CO-NO}^{b}
	$CO[S] + O[S] \rightleftharpoons CO_2[S] + [S]$	K_{CO-O}^{eq}
	$N[S] + N[S] \rightleftharpoons N_2[S] + [S]$	K_{N-N}^{eq}
	$NO[S] + O[S] \rightleftharpoons NO_2[S] + [S]$	K_{NO-O}^{eq}
Desorption	$CO_2[S] \rightleftharpoons CO_2 + [S]$	$k_{CO_2}^{ads}$, $k_{CO_2}^{des}$
	$NO_2[S] \rightleftharpoons NO_2 + [S]$	$K_{NO_2}^{des}$
	$N_2[S] \rightleftharpoons N_2 + [S]$	$K_{N_2}^{des}$
Inert	$H_2O + [S] \rightleftharpoons H_2O[S]$	$K_{H_2O}^{ads}$

$$r_{NO_2} = \frac{\left(k_{NO}^{ads} P_{NO} - \frac{k_{NO}^{des}}{K_{NO_2}^{des}\ K_{NO-O}^{eq}\sqrt{K_{O_2}^{ads}}}\left(\frac{P_{NO_2}}{\sqrt{P_{O_2}}}\right)\right)}{\left(1 + P_{CO}K_{CO}^{ads} + \frac{1}{K_{NO_2}^{des}\ K_{NO-O}^{eq}\sqrt{K_{O_2}^{ads}}}\left(\frac{P_{NO_2}}{\sqrt{P_{O_2}}}\right)\right.}$$
$$\left. + \sqrt{\frac{P_{N_2}}{K_{N_2}^{des}K_{N-N}^{eq}}} + \sqrt{K_{O_2}^{ads}\ P_{O_2}} + K_{CO-O}^{eq}K_{CO}^{ads}\sqrt{K_{O_2}^{ads}\ P_{O_2}}P_{CO}\right.$$
$$\left. + \frac{P_{N_2}}{K_{N_2}^{des}} + \frac{P_{NO_2}}{K_{NO_2}^{des}} + K_{H_2O}^{ads}\ P_{H_2O}\right)^2 \quad \text{(C30)}$$

Kinetic Model Form 13

$$r_{CO_2} = \frac{\left(k^{ads}_{CO_2}\left(\frac{K^{eq}_{CO-O}K^{ads}_{CO}}{K^{eq}_{NO-O}\,K^{des}_{NO_2}K^{ads}_{NO}}\right)\left(\frac{P_{CO}P_{NO_2}}{P_{NO}}\right) - k^{des}_{CO_2}P_{CO_2}\right)}{\left(1 + P_{CO}K^{ads}_{CO} + P_{NO}K^{ads}_{NO} + \sqrt{\frac{P_{N_2}}{K^{des}_{N_2}K^{eq}_{N-N}}} + \left(\frac{1}{K^{eq}_{NO-O}\,K^{des}_{NO_2}K^{ads}_{NO}}\right)\left(\frac{P_{NO_2}}{P_{NO}}\right) + \left(\frac{K^{eq}_{CO-O}K^{ads}_{CO}}{K^{eq}_{NO-O}\,K^{des}_{NO_2}K^{ads}_{NO}}\right)\left(\frac{P_{CO}P_{NO_2}}{P_{NO}}\right) + \frac{P_{N_2}}{K^{des}_{N_2}} + \frac{P_{NO_2}}{K^{des}_{NO_2}} + K^{ads}_{H_2O}\,P_{H_2O}\right)} \quad \text{(C31)}$$

$$r_N = \frac{\left(k^{f}_{CO-NO}P_{NO}K^{ads}_{NO} - k^{b}_{CO-NO}\left(\frac{1}{\sqrt{K^{des}_{N_2}K^{eq}_{N-N}}K^{eq}_{NO-O}\,K^{des}_{NO_2}K^{ads}_{NO}}\right)\left(\frac{P_{NO_2}\sqrt{P_{N_2}}}{P_{NO}}\right)\right)}{\left(1 + P_{CO}K^{ads}_{CO} + P_{NO}K^{ads}_{NO} + \sqrt{\frac{P_{N_2}}{K^{des}_{N_2}K^{eq}_{N-N}}} + \left(\frac{1}{K^{eq}_{NO-O}\,K^{des}_{NO_2}K^{ads}_{NO}}\right)\left(\frac{P_{NO_2}}{P_{NO}}\right) + \left(\frac{K^{eq}_{CO-O}K^{ads}_{CO}}{K^{eq}_{NO-O}\,K^{des}_{NO_2}K^{ads}_{NO}}\right)\left(\frac{P_{CO}P_{NO_2}}{P_{NO}}\right) + \frac{P_{N_2}}{K^{des}_{N_2}} + \frac{P_{NO_2}}{K^{des}_{NO_2}} + K^{ads}_{H_2O}\,P_{H_2O}\right)^2} \quad \text{(C32)}$$

$$r_{NO_2} = \frac{\left(k^{ads}_{O_2}P_{O_2} - k^{des}_{O_2}\left[\left(\frac{1}{K^{eq}_{NO-O}\,K^{des}_{NO_2}K^{ads}_{NO}}\right)\left(\frac{P_{NO_2}}{P_{NO}}\right)\right]^2\right)}{\left(1 + P_{CO}K^{ads}_{CO} + P_{NO}K^{ads}_{NO} + \sqrt{\frac{P_{N_2}}{K^{des}_{N_2}K^{eq}_{N-N}}} + \left(\frac{1}{K^{eq}_{NO-O}\,K^{des}_{NO_2}K^{ads}_{NO}}\right)\left(\frac{P_{NO_2}}{P_{NO}}\right) + \left(\frac{K^{eq}_{CO-O}K^{ads}_{CO}}{K^{eq}_{NO-O}\,K^{des}_{NO_2}K^{ads}_{NO}}\right)\left(\frac{P_{CO}P_{NO_2}}{P_{NO}}\right) + \frac{P_{N_2}}{K^{des}_{N_2}} + \frac{P_{NO_2}}{K^{des}_{NO_2}} + K^{ads}_{H_2O}\,P_{H_2O}\right)^2} \quad \text{(C33)}$$

Table C11 Elementary reaction steps for 'Form-13'

Type of Reaction	Elementary Step	Kinetic/Equilibrium Constant
Adsorption	$CO + [S] \rightleftharpoons CO[S]$	K_{CO}^{ads}
	$NO + [S] \rightleftharpoons NO[S]$	K_{NO}^{ads}
	$O_2 + 2[S] \rightleftharpoons 2O[S]$	$k_{O_2}^{ads}$, $k_{O_2}^{des}$
Surface Reactions	$NO[S] + [S] \rightleftharpoons N[S] + O[S]$	k_{CO-NO}^{f}, k_{CO-NO}^{b}
	$CO[S] + O[S] \rightleftharpoons CO_2[S] + [S]$	K_{CO-O}^{eq}
	$N[S] + N[S] \rightleftharpoons N_2[S] + [S]$	K_{N-N}^{eq}
	$NO[S] + O[S] \rightleftharpoons NO_2[S] + [S]$	K_{NO-O}^{eq}
Desorption	$CO_2[S] \rightleftharpoons CO_2 + [S]$	$k_{CO_2}^{ads}$, $k_{CO_2}^{des}$
	$NO_2[S] \rightleftharpoons NO_2 + [S]$	$K_{NO_2}^{des}$
	$N_2[S] \rightleftharpoons N_2 + [S]$	$K_{N_2}^{des}$
Inert	$H_2O + [S] \rightleftharpoons H_2O[S]$	$K_{H_2O}^{ads}$

Kinetic Model Form 14

$$r_{CO_2} = \frac{\left(k_{CO_2}^{ads} K_{CO-O}^{eq} K_{CO}^{ads} \sqrt{K_{O_2}^{ads}\, P_{O_2}} P_{CO} - k_{CO_2}^{des} P_{CO_2}\right)}{\left(1 + P_{CO} K_{CO}^{ads} + P_{NO} K_{NO}^{ads} + \sqrt{\frac{P_{N_2}}{K_{N_2}^{des} K_{N-N}^{eq}}} + \right.}$$
$$\left. \sqrt{K_{O_2}^{ads}\, P_{O_2}} + K_{CO-O}^{eq} K_{CO}^{ads} \sqrt{K_{O_2}^{ads}\, P_{O_2}} P_{CO} + \frac{P_{N_2}}{K_{N_2}^{des}} + \frac{P_{NO_2}}{K_{NO_2}^{des}} + K_{H_2O}^{ads}\, P_{H_2O}\right) \quad \text{(C34)}$$

$$r_{N} = \frac{\left(k_{CO-NO}^{f} K_{NO}^{ads} P_{NO} - k_{CO-NO}^{b} \sqrt{\frac{K_{O_2}^{ads}}{K_{N_2}^{des} K_{N-N}^{eq}}}\, \sqrt{P_{N_2} P_{O_2}}\right)}{\left(1 + P_{CO} K_{CO}^{ads} + P_{NO} K_{NO}^{ads} + \sqrt{\frac{P_{N_2}}{K_{N_2}^{des} K_{N-N}^{eq}}} + \right.}$$
$$\left. \sqrt{K_{O_2}^{ads}\, P_{O_2}} + K_{CO-O}^{eq} K_{CO}^{ads} \sqrt{K_{O_2}^{ads}\, P_{O_2}} P_{CO} + \frac{P_{N_2}}{K_{N_2}^{des}} + \frac{P_{NO_2}}{K_{NO_2}^{des}} + K_{H_2O}^{ads}\, P_{H_2O}\right)^2 \quad \text{(C35)}$$

Table C12 Elementary reaction steps for 'Form-14'

Type of Reaction	Elementary Step	Kinetic/Equilibrium Constant
Adsorption	$CO + [S] \rightleftharpoons CO[S]$	K_{CO}^{ads}
	$NO + [S] \rightleftharpoons NO[S]$	K_{NO}^{ads}
	$O_2 + 2[S] \rightleftharpoons 2O[S]$	$K_{O_2}^{ads}$
Surface Reactions	$NO[S] + [S] \rightleftharpoons N[S] + O[S]$	k_{CO-NO}^{f}, k_{CO-NO}^{b}
	$CO[S] + O[S] \rightleftharpoons CO_2[S] + [S]$	K_{CO-O}^{eq}
	$N[S] + N[S] \rightleftharpoons N_2[S] + [S]$	K_{N-N}^{eq}
	$NO[S] + O[S] \rightleftharpoons NO_2[S] + [S]$	k_{NO-O}^{f}, k_{NO-O}^{b}
Desorption	$CO_2[S] \rightleftharpoons CO_2 + [S]$	$k_{CO_2}^{ads}$, $k_{CO_2}^{des}$
	$NO_2[S] \rightleftharpoons NO_2 + [S]$	$K_{NO_2}^{des}$
	$N_2[S] \rightleftharpoons N_2 + [S]$	$K_{N_2}^{des}$
Inert	$H_2O + [S] \rightleftharpoons H_2O[S]$	$K_{H_2O}^{ads}$

$$r_{NO_2} = \frac{\left(k_{NO-O}^{f}\sqrt{K_{O_2}^{ads}}K_{NO}^{ads}P_{NO}\sqrt{P_{O_2}} - \frac{k_{NO-O}^{b}}{K_{NO_2}^{des}}P_{NO_2}\right)}{\left(1 + P_{CO}K_{CO}^{ads} + P_{NO}K_{NO}^{ads} + \sqrt{\frac{P_{N_2}}{K_{N_2}^{des}K_{N-N}^{eq}}} + \right.}$$

$$\left.\sqrt{K_{O_2}^{ads}\ P_{O_2}}\ + K_{CO-O}^{eq}K_{CO}^{ads}\sqrt{K_{O_2}^{ads}\ P_{O_2}}P_{CO} + \frac{P_{N_2}}{K_{N_2}^{des}} + \frac{P_{NO_2}}{K_{NO_2}^{des}} + K_{H_2O}^{ads}\ P_{H_2O}\right)^2 \quad \text{(C36)}$$

Kinetic Model Form 15

$$r_{CO_2} = \frac{\left(k^{ads}_{CO_2} K^{eq}_{CO-O} K^{ads}_{CO} \sqrt{K^{ads}_{O_2} P_{O_2}} P_{CO} - k^{des}_{CO_2} P_{CO_2}\right)}{\left(1 + P_{CO} K^{ads}_{CO} + P_{NO} K^{ads}_{NO} + \sqrt{\frac{P_{N_2}}{K^{des}_{N_2} K^{eq}_{N-N}}} + \sqrt{K^{ads}_{O_2} P_{O_2}} + K^{eq}_{CO-O} K^{ads}_{CO} \sqrt{K^{ads}_{O_2} P_{O_2}} P_{CO} + \frac{P_{N_2}}{K^{des}_{N_2}} + K^{eq}_{NO-O} K^{ads}_{NO} \sqrt{K^{ads}_{O_2} P_{O_2}} P_{NO} + K^{ads}_{H_2O} P_{H_2O}\right)} \quad \text{(C37)}$$

Table C13 Elementary reaction steps for 'Form-15'

Type of Reaction	Elementary Step	Kinetic/Equilibrium Constant
Adsorption	$CO + [S] \rightleftharpoons CO[S]$	K^{ads}_{CO}
	$NO + [S] \rightleftharpoons NO[S]$	K^{ads}_{NO}
	$O_2 + 2[S] \rightleftharpoons 2O[S]$	$K^{ads}_{O_2}$
Surface Reactions	$NO[S] + [S] \rightleftharpoons N[S] + O[S]$	k^{f}_{CO-NO}, k^{b}_{CO-NO}
	$CO[S] + O[S] \rightleftharpoons CO_2[S] + [S]$	K^{eq}_{CO-O}
	$N[S] + N[S] \rightleftharpoons N_2[S] + [S]$	K^{eq}_{N-N}
	$NO[S] + O[S] \rightleftharpoons NO_2[S] + [S]$	K^{eq}_{NO-O}
Desorption	$CO_2[S] \rightleftharpoons CO_2 + [S]$	$k^{ads}_{CO_2}$, $k^{des}_{CO_2}$
	$NO_2[S] \rightleftharpoons NO_2 + [S]$	$k^{ads}_{NO_2}$, $k^{des}_{NO_2}$
	$N_2[S] \rightleftharpoons N_2 + [S]$	$K^{des}_{N_2}$
Inert	$H_2O + [S] \rightleftharpoons H_2O[S]$	$K^{ads}_{H_2O}$

$$r_N = \frac{\left(k^f_{CO-NO} K^{ads}_{NO} P_{NO} - k^b_{CO-NO} \sqrt{\frac{K^{ads}_{O_2}}{K^{des}_{N_2} K^{eq}_{N-N}}} \sqrt{P_{N_2} P_{O_2}}\right)}{\left(1 + P_{CO} K^{ads}_{CO} + P_{NO} K^{ads}_{NO} + \sqrt{\frac{P_{N_2}}{K^{des}_{N_2} K^{eq}_{N-N}}} + \sqrt{K^{ads}_{O_2} P_{O_2}} + K^{eq}_{CO-O} K^{ads}_{CO} \sqrt{K^{ads}_{O_2} P_{O_2}} P_{CO} + \frac{P_{N_2}}{K^{des}_{N_2}} + K^{eq}_{NO-O} K^{ads}_{NO} \sqrt{K^{ads}_{O_2} P_{O_2}} P_{NO} + K^{ads}_{H_2O} P_{H_2O}\right)^2} \quad \text{(C38)}$$

$$r_{NO_2} = \frac{\left(k^{ads}_{NO_2} K^{eq}_{NO-O} K^{ads}_{NO} \sqrt{K^{ads}_{O_2} P_{O_2}} P_{NO} - k^{des}_{NO_2} P_{NO_2}\right)}{\left(1 + P_{CO} K^{ads}_{CO} + P_{NO} K^{ads}_{NO} + \sqrt{\frac{P_{N_2}}{K^{des}_{N_2} K^{eq}_{N-N}}} + \sqrt{K^{ads}_{O_2} P_{O_2}} + K^{eq}_{CO-O} K^{ads}_{CO} \sqrt{K^{ads}_{O_2} P_{O_2}} P_{CO} + \frac{P_{N_2}}{K^{des}_{N_2}} + K^{eq}_{NO-O} K^{ads}_{NO} \sqrt{K^{ads}_{O_2} P_{O_2}} P_{NO} + K^{ads}_{H_2O} P_{H_2O}\right)^2} \quad \text{(C39)}$$

Appendix D : Résumé

Déclaration : Ce résumé concerne spécifiquement ***la Région Hauts-de-France*** *et résume les différents résultats et conclusions de cette thèse.*

L'objectif principal de cette thèse est de développer des matériaux catalytiques pour la réduction du NO par la réaction du CO dans des conditions proches de celles d'une émission de gaz de combustion industries et les gaz de combustion produits par le processus d'*oxycombustion* (le processus de combustion sous oxygène presque pur), en particulier dans les industries du ciment. Le matériau catalytique choisi à cette fin doit être économiquement réalisable compte tenu de son application à l'échelle industrielle, démontrer une bonne performance dans l'activité de réduction du NO et être stable dans les conditions difficiles des gaz de combustion industrielle. Pour cette recherche, différents matériaux à base d'oxyde mixte ont été synthétisés et testés pour déterminer leur activité catalytique et leur stabilité. Le matériau catalytique le plus performant a été synthétisé à grande échelle pour être utilisé dans une installation de réacteur catalytique à échelle semi-pilote. En outre, un modèle cinétique régissant les réactions dans le système a été proposé. Enfin, l'utilisation de pérovskites comme matériaux catalytiques actifs pour la réduction du NO par la réaction du CO dans ces conditions de gaz de combustion industriel semblent être intéressante à approfondir dans les études ultérieures du laboratoire.

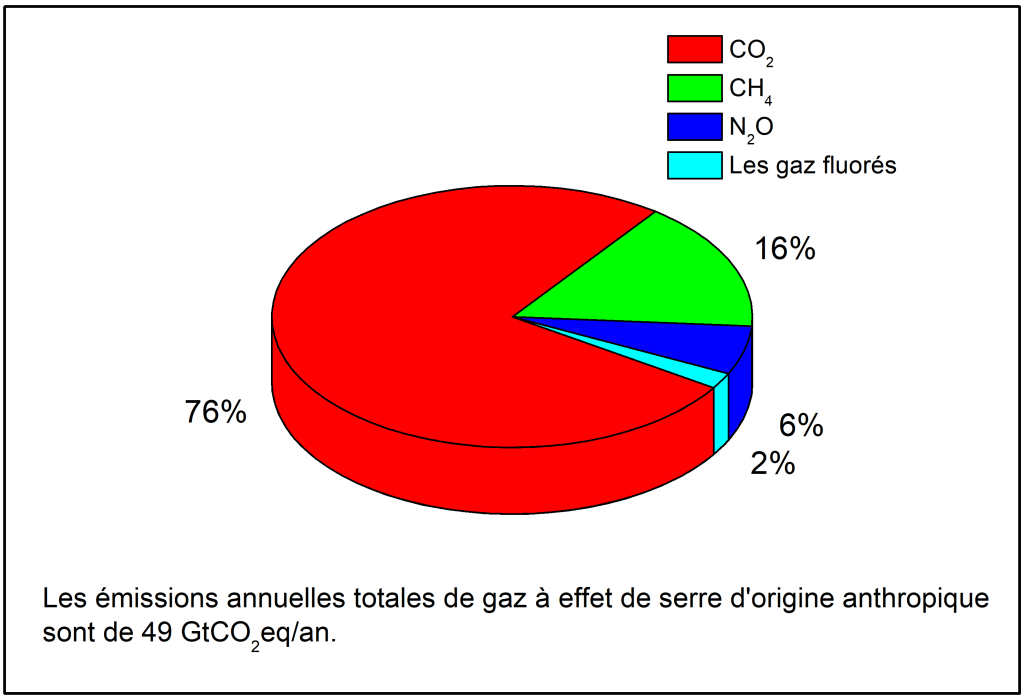

FIGURE D1 Émissions annuelles totales de gaz à effet de serre anthropiques par groupes de gaz en 2010

Contexte de la thèse

Le réchauffement de la planète est devenu l'un des problèmes les plus préoccupants dans le monde entier. La libération incontrôlée de gaz à effet de serre, dont les deux principaux sont le dioxyde de carbone (CO_2) et le méthane (CH_4) (voir Figure D1) [1], par des sources anthropiques, a directement et indirectement affecté l'écosystème vivant de la planète. Par conséquent, il est devenu prioritaire de prendre des mesures drastiques pour atténuer les émissions de gaz à effet de serre (GES) afin de limiter l'augmentation de la température mondiale à 1,5°C par rapport aux niveaux préindustrielle, comme convenu dans l'Accord de Paris lors de la Conférence des Parties (COP21) en novembre 2015 et réaffirmé lors du sommet COP26 qui s'est tenu à Glasgow en 2021.

Le CO_2 est l'un des principaux gaz à effet de serre émis dans le monde. Ses émissions proviennent principalement des secteurs de l'électricité et de l'énergie, de l'industrie et des transports, et représentent 86% du total des

Tableau D1 Composition des gaz de combustion de différentes industries

Composant du gaz	Cimenterie de Brevik	Cimenteries à oxy-combustion
CO_2	20,4 mol%	83,13 mol%
N_2	64,7 mol%	11,11 mol%
O_2	8,56 mol%	3,27 mol%
H_2O	6,2 mol%	1 mol%
Ar	––	1,34 mol%
NO	475 ppm	861 ppm
CO	1330 ppm	397 ppm
SO_2	110 ppm	156 ppm
NO_2	1,77 ppm	96 ppm

émissions mondiales de carbone par an provenant de sources anthropiques. De plus, dans le secteur industriel, les industries du ciment, du fer et de l'acier sont les principaux contributeurs aux émissions mondiales de carbone, représentant 52% du total des émissions mondiales de CO_2 an du secteur industriel. La plupart de ces émissions de carbone peuvent être réduites en adoptant des combustibles à faible teneur en carbone pour répondre aux besoins énergétiques des procédés et en améliorant l'efficacité des procédés en évitant les pertes d'énergie et autres dans les procédés, mais il existe certaines émissions de carbone difficiles à réduire, en particulier dans les industries du ciment où les principales émissions de CO_2 proviennent du procédé de base [2]. Dans ce cas, une unité de captage, d'utilisation et de stockage du carbone (CCUS) peut être mise en place pour capter le CO_2 des gaz de combustion. Cependant, les gaz de combustion industrielle contiennent également des NO_x et des SO_x qui sont non seulement dangereux pour la santé humaine, mais qui déclenchent également en aval la corrosion et la dégradation des solvants aminés qui sont généralement utilisés pour la capture du carbone. Il est donc important d'éliminer ces éléments toxiques des gaz de combustion avant de les introduire dans l'unité CCUS. Cette étape est appelée purification du CO_2. Il existe principalement deux technologies pour éliminer ces éléments toxiques : (1) la compression acide [3,4] et (2) la réduction catalytique des NO_x en utilisant différents réducteurs comme le NH_3 [5] et le CO [6]. Dans cette thèse, l'accent est mis sur la réduction catalytique du NO (prédominant dans le mélange de

NO_x dans les gaz de combustion industrielle ,voir Tableau D1 [3,7]) en utilisant comme réducteur le CO, coexistant dans les gaz de combustion industrielle.

Études bibliographiques

La principale réaction étudiée dans cette thèse est la réduction du NO par le CO pour former du N_2 non toxique et du CO_2. La réaction principale entre le NO et le CO est représentée par l'équation D1. Afin de développer des matériaux catalytiques actifs pour la réaction de réduction du NO par le CO, une étude bibliographique approfondie a été réalisée, et les métaux actifs potentiels ont été recherchés pour la synthèse et les tests d'activité catalytique. Les rapports de la littérature indiquent que le type de métal actif (tels que Cu, Co, Mn et Fe) et sa teneur [8–13], les supports [8,14–17] et la méthode de préparation [18–20] affectent grandement la performance catalytique. Outre la composition des matériaux, la composition du gaz réactif [19,21–24] (voir Figure D2) et les conditions de prétraitement [9,11,25–33] affectent également les performances catalytiques. Comme le gaz de combustion industriel est un mélange gazeux oxydant et humide, la présence d'un excès de O_2 réagit avec le CO et le NO pour former respectivement du CO_2 (voir l'équation D2) et du NO_2 (voir l'équation D3), ce qui entrave la réaction entre le NO et le CO et diminue la sélectivité de la réduction du NO en N_2. La présence d'eau entre en compétition avec les composants du réactif sur les sites actifs du catalyseur et inhibe la réaction ou facilite la réaction de déplacement de gaz vers l'eau qui produit du H_2, un réducteur plus puissant que le CO pour le NO, ce qui améliore la sélectivité de la réduction du NO [22].

$$\mathrm{CO} + \mathrm{NO} \rightarrow \mathrm{CO_2} + \frac{1}{2}\mathrm{N_2} \tag{D1}$$

$$\mathrm{CO} + \frac{1}{2}\mathrm{O_2} \rightarrow \mathrm{CO_2} \tag{D2}$$

$$\mathrm{NO} + \frac{1}{2}\mathrm{O_2} \rightarrow \mathrm{NO_2} \tag{D3}$$

De plus, une étude bibliographique approfondie des modèles cinétiques pour le système réactionnel considéré dans cette thèse a été réalisée. Plusieurs auteurs ont rapporté un modèle de Langmuir-Hinshelwood-Hougen-Watson

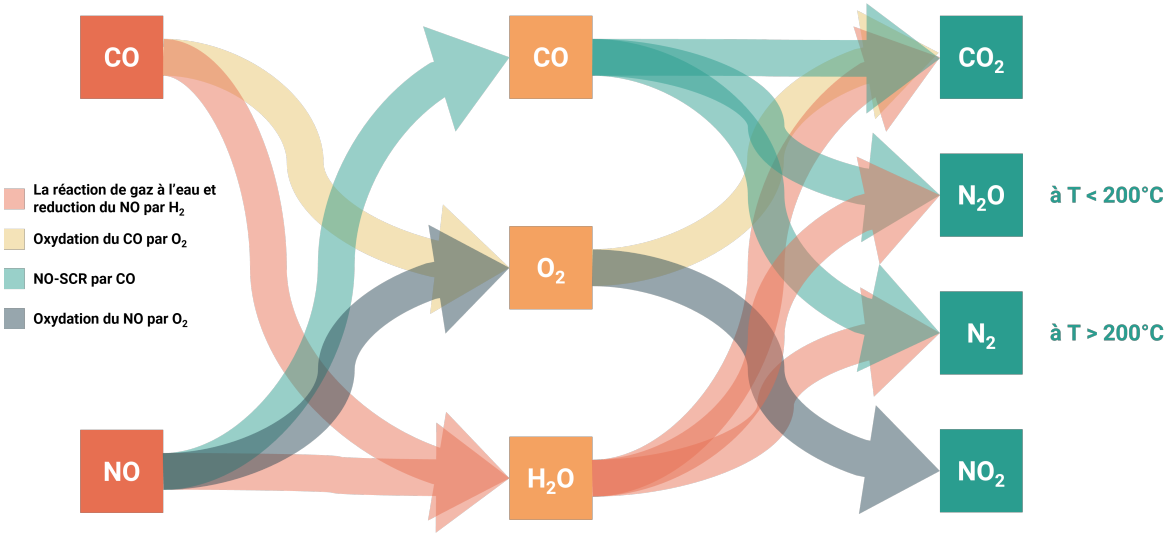

FIGURE D2 Réactions secondaires possibles en fonction de la composition du gaz réactif

(LHHW) et un modèle d'Eley Rideal (ER) pour la réaction de réduction de NO par CO [17,23,34–38]. La dissociation du NO en espèces atomiques N et O sur la surface catalytique a été généralement considérée comme l'étape limitant le taux de réaction et les expressions du taux de réaction basées sur cette hypothèse ont été dérivées et rapportées dans la littérature. Cependant, les études cinétiques de la réduction du NO par la réaction du CO sur des matériaux catalytiques à base d'oxyde de métal de transition dans des conditions de gaz de combustion industrielle ont été rarement rapportées dans la littérature. En outre, compte tenu de la complexité du système réactionnel qui conduit à des expressions de taux de réaction compliquées, les rapports de la littérature sur les différentes routines d'optimisation globale utilisées pour déterminer les paramètres inconnus du modèle ont également été largement étudiés [39–43]. Ainsi, dans cette thèse, le modèle cinétique de la réaction a été développé sur la base des étapes élémentaires de la cinétique LHHW rapportées dans la littérature et la boîte à outils d'optimisation globale fournie par MATLAB 2020a a été utilisée pour régresser les paramètres du modèle.

Catalyseurs à base d'oxydes mixtes de cuivre et de cobalt

Le cuivre a été utilisé comme matériau de départ pour la réaction de réduction du NO par le CO car il a été largement étudié dans la littérature pour cette réaction. Dans cette thèse, des matériaux à base d'oxydes mixtes ont été utilisés comme catalyseurs. Ainsi, l'oxyde mixte Cu-Al a été synthétisé par traitement thermique de son précurseur, l'hydroxyde Double lamellaire (HDL), obtenu par coprécipitation d'un mélange de sels de nitrates métalliques correspondants et de carbonate de sodium à un pH de 10,5. Afin d'étudier l'effet du type de gaz de prétraitement sur l'activité catalytique de l'échantillon d'oxyde mixte résultant, le parent CuAl-LDH a été traité sous le flux de He, air, 1 vol% CO/He et CO_2 et les échantillons d'oxyde mixte résultants ont été caractérisés et testés pour leurs performances catalytiques.

Différentes techniques de caractérisation des matériaux, comme la physisorption de N_2, la Diffraction des Rayons X (DRX), la Réduction en Température Programmée de H_2 (RTP), l'Analyse ThermoGravimétrique (ATG) et l'Infrarouge à Transformée de Fourier (IFTR), ont été utilisées pour étudier les propriétés des matériaux de ces échantillons de CuAl-X (X = He, air, 1 vol% CO/He et CO_2). La caractérisation des matériaux a révélé que les natures du gaz de prétraitement n'avaient aucun effet sur la surface spécifique, la taille cristalline moyenne de CuO et la réductibilité, à l'exception de l'échantillon CuAl-CO/He qui présente la surface spécifique la plus faible, la taille cristalline la plus grande pour le Cu métallique et la réductibilité la plus faible par rapport aux autres échantillons de CuAl-X. En outre, les analyses ATG et IFTR ont révélé que l'échantillon CuAl-CO_2 était composé d'espèces carbonates bidentates et/ou polydentates supplémentaires formées en raison de l'interaction du matériau avec le CO_2 pendant le processus de prétraitement. Il a été conclu que la présence de carbonates était responsable de l'activité de réduction du NO sur le CuAl-CO_2 dans des conditions de réaction sèches et humides (voir Tableau D2) pour la composition du gaz réactif puisque seul le CuAl-CO_2 a montré une activité de réduction du NO dans des conditions de réaction sèches (voir Figure 1.3). De plus, tous les échantillons de CuAl-X ont montré une activité de réduction du NO dans des conditions de réaction en milieu humide (voir la

Tableau D2 Composition du gaz réactif utilisé pour les tests d'activité catalytique

Composant du gaz	Composition
CO	0,13 vol%
CO_2	20,4 vol%
NO_2	475 ppm
O_2	8,6 vol%
H_2O	0 (réaction sèches) ou 8,2 vol% (réaction humide)
N_2 or He	gaz vecteur

Figure 1.3), ce qui indique une réaction semblable à un déplacement de gaz à l'eau qui facilite la dissociation du NO en produisant de l'hydrogène et conduit donc à sa réduction en N_2 [44–46].

Bien que le traitement au CO_2 du HDL CuAl ait conduit à une amélioration de l'activité de réduction du NO de l'oxyde mixte résultant, une amélioration supplémentaire de la performance catalytique peut être réalisée en introduisant un second métal actif. Pour cela, le Co a été choisi. De plus, l'effet de la teneur en Co dans les échantillons d'oxyde mixte prétraités au CO_2 sur la performance catalytique a été étudié. Les résultats catalytiques (voir Tableau D3 et Figure D4) montrent que l'augmentation de la teneur en Co améliore l'activité de conversion du NO et du CO. La conversion du CO (voir Tableau D3) a été déplacée vers des températures de réaction plus basses que dans le cas de CuAl-CO_2, tandis que le rendement de conversion du NO et la sélectivité vers la réduction du NO ont été améliorés avec des températures de pic de réduction du NO situées à des températures de réaction plus basses que dans le cas de l'échantillon CuAl-CO_2 (voir Figure D4). Cette amélioration de l'activité catalytique peut être liée à l'amélioration du comportement redox par l'introduction de Co dans l'échantillon d'oxyde mixte, comme observé à partir de l'analyse H_2-RTP des échantillons.

Cependant, la différence dans l'activité catalytique était négligeable entre les échantillons avec un rapport molaire Cu :Co de 0,5 et 0. De plus, le Co est un métal plus coûteux que le Cu et par conséquent, la diminution de sa teneur dans l'oxyde mixte réduira le coût global du catalyseur et la présence de Cu avec le Co forme des structures spinelles qui stabilisent les espèces de Co et

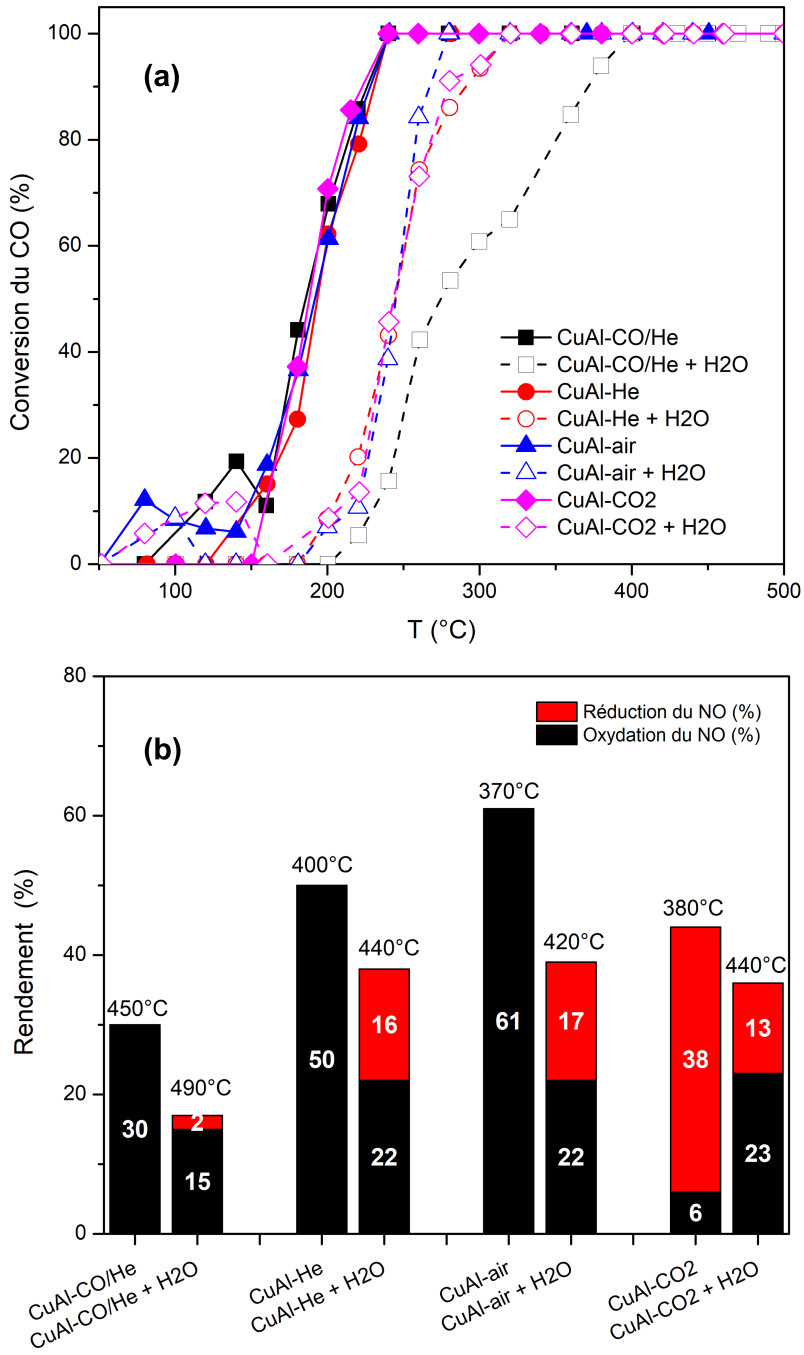

FIGURE D3 (a) Conversion du CO en fonction de la température de réaction, pour les matériaux CuAl-X, en présence et en l'absence d'eau (b) Rendement d'oxydation et de réduction du NO à la température correspondant au pic de réduction du NO (ou d'oxydation lorsqu'aucune activité de réduction du NO n'est observée) pour les matériaux CuAl-X

TABLEAU D3 Températures T_{50} et T_{90} de conversion du CO pour différents échantillons de CoCuAl traités sous CO_2

Echantillon	T_{50} (°C)	T_{90} (°C)
CuAl	240	270
Co_2Cu_4Al	220	260
Co_4Cu_2Al	200	240
CoAl	200	240

évitent le frittage des particules pendant la réaction. Par conséquent, l'oxyde mixte Co_4Cu_2Al a été considéré pour des recherches plus approfondies.

En outre, afin d'optimiser davantage la performance catalytique, l'effet de la température de prétraitement sur la performance catalytique de l'échantillon d'oxyde mixte Co_4Cu_2Al-CO_2 a été étudié. Pour cette étude, la forme HDL du Co_4Cu_2Al a été traitée sous le flux de CO_2 à différentes températures de traitement : 350°C, 400°C, 450°C et 500°C. Les tests de caractérisation du matériau sur les échantillons d'oxydes mixtes CoCu-T correspondants (CoCu = Co_4Cu_2Al traité sous CO_2 et T = température de traitement correspondante)

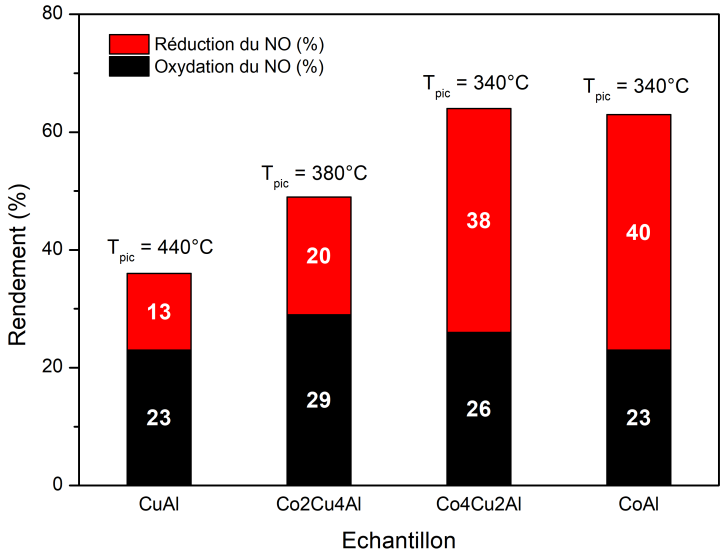

FIGURE D4 Rendement d'oxydation et de réduction de NO pour différents échantillons de Co-Cu traités au CO_2 dans des conditions de réaction humide (T_{pic} = température de réaction au pic du rendement d'oxydation/réduction de NO)

TABLEAU D4 Rendement de conversion du NO et sélectivité de N_2 pour les échantillons de CoCu-T dans des conditions de réaction humide

Echantillon	T_{pic} (°C)	**Conversion du NO (%)**	**Sélectivité du N_2 (%)**
CoCu-350	280	87	52
CoCu-400	260	58	84
CoCu-450	240	23	77
CoCu-500	240	17	79

ont révélé que l'augmentation de la température de traitement augmentait la cristallinité de l'échantillon mais n'avait aucun effet sur la surface spécifique et le volume des pores correspondants. De plus, en comparant les activités catalytiques de ces échantillons de CoCu-T dans des conditions de réaction humide (voir Figure D5), il a été observé que la température de traitement n'a aucun effet sur l'activité de conversion du CO (voir Figure D5(a)) mais affecte grandement le rendement de conversion du NO et la sélectivité vers la réduction du NO (voir Figure D5(b) et Tableau D4). Ce comportement peut être dû à plusieurs raisons comme :

- le frittage des métaux actifs dans les oxydes mixtes avec l'augmentation de la température de traitement (indiqué par l'augmentation de la cristallinité des échantillons de CoCu-T avec la température de traitement comme observé sous DRX) qui pourrait expliquer la diminution du rendement de conversion de NO et définitivement l'activité de réduction de NO [25,30,31,33].
- certaines espèces de carbonate trouvées aux températures de traitement inférieures peuvent réagir avec le NO pour former des espèces de nitrate pontées et/ou monodentées. Ces nitrates peuvent ensuite réagir avec le NO pour former du NO_2. Cette réaction ne se produit qu'en présence d'espèces actives facilement réductible dans le matériau catalytique [47].

Puisqu'il n'y a pas de corrélation directe entre la sélectivité vers N_2 et la température de traitement, on peut s'attendre à ce que les deux phénomènes se produisent. Cela signifie que l'échantillon de CoCu-400 possède la concentration optimale d'espèces de carbonate et de cristallinité pour la sélectivité maximale de N_2.

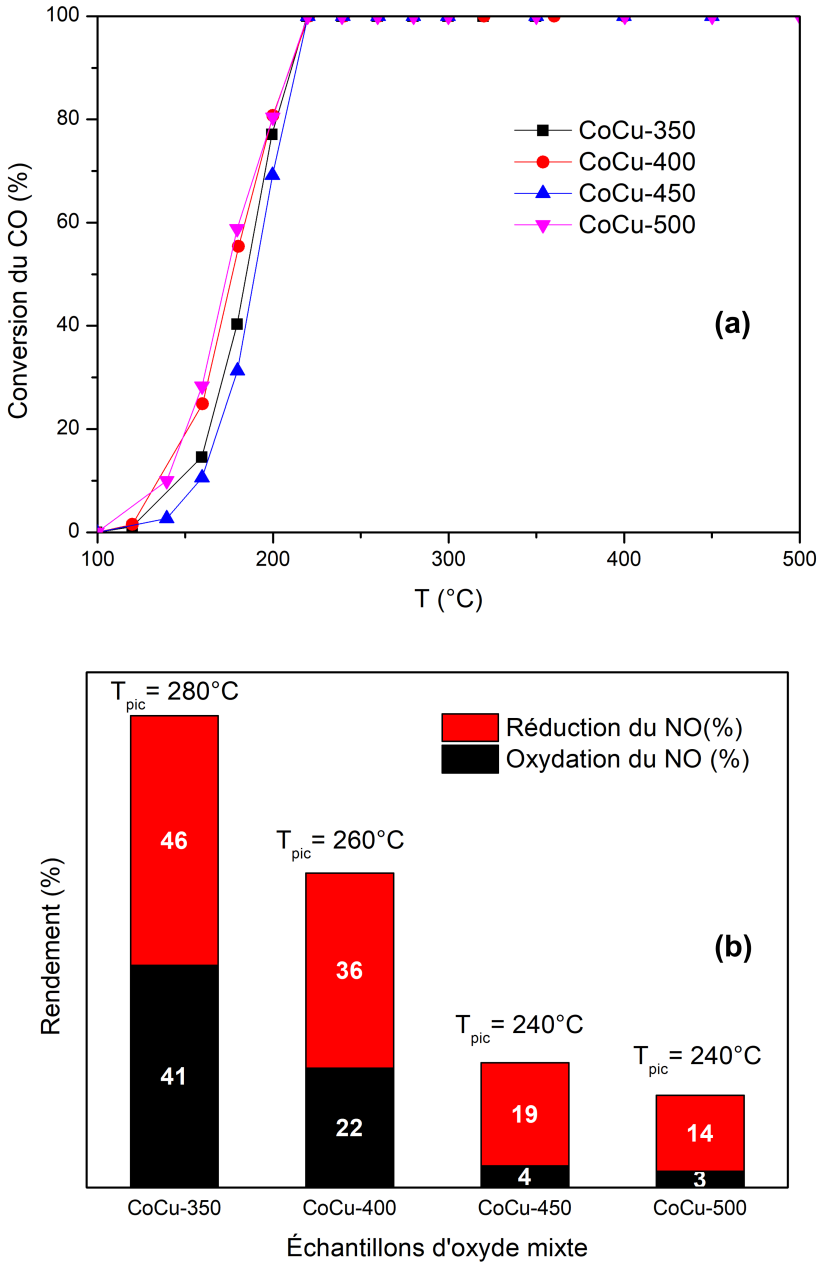

FIGURE D5 Activité catalytique des échantillons de CoCu-T dans des conditions de réaction humide (a) activité de conversion du CO et (b) rendement d'oxydation/réduction du NO

Enfin, la stabilité thermique de cet échantillon de CoCu-400 a été évaluée par le biais d'un vieillissement thermique rapide via 6 light-offs dans les conditions de réaction humide. Le changement de l'activité catalytique observé à partir de la courbe d'extinction correspondante pendant chaque essai a été enregistré. Les résultats sont présentés à la Figure D6. En comparant les

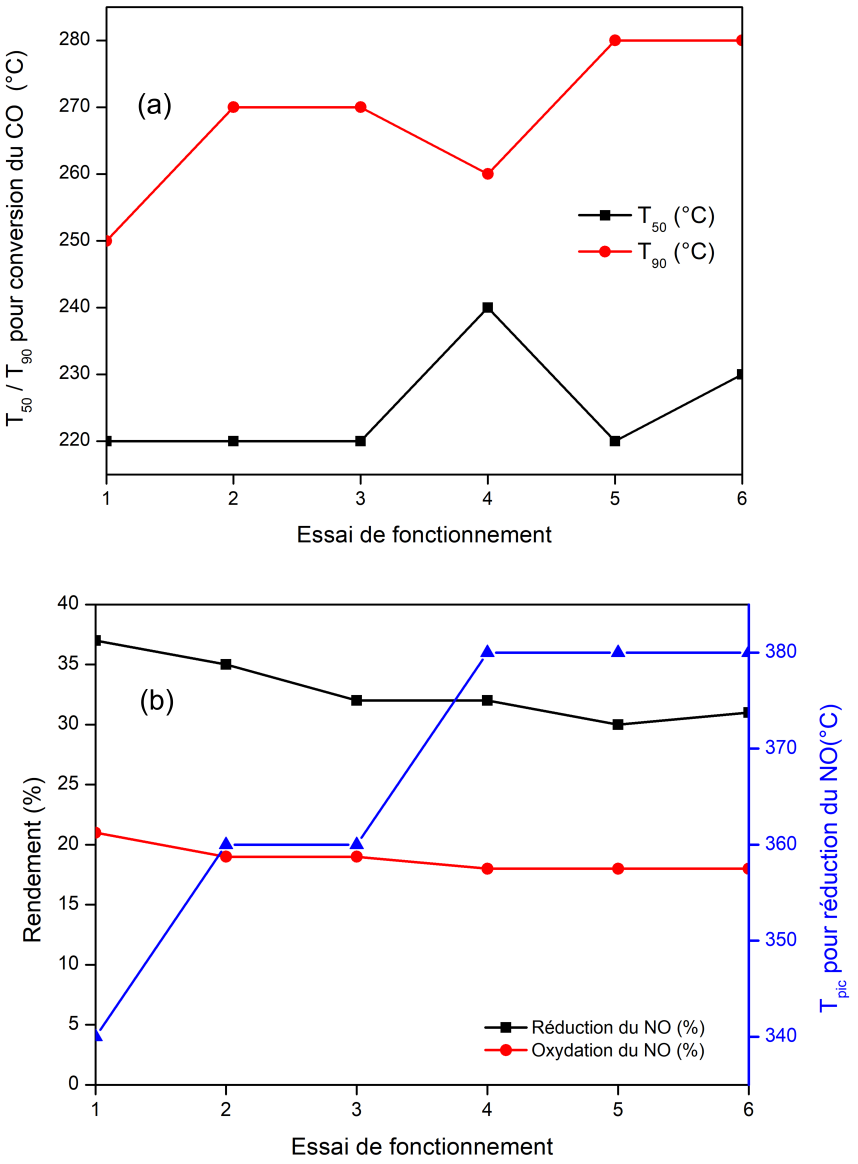

FIGURE D6 Variation des températures (a) T_{50} et T_{90} pour la conversion du CO et (b) du rendement de conversion du NO en fonction des essais d'activité catalytique

températures T_{50} et T_{90} de la conversion du CO pendant chaque essai (voir Figure D6(a)), on peut observer que les températures T_{90} augmentent avec le nombre d'essais, tandis que la température T_{50} de la conversion du CO ne change pas beaucoup. En outre, en comparant le rendement de réduction du NO pendant les essais (voir Figure D6(b)), on peut conclure que le rendement de réduction du NO a diminué entre le premier essai (rendement = 38%) et le troisième essai (rendement = 32%) puis est resté presque stable jusqu'au

sixième essai (30% < rendement < 32%). Il est intéressant de noter que le rendement de l'oxydation du NO n'a pas beaucoup changé au cours des essais (18% < rendement < 21%). De plus, en comparant les températures T_{pic} pour le pic de rendement de réduction de NO correspondant (se référer à la Figure D6(b)), on peut conclure que le T_{pic} augmenté de 340°C dans le 1er essai à 380°C dans le 4ème essai et est resté stable jusqu'au 6ème essai. Ces résultats suggèrent que le matériau CoCu-400 possède une bonne stabilité thermique.

Comparaison de l'activité catalytique avec les catalyseurs commerciaux

L'activité catalytique de l'échantillon de CoCu-400 synthétisé au laboratoire a été comparée aux matériaux catalytiques à base de métaux du groupe du platine disponibles dans le commerce, à savoir 1 wt% Pt/CeO_2 et 1 wt% Pt/Al_2O_3. Il a été démontré précédemment que les matériaux catalytiques à base de métaux du groupe du platine étaient actifs pour la réduction du NO par réaction avec le CO dans des conditions de gaz de combustion industrielle [48,49]. En comparant les activités catalytiques des catalyseurs commerciaux et synthétisés en laboratoire dans des conditions de réaction humide et en utilisant N_2 au lieu de He comme gaz vecteur (voir Figure D7), on a observé que les catalyseurs commerciaux présentaient une bien meilleure activité de conversion du CO que l'échantillon de CoCu-400 (voir Figure D7(a)). Cependant, en ce qui concerne l'activité de conversion du NO (voir la Figure D7(b)), l'échantillon de CoCu-400 a montré un rendement de réduction du NO plus élevé que les échantillons de catalyseurs commerciaux contenant du Pt. Même si les platinoïdes sont connus pour posséder une activité catalytique élevée pour la réduction des NO_x, leur activité est principalement diminuée en présence d'une quantité excessive d'O_2 et de H_2O en raison du blocage des sites actifs par l'O_2 [50], de la consommation des molécules réactives par l'excès d'O_2 pour former du NO_2 et du CO_2 [51] et du frittage des particules métalliques actives dans des conditions humides, réduisant ainsi l'accessibilité métallique et diminuant l'activité de réduction des NO [48]. Par conséquent, il est conclu que l'échantillon de CoCu-400 synthétisé en laboratoire surpasse les échantillons commerciaux contenant du Pt (1 wt% Pt/Al_2O_3) et les échantillons synthétisés en laboratoire (1 wt% Pt/CeO_2) dans l'activité de réduction de NO dans une condition de réaction

oxydante et humide.

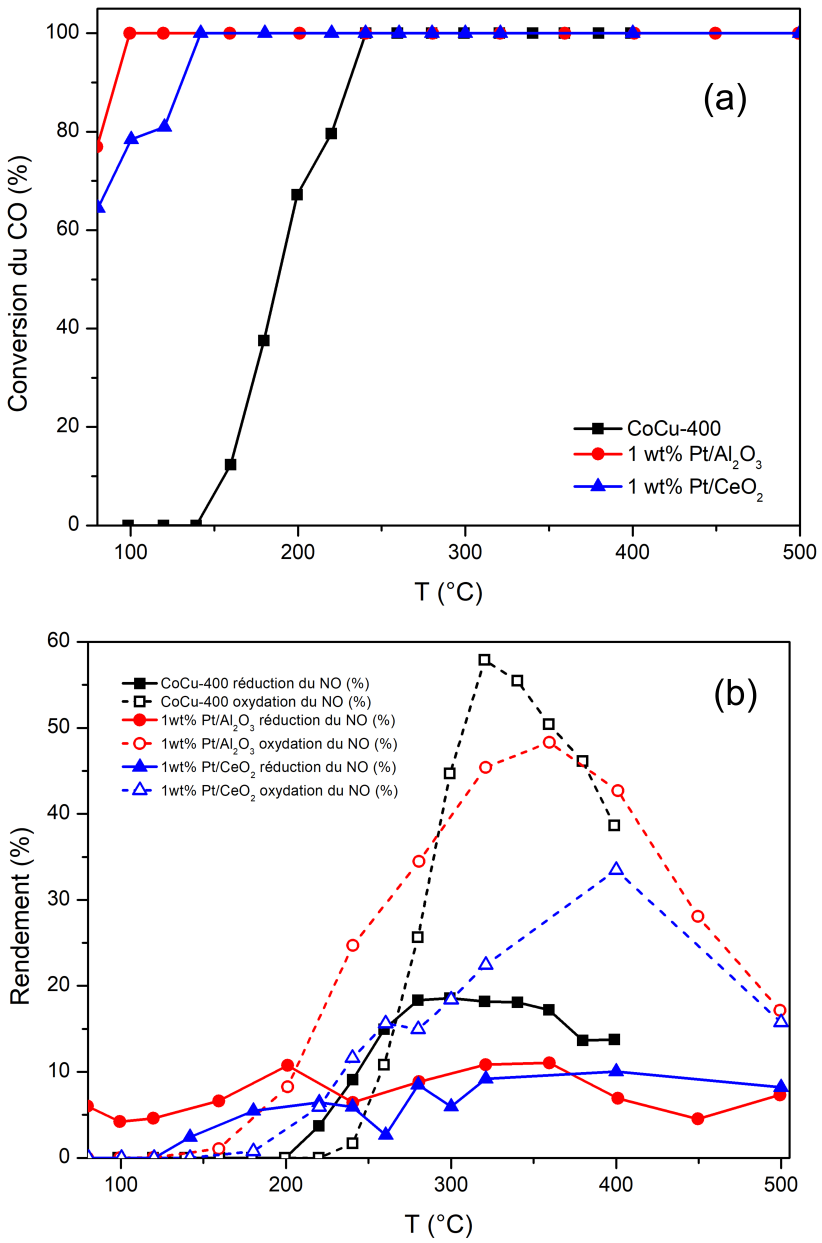

FIGURE D7 Comparaison (a) de la conversion du CO et (b) du rendement d'oxydation/réduction du NO sur CoCu-400 avec 1 wt% Pt/Al_2O_3 et 1 wt% Pt/CeO_2 dans des conditions de réaction humide en utilisant N_2 comme gaz vecteur

Synthèse à grande échelle

Sur la base de l'activité catalytique supérieure et de la stabilité dans les conditions de réaction de l'oxyde mixte correspondant, la forme HDL de Co_4Cu_2Al a été synthétisée à grande échelle afin d'être utilisée pour une installation de test semi-pilot développée à l'Université de Mons (Belgique). Le précurseur HDL parent a été synthétisé dans un réacteur batch de 10 L au laboratoire de l'Unité de Catalyse et Chimie du Solide (UCCS) de l'Université de Lille selon la méthode de coprécipitation. La représentation schématique de l'appareil de synthèse à grande échelle est présentée à la Figure D8. De plus, des analyses DRX ont été réalisées sur les deux lots afin d'assurer la cohérence des propriétés structurelles du HDL. Ensuite, le lot de HDL préparé a été broyé et extrudé en faisant une pâte de HDL (60% d'eau et le reste de HDL) et en la poussant à travers une buse de 3 mm de diamètre (voir Figure D9). Les extrudés ainsi préparés ont ensuite été séchés dans un four pendant plusieurs jours à une température de 35-40°C afin de développer une résistance mécanique adéquate. Ces extrudés seront ensuite traités sous flux de CO_2 dans un réacteur à l'échelle semi-pilote pour obtenir la forme d'oxyde métallique mixte avant de réaliser le

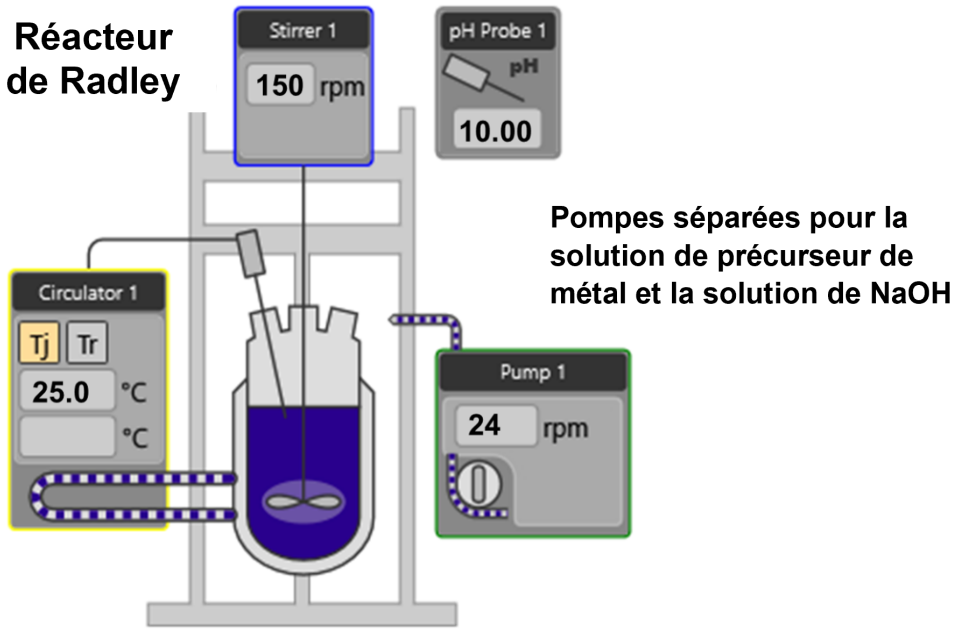

FIGURE D8 Représentation schématique de l'installation de synthèse à grande échelle

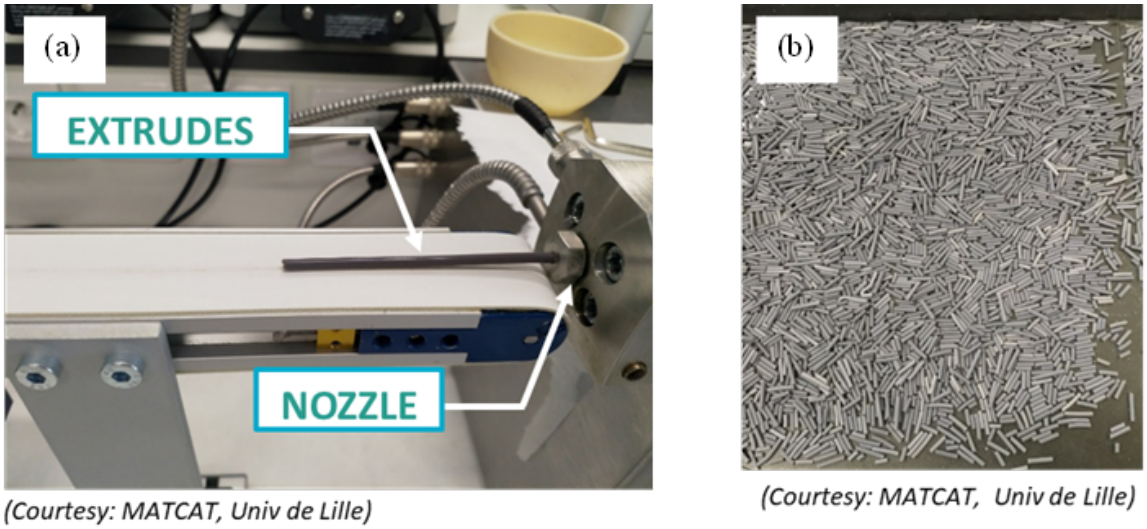

FIGURE D9 Mise en forme d'un échantillon de Co_4Cu_2Al-LDH synthétisé à grande échelle

test catalytique.

Influence de la composition du gaz d'alimentation et modélisation cinétique

Afin de prédire le comportement du catalyseur dans des conditions réelles de gaz de combustion, un modèle mathématique régissant la cinétique de réaction du système devait être développé, ce qui nécessitait un ensemble de données expérimentales. Par conséquent, l'activité catalytique de l'échantillon de Co_4Cu_2Al-400-CO_2 sous différents mélanges de gaz réactifs a été étudiée. Un modèle cinétique a été développé sur la base de ces données expérimentales et les paramètres du modèle ont été régressés en utilisant un algorithme d'optimisation globale adéquat.

Influence de la composition du gaz d'alimentation

L'effet de la composition du gaz d'alimentation sur la performance catalytique de l'échantillon de Co_4Cu_2Al-400-CO_2 a été évalué en modifiant chacun des composants du gaz et en enregistrant la courbe d'extinction correspondante. L'effet de la composition des différents composants du gaz sur la performance catalytique est présenté dans le Tableau D5. En outre, en plus de la composition du gaz réactif, l'effet de la quantité de catalyseur (en maintenant un débit

volumétrique constant à l'entrée du réacteur et le volume du lit du réacteur en utilisant du SiC) dans le réacteur sur la performance catalytique a été évalué et l'influence est également indiquée dans le Tableau D5.

Tableau D5 Effet de la composition du gaz d'alimentation et du poids du catalyseur sur la performance catalytique.

Composant du gaz	**Plage de variation**	**Effet**
CO	0,13 et 0,5 vol%	Augmentation de la teneur en CO : • a retardé la conversion du CO • retardement de l'oxydation du NO mais diminution de son rendement • a retardé la réduction du NO sans effet sur le rendement maximal
NO	300 et 475 ppm	Aucun effet considérable n'a été observé
CO_2	20,4 et 60 vol%	Augmentation de la teneur en CO_2 : • a légèrement retardé la conversion du CO et la réduction du NO (sans effet sur le rendement maximal) • forte diminution du rendement de l'oxydation du NO

H_2O	0, 4,2 et 8,2 vol%	Augmentation de la teneur en H_2O : • retarde la conversion du CO et du NO • diminution du rendement de la réduction et de l'oxydation du NO
O_2	4 vol% et 8,6 vol%	Augmentation de la teneur en O_2 : • Aucun changement dans l'activité de réduction du CO et du NO • Le rendement de l'oxydation du NO diminue de 20% à 15%
Poids du catalyseur	150, 381 et 782 mg	Augmentation du poids du catalyseur : • déplacement de la conversion du CO et du rendement de réduction du NO vers des températures de réaction plus basses • augmentation du rendement de la réduction du NO • aucun effet sur le rendement de l'oxydation du NO.

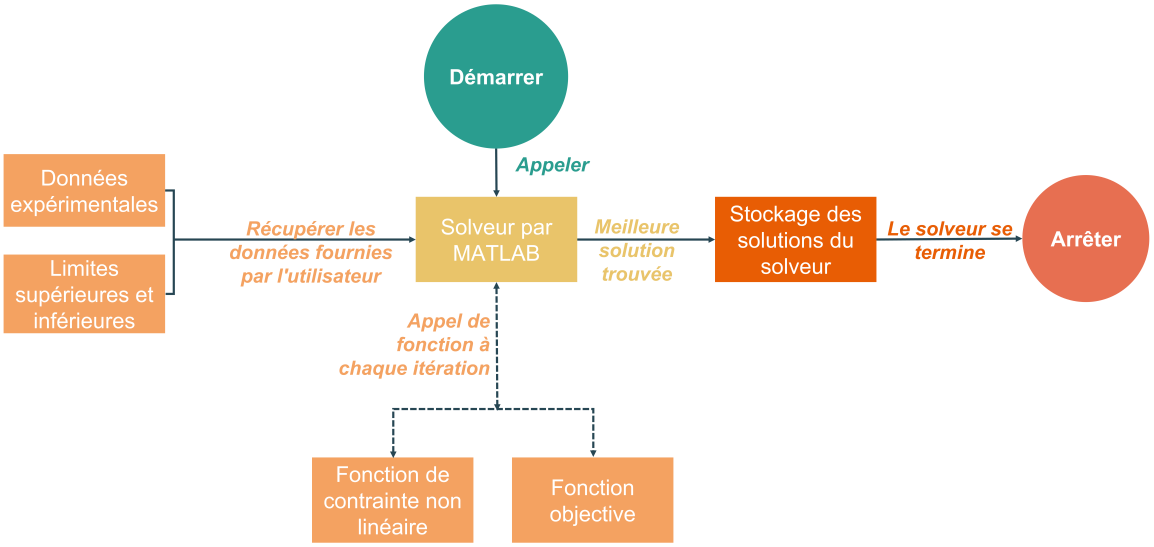

FIGURE D10 Diagramme de flux de travail pour la routine de régression des paramètres à l'aide de MATLAB 2020a

Modèle cinétique

Dans cette thèse, la cinétique Langmuir-Hinshelwood-Hougen-Watson a été choisie pour le développement du modèle cinétique sur la base des différents rapports de la littérature pour des systèmes de réaction similaires. Certaines hypothèses telles que : (1) un seul type de sites actifs est présent dans le catalyseur (2) le CO_2 et le H_2O ne participent pas à la réaction mais entrent en compétition avec les molécules réactives pour les sites actifs communs et (3) il n'y a pas de formation de N_2O et donc, le NO se réduit uniquement en N_2. En outre, différentes expressions de la vitesse de réaction ont été dérivées sur la base des différents ensembles d'étapes limitant la vitesse supposée dans le modèle. La forme générique de l'expression de la vitesse de réaction est présentée dans l'équation D4. Dans cette équation, n = nombre d'espèces dans l'étape de limitation de la vitesse.

$$\text{vitesse de reaction} = \frac{\text{facteur cintique} \times \text{force motrice}}{(\text{terme d'adsorption})^n} \tag{D4}$$

Chacun de ces ensembles de taux de réaction était composé de 14 constantes d'équilibre cinétique/adsorption ou désorption/réaction. Pour relier ces constantes à la température de réaction, on a considéré la relation d'Arrhenius, ce qui a donné lieu à 28 paramètres de modèles inconnus (14 coefficients

de fréquence + 14 énergies d'activation). Pour déterminer ces paramètres du modèle, l'algorithme GPS (*General Pattern Search*) a été utilisé pour un système d'équations différentielles ordinaires développées par bilan matière en considérant un modèle de réacteur '*packed-bed*' isotherme et unidimensionnel. Cet algorithme GPS est disponible dans le logiciel MATLAB 2020a. L'organigramme du fichier script MATLAB développé pour exécuter cette routine de régression est présenté à la Figure D10. Le solveur minimise une fonction objective (F_{obj}) qui est la somme du carré de la différence entre les conversions molaires expérimentales $({x_{i,j}}^{exp})$ et calculées $({x_{i,j}}^{cal})$ pour le NO et le CO (voir l'équation (D5)).

$$\mathrm{F_{obj}} = \sum_{i=1}^{2} \sum_{j=1}^{N_{exp}} \left({x_{i,j}}^{exp} - {x_{i,j}}^{cal} \right)^2 \tag{D5}$$

Évaluation de l'adéquation des modèles

Différentes expressions de la vitesse de réaction ont été développées en considérant différents ensembles d'étapes limitant la vitesse. De plus, la méthode intégrale a été suivie et un système d'équations différentielles a été développé pour calculer la concentration des composants gazeux à la sortie du réacteur. La différence entre les valeurs de conversion molaire calculées et expérimentales (voir Eq. (D5)) a été minimisée à l'aide du solveur patternsearch du logiciel MATLAB 2020a. Le coefficient de détermination (R^2) entre les valeurs expérimentales et calculées pour chacune des formes du modèle cinétique est présenté dans le Tableau D6.

Le tableau (voir Tableau D6) montre que la forme 1 (les étapes limitant la vitesse : Adsorption du CO et du NO et dissociation du NO en espèces N et O adsorbées) et la forme 8 (les étapes limitant la vitesse : adsorption du NO, réaction de surface entre les espèces de CO et de O adsorbées pour former des espèces de CO_2 adsorbées et dissociation du NO en espèces de N et de O adsorbées) s'adaptent très bien à toutes les formes de modèles cinétiques. De plus, la Forme-1 a montré une meilleure adaptation aux données expérimentales pour la conversion du CO que la Forme-8 et donc, la Forme-1 a été le modèle cinétique choisi. Cela signifie que l'adsorption de CO et de NO ainsi que la décomposition de NO en surface en espèces atomiques N et O sont les étapes limitant la vitesse dans le système de réaction. La corrélation entre les valeurs

Tableau D6 Coefficient de détermination (R^2) pour différentes formes de modèles cinétiques

Forme du modèle cinétique	Correlation de Détermination (R^2)			
	Conversion du NO (X_{NO})	Conversion du CO (X_{CO})	Pressions Partielles	
			P_{N_2}	P_{NO_2}
Forme-1	0,90	0,92	0,85	0,79
Forme-3	0,89	0,91	0,20	0,79
Forme-4	0,87	0,91	0,83	0,19
Forme-8	0,85	0,89	0,75	0,83
Forme-9	0,90	0,84	0,82	0,42
Forme-10	0,90	0,93	0,07	0,82
Forme-11	0,86	0,89	0,07	0,79
Forme-12	0,90	0,93	0,46	0,85
Forme-14	0,59	0,44	0,54	0,49

expérimentales et calculées pour la conversion molaire de CO et de NO et les pressions partielles de N_2 et de NO_2 est présentée dans la Figure D11. Pour une meilleure adaptation aux données expérimentales, certaines modifications du modèle cinétique, comme l'utilisation d'un mécanisme à double site, doivent être développées.

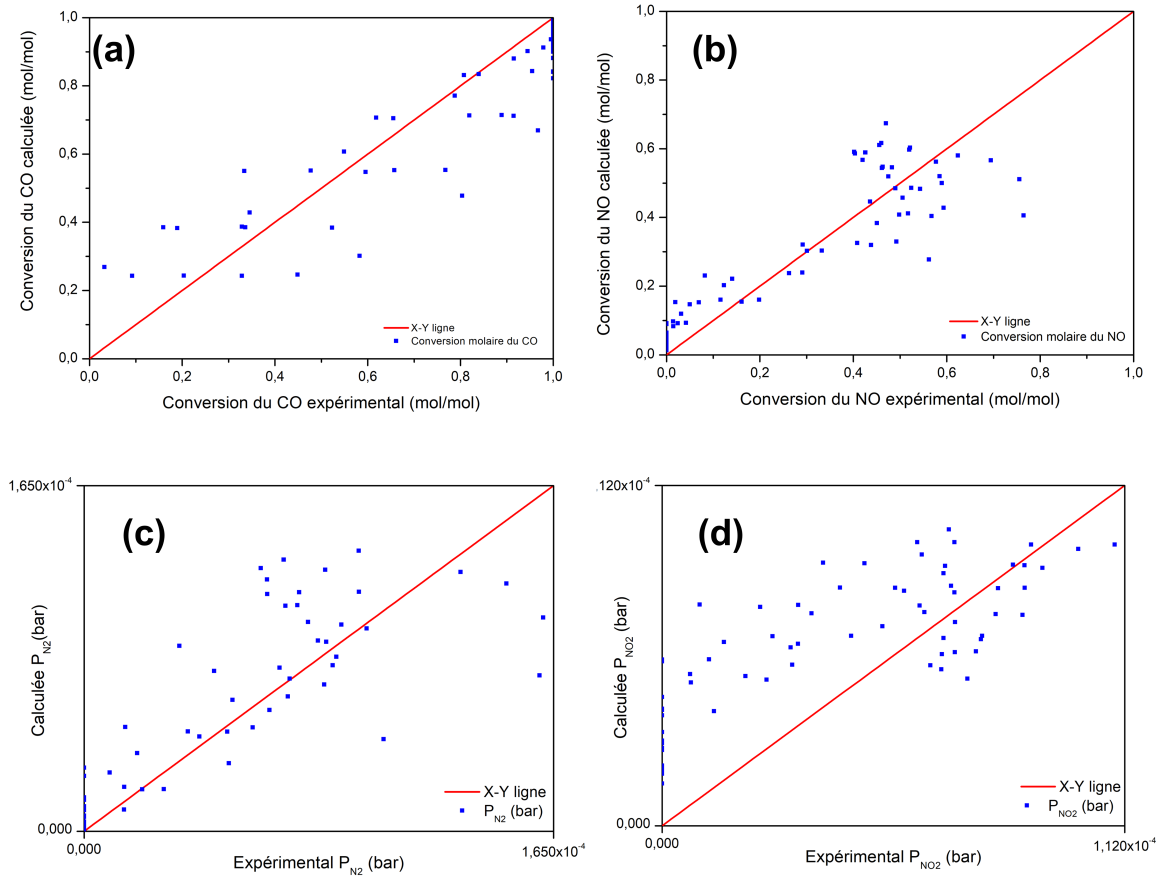

FIGURE D11 Corrélation entre les valeurs expérimentales et calculées pour (a) la conversion du CO (b) la conversion totale du NO (c) la pression partielle de N_2 et (d) la pression partielle de NO_2 selon le modèle cinétique Forme-1

Les pérovskites : un matériau catalytique

Afin d'explorer d'autres oxydes mixtes actifs pour la réduction du NO par réaction avec le CO dans les conditions des gaz de combustion industrielle, la structure atomique des matériaux pérovskites (voir la Figure D12 pour la structure cristalline des pérovskites) a été explorée. Pour ce faire, une étude documentaire approfondie a été menée afin de trouver différents métaux actifs et compositions de matériaux présentant une activité catalytique prometteuse. Cette étude a montré que la méthodologie de préparation, la substitution partielle aux sites A et B de la pérovskite, la température de calcination et la composition du mélange gazeux réactif affectent grandement la performance catalytique des pérovskites. L'étude bibliographique a également indiqué que, bien que l'utilisation de pérovskites pour la réduction du NO par le CO ait

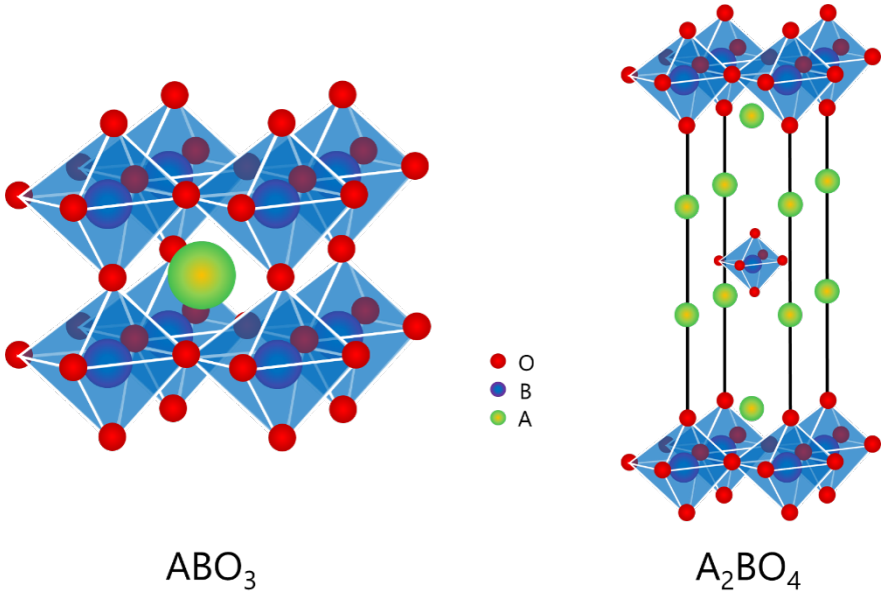

FIGURE D12 Structure cristalline des pérovskites et des matériaux de type pérovskite

été largement rapportée, ses performances dans la réduction du NO dans des conditions de gaz de combustion industrielle ont été rarement rapportées. Par conséquent, différents échantillons de pérovskite ont été préparés en utilisant la méthode conventionnelle du citrate, caractérisés pour déterminer les différentes propriétés des matériaux et testés pour leurs performances catalytiques (N_2 a été utilisé comme gaz vecteur au lieu de He).

Dans un premier temps, des échantillons de pérovskite de la forme ABO_3 avec différents cations du site B (Co, Mn et Fe) ont été considérés pour comparaison. Les analyses DRX ont montré que la structure pérovskite était formée dans chacun des échantillons et que la surface spécifique des échantillons variait entre 9-12 $m^2.g^{-1}$. Le type de cation du site B a grandement influencé le comportement redox de la pérovskite. $LaCoO_3$ a montré la consommation spécifique de H_2 la plus élevée, indiquant la disponibilité du plus grand nombre d'espèces réductibles, tandis que la consommation spécifique de H_2 la plus faible et, par conséquent, la disponibilité du plus petit nombre d'espèces réductibles a été enregistrée pour $LaFeO_3$. De plus, en comparant les activités catalytiques de ces échantillons de pérovskite dans des conditions de réaction humide et sèche, il a été observé que dans les conditions de réaction sèche (se référer à la Figure D13), l'ordre des échantillons de pérovskite pour l'activité de conversion du CO était $LaMnO_3 > LaCoO_3 \sim LaFeO_3$ alors que dans les conditions de

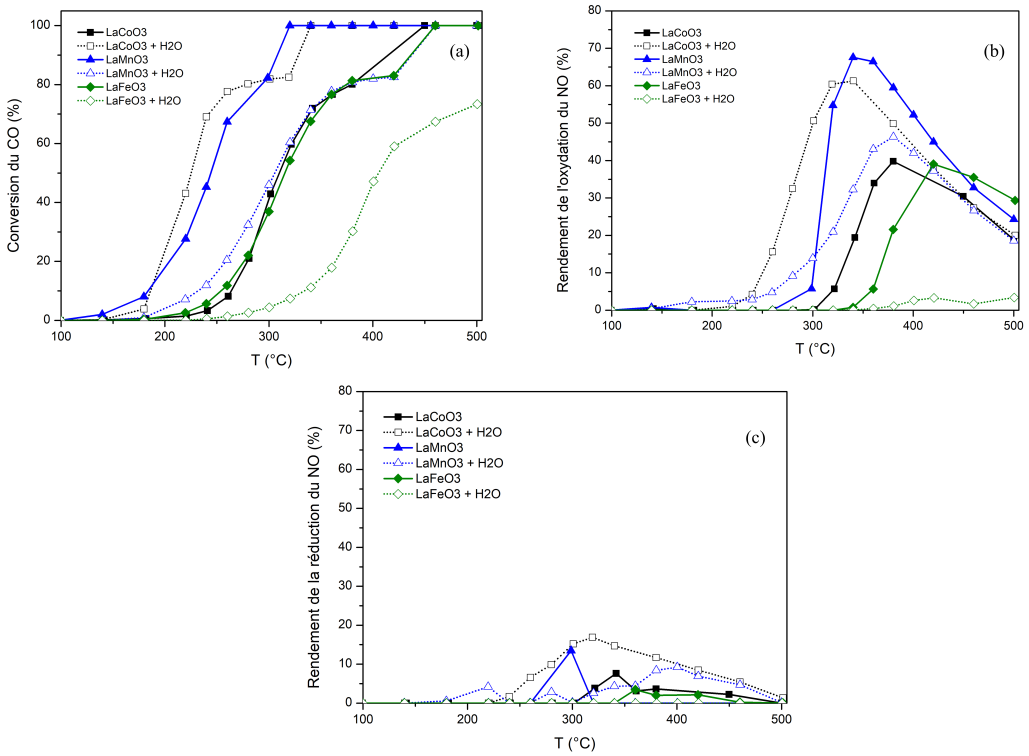

FIGURE D13 Activité catalytique des pérovskites $LaAO_3$ dans des conditions de réaction sèches et humides ($+H_2O$) : (a) conversion du CO, (b) rendement de l'oxydation du NO et (c) rendement de la réduction du NO.

réaction humide, cette tendance change en $LaCoO_3 > LaMnO_3 > LaFeO_3$. De plus, pour le rendement de réduction et d'oxydation du NO dans des conditions de réaction sèche et humide, les ordres des échantillons de pérovskite sont $LaMnO_3 > LaCoO_3 \sim LaFeO_3$ et $LaCoO_3 > LaMnO_3 > LaFeO_3$ respectivement. Cependant, ces activités catalytiques n'ont pas permis d'établir une corrélation directe entre l'activité catalytique et le comportement redox correspondant, ou les propriétés du matériau. Par conséquent, il a été conclu que des expériences de caractérisation supplémentaires, comme la spectroscopie de photoélectrons émis par rayons X (SPX), sont nécessaires pour déterminer la composition de la surface et la concentration des sites vacants d'oxygène dans les échantillons de catalyseur qui jouent un rôle crucial dans la performance catalytique de l'échantillon de pérovskite.

De plus, l'effet de la teneur en La dans la pérovskite sur l'activité catalytique a été étudié. Pour cela, le Co comme cation du site B a été considéré en raison de son activité catalytique supérieure observée précédemment et le

rapport molaire La :Co a été diminué de 1 à 0,85. Cette diminution de La a drastiquement réduit la surface spécifique de 8,4 m^2 g^{-1} à 0,9 m^2 g^{-1} et a formé l'oxyde Co_3O_4 avec la structure pérovskite comme observé dans l'analyse DRX qui a également expliqué la consommation spécifique de H_2 plus élevée que $LaCoO_3$ pendant l'analyse H_2-RTP. De plus, en comparant l'activité catalytique dans des conditions de réaction humides et sèches (voir Figure D14), il a été observé que la diminution de la teneur en La améliore la conversion du CO en déplaçant la courbe de conversion vers des températures de réaction plus basses dans les conditions de réactions sèches. Cette conversion précoce du CO peut être due à la présence de Co_3O_4 (déjà vu sous DRX) [52] et à sa forte concentration en espèces actives de cobalt (Co_3O_4) à la surface du $La_{0,85}CoO_3$ [53]. Alors, sous conditions humides, aucune différence appréciable dans la température T_{50} pour conversion du CO mais une augmentation de la température T_{90} pour la conversion du CO a été remarquée. Pour l'activité de conversion du NO, dans des conditions de réaction à sec, la diminution de la teneur en La augmente le rendement d'oxydation du NO mais diminue le rendement de réduction du NO, alors que dans des conditions de réaction humide, aucune différence appréciable dans le rendement d'oxydation du NO n'a été observée mais le rendement de réduction du NO a été réduit en diminuant la teneur en La. De plus, l'effet promotionnel de l'eau sur l'activité de réduction de NO a été observé pour les deux échantillons.

Enfin, l'effet de la substitution partielle du cation du site B par un autre cation métallique actif sur l'activité catalytique a été étudié. Pour cette étude, Cu a été utilisé comme deuxième cation métallique actif pour remplacer partiellement Co (les échantillons sont indiqués comme $La_{0,85}Co_{1-x}Cu_xO_3$ ($0 \leq x \leq 0,25$)) et un rapport molaire de La :(Co+Cu) = 0,85 a été considéré La substitution partielle de Co par Cu (pour $x = 0 \rightarrow 0,2$) a amélioré la surface spécifique des pérovskites de 0,9 à 10,7 $m^2.g^{-1}$ mais lors d'une substitution supplémentaire, la surface spécifique a diminué à 9,4 $m^2.g^{-1}$. De plus, cette substitution partielle modifie la structure cristallographique de la pérovskite pour $x \geq 0,2$ comme observé dans les analyses DRX de ces échantillons. En outre, le degré de substitution de Cu au site B affecte également la réductibilité des pérovskites qui a augmenté jusqu'à x = 0,1 puis a diminué lors d'une substitution supplémentaire jusqu'à x = 0,25. En comparant les activités catalytiques

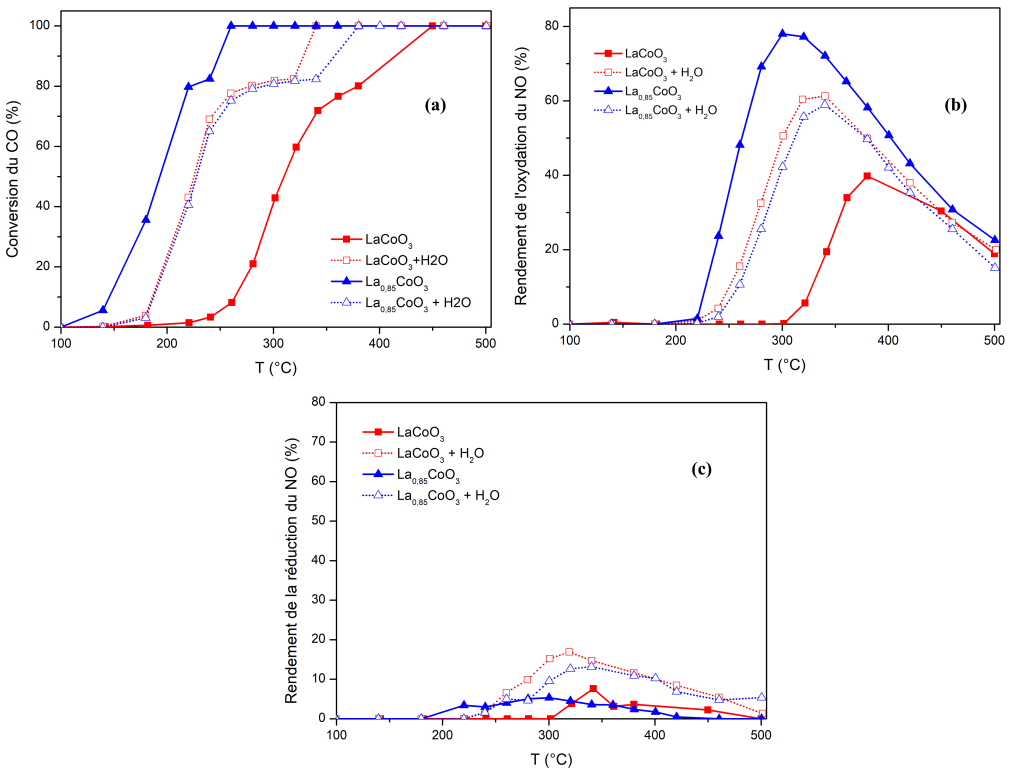

FIGURE D14 Comparaison des activités catalytiques de $LaCoO_3$ et $La0.85CoO_3$ basée sur (a) la conversion du CO (%), (b) le rendement d'oxydation du NO (%) et (c) le rendement de réduction du NO (%)

de ces échantillons de pérovskite (voir Figure D15), l'échantillon avec x = 0 et x = 0,25 a montré la meilleure et la pire activité de conversion du CO respectivement dans les conditions de réaction à sec et en milieu humide. De plus, en comparant l'activité d'oxydation du NO, l'échantillon avec x = 0,25 a montré la plus faible activité et les autres échantillons ont montré des rendements similaires dans des conditions de réaction sèches et humides. Cependant, en comparant les activités de réduction de NO de l'échantillon, l'échantillon avec x = 0,2 et x = 0,25 a montré le rendement de réduction de NO le plus élevé dans des conditions de réaction sèches et humides respectivement. De plus, l'effet promotionnel de l'eau sur l'activité de réduction de NO a également été observé pour ces échantillons.

Il a donc été conclu que les pérovskites sont actives pour la réduction du NO par la réaction du CO dans des conditions de gaz de fumée industrielle et que des techniques supplémentaires de caractérisation des matériaux comme

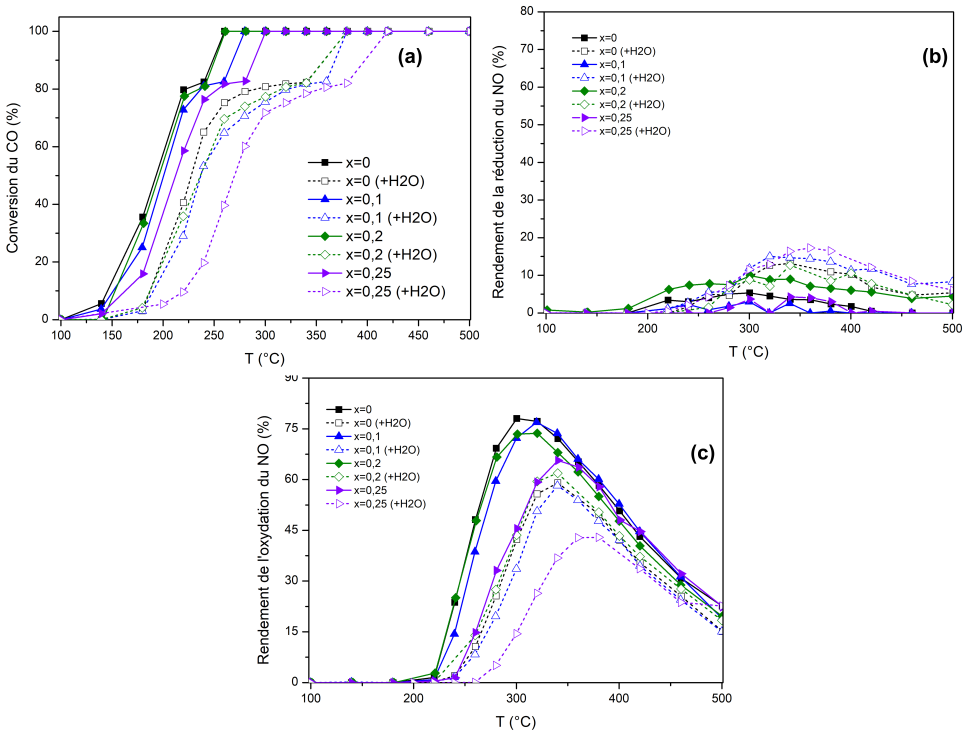

FIGURE D15 Conversions de CO et de NO pour les échantillons de pérovskite $La_{0,85}Co_xCu_{1-x}O_3$ (a) conversion de CO (b) rendement de réduction de NO et (c) rendement d'oxydation de NO

la SPX sont nécessaires pour déterminer la composition de la surface et la concentration des sites vacants d'oxygène dans les échantillons de catalyseurs

Conclusions et Perspectives

Conclusions

L'objectif de cette thèse était de développer un matériau catalytique économiquement réalisable, stable dans les conditions de réaction et démontrant une forte activité de réduction du NO. Dans cette thèse, des matériaux à base d'oxydes de métaux de transition ont été synthétisés en raison de leur coût compétitif et de leur activité catalytique comparable à celle des matériaux catalytiques à base de métaux précieux. Différents oxydes mixtes ont été synthétisés par la méthode des Hydroxydes Doubles Lamellaire (HDL), caractérisés pour déterminer les diverses propriétés des matériaux et évalués pour leur activité catalytique. Sur la base des résultats et des discussions, les conclusions

suivantes ont été tirées :

1. L'effet de l'atmosphère gazeuse de prétraitement sur la performance catalytique a été étudié sur des échantillons d'oxyde mixte CuAl dérivés du traitement thermique de leur HDL parent. Les résultats ont montré que le traitement au CO_2 du HDL forme des espèces carbonates bidentées et/ou polydentées supplémentaires qui sont stables et facilitent la réaction de réduction du NO. C'est la raison de l'activité de réduction de NO sur l'échantillon CuAl-CO_2 dans des conditions de réaction sèche. Cependant, l'activité catalytique était similaire à celle de l'échantillon traité à l'air et à l'He dans des conditions de réaction humide en raison de la dégradation possible de ces espèces de carbonate en espèces de formiate inactives. Néanmoins, il a été conclu que le traitement au CO_2 du HDL peut donner lieu à un oxyde mixte actif pour la réduction du NO par le CO dans des conditions de gaz de combustion industriel.

2. Pour améliorer encore les performances catalytiques, un second métal actif, le Co, a été introduit en différentes quantités dans l'échantillon d'oxyde mixte et son effet sur les performances catalytiques correspondantes a été étudié. Il a été conclu que l'augmentation de la teneur en Co dans l'oxyde mixte améliorait la réductibilité de l'échantillon et donc la performance catalytique. Cependant, les échantillons avec un rapport molaire Cu/Co de 0,5 et 0 ont montré une activité catalytique similaire dans des conditions de réaction humide et sèche. Compte tenu du coût élevé du Co et de la stabilité des espèces de Co par le Cu, Co_4Cu_2Al a été choisi pour des études ultérieures.

3. Pour améliorer encore l'activité catalytique, l'effet de la température de traitement sur la performance catalytique de l'échantillon de Co_4Cu_2Al a été étudié. Sur la base de la caractérisation du matériau et des résultats des tests catalytiques, il a été conclu que l'augmentation de la température de traitement augmente la cristallinité de l'échantillon d'oxyde mixte et la concentration des espèces de carbonate dans l'échantillon d'oxyde mixte, qui sont toutes deux cruciales pour la performance catalytique, en particulier la sélectivité de N_2. Sur la base de la sélectivité de N_2, 400°C a été choisi comme la température optimale pour le traitement du Co_4Cu_2Al

HDL sous le flux de CO_2.

4. La stabilité thermique du Co_4Cu_2Al-400-CO_2 a été étudiée par un vieillissement thermique rapide via 6 'light-offs' dans les conditions de réaction humide et il a été conclu que l'oxyde mixte est considérablement stable dans les conditions de réaction.

5. En outre, l'activité catalytique du Co_4Cu_2Al-400-CO_2 a été comparée à celle de catalyseurs actifs et disponibles dans le commerce, à savoir 1 wt% Pt/Al_2O_3 et 1 wt% Pt/CeO_2, dans des conditions de réaction par voie humide. Sur la base des résultats catalytiques, il a été conclu que les catalyseurs commerciaux sont supérieurs au Co_4Cu_2Al-400-CO_2 en termes d'activité de conversion du CO, mais présentent une activité de réduction du NO bien inférieure à celle de l'échantillon d'oxyde mixte de Co_4Cu_2Al-400-CO_2. Enfin, sur la base de l'activité catalytique et de la stabilité supérieure, la forme HDL du Co_4Cu_2Al a été synthétisée à grande échelle dans un réacteur batch de 10 L et a été façonnée sous forme d'extrudés pour être utilisée dans un réacteur à échelle semi-pilote et étudier ses performances catalytiques.

6. En outre, l'influence du mélange de gaz d'alimentation sur la performance catalytique a également été étudiée. On a fait varier chacun des composants gazeux du mélange de gaz d'alimentation et la quantité de catalyseur dans le réacteur et on a enregistré le changement correspondant de l'activité catalytique. Il a été conclu que le catalyseur présente différentes activités pour différentes compositions de gaz d'alimentation et poids de catalyseur. Ces données ont ensuite été utilisées pour développer un modèle cinétique basé sur la cinétique de Langmuir Hinshelwood Hougen Watson (LHHW). Les paramètres du modèle ont été régressés à l'aide de l'algorithme général de recherche de motifs disponible dans le logiciel MATLAB 2020a. De plus, les paramètres les plus sensibles du modèle ont été déterminés et régressés davantage afin d'obtenir une meilleure adaptation aux données expérimentales.

7. Enfin, une étude bibliographique approfondie a été réalisée sur les pérovskites comme matériau catalytique potentiel pour la réduction du NO par le CO. Dans cette thèse, des études préliminaires sur différentes pérovskites

ont été réalisées et leur activité catalytique dans des conditions de gaz de fumée industrielle a été évaluée. Dans un premier temps, des échantillons de pérovskite avec différents cations de site B (Co, Mn et Fe) ont été étudiés pour leurs propriétés matérielles et leur performance catalytique. $LaCoO_3$ a montré une activité catalytique supérieure aux autres et a donc été choisi pour des études ultérieures. Ensuite, l'influence de la faible teneur en La (La :Co = 0,85) sur le site A de l'échantillon de pérovskite sur la performance catalytique a été étudiée et il a été conclu que la diminution de la teneur en La ($La_{0,85}CoO_3$) a amélioré l'activité de conversion du CO mais a augmenté l'activité indésirable d'oxydation du NO dans des conditions de réaction sèche, tandis que dans des conditions de réaction humide, aucun changement appréciable dans l'activité de conversion du NO entre les échantillons $LaCoO_3$ et $La_{0,85}CoO_3$ n'a été observé. Enfin, le Co dans $La_{0,85}CoO_3$ a été partiellement substitué par du Cu et l'influence de différents degrés de cette substitution sur les propriétés du matériau et l'activité catalytique a été étudiée. Il a été conclu qu'aucune corrélation claire n'a pu être établie entre la réductibilité des espèces métalliques actives, la surface spécifique et l'activité catalytique. Par conséquent, d'autres techniques de caractérisation des matériaux, comme le SPX, pour déterminer les espèces métalliques de surface et la concentration des sites vacants d'oxygène dans les échantillons, ont été proposées pour expliquer les différents comportements catalytiques.

Perspectives

Les résultats de cette thèse ont montré que le CO peut être un bon réducteur de NO dans des conditions de gaz de combustion industriel et sur des matériaux à base de cobalt-cuivre comme catalyseur. Cependant, une activité maximale de réduction de NO de 40 % a été atteinte (en considérant N_2 comme vecteur gazeux). Néanmoins, cette étude ouvre la possibilité d'utiliser des catalyseurs à base de métaux de transition pour la réduction du NO dans des conditions de gaz de combustion industrielle.

1. Dans cette étude, les oxydes mixtes Co_4Cu_2Al ont été synthétisés à différentes températures de traitement, ce qui a différentes activités catalytiques. La présence de différentes concentrations de carbonates dans

l'échantillon d'oxyde mixte peut être l'une des raisons plausibles d'un tel comportement catalytique. Cependant, il est important de quantifier le type d'espèces de carbonates (tels que les carbonates monodentés ou bidentés) présentes dans les échantillons via des techniques comme la spectroscopie Raman et de comparer leurs propriétés d'acido-basicité déterminées par CO_2 ou NH_3-TPD pour comprendre pleinement leur comportement catalytique correspondant. En outre, le Co_4Cu_2Al synthétisé à grande échelle devrait être testé sur le dispositif d'essai semi-pilote qui est actuellement en cours de développement dans le laboratoire Université de Mons (UMONS). Les résultats de cette installation devraient être comparés à ceux des tests à l'échelle du laboratoire afin de visualiser l'effet de la mise à l'échelle sur l'activité catalytique.

2. L'autre aspect qui peut être étudié est l'utilisation de différents promoteurs acides comme Ce et Zr, des promoteurs basiques comme Mg et des promoteurs de métaux alcalins comme K dans les matériaux catalytiques et leur effet sur la performance catalytique correspondante. Le Ce et le Zr sont connus pour leur capacité exceptionnelle de stockage de l'oxygène et leurs propriétés redox qui peuvent être un avantage pour les métaux actifs, tandis que le Mg peut améliorer la dispersion du métal actif dans le matériau et l'interaction du métal actif avec d'autres métaux promoteurs, ce qui peut améliorer l'activité catalytique, et le K peut améliorer l'adsorption des molécules réactives et donc augmenter la probabilité de réaction en surface.

3. Dans le dernier chapitre de cette thèse, il a été démontré que les matériaux pérovskites sont également actifs pour la réduction du NO par le CO dans des conditions de gaz de fumée industrielle. Le cuivre semble être actif pour la réaction de réduction du NO dans ces conditions et peut donc être utilisé comme métal actif secondaire dans la pérovskite en substituant partiellement différents cations du site B comme Fe et Mn et l'influence du degré de substitution sur leurs performances catalytiques peut être étudiée. De plus, des techniques de caractérisation de surface comme la SPX peuvent être utilisées pour déterminer la composition du matériau à la surface du catalyseur et la concentration des sites vacants d'oxygène sur le catalyseur, deux facteurs importants qui influencent les matériaux

catalytiques. En outre, l'effet de l'inclusion d'une faible concentration de métaux précieux provenant des métaux du groupe du platine (MGP) comme le Pt, le Pd et/ou le Rh sur l'activité catalytique peut également être étudié. De telles études avec des pérovskites comme catalyseur dans des conditions de gaz de fumée industrielle ont été rarement rapportées dans la littérature et, par conséquent, ces études peuvent fournir de nouveaux résultats.

4. Dans cette thèse, le modèle cinétique est développé pour le système réactionnel en considérant un seul type de site actif dans le matériau catalytique. Cependant, dans le cas de catalyseurs binaires à base d'oxyde métallique, plus d'un type de site actif est attendu. Par conséquent, le modèle cinétique actuel peut être développé davantage pour inclure un mécanisme à double site considérant différents sites actifs pour l'adsorption de diverses molécules réactives. De plus, des tests catalytiques avec différentes GHSV peuvent également être réalisés et les résultats peuvent être utilisés pour la régression des paramètres du modèle cinétique. De plus, le modèle cinétique développé dans cette thèse ne suit pas le modèle de cinétique LHHW recommandé dans Aspen Plus et donc, une routine FORTRAN doit être développée qui utilise la cinétique définie par l'utilisateur et simulée en utilisant le réacteur RPLUG disponible dans le logiciel. Enfin, le modèle cinétique développé précédemment peut également être étendu aux matériaux à base de pérovskite.

References

[1] O. Edenhofer, Y. Sokona, J.C. Minx, E. Farahani, S. Kadner, K. Seyboth, A. Adler, I. Baum, S. Brunner, B. Kriemann, J. Savolainen Web Manager Steffen Schlömer, C. von Stechow, T. Zwickel Senior Scientist, Climate Change 2014 Mitigation of Climate Change Working Group III Contribution to the Fifth Assessment Report of the Intergovernmental Panel on Climate Change, 2014.

[2] International Energy Agency ;, Transforming Industry through CCUS, 2019. https ://doi.org/10.1787/09689323-en.

[3] N. Meunier, S. Laribi, L. Dubois, D. Thomas, G. De Weireld, CO_2 capture in cement production and re-use : First step for the optimization of the overall process, Energy Procedia. 63 (2014) 6492–6503.
https ://doi.org/10.1016/j.egypro.2014.11.685.

[4] L.T. Murciano, V. White, F. Petrocelli, D. Chadwick, Sour compression process for the removal of SO_x and NO_x from oxyfuel-derived CO_2, Energy Procedia. 4 (2011) 908–916.
https ://doi.org/10.1016/j.egypro.2011.01.136.

[5] H. Sjövall, L. Olsson, E. Fridell, R.J. Blint, Selective catalytic reduction of NO_x with NH_3 over Cu-ZSM-5-The effect of changing the gas composition, Appl. Catal. B Environ. 64 (2006) 180–188.
https ://doi.org/10.1016/j.apcatb.2005.12.003.

[6] M.M. Behera, C. Ciotonea, L. Olivet, L. Tidahy, S. Royer, D. Thomas, R. Cousin, G. De Weireld, C. Poupin, Impact of gas treatment of CuAl-LDH on NO reduction by CO under oxidative conditions, Chem. Eng. J. 452 (2023).
https ://doi.org/10.1016/j.cej.2022.139543.

[7] L. Dubois, D. Thomas, Simulations of various Configurations of the Post-

combustion CO_2 Capture Process Applied to a Cement Plant Flue Gas : Parametric Study with Different Solvents, Energy Procedia. 114 (2017) 1409–1423. https ://doi.org/10.1016/j.egypro.2017.03.1265.

[8] Y. Hu, L. Dong, M. Shen, D. Liu, J. Wang, W. Ding, Y. Chen, Influence of supports on the activities of copper oxide species in the low-temperature NO + CO reaction, 2001.
https ://doi.org/10.1016/S0926-3373(00)00269-1.

[9] C.L. Oliveira Corrêa, Y.E. Licea, L. Amparo Palacio, F.M. Zanon Zotin, Effect of composition and thermal treatment in catalysts derived from Cu-Al hydrotalcites-like compounds in the NO reduction by CO, Catal. Today. 289 (2017) 133–142.
https ://doi.org/10.1016/j.cattod.2016.08.023.

[10] A. Patel, T.E. Rufford, V. Rudolph, Z. Zhu, Selective catalytic reduction of NO by CO over CuO supported on SBA-15 : Effect of CuO loading on the activity of catalysts, Catal. Today. 166 (2011) 188–193.
https ://doi.org/10.1016/j.cattod.2010.05.040.

[11] X. Gu, H. Li, L. Liu, C. Tang, F. Gao, L. Dong, Promotional effect of CO pretreatment on CuO/CeO_2 catalyst for catalytic reduction of NO by CO, J. Rare Earths. 32 (2014) 139–145.

https ://doi.org/10.1016/S1002-0721(14)60043-0.

[12] X. Zhang, C. Ma, X. Cheng, Performance of Fe-Ba/ZSM-5 catalysts in $NO+O_2$ adsorption and NO+CO reduction, Int. J. Hydrogen Energy. 42 (2017) 7077–7088.
https ://doi.org/10.1016/j.ijhydene.2017.01.067.

[13] T. Yamamoto, T. Tanaka, R. Kuma, S. Suzuki, F. Amano, Y. Shimooka,

Y. Kohno, T. Funabiki, S. Yoshida, NO reduction with CO in the presence of O_2 over Al_2O_3-supported and Cu-based catalysts, Phys. Chem. Chem. Phys. 4 (2002) 2449–2458.
https ://doi.org/10.1039/b201120b.

[14] Y. Wang, A. Zhu, Y. Zhang, C.T. Au, X. Yang, C. Shi, Catalytic reduction of NO by CO over NiO/CeO_2 catalyst in stoichiometric NO/CO and $NO/CO/O_2$ reaction, Appl. Catal. B Environ. 81 (2008) 141–149.
https ://doi.org/10.1016/j.apcatb.2007.12.005.

[15] Q. Yu, X. Yao, H. Zhang, F. Gao, L. Dong, General Effect of ZrO_2 addition method on the activity of Al_2 O_3-supported CuO for NO reduction with CO : Impregnation vs . coprecipitation, "Applied Catal. A, Gen. 423–424 (2012) 42–51.
https ://doi.org/10.1016/j.apcata.2012.02.017.

[16] R. Nickolov, N. Stankova, M. Khristova, D. Mehandjiev, Copper oxide supported on carbon modified alumina as catalyst for reduction of NO with CO, J. Colloid Interface Sci. 265 (2003) 121–128.
https ://doi.org/10.1016/S0021-9797(03)00278-9.

[17] X. Jiang, G. Ding, L. Lou, Y. Chen, X. Zheng, Effect of ZrO_2 addition on CuO/TiO_2 activity in the NO+CO reaction, Catal. Today. 93–95 (2004) 811–818.
https ://doi.org/10.1016/j.cattod.2004.06.074.

[18] X. Yao, F. Gao, Q. Yu, L. Qi, C. Tang, L. Dong, Y. Chen, NO reduction by CO over $CuO\text{-}CeO_2$ catalysis : effect of preparation methods, Catal. Sci. Technol. (2013).
https ://doi.org/10.1039/c3cy20805b.

[19] Z. Gholami, G. Luo, Low-temperature selective catalytic reduction of NO

by CO in the presence of O_2 over Cu : Ce catalysts supported by multi-walled carbon nanotubes, Ind. Eng. Chem. Res. (2018).
https ://doi.org/10.1021/acs.iecr.8b01343.

[20] J. Sun, C. Ge, X. Yao, W. Zou, X. Hong, C. Tang, L. Dong, Influence of different impregnation modes on the properties of CuO-CeO_2 /Al_2O_3 catalysts for NO reduction by CO, Appl. Surf. Sci. 426 (2017) 279–286.
https ://doi.org/10.1016/j.apsusc.2017.07.069.

[21] X. Cheng, L. Wang, Z. Wang, M. Zhang, C. Ma, Catalytic Performance of NO Reduction by CO over Activated Semicoke Supported Fe / Co Catalysts, Ind. Eng. Chem. Res. (2016).
https ://doi.org/10.1021/acs.iecr.6b00804.

[22] B. Wen, M. He, E. Schrum, C. Li, NO reduction and CO oxidation over Cu/Ce/Mg/Al mixed oxide catalyst in FCC operation, J. Mol. Catal. A Chem. 180 (2002) 187–192.
https ://doi.org/10.1016/S1381-1169(01)00427-7.

[23] J. Li, S. Wang, L. Zhou, G. Luo, F. Wei, NO reduction by CO over a Fe-based catalyst in FCC regenerator conditions, Chem. Eng. J. 255 (2014) 126–133.

https ://doi.org/10.1016/j.cej.2014.06.015.

[24] C.A. Sierra-Pereira, E.A. Urquieta-González, Reduction of NO with CO on CuO or Fe_2O_3 catalysts supported on TiO_2 in the presence of O_2, SO_2 and water steam, Fuel. 118 (2014) 137–147.
https ://doi.org/10.1016/j.fuel.2013.10.054.

[25] A. Alejandre, F. Medina, P. Salagre, X. Correig, J.E. Sueiras, Preparation and study of Cu-Al mixed oxides via hydrotalcite-like precursors, Chem. Mater. 11 (1999) 939–948.

https ://doi.org/10.1021/cm980500f.

[26] C. Ge, L. Liu, X. Yao, C. Tang, F. Gao, L. Dong, Treatment induced remarkable enhancement of low-temperature activity and selectivity of copper-based catalysts for NO reduction, Catal. Sci. Technol. 3 (2013) 1547–1557.
https ://doi.org/10.1039/c3cy20698j.

[27] C.D.O.P. Teixeira, S.D.S. Montani, L.A. Palacio, F.M.Z. Zotin, The effect of preparation methods on the thermal and chemical reducibility of Cu in Cu-Al oxides, Dalt. Trans. 47 (2018) 10989–11001.
https ://doi.org/10.1039/c8dt01150h.

[28] J. Chen, J. Zhu, Y. Zhan, X. Lin, G. Cai, K. Wei, Q. Zheng, Characterization and catalytic performance of Cu/CeO_2 and Cu/MgO-CeO_2 catalysts for NO reduction by CO, Appl. Catal. A Gen. 363 (2009) 208–215.
https ://doi.org/10.1016/j.apcata.2009.05.017.

[29] L.F. Liotta, G. Pantaleo, G. Di Carlo, G. Marcì, G. Deganello, Structural and morphological investigation of a cobalt catalyst supported on alumina-baria : Effects of redox treatments on the activity in the NO reduction by CO, Appl. Catal. B Environ. 52 (2004) 1–10.
https ://doi.org/10.1016/j.apcatb.2004.03.003.

[30] J.S. Shu, W.S. Xia, Y.J. Zhang, T. Cheng, M.R. Gao, Low-temperature catalytic reduction of nitrogen monoxide with carbon monoxide on copper iron and copper cobalt composite oxides, Chinese J. Chem. Phys. 21 (2008).
https ://doi.org/10.1088/1674-0068/21/04/393-400.

[31] X. Du, T.L. Yao, Q. Wei, H. Zhang, Y. Huang, Investigation of FeNi Mixed-Oxide Catalysts for the Reduction of NO by CO : Physicochemical Properties and Catalytic Performance, Chem.-An Asian J. 14 (2019) 2966–2978.
https ://doi.org/10.1002/asia.201900782.

[32] T.J. Huang, T.C. Yu, Calcination conditions on copper/alumina catalysts for carbon monoxide oxidation and nitric oxide reduction, Appl. Catal. 71 (1991) 275–282.
https ://doi.org/10.1016/0166-9834(91)85085-A.

[33] J. Yan, M.C. Kung, W.M.H. Sachtler, H.H. Kung, Co/Al_2O_3 Lean NO_x Reduction Catalyst, J. Catal. 172 (1997) 178–186.

[34] X. Chen, J. Zhang, Y. Huang, Z. Tong, M. Huang, Catalytic reduction of nitric oxide with carbon monoxide on copper-cobalt oxides supported on nano-titanium dioxide, J. Environ. Sci. 21 (2009) 1296–1301.
https ://doi.org/10.1016/S1001-0742(08)62418-3.

[35] G.Z. Gassan–zedeh, S.F. Seyidbayova, The heterogeneous catalytic reduction of NO and N_2O mixture by carbon monoxide, Appl. Catal. B Environ. 42 (2003) 359–367.
https ://doi.org/10.1016/j.apsusc.2010.01.075.

[36] C. V. Ovesen, P. Stoltze, J.K. Nørskov, C.T. Campbell, A kinetic model of the water gas shift reaction, J. Catal. 134 (1992) 445–468.
https ://doi.org/10.1016/0021-9517(92)90334-E.

[37] A.A. Gokhale, J.A. Dumesic, M. Mavrikakis, On the mechanism of low-temperature water gas shift reaction on copper, J. Am. Chem. Soc. 130 (2008) 1402–1414.
https ://doi.org/10.1021/ja0768237.

[38] C.H. Lin, C.L. Chen, J.H. Wang, Mechanistic studies of water-gas-shift reaction on transition metals, J. Phys. Chem. C. 115 (2011) 18582–18588.
https ://doi.org/10.1021/jp2034467.

[39] A. Eftaxias, J. Font, A. Fortuny, A. Fabregat, F. Stu, Nonlinear kinetic parameter estimation using simulated annealing, 26 (2002) 1725–1733.

[40] A. Pandya, J. Mmbaga, R.E. Hayes, W. Hauptmann, M. Votsmeier, Global Kinetic Model and Parameter Optimization for a Diesel Oxidation Catalyst, Top. Catal. 52 (2009) 1929–1933.
https ://doi.org/10.1007/s11244-009-9361-7.

[41] S. Fatemi, M. Masoori, R. Bozorgmehry Boozarjomehry, Application of genetic algorithm in kinetic modeling and reaction mechanism studies, Iran. J. Chem. Chem. Eng. 24 (2005) 37–46.

[42] S.K. Rao, R. Imam, K. Ramanathan, S. Pushpavanam, Sensitivity analysis and kinetic parameter estimation in a three way catalytic converter, Ind. Eng. Chem. Res. 48 (2009) 3779–3790.
https ://doi.org/10.1021/ie801244w.

[43] H.M. Gutmann, A Radial Basis Function Method for Global Optimization, J. Glob. Optim. 19 (2001) 201–227.
https ://doi.org/10.1023/A :1011255519438.

[44] D.B. Pal, R. Chand, S.N. Upadhyay, P.K. Mishra, Performance of water gas shift reaction catalysts : A review, Renew. Sustain. Energy Rev. 93 (2018) 549–565.
https ://doi.org/10.1016/j.rser.2018.05.003.

[45] J. Akil, C. Ciotonea, S. Siffert, S. Royer, L. Pirault-Roy, R. Cousin, C. Poupin, NO reduction by CO under oxidative conditions over CoCuAl mixed oxides derived from hydrotalcite-like compounds : Effect of water, Catal. Today. (2021).
https ://doi.org/10.1016/j.cattod.2021.05.014.

[46] G.C. Chinchen, M.S. Spencer, K.C. Waugh, D.A. Whan, Promotion of metha-

nol synthesis and the water-gas shift reactions by adsorbed oxygen on supported copper catalysts, J. Chem. Soc. Faraday Trans. 1 Phys. Chem. Condens. Phases. 83 (1987) 2193–2212.
https ://doi.org/10.1039/F19878302193.

[47] K. Liu, F. Liu, L. Xie, W. Shan, H. He, DRIFTS study of a Ce-W mixed oxide catalyst for the selective catalytic reduction of NO_x with NH_3, Catal. Sci. Technol. 5 (2015) 2290–2299.
https ://doi.org/10.1039/c4cy01550a.

[48] J. Akil, S. Siffert, L. Pirault-Roy, S. Royer, F. Shen, W. Chen, R. Cousin, C. Poupin, Investigation of catalysts M/CeO_2 (M = Pt, Rh, or Pd) for purification of CO_{22} derived from oxycombustion in the absence or presence of water, Environ. Sci. Pollut. Res. 28 (2021) 12521–12532.
https ://doi.org/10.1007/s11356-020-11252-7.

[49] J. Akil, S. Siffert, P.R. Laurence, D.P. Debecker, F. Devred, R. Cousin, C. Poupin, Effect of precious metals on NO reduction by CO in oxidative conditions, Appl. Sci. 10 (2020).
https ://doi.org/10.3390/app10093042.

[50] D. Mantri, P. Aghalayam, Detailed surface reaction mechanism for reduction of NO by CO, Catal. Today. 119 (2007) 88–93.
https ://doi.org/10.1016/j.cattod.2006.08.002.

[51] T. Kolli, K. Rahkamaa-Tolonen, U. Lassi, A. Savimäki, R.L. Keiski, Comparison of catalytic activity and selectivity of Pd/(OSC + Al_2O_3) and (Pd + OSC)/Al_2O_3 catalysts, Catal. Today. 100 (2005) 297–302.
https ://doi.org/10.1016/j.cattod.2004.09.064.

[52] S. Wang, P. Xiao, X. Xu, H. Bi, X. Liu, J. Zhu, Catalytic CO oxidation and CO+NO reduction conducted on La-Co-O composites : The synergistic effects

between Co_3O_4 and $LaCoO_3$, Catal. Today. (2020) 1–7.
https ://doi.org/10.1016/j.cattod.2020.05.035.

[53] A. Schön, C. Dujardin, J.P. Dacquin, P. Granger, Enhancing catalytic activity of perovskite-based catalysts in three-way catalysis by surface composition optimisation, Catal. Today. 258 (2015) 543–548.
https ://doi.org/10.1016/j.cattod.2014.11.002.